Research on production of new medical radioisotopes with cyclotron

Mateusz Sitarz

UNIVERSITY OF WARSAW

UNIVERSITÉ DE NANTES

DOCTORAL THESIS

Research on production of new medical radioisotopes with cyclotron

by Mateusz Sitarz

A thesis prepared at

University of Warsaw, Faculty of Physics, Nuclear Physics Division

University of Nantes, Doctoral School N° 596 *Matière, Molécules et Matériaux*

within the *cotutelle* agreement

and presented in Warsaw on 23.09.2019

Reviewers:	
Prof. Jerzy Mietelski	Institute of Nuclear Physics, Polish Academy of Sciences
DSc. Gilles De France	Grand Accélérateur National d'Ions Lourds, France
Examiners:	
DSc. Jarosław Żygierewicz	Faculty of Physics, University of Warsaw, Poland
Prof. Ulli Köster	Institute Laue-Langevin, France
Supervisors:	
Prof. Tomasz Matulewicz	Faculty of Physics, University of Warsaw, Poland
Prof. Férid Haddad	GIP ARRONAX & University of Nantes, France
Co-supervisor:	
Dr. Agnieszka Trzcińska	Heavy Ion Laboratory, University of Warsaw, Poland

"*And thus the bitter task forego*
Of saying the things I do not know,–
That I may detect the inmost force
Which binds the world, and guides its course;
Its germs, productive powers explore,
And rummage in empty words no more"

Johann Wolfgang von Goethe, *Faust*
trans. Bayard Taylor

Research on production of new medical radioisotopes with cyclotron

Today, radioisotopes are commonly used in medicine, both in diagnosis and therapy. However, steady development of nuclear medicine demands the application of new medical radioisotopes. The investigation of their possible large-scale production is a first step in a long research process before they can be used in clinical trials.

In this thesis, the production routes were studied for the formation of medically interesting ^{43}Sc, ^{44m,g}Sc, ^{47}Sc, ^{97}Ru, and ^{105}Rh with the use of cyclotrons. The scandium radioisotopes were produced with calcium and titanium targets and proton or deuteron beams; ^{97}Ru was obtained through the irradiation of molybdenum with α particles; and production of ^{105}Rh was studied with ruthenium targets and deuteron beam. Two parameters were determined experimentally: nuclear reaction cross-section, $\sigma(E)$, and Thick Target Yield, $TTY(E)$, which were used to discuss the possibility of optimal large-scale production conditions of discussed radioisotopes. Additionally, the conversion of $\sigma(E)$ to $TTY(E)$ was automatized by developing a dedicated software, and an algorithm for the reconstruction of $\sigma(E)$ based on $TTY(E)$ measurements was introduced.

Badania cyklotronowej produkcji nowych radioizotopów medycznych

Obecnie, radioizotopy są powszechnie używane w medycynie, zarówno do diagnostyki jak i do terapii. Jednak ciągły rozwój medycyny nuklearnej wymaga zastosowania nowych radioizotopów medycznych. Poszukiwania ich możliwej produkcji na dużą skalę to pierwszy krok w długim procesie badań, zanim trafią one do prób klinicznych.

W tej rozprawie, zbadano drogi produkcji medycznych radioizotopów ^{43}Sc, ^{44m,g}Sc, ^{47}Sc, ^{97}Ru oraz ^{105}Rh z użyciem cyklotronów. Radioizotopy skandu zostały wyprodukowane z użyciem tarcz wapiennych i tytanowych oraz wiązek protonów i deuteronów; ^{97}Ru był otrzymany przez aktywację molibdenu wiązką cząstek α; natomiast produkcja ^{105}Rh została zbadana z użyciem tarcz rutenowych i wiązki deuteronów. Dwa parametry zostały zmierzone: przekrój czynny na reakcję jądrową, $\sigma(E)$, oraz wydajność produkcji, $TTY(E)$, które posłużyły do oszacowania warunków do optymalnej produkcji badanych radioizotopów na dużą skalę. Dodatkowo, zautomatyzowano przeliczenie $\sigma(E)$ do $TTY(E)$ za pomocą stworzonego oprogramowania, oraz zaproponowano algorytm rekonstrukcji $\sigma(E)$ na podstawie pomiarów $TTY(E)$.

Recherche sur la production des nouveaux radio-isotopes médicaux par cyclotron

Aujourd'hui, les radio-isotopes sont fréquemment utilisés en médecine, pour le diagnostic et la thérapie. Cependant, le développement constant de la médecine nucléaire provoque l'application de nouveaux radio-isotopes médicaux. La recherche sur leur production possible à grande échelle est la première étape d'un long processus d'études avant de pouvoir de les utilisé dans des essais cliniques.

Dans cette thèse, les voies de production ont été étudiées pour la formation de médicalement intéressants ^{43}Sc, ^{44m,g}Sc, ^{47}Sc, ^{97}Ru et ^{105}Rh en utilisant de cyclotrons. Les radioisotopes de scandium ont été produits avec des cibles en calcium et en titane et avec des faisceaux de protons ou de deutérons; ^{97}Ru a été obtenu par irradiation de molybdène avec des particules α; et la production de ^{105}Rh a été étudiée avec des cibles en ruthénium et avec un faisceau de deutéron. Deux grandeurs ont été déterminés expérimentalement: la section efficace de réaction nucléaire, $\sigma(E)$, et l'efficacité de la production, $TTY(E)$, qui ont été utilisés pour discuter des conditions possibles de production optimale à grande échelle de ces radio-isotopes. De plus, la conversion de $\sigma(E)$ en $TTY(E)$ a été automatisée en développant un logiciel spécialisé, et un algorithme de reconstruction de $\sigma(E)$ avec des valuers de $TTY(E)$ a été introduit.

Acknowledgements

During my studies I have met several extraordinary people and a simple *Acknowledgements* section is not enough to express how much I appreciate their support. It was an incredible pleasure to work with them and I thank them from the bottom of my heart:

Prof. Tomasz Matulewicz – for his inspiring lust for knowledge, for his overextended commitment to all my activities, for always having my back, for answering any question, and for the enlightening debates about nuclear physics and world in general.

Prof. Férid Haddad – for always seeing the bigger picture, for his trust and positive thinking, for doing way too much job for me, for being always there if needed, for supporting me in the moments of scientific crises, and for showing me how to throw stones to track them back.

Dr. Agnieszka Trzcińska – for her help in solving numerous small and big problems alike, for her patience and friendly guidance during several years, and for carrying for my health better than me.

Prof. Jerzy Jastrzębski – for his encouragements and motivations, for always having my interest at heart, for his full dedication and leadership, and for introducing me to the modern scientific community.

DSc. Anna Stolarz – for the open-minded discussions, for her courage to address difficult questions, and for the editorial help.

MSc. Etienne Nigron – for helping me with every single experiment in France, and for the "french lessons".

Dr. Arnaud Guertin – for always finding better solutions, both in the laboratory and in the manuscripts.

Dr. Katarzyna Szkliniarz – for her fully dependable assistance in the data analysis.

Prof. Wiktor Zipper – for providing the reliable methodology and looking after it.

MSc. Rafał Walczak – for his continuous feedback.

Prof. Aleksander Bilewicz – for encouraging collaboration, and for his interesting ideas.

Prof. Ulli Köster – for sharing his knowledge regardless of distance limitations, and for the *Gedankenexperimente*.

Experiments performed in Poland would not be possible without the teams of Heavy Ion Laboratory, University of Warsaw and National Centre for Nuclear Research, whose hard work and professional help are greatly acknowledged. Special thanks go to the team of GIP ARRONAX for their competent assistance during experiments performed in France and for accepting me in their small family.

I would like to thank Faculty of Physics, University of Warsaw for the scholarship during my studies and Heavy Ion Laboratory, University of Warsaw for the financial support during my work in Poland. I would also like to express my gratitude for the French Government Scholarship *cotutelle* during my stay in France.

Part of the work was performed within the framework of the EU Horizon 2020 project RIA-ENSAR2 (654 002). This research was also partly supported by the Polish Funding Agency, National Centre for Research and Development, grant no. DZP/PBS3/2319/2014, a grant from the French National Agency for Research called "Investissements d'Avenir", Equipex Arronax-Plus no. ANR-11-EQPX-0004, Labex IRON no. ANR-11-LABX-18-01 and ISITE NEXT no. ANR-16-IDEX-0007. The cyclotron ARRONAX is supported by CNRS, Inserm, INCa, the Nantes University, the Regional Council of Pays de la Loire, local authorities, the French government, and the European Union.

Contents

Chapter 1

Introduction

1.1 Brief history of nuclear medicine

In 20th century, Karl Popper concluded that we study the ideas of the universe based on their manifestations in the reality and so it is relatively easy to advance in natural sciences, where many manifestations are stable [1]. And indeed, Popper's times flourished with amazing discoveries in physics, engineering, chemistry and biology as well as with the interesting insight to bring their advanced methods to the medicine.

The fusion between modern physics and medicine started in 1895 when Wilhelm Roentgen discovered the x-ray and its application to visualize the internal structures of the human body without the necessity of surgery (Nobel Prize in 1901). Later, the phenomena of radioactivity and the methods for its measurements were discovered by Marie Skłodowska Curie who received two Nobel Prizes, in 1903 and 1911 (the first one jointly with Pierre Curie and Henri Becquerel). Shortly after, Irène (the daughter of Marie and Pierre) and Frédéric Joliot-Curie succeeded in using the radiation to induce radioactivity in previously stable material (Nobel Prize in 1935). Then, tools were provided for the large-scale production of radioactive materials. In 1938, Otto Hahn and Fritz Strassmann observed for the first time a nuclear fission (Nobel Prize in 1944) which soon led to the nuclear reactors [2], while in 1939 Ernest Lawrence won the Nobel Prize for his invention of the cyclotron. At this time, John Lawrence (the brother of Ernest) and many other researchers, started the clinical trials using dedicated radioactive substances to treat tumors [3]. The key in these studies, the tracer principle, brought the Nobel Prize to George de Hevesy in 1943. Several years of research passed before the emission reconstruction tomography was introduced by David Kuhl and Roy Edwards in 1963 (summarised in [4]), which eventually gave rise to computed tomography (CT), single-photon emission computed tomography (SPECT), and positron emission tomography (PET), the versatile and reliable diagnostic techniques.

Today, we benefit from above-mentioned milestones in the field of nuclear medicine, "a speciality that involves the use of radioactive isotopes in the diagnosis and treatment of disease" [5], in particular of tumors, the second leading cause of death equally in developed and underdeveloped countries [6]. Over 40 million nuclear medicine procedures are performed each year [7] fueled by around 50 different radioisotopes [7] produced mainly either in around 80 dedicated nuclear reactors [8] or in over 1200 dedicated cyclotrons [9]. The use of radioisotopes often comes with complementary techniques, like in the case of the hybrid imaging with PET/MRI [10, 11] or PET/CT [12], which substantially improve the effectiveness of these modalities. Similarly, the radioisotope-based therapy is accompanied by various procedures (including surgery, chemotherapy or external beam therapy) to improve the effects of the treatment [13]. More importantly, many innovative solutions were introduced recently to the nuclear medicine, mainly: $\beta^+\gamma$ coincidence imaging and new detector systems (like XEMIS or J-PET) (see Appendix B), the procedure of labelling of nanoparticles [14] and microspheres [15], radioimmunotherapy with the use of monoclonal antibodies [16], combination therapy (which uses multiple radioisotopes) [17], and theranostic (which is a fusion of diagnostic and therapeutic approaches) (see Section 2.3.5). At the same time, new methods for optimal production of other attractive radioisotopes are being constantly developed [18, 19]. In the light of the increasing cases of cancer each year [20], this evolution of nuclear medicine is really paramount.

1.2 Aim of this thesis

One could say that nuclear medicine is like a clock since it is based on the collective work of several specialists from multiple disciplines. However it is a special, self-improving clock which elements stimulate one another. For example, the development of modalities in medicine demands the research and production of new radioisotopes. At the same time, studies of innovative production routes encourage the use of new techniques for imaging or therapy.

This thesis is an attempt to outline this particular relation: between the nuclear physics behind the production of radioisotopes and modern solutions in nuclear medicine. Following radioisotopes were selected for this purpose: ^{97}Ru, ^{105}Rh, and ^{43,44g,m,47}Sc. Their cross-sections and Thick Target Yields are studied with the use of cyclotrons located in three laboratories:

- Heavy Ion Laboratory, University of Warsaw, Poland,
- GIP ARRONAX, Saint-Herblain, France,
- National Centre for Nuclear Research, Świerk, Poland.

The aim of these studies is to confirm the efficient production routes offered by the cyclotrons for above-mentioned (and other) medical radioisotopes. Additionally, a software for the calculation of Thick Target Yield is developed, and an algorithm for the cross-section reconstruction is introduced. The conclusions and tools presented in this thesis might help other physicists working on the production of the medical radioisotopes to push the evolution of nuclear medicine even further.

The following articles have been published based on the results from this work:

- Mateusz Sitarz, Katarzyna Szkliniarz, Jerzy Jastrzębski, Jarosław Choiński, Arnaud Guertin, Férid Haddad, Andrzej Jakubowski, Kamil Kapinos, Maciej Kisieliński, Agnieszka Majkowska, Etienne Nigron, Malihe Rostampour, Anna Stolarz, Agnieszka Trzcińska, Rafał Walczak, Jolanta Wojtkowska, Wiktor Zipper, Aleksander Bilewicz. "Production of Sc medical radioisotopes with proton and deuteron beams". *Applied Radiation and Isotopes* 142 (2018), pp. 104–112.
- Mateusz Sitarz, Etienne Nigron, Arnaud Guertin, Férid Haddad, Tomasz Matulewicz. "New Cross-Sections for ^{nat}Mo(α,x) Reactions and Medical ^{97}Ru Production Estimations with Radionuclide Yield Calculator". *Instruments* 3.1 (2019), p. 7.
- Mateusz Sitarz, Jerzy Jastrzębski, Férid Haddad, Tomasz Matulewicz, Katarzyna Szkliniarz, Wiktor Zipper. "Can We Extract Production Cross-Sections from Thick Target Yield Measurements? A Case Study Using Scandium Radioisotopes". *Instruments* 3.2 (2019), p. 29.

Chapter 2

Theoretical background

2.1 Nuclear Physics

2.1.1 Structure of nucleus

It was presumed in Ancient Greece that all objects consist of many, very small elements. Today, we would rather say more precisely that the observable matter consists of atoms of the size in the order of 10^{-10} m. However, their true name, *atomos* (gr. indivisible), is not valid since the introduction of the atom model by Niels Bohr (Nobel Prize in 1922). We know that atom has an internal structure, with the very dense (~10^{15} g/cm^3) and very small (~10^{-14} m) nucleus at its center, and low-mass electrons orbiting around it. The nucleus itself is a collection of nucleons (Z protons and N neutrons) that define the atomic mass $A = Z + N$ of isotope they form. On the energy scale, the masses of nuclei are about $A \cdot m_n$ where m_n is in the order of 1 GeV/c^2. The parameter Z, called atomic number, translates to the number of electrons that the nucleus can hold via electromagnetic interaction and therefore defines the chemical properties of the atom.

The electrostatic repulsion of positively charged protons is countered by much stronger nuclear force between nucleons. Nuclear force originates from the attractive, strong fundamental force between quarks that form each nucleon. Figure 2.1 shows the proposed potentials $V(r)$ of such interaction depending on the distance r between two nucleons (figure taken from [21]). Every model confirms the following regions:

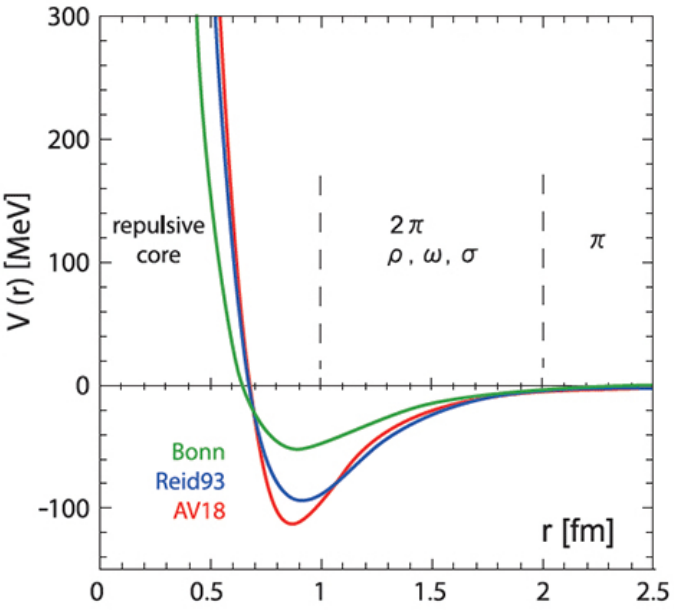

FIGURE 2.1: Three examples of the modern nucleon-nucleon potential (see [21] for more details).

- the repulsive core ($r < 1\,\text{fm}$),
- the intermediate range part ($1\,\text{fm} \leq r \leq 2\,\text{fm}$), dominated by the exchange of two mesons π or heavy mesons ρ, ω, and σ,
- the long range part ($r > 2\,\text{fm}$), with the exchange of one meson π.

The mesons manage to transfer strong quark interaction between different nucleons (transforming protons to neutrons and neutrons to protons in the process) which keeps the nucleus together. However, this effect diminishes rapidly with distance. But if the distance between two nucleons is small enough, they interact and reach the minimum of the potential well.

The binding energy of a nucleus is in the order of about 8 MeV per each nucleon. In a quantum mechanical description, assuming a nucleon in a potential created by the cumulative interaction with all other nucleons, the nucleon occupies certain energy levels (which are obviously model-dependent). As nucleons are spin 1/2 fermions, they obey Pauli exclusion principle, and so protons and neutrons populate different energy levels in their potential wells (as shown in Figure 2.2) with different parity, angular momentum and spin. As in any other physical system, nucleons too aim for the lowest energy possible and, if excited, they will de-excite and reach the lowest available energy state while emitting the γ quanta of the energy corresponding to the energy difference between levels[1] (typically in the order of keV or MeV). The γ quanta may be then absorbed by the electron of the atom (see Section 2.2.3) in the process of the internal conversion.

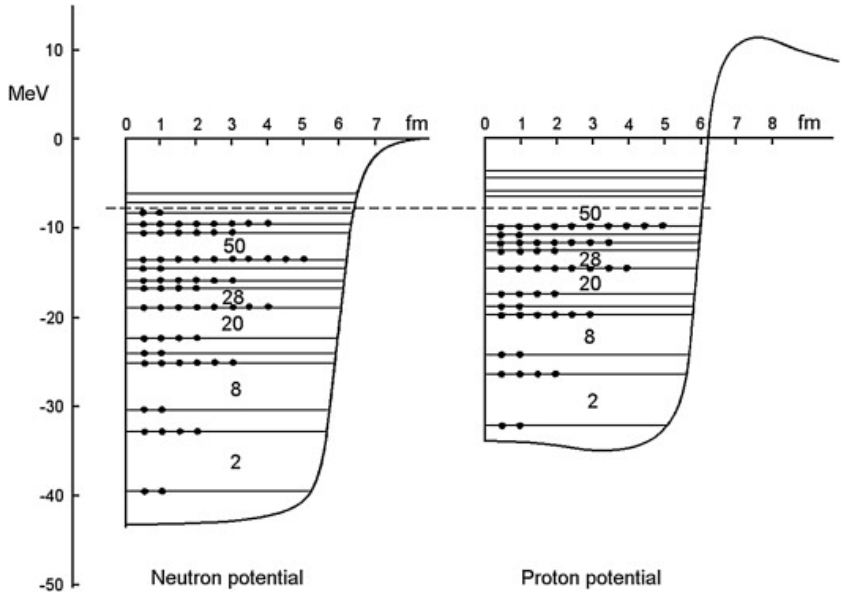

FIGURE 2.2: Protons and neutrons populating the energy levels of the ^{116}Sn potential well [22].

The potential well for protons (Figure 2.2) is less deep compared to neutrons, what is the effect of long-range electrostatic repulsion between protons. Additionally, between certain energy levels, a pronounced energy gap appears. It makes the nucleonic system filled to this gap exceptionally bound (so called "magic numbers" shown in Figures 2.2 and 2.3). The nucleus potential is studied more thoroughly within the shell model.

Another approach, the droplet model, helps to understand the total energy of nuclei. This phenomenological model accounts for the short range of effective strong interaction between nucleons and the long-range electrostatic repulsion between protons. The surface effect is accounted for as well as the symmetry energy (being the consequence of the Fermi gas model). The model explains well why the nucleon binding energy per nucleon initially

[1] The decay of an excited nuclear level may occur in various modes. In principle, different decay chains (with corresponding γ quanta of different energies) may be activated. The time-resolved γ spectroscopy is a powerful tool to identify decaying nuclei.

increases with atomic mass A and starts to decrease from $A \approx 60$. Simply put, more nucleons translate to increased number of strong interactions but many nucleons form a big nucleus with considerable electrostatic repulsion. There is broad maximum of about 8 MeV which is the approximative energy required to remove one nucleon from the nuclei (it also explains the shift between excitation function for the evaporation of consecutive nucleus from the CN seen in Figure 2.5).

More precise values of total binding energy of the nucleus can be obtained from the droplet model calculations which consider nuclear interaction between nucleons inside the nucleus volume and on the surface, electrostatic repulsion of protons, asymmetry between protons and neutrons, and pairing effect. The surface and Coulomb factors are additionally affected by the deformation of the nucleus. More advanced theoretical models, like the Density Functional Theory, are developed to provide mass predictions for heavy nuclei.

2.1.2 Stability and radioactivity

Conditions and types of decay

The symmetry between protons and neutrons is a very important factor for the stability of a nucleus. Similar amount of protons and neutrons (populated as in Figure 2.2) is the configuration of the lowest potential energy that forms stable nuclei of low mass. However, the repulsive interaction of the Coulomb force between protons gains importance for heavy nuclei, what results in significant neutron excess in stable heavy nuclei. For example, ^{208}Pb has the neutron-to-proton ratio of about 3 : 2. Any deviation from the minimal energy in a nucleus system causes the weak decay, effectively changing one proton to one neutron (or neutron to proton). For the heaviest nuclei, electric repulsion may induce another transformation in which the entire chunks of the nucleus are ejected, usually in the form of α particles (or in some cases as the spontaneous fission). All these processes are summarized in Table 2.1 and result in the transformation from initial nuclei (of the wave function ψ_i) to the new final nuclei (ψ_f). Sometimes after the decay, excited levels of the nucleus are populated (nucleus marked with star in Table 2.1), followed by IT – a fast emission of electromagnetic radiation, or the internal conversion.

TABLE 2.1: Types of most common radioactive decays.

Name	Decay process	Intermediate process
β^+ decay	${}^{A}_{Z}\mathrm{X} \rightarrow {}^{A}_{Z-1}\mathrm{X} + \mathrm{e}^+ + \nu_\mathrm{e}$	$\mathrm{p} \rightarrow \mathrm{n} + \mathrm{e}^+ + \nu_\mathrm{e}$
β^- decay	${}^{A}_{Z}\mathrm{X} \rightarrow {}^{A}_{Z+1}\mathrm{X} + \mathrm{e} + \bar{\nu}_\mathrm{e}$	$\mathrm{n} \rightarrow \mathrm{p} + \mathrm{e} + \bar{\nu}_\mathrm{e}$
electron capture (EC)	${}^{A}_{Z}\mathrm{X} \rightarrow {}^{A}_{Z-1}\mathrm{X} + \nu_\mathrm{e}$	$\mathrm{p} + \mathrm{e} \rightarrow \mathrm{n} + \nu_\mathrm{e}$
α decay	${}^{A}_{Z}\mathrm{X} \rightarrow {}^{A-4}_{Z-2}\mathrm{X} + \alpha$	
isomeric transition (IT)	${}^{A}_{Z}\mathrm{X}^* \rightarrow {}^{A}_{Z}\mathrm{X} + \gamma$	nucleus de-excitation

The weak decay is a spontaneous process which has a certain probability to occur in each unit of time. Its probability, λ [s^{-1}], is related to the Hamiltonian $\hat{V}$ of the weak interaction and the phase space:

$$\lambda \sim \left| \left\langle \psi_f \middle| \hat{V} \middle| \psi_i \right\rangle \right|^2 \tag{2.1}$$

This probability is also related to the mean life-time, τ, of unstable isotopes (radioisotopes) as they are expected to decay:

$$\tau = \frac{1}{\lambda} \tag{2.2}$$

Alternatively, radioisotope half-life (the time after which half of unstable nuclei will decay) is given as:

$$T_{1/2} = \frac{\ln(2)}{\lambda} \tag{2.3}$$

Half-lives vary from few nanoseconds to years (in the scale comparable to the age of Earth), depending on the nuclide and decay type. Usually, decays (other than IT) leave the residual nucleus in the excited state, which de-excite by emitting γ rays (photons) of energies E_γ characteristic for its energy levels (Figure 2.2) with different observed intensities I_γ (probability corrected for internal conversion). The γ emission occurs almost instantly after the decay (up to few picoseconds). Still, some isotopes can have a metastable (isomeric) state[2], which represents the excited state of nuclei with a $T_{1/2}$ comparable to half-lives of other decays.

Over 3000 nuclides with different N and Z, stable and unstable, are categorized in the form of chart of nuclides – a simplified version is shown in Figure 2.3. Each stable isotope of the same element is characterized by its natural abundance – the proportion in which it is found on Earth. The nuclei with the same Z are called isotopes, and with the same A – isobars.

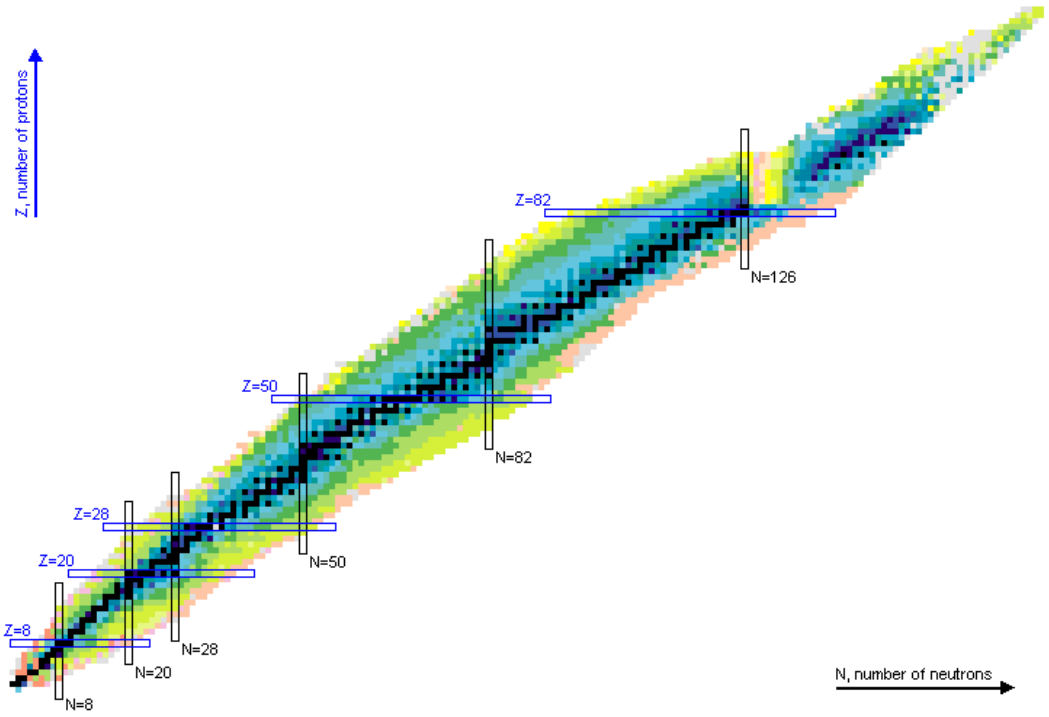

FIGURE 2.3: Simple version of chart of nuclides [23]. The stable nuclei are marked in black and unstable in color, based on their half-lives. Values denote the magic numbers.

Definitions of radioactivity

The decay is a quantum, statistical process, therefore it is not possible to predict when one given nuclei will decay. However, it is possible to observe number of decays $\mathrm{d}N_1$ of N_1 unstable nuclei in the time period $\mathrm{d}t$. This value is called activity, $A(t)$, and it is measured in Becquerel [Bq] (the number of decays per second). Activity is related to the number of nuclei

[2] In these cases, ground and metastable states are distinguished by noting "g" and "m" correspondingly after atomic number.

and their probability λ of decay per second:

$$\frac{\mathrm{d}N_1(t)}{\mathrm{d}t} = -A(t) = -\lambda \cdot N_1(t) \tag{2.4}$$

This equation can be solved to show the exponential decay law:

$$A(t) = A(t{=}0) \cdot \exp(-\lambda \cdot t) \tag{2.5}$$

Here, the parameter $A(t{=}0)$ is the activity at the beginning of the decay process (for example at the End of Bombardment, A_{EOB}, or at the beginning of the measurement, A_0, as discussed later).

If the decay product is also unstable, the subsequent decay is expected. The activity of each radioisotope in such decay chain is given by the Bateman equations. In particular, for double steps decay:

$$N_1 \xrightarrow{\lambda_1 \cdot P_{dec}} N_2 \xrightarrow{\lambda_2} \text{stable product}$$

the production rate of nuclei N_2 is given as:

$$\frac{\mathrm{d}N_2(t)}{\mathrm{d}t} = -\lambda_2 \cdot N_2(t) + P_{dec} \cdot \lambda_1 \cdot N_1(t) \tag{2.6}$$

where P_{dec} denotes the probability that N_1 will decay to N_2. Solving the system of Equations 2.4 and 2.6 for $A_2(t)$ yields the solution for "mother-daughter" decay (this relation is also shown in Figure 4.24):

$$A_2(t) = A_1(t{=}0) \cdot \frac{\lambda_2 \cdot P_{dec}}{\lambda_2 - \lambda_1} \cdot (\exp(-\lambda_1 \cdot t) - \exp(-\lambda_2 \cdot t)) + A_2(t{=}0) \cdot \exp(-\lambda_2 \cdot t) \tag{2.7}$$

Additionally, for a given radioisotope, the specific activity, $SA(t)$ [Bq/mol], is defined[3]:

$$SA(t) = \frac{A(t)}{W(t)} \tag{2.8}$$

where W is the amount of all isotopes (stable and unstable) of this element in moles at time t. Specific activity can be used in post-irradiation chemical procedures to assess the contribution of isotopic impurities of produced radioisotope of interest.

2.1.3 Nuclear reactions

Types of nuclear reactions

All radioactive isotopes decay therefore most of them do not exist in our environment in high concentration. However, as discovered by Frédéric and Irène Joliot-Curie (see Section 1.1), they can be synthetically produced by irradiating stable matter. In practice, this means colliding a particle (projectile) with the stable nucleus (target)[4] using dedicated machines and set-ups (for example, see Section 3.1). It is a challenge because nucleus is few orders of magnitude smaller than the whole atom (see Section 2.1.1) and projectiles usually pass through matter without interacting with the nuclei. To assure measurable amounts of events, high projectile flux is needed.

If the projectile manage to pass near the nuclei, three main processes may happen (shown in Figure 2.4).

1. Scattering. This can be elastic or inelastic process in which well-known electrostatic potential bounces the projectile off the target. In the first case, kinetic energy remains

[3] Another definition of specific activity found in the literature is $SA = \lambda \cdot N_A / M$, with M as molar mass [g/mol]. This definition is a constant value for each isotope, and is not used in this work.

[4] Unstable targets are usually used in the extreme cases of synthesising super-heavy nuclei.

the same before and after scattering in the center of mass system. In the latter, part of the kinetic energy is transferred to excite the target and/or projectile nucleus.

2. Creation of compound nucleus (CN). In this process, projectile collides with target and interacts through the nuclear force. After mixing their momenta (balance cascade), they usually form a system with high angular momentum and excitation energy (CN). These steps can also populate scattering channels and direct processes when emitting particles in the same manner. Typically, CN decays after ~10^{-16} s. This decay is usually composed of a sequence of emission of neutrons followed by γ de-excitations. For heavy system, CN might decay via fission. In both cases, new elements (residual) are produced.
3. Direct processes. These include peripheral collisions or reactions with projectiles of sufficient energy that can eject a fragment from the target (knock-out), transfer its fragment to the target (stripping), or collect nucleons from the target (pick-up).

Reactions are written in the following equivalent notations:

$$\text{projectile} + \text{target} \rightarrow \text{residual} + \text{ejectile}$$

$$\text{target}\,(\text{projectile}, \text{ejectile})\,\text{residual}$$

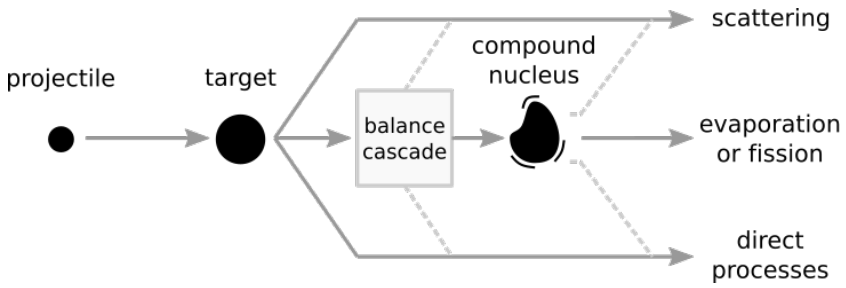

FIGURE 2.4: Possible processes through the interaction of projectile with the target nucleus.

Reaction cross-section

For the production of medical radioisotopes, the most practical route leads via the formation of CN. In quantum mechanics, to estimate the probability of the reaction of interest, the commonly used approach is the optical model. Here, the nucleus is considered as a space with potential that affects the behaviour of the waves representing particles (similar to the glass that refracts the light). The typical wave function of a particle with momentum $\hbar\vec{k}$ and position $\vec{r}$ is a complex quantity:

$$\psi \sim \exp\left(\mathrm{i} \cdot \vec{k} \cdot \vec{r}\right) \tag{2.9}$$

In the nuclear reaction, the wave of the incoming projectile, ψ_{in}, passes through the potential $V(r)$, and changes to outgoing projectile (ejectile), ψ_{out}, scattered at the solid angle Ω. The quantity we can observe is the probability, or cross-section (σ), for the process of changing ψ_{in} into ψ_{out} affected by the nuclear interaction $\hat{V}$ in given phase space:

$$\frac{\mathrm{d}\sigma}{\mathrm{d}\Omega} \sim \left| \langle \psi_{out} | \hat{V} | \psi_{in} \rangle \right|^2 \tag{2.10}$$

The total cross-section is therefore:

$$\sigma = \int_{4\pi} \frac{\mathrm{d}\sigma}{\mathrm{d}\Omega} \mathrm{d}\Omega \tag{2.11}$$

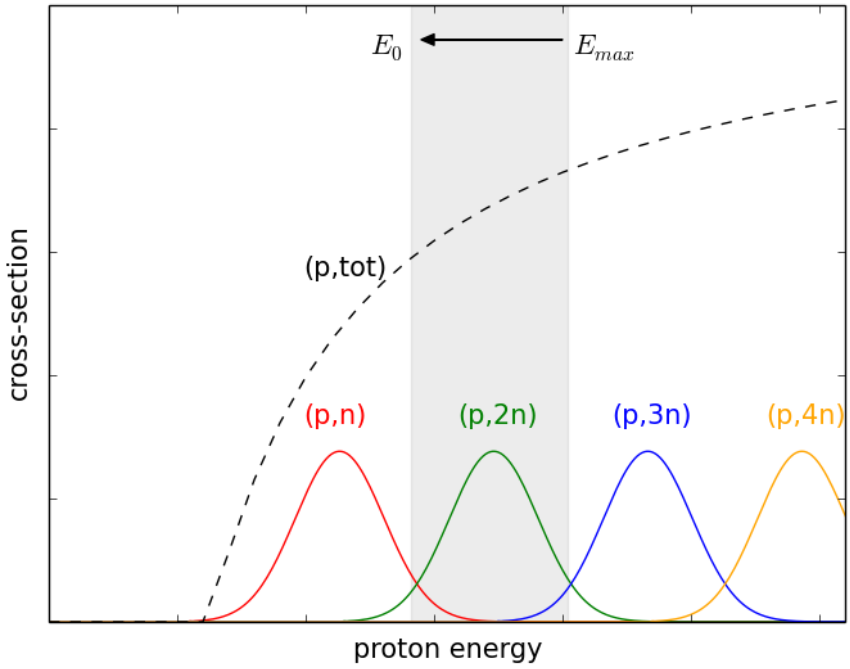

FIGURE 2.5: The idea of total cross-section and separate channels for proton (p) induced reactions with evaporation of different number neutrons (n) from CN. The grey area represents the energy range $E_{max} \rightarrow E_0$ that favours (p,2n) reaction. Other reactions channels are ignored for the simplicity of the graph.

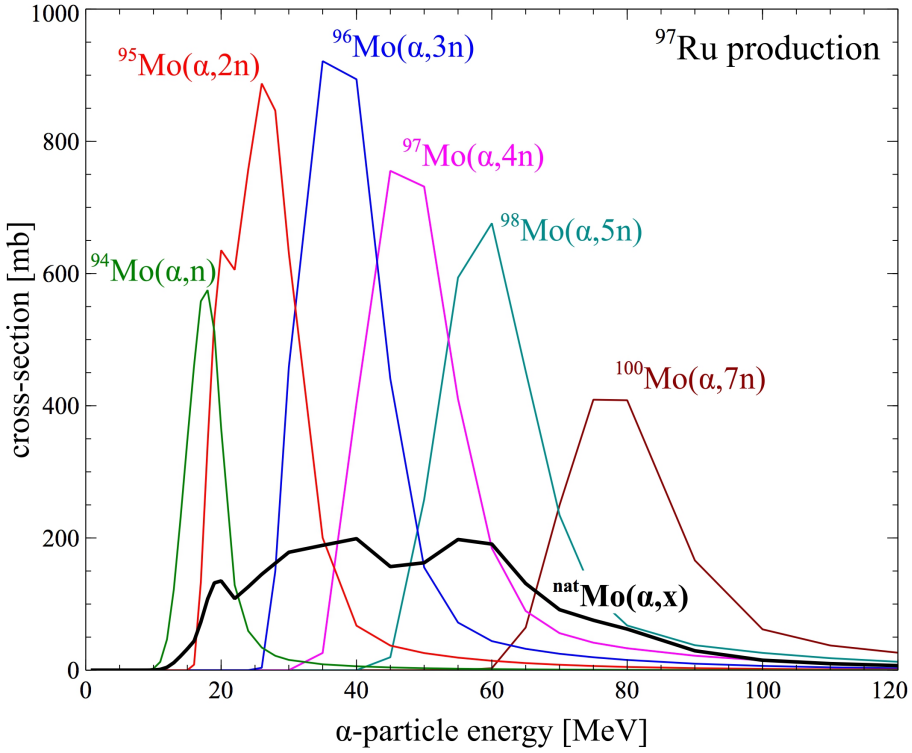

FIGURE 2.6: Cross-section for production of ^{97}Ru with α-particles on stable molybdenum isotopes (data from [24]). The natural abundance of molybdenum is given in Table C.1 (Appendix C).

Cross-section has a sense of a surface with the unit of [m^2], or more commonly barn[5] [b]. It corresponds to the effective surface of the literal cross-section of the target as seen by the incoming projectile for a given process – if hit, the reaction occurs.

Using Born's approximation, it is possible to reach the conclusion that the total probability for all reactions is given by:

$$\sigma = \frac{\pi}{k^2} \cdot L_{max}^2 \tag{2.12}$$

where: L_{max} – maximal angular momentum transfer during the collision; k – projectile's wavenumber. Both these factors are related to the energy E of the projectile (in laboratory frame of reference) and provide the excitation curve, $\sigma(E)$, seen in Figure 2.5 as dashed line. It saturates at high energy, reaching so called geometrical cross-section representing the effective area of the target. The total cross-section splits for different reaction channels. The emission of more ejectiles from CN increases with the projectile energy. While it is difficult to calculate cross-section theoretically, certain softwares (like EMPIRE [25] or TALYS [26], and its evaluation TENDL [24]) help to obtain these values with semi-empirical models.

Isotopes can be formed via various nuclear reactions on various nuclei. For example, α-particle can produce isotope of ^{97}Ru on many naturally abundant molybdenum isotopes. The excitation functions for these reactions are shown in Figure 2.6. To calculate the cross-section for ^{nat}Mo(α,x)^{97}Ru reaction, all contributing cross-sections are added after the multiplication by the abundance of their target isotope.

Energy threshold and Q-value

For an interaction of projectile nuclei of mass m_1, and target nuclei of mass m_2, the Q-value (Q [MeV]) is defined as:

$$Q = m_1 \cdot c^2 + m_2 \cdot c^2 - \sum_i m_i \cdot c^2 \tag{2.13}$$

where m_i denotes the mass of i-th produced nucleus. Obviously, for elastic scattering, $Q = 0$. For other processes, two cases are possible:

- $Q < 0$ then the reaction is endo-energetic, and the final system has higher mass (that has to be delivered in the form of kinetic energy of colliding particles),
- $Q > 0$ then the reaction is exo-energetic, and the final system has lower mass.

The exo-energetic reaction may occur at any energy. For the endo-energetic reaction, a laboratory energy limit, called threshold energy (E_{thr}), sets the minimum energy needed for the reaction to occur. The laboratory energy threshold can be calculated from the conservation of momentum and energy to link it with Q-value:

$$E_{thr} = |Q| \cdot \left(1 + \frac{m_1}{m_2}\right) \tag{2.14}$$

Detailed formulas for two nuclei in the exit channel can be found in [27].

2.1.4 Production of radionuclides using charged particles

Irradiation

Let's consider a flux f_p of charged projectiles per second impinging perpendicularly on mono-layer solid target (foil) of the surface S consisting of N_{stab} stable nuclei of cross-section σ for the interaction (Figure 2.7).

The probability P_{hit} of hitting the target nuclei leading to a given reaction process is therefore:

$$P_{hit} = \frac{\sigma \cdot N_{stab}}{S} \tag{2.15}$$

[5] The cross-sections values vary usually from few millibarns to few barns. The conversion $1\,b = 10^{-28}\,m^2$ shows how small is the area equivalent for the reactions.

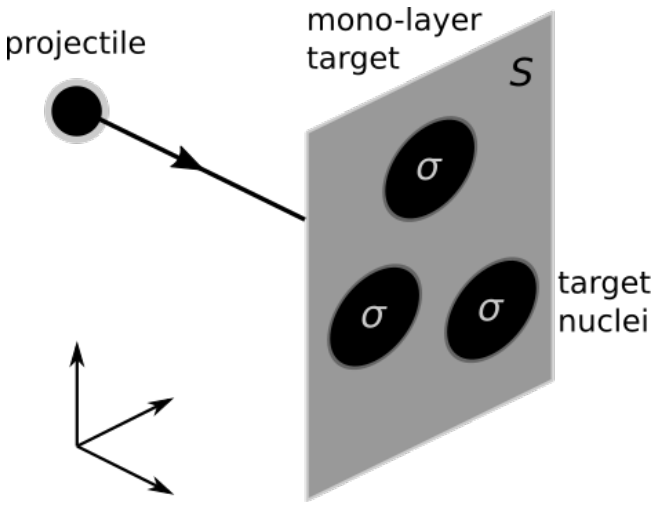

FIGURE 2.7: Flux of projectiles hitting the mono-layer target (foil) of surface S, with N_{stab} stable target nuclei of cross-section σ.

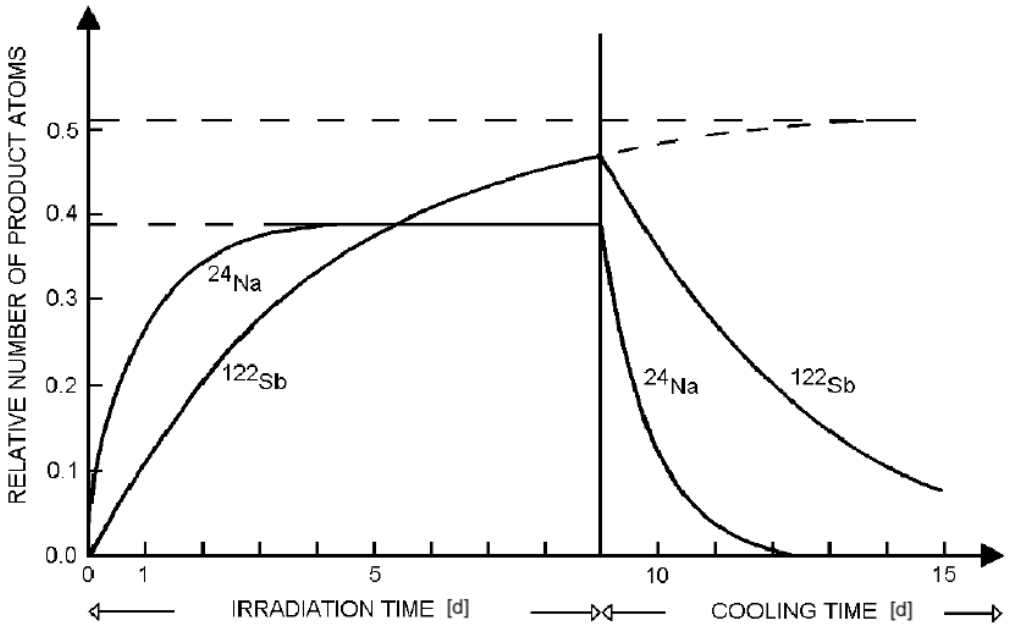

FIGURE 2.8: Relative production of ^{24}Na ($T_{1/2}$ = 15.0 h) and ^{122}Sb ($T_{1/2}$ = 2.7 d) showing the saturation of ^{24}Na production after around 4 d of the irradiation (figure taken from [28]).

The number R of nuclear reaction per second is then:

$$R = P_{hit} \cdot f_p = \frac{\sigma \cdot N_{stab}}{S} \cdot f_p = N_{stab} \cdot \sigma \cdot f_s \tag{2.16}$$

where f_s is the number of projectiles per second per unit area. After each successful hit, a new nuclide is produced, which decays with probability λ (a stable element will have a probability of decay equal to 0). The number $\mathrm{d}N_{rad}$ of radioactive nuclei formed in time $\mathrm{d}t$ is therefore the number of nuclear reaction per second (R) diminished by the number of decays per second:

$$\frac{\mathrm{d}N_{rad}(t)}{\mathrm{d}t} = N_{stab} \cdot \sigma \cdot f_s - \lambda \cdot N_{rad} \tag{2.17}$$

which can be solved (assuming N_{stab} as constant) for $N_{rad}(t)$ and recalculated (using Equation 2.4) for the activity A_{EOB} produced after the bombardment during time t_{irr}:

$$N_{rad}(t_{irr}) = \frac{N_{stab} \cdot \sigma \cdot f_s}{\lambda} \cdot (1 - \exp(-\lambda \cdot t_{irr})) \tag{2.18}$$

$$A_{EOB}(t_{irr}) = N_{stab} \cdot \sigma \cdot f_s \cdot (1 - \exp(-\lambda \cdot t_{irr})) \tag{2.19}$$

For practical purposes, it is better to consider number of nuclei per unit area, $\mathcal{N}$ [m^{-2}], and number of projectiles per second, f_p [s^{-1}], instead of N_{stab} and f_s [$\mathrm{s}^{-1} \cdot \mathrm{m}^{-2}$]:

$$A_{EOB}(t_{irr}) = \mathcal{N} \cdot \sigma \cdot f_p \cdot (1 - \exp(-\lambda \cdot t_{irr})) \tag{2.20}$$

This formula can be modified using the relations from the next Sections (Equations 2.24 and 2.29) to:

$$A_{EOB}(t_{irr}) = H \cdot \frac{N_A}{M} \cdot \frac{I}{Z_p \cdot e} \cdot x \cdot \sigma \cdot (1 - \exp(-\lambda \cdot t_{irr})) \tag{2.21}$$

where: H – target enrichment, N_A – Avogadro's constant, M – molar mass of the target, I – projectile beam current, Z_p – atomic number of the projectile, e – elementary charge, x – range of projectile (areal density). For thick targets, where the energy loss of the traversing charged particle is not negligible ($E_{max} \rightarrow E_0$), the convolution of energy-dependant cross-section, $\sigma(E)$, and projectile's stopping-power, $\mathrm{d}E/\mathrm{d}x$, is required. Then, using Equation 2.47, A_{EOB} becomes:

$$A_{EOB}(t_{irr}) = H \cdot \frac{N_A}{M} \cdot \frac{I}{Z_p \cdot e} \cdot \int_{E_0}^{E_{max}} \frac{\sigma(E)}{\mathrm{d}E/\mathrm{d}x} \mathrm{d}E \cdot (1 - \exp(-\lambda \cdot t_{irr})) \tag{2.22}$$

Equations 2.18 and 2.21 describe the shape of the build-up of number of nuclei or activity produced during the irradiation time. An example of activity production of ^{24}Na and ^{122}Sb is shown in Figure 2.8. As irradiation time goes, more atoms of ^{24}Na ($T_{1/2}$ = 15.0 h) and ^{122}Sb ($T_{1/2}$ = 2.7 d) are formed. However, after about 4 days, the production of ^{24}Na reaches the saturation – the number of newly produced radionuclides is equal to the number of decay leading to an equilibrium. After EOB, the number of both radioisotopes drops during the cooling time (according to Equation 2.5).

Flux of projectiles

In the case of accelerators, the flux of projectiles delivered by the machine is a beam intensity I given in Amperes[6]. Fully-stripped projectile has Z_p protons, each with elementary charge e (if the projectile is not fully stripped, its total charge is lower correspondingly to its ionisation state). It is therefore possible to calculate I based on the measurement of total

[6]This way of beam intensity definition originates from the current measurement from the Faraday Cup. At high energies, the beam intensity is simply defined number of particles per second (f_p).

charge q_{tot} delivered during the irradiation time t_{irr}:

$$I = \frac{q_{tot}}{t_{irr}} \tag{2.23}$$

The total number of projectiles is $q_{tot} \cdot (Z_p \cdot e)^{-1}$ hence number of particles per second, f_p, is:

$$f_p = \frac{q_{tot} \cdot (Z_p \cdot e)^{-1}}{t_{irr}} = \frac{I}{Z_p \cdot e} \approx 6.3 \cdot 10^{12} \cdot \frac{I\,[\mu A]}{Z_p} \tag{2.24}$$

Since the value of beam current I depends on the charge of the projectile and its ionisation state, the same beam current value might not correspond to the same flux. The so-called particle beam current, I_{par}, takes this factor into account, and is defined as beam current normalized for its charge:

$$I_{par} = \frac{I}{Z_p} \tag{2.25}$$

The unit of such value is typically referred to as "particle Ampere" ["pA"], in contrast to standard beam current unit, sometimes referred to as "electrical Ampere" ["eA" = A] for the disambiguation.

Thickness and mass of target

In general, the number $\mathcal{N}$ of nuclei per unit area [cm^{-2}] is related to the number n_{stab} of stable nuclei per unit mass [g^{-1}], the thickness d [cm] of the target (foil), and its density ρ [g/cm^3]:

$$\mathcal{N} = d \cdot \rho \cdot n_{stab} \tag{2.26}$$

The number of stable target nuclei per unit mass, n_{stab}, is the number of this nuclei in one mole (Avogadro's constant, N_A) divided by the molar mass M of the target:

$$n_{stab} = H \cdot \frac{N_A}{M} \tag{2.27}$$

where H is the abundance of the target isotope (which corresponds to the nuclear reaction of interest[7]) and purity of the target material. For example, in the case of the irradiation of ^{40}Ca in the form of compound, like $^{40}CaCO_3$, we must consider $M = 100\,g/mol$ as one target nuclei corresponds to one molecule.

The thickness of the target, d, has a linear unit but it is better to expressed it in areal density x [g/cm^2] (discussed in Section 2.3.1):

$$x = d \cdot \rho \tag{2.28}$$

From Equations 2.26, 2.27, 2.28, the number of nuclei per unit area can be calculated as:

$$\mathcal{N} = x \cdot H \cdot \frac{N_A}{M} \tag{2.29}$$

Thick Target Yield

During the production of the radioisotopes by irradiating the target material with projectiles (Figure 2.7) it is important to know the efficiency of such process for each given radioisotope and irradiation conditions. Such parameter is called Target Yield, TY (in special case: Thick Target Yield, TTY), and intuitively it would be the amount of produced activity [Bq] normalized to the beam intensity [A] and the irradiation time [s]:

$$TY \approx \frac{A_{EOB}}{I \cdot t_{irr}} \tag{2.30}$$

[7] In case of reactions induced on all stable isotopes of given element, the abundance is 1.

However, this relation assumes that A_{EOB} is proportional to t_{irr} which is not correct because part of the produced activity decays during longer irradiation, resulting in lower A_{EOB}. Therefore the decay factor should be considered (like in Equation 2.18):

$$TY = \frac{A_{EOB}}{I \cdot \tau \cdot (1 - \exp(-\lambda \cdot t_{irr}))} \tag{2.31}$$

This way the sense of Equation 2.30 is preserved as for short irradiation times, the function $(1 - \exp(-\lambda \cdot t_{irr}))$ is similar to $\lambda \cdot t_{irr}$, resulting in the original approximation:

$$TY = \frac{A_{EOB}}{I \cdot \tau \cdot (1 - \exp(-\lambda t_{irr}))} \xrightarrow{t_{irr} \ll T_{1/2}} \frac{A_{EOB}}{I \cdot \tau \cdot \lambda \cdot t_{irr}} = \frac{A_{EOB}}{I \cdot t_{irr}} \tag{2.32}$$

Equation 2.31, solved for A_{EOB}, shows the similarity to A_{EOB} derived for thick target (Equation 2.22):

$$A_{EOB}(t_{irr}) = TY \cdot \tau \cdot I \cdot (1 - \exp(-\lambda \cdot t_{irr})) \tag{2.33}$$

Therefore, the factor TY, for the projectile covering the energy range $E_{max} \rightarrow E_0$, is given as:

$$TY = \frac{H \cdot N_A}{\tau \cdot M \cdot Z_p \cdot e} \cdot \int_{E_0}^{E_{max}} \frac{\sigma(E)}{\mathrm{d}E/\mathrm{d}x} \, \mathrm{d}E \tag{2.34}$$

Usually, to produce high amount of activity, the production process involves the irradiation of targets that are thick enough to reduce the initial energy E_{max} of the projectile up to the threshold of the reaction of interest (E_{thr}). This maximizes the produced activity A_{EOB} as a function of the target thickness (but not considering all others parameters like thermal constrain, cost of the material, or machining). In this case, Target Yield is called Thick Target Yield, TTY:

$$TTY(E_{max}) = \frac{H \cdot N_A}{\tau \cdot M \cdot Z_p \cdot e} \cdot \int_{E_{thr}}^{E_{max}} \frac{\sigma(E)}{\mathrm{d}E/\mathrm{d}x} \, \mathrm{d}E \tag{2.35}$$

The formal unit of TY and TTY is $[(\mathrm{C} \cdot \mathrm{s})^{-1}]$ = $[\mathrm{Bq} \cdot (\mathrm{A} \cdot \mathrm{s})^{-1}]$ but more commonly used is $[\mathrm{MBq} \cdot (\mu\mathrm{A} \cdot \mathrm{h})^{-1}]$ = [MBq/μAh]. To automatize the calculation of TY and TTY for given scenario, Radionuclide Yield Calculator software was prepared during this work (see Appendix A) .

Sometimes in the literature, instead of comparing the production yields (TY or TTY) of different production routes, a saturation activity (A_{sat} [MBq/μA]) is addressed. The saturation activity is the activity of the radioisotope per 1 μA of beam current which is produced after the "infinite" irradiation (as shown in Figure 2.8). It is given as:

$$A_{sat} = \frac{TY}{\tau} \tag{2.36}$$

Indirect production

Sometimes the radioisotope with number of nuclei N_2 and decay constant λ_2 is produced during the irradiation throught two mechanisms at once: the direct production via nuclear reaction with cross-section σ_2, and via the decay with probability P_{dec} of another produced simultaneously radioisotope characterized by N_1 and λ_1. If both are formed from the same target nuclei of N_{stab} then the scenario is following:

$$\begin{array}{ccccc} N_1 & \xrightarrow{\lambda_1 \cdot P_{dec}} & N_2 & \xrightarrow{\lambda_2} & \text{stable product} \\ \sigma_1 \uparrow & & \sigma_2 \uparrow & & \\ N_{stab} & & N_{stab} & & \end{array}$$

The production rates of these two radioisotopes are related in the system of differential equations (see Section 2.1.2):

$$\begin{cases} \frac{\mathrm{d}N_1(t)}{\mathrm{d}t} = -\lambda_1 \cdot N_1(t) + N_{stab} \cdot \sigma_1 \cdot f_s \\ \frac{\mathrm{d}N_2(t)}{\mathrm{d}t} = -\lambda_2 \cdot N_2(t) + P_{dec} \cdot \lambda_1 \cdot N_1(t) + N_{stab} \cdot \sigma_2 \cdot f_s \end{cases} \tag{2.37}$$

Such system has been solved in [29] and [30], and recalculated for A_{EOB} of each radioisotope produced during the irradiation time t:

$$\begin{cases} A_{EOB,1}(t_{irr}) = N_{stab} \cdot f_s \cdot \sigma_1 \cdot (1 - \exp(-\lambda_1 \cdot t_{irr})) \\ A_{EOB,2}(t_{irr}) = N_{stab} \cdot f_s \cdot \Big((\sigma_2 + P_{dec} \cdot \frac{\lambda_1}{\lambda_1 - \lambda_2} \cdot \sigma_1) \cdot (1 - \exp(-\lambda_2 \cdot t_{irr})) - \\ \qquad - P_{dec} \cdot \frac{\lambda_2}{\lambda_1 - \lambda_2} \cdot \sigma_1 \cdot (1 - \exp(-\lambda_1 \cdot t_{irr})) \Big) \end{cases} \tag{2.38}$$

The recalculation to TTY_1 and TTY_2 (as defined in Equation 2.35) for thick targets (with not negligible projectile energy loss) shows that the production yield of both radioisotopes affect A_{EOB} of "daughter" in a complicated way:

$$\begin{cases} A_{EOB,1}(t_{irr}) = TTY_1 \cdot \tau_1 \cdot I \cdot (1 - \exp(-\lambda_1 \cdot t_{irr})) \\ A_{EOB,2}(t_{irr}) = I \cdot \Big((TTY_2 \cdot \tau_2 + P_{dec} \cdot \frac{1}{\lambda_1 - \lambda_2} \cdot TTY_1) \cdot (1 - \exp(-\lambda_2 \cdot t_{irr})) - \\ \qquad - P_{dec} \cdot \frac{\lambda_2}{\lambda_1 - \lambda_2} \cdot TTY_1 \cdot \tau_1 \cdot (1 - \exp(-\lambda_1 \cdot t_{irr})) \Big) \end{cases} \tag{2.39}$$

After the end of irradiation, activity $A_{EOB,1}$ decays with time according to Equation 2.5 while activity $A_{EOB,2}$ follows the Equation 2.7 and therefore is also affected by $A_{EOB,1}$.

Stable products

To estimate specific activity (see Equation 2.8) it is important to estimate also the production of N_0 of each stable isotope. If the production cross-section is σ_0 then:

$$\begin{array}{l} N_0 = \text{stable product} \\ {\scriptstyle \sigma_0}\uparrow \\ N_{stab} \end{array}$$

Stable product does not decay so its amount progressively increases with time:

$$\frac{\mathrm{d}N_0(t)}{\mathrm{d}t} = N_{stab} \cdot \sigma_0 \cdot f_s \tag{2.40}$$

$$N_0(t_{irr}) = H \cdot \frac{N_A}{M} \cdot \frac{I}{Z_p \cdot e} \cdot \int_{E_0}^{E_{max}} \frac{\sigma(E)}{\mathrm{d}E/\mathrm{d}x} \, \mathrm{d}E \cdot t_{irr} \tag{2.41}$$

The production rate, as the factor normalized for beam current and irradiation time, could be defined here as Thick Target Yield for stable products, $TTY_0(E_{max})$ [nuclei $\cdot$ (μA $\cdot$ h)$^{-1}$] (similar to the definition in Equation 2.35):

$$TTY_0(E_{max}) = \frac{H \cdot N_A}{M \cdot Z_p \cdot e} \cdot \int_{E_{thr}}^{E_{max}} \frac{\sigma(E)}{\mathrm{d}E/\mathrm{d}x} \, \mathrm{d}E \tag{2.42}$$

Equation 2.42 can be used to calculate number of produced stable nuclei during the irradiation time t_{irr} and beam current I of the initial energy E_{max}:

$$N_0(t_{irr}) = TTY_0(E_{max}) \cdot I \cdot t_{irr} \tag{2.43}$$

2.2 Radiation material science

2.2.1 Interaction of ions with matter

The range of nuclear forces and the size of nuclei are relatively small (see Section 2.1.1) so most of the projectiles irradiating the target material (as in Figure 2.7) pass through it without inducing a nuclear reaction. However, the range of electromagnetic forces (F_e) is considerably higher and every charged projectile interacts with target's electrons[8]. Sometimes this interaction is so intense that it causes the ionization[9] – the electrons leave their orbits and may induce even more ionization (see Section 2.2.2) as well as break the chemical bonds (ultimately decomposing the target). At the same time, the track of heavy projectiles (protons, α particles, heavy ions, ...) does not change much because they are several orders of magnitude heavier than the electrons. However, they lose energy and gradually slow down until a complete standstill, unless they leave the target material.

To quantify the change of projectiles' energy, $\mathrm{d}E$ [eV], inside the fragment of target material, $\mathrm{d}x$ [g/m^2], we should consider the perpendicular component of electromagnetic force F_e between projectile and electron, integrate it over interaction time to obtain the change of momentum, recalculate it to the change of energy, and multiply it by electron density in the medium. The solution to this simplified procedure is well-known as Bethe-Bloch formula:

$$-\frac{\mathrm{d}E}{\mathrm{d}x} \approx \frac{4 \cdot \pi \cdot Z_p^2 \cdot e^4 \cdot n_e}{m_e \cdot v_p^2} \cdot \ln\left(\frac{2 \cdot m_e \cdot v_p^2}{I_{av}}\right) \tag{2.44}$$

where: Z_p is the atomic number of the projectile, n_e is the number of electrons per unit mass [g^{-1}], v_p is the speed of projectile [m/s], and I_{av} is the average ionization potential [eV]. The latter is related to the atomic number Z_t of the target material:

$$I_{av} \approx 9.1 \cdot Z_t \cdot (1 + 1.9 \cdot Z_t^{2/3}) \tag{2.45}$$

The value $\mathrm{d}E/\mathrm{d}x$, called stopping-power, is measured in eV $\cdot$ (g/m^2)$^{-1}$, or more commonly in MeV $\cdot$ (mg/cm^2)$^{-1}$, and describes how energy $\mathrm{d}E$ is lost by the projectile when passing through the layer of the material of thickness $\mathrm{d}x$. The main behaviour of the stopping-power is that:

$$-\frac{\mathrm{d}E}{\mathrm{d}x} \sim \frac{Z_p^2}{v_p^2} \tag{2.46}$$

which reproduces the Bragg curve seen in Figure 2.9. In general, the lower the energy of the projectile, the lower is its speed, and more time is available for the interaction, which translates to higher energy transfer, higher stopping-power, and ultimately more ionization (observed in Figure 2.9 as Bragg peak).

The above equations are simplified and today many corrections have been applied for more precise estimations of $\mathrm{d}E/\mathrm{d}x$ and I_{av}, including relativistic and quantum mechanics effects [31]. The stopping-power in various materials can be calculated with the use of SRIM software [32]. Among its many applications, SRIM allows to estimate the statistical energy straggling of originally monoenergetic projectiles (solid line in Figure 2.9).

[8] The electromagnetic interaction between projectile and target's nuclei is negligible due to the electron screening.

[9] Other interactions of ions with matter may include scattering, Bremsstrahlung, different excitations, and scintillation which are not discussed here due to the type of projectile and energies under considerations.

The distance x [g/m^2] that charged projectile travels in straight line in a material (in the energy range $E_{max} \rightarrow E_0$) is given as:

$$x = \int_{E_0}^{E_{max}} \frac{1}{-\,\mathrm{d}E/\mathrm{d}x}\,\mathrm{d}E \tag{2.47}$$

This is the mean value since the range of a beam of particles shows statistical fluctuation (that can be also simulated with SRIM).

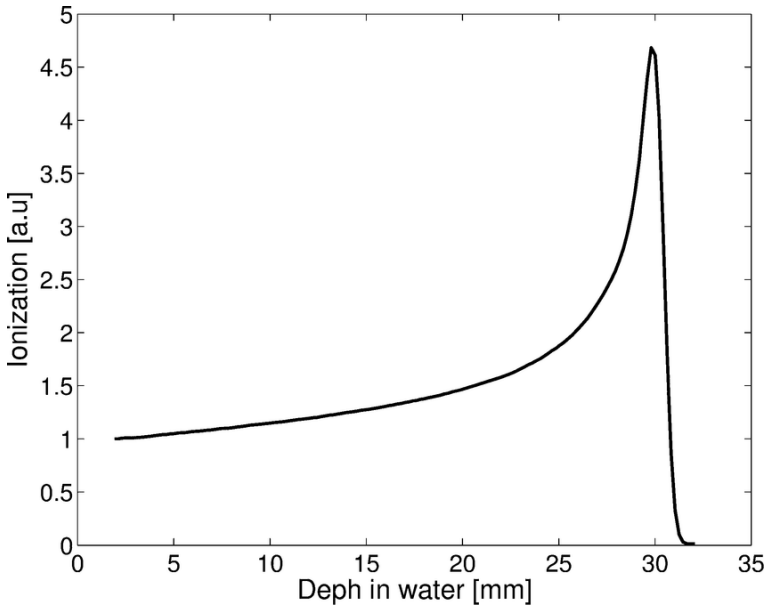

FIGURE 2.9: Bragg curve of 62 MeV proton beam acquired in a water-tank (figure taken from [33]). The width of the Bragg peak is related to the energy straggling.

2.2.2 Interaction of electrons with matter

Similarly to ions, electrons also have stopping-power, however their track is not a straight line. Projectile electron, having the same mass as electron of an atom, scatters significantly while exciting and ionizing the medium (which is defined as mass scattering power). This causes increase of the temperature or releasing more electrons from the atoms. In the latter case, if the ejected electron has energy greater than the binding energy of an electron in an the atom, it can cause secondary ionizations (Figure 2.10)). Because of that, primary electron (projectile) deposit all its energy on much shorter effective distance than nuclei projectiles. The characteristic distance is the radiation length, which is the mean distance over which the energy of an electron is reduced by the factor $1/e$.

In the case of anti-matter electron (positron), for example from β^+ decay, it annihilates with an electron from the medium after loosing some of the energy. At low to moderate energies, the annihilation is done via the formation of a short-lived positronium system (τ in the order of ~ns), and produces usually two γ quanta of the energy around 511 keV each, emitted in the opposite directions in the center-of-mass system (this ensures the conservation of energy and momentum). The electron-positron annihilation is very important from the nuclear medicine point of view as it plays a key role in PET technique (see Section 2.3.3).

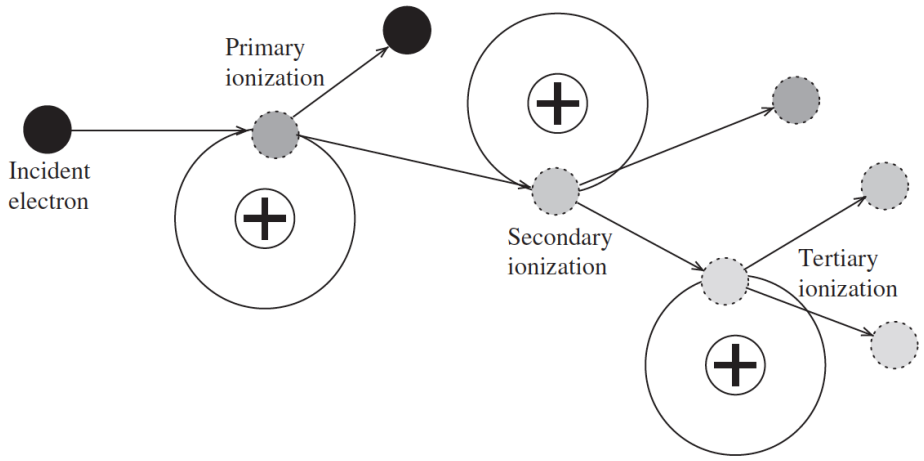

FIGURE 2.10: Electron scattering and ionizing the matter (figure taken from [31]).

2.2.3 Interaction of γ radiation with matter

Types of photon interaction with matter

The γ radiation (photon) is an electromagnetic wave of high energy (originated typically from the nucleus), and thus it affects all electric charges inside the medium where it propagates. Usually this influences the electrons, as they have considerably lower mass and are bounded with much less energy than the nuclei. The γ induced nuclear reactions, similar to the ones described in Section 2.1.3, are also possible but are not the subject of this work.

The main interactions of γ radiation with matter include photoelectric effect (photoeffect), Compton effect, and nuclear pair production[10]. Their description also requires the wave-particle duality approach, treating the γ quanta as a massless particle with energy E_γ and momentum E_γ / c.

The probability of Photoelectric effect, Compton effect, and nuclear pair production depends on E_γ, as shown in Figure 2.11 and discussed in next Sections. All these processes absorb the initial γ quanta and thus are responsible for the attenuation of γ radiation beam passing through matter.

Photoelectric effect

The photoelectric effect dominates at lower γ energies. Here, the incident photon interacts with tightly bound orbital electron and converts all its energy into the binding and kinetic energy of the electron[11]. The photon disappears and the electron (called photoelectron) is knocked off from the atom. The process is shown in Figure 2.12.

[10] Other processes include Rayleigh scattering which does not cause ionization, and low-probable electronic pair production (both not discussed).

[11] The binding energy of a valence electron is in the order of ~eV which is negligible compared to its ~keV kinetic energy inherited from the photon.

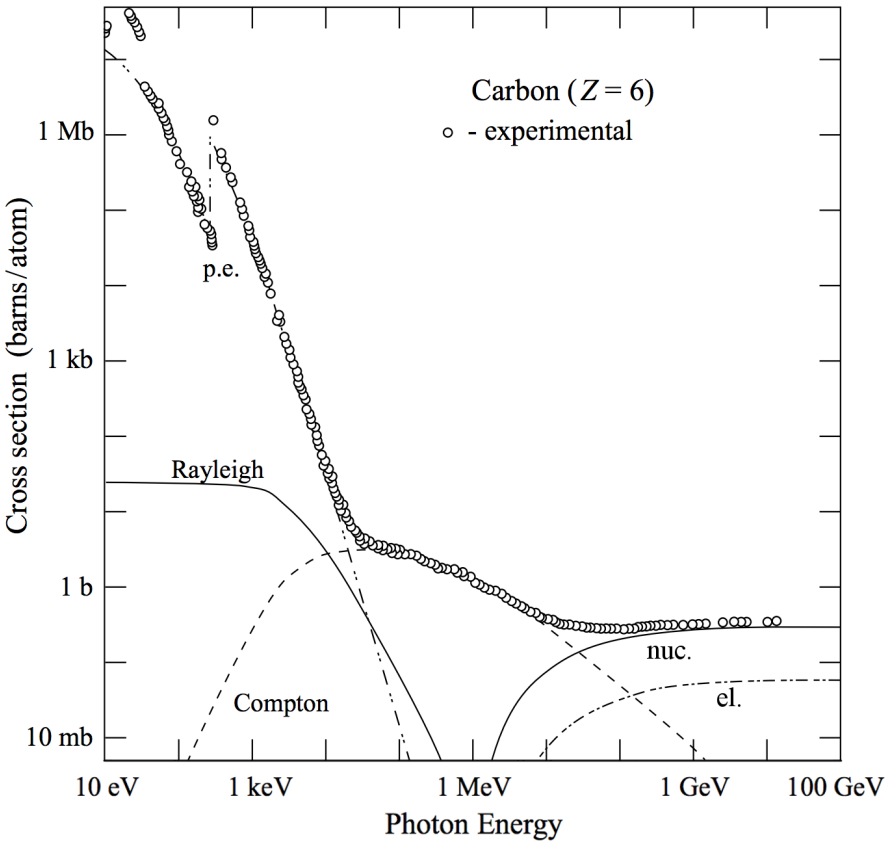

FIGURE 2.11: Photon total cross sections as a function of energy showing the contributions of different processes: photoelectric effect (p.e.), Compton and Rayleigh scattering, and pair production in nuclear (nuc.) and electron (el.) field (figure taken from [34]).

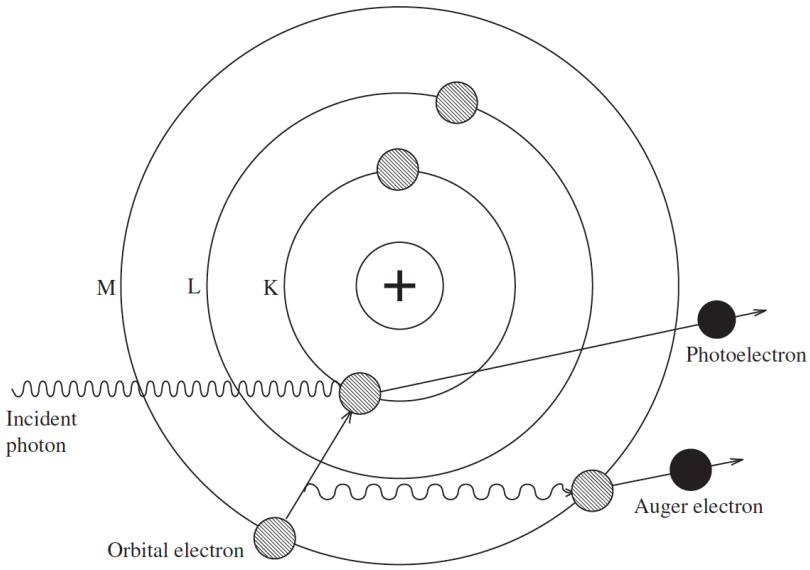

FIGURE 2.12: Photoelectric effect on atom with K, L, M orbits, leading to the emission of an Auger electron (figure taken from [31]).

Compton effect

The Compton effect (or Compton scattering) can be observed at low, medium, and high energy of γ radiation. In this process, the incident photon transfers a part of its energy to knock off the electron (of the mass m_e), and scatters with lower energy E'_γ. The energy transfer depends on the energy E_γ of initial photon and the scattering angle θ, hence the beam of mono-energetic γ rays produces several electrons of different kinetic energies. The energy E'_γ of the scattered photon is given as

$$E'_\gamma = \frac{E_\gamma}{1 + (1 - \cos(\theta)) \cdot \frac{E_\gamma}{m_e c^2}} \tag{2.48}$$

which can be derived from the energy and momentum conservation.

Pair production

When a photon with the energy exceeding $2m_e c^2 = 1.022\,\text{MeV}$ passes near the strong electric field of atomic nucleus, the photon may transform into positron-electron pair. This is known as nuclear pair production and the products inherit the energy excess from the photon in the form of kinetic energy, following the scenario from Section 2.2.2.

2.2.4 Auger electrons

Processes discussed previously (internal conversion, electron capture, ion-atom interaction, electron scattering, photoelectric effect, Compton effect) can produce the inner-shell vacancy of an atom. Full relaxation of this vacancy creates a cascade involving X-ray and Auger as well as Coster-Kronig transitions. The typical relaxation time of a single ionisation event is around 10^{-15} s and may consist of many vacancy cascades (as shown in Figure 2.13) resulting in emission of multiple X-ray photons and electrons. More details are given in [35].

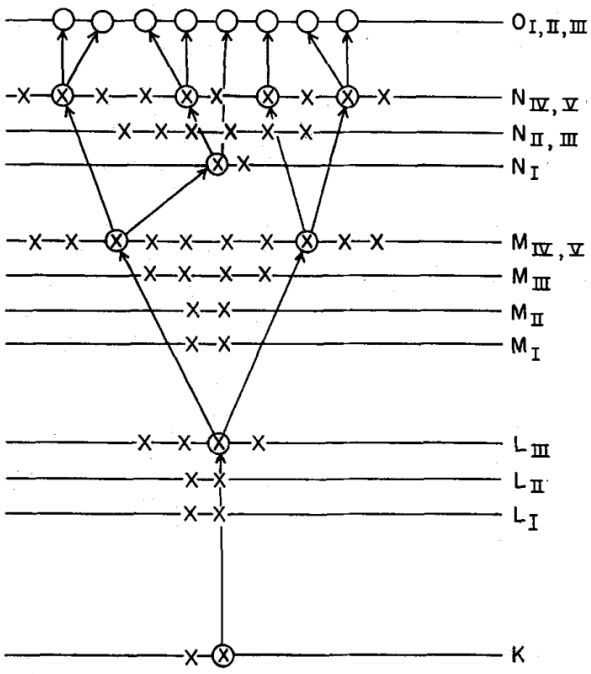

FIGURE 2.13: Typical vacancy cascade in Xe following K shell ionization with ultimate loss of all electrons of the O-shell (figure taken from [35]).

2.3 Nuclear medicine

2.3.1 Medical radioisotopes and their availability

Characteristics of medical radioisotopes

Among many radioactive isotopes emitting different types of radiation only few are applicable for medical purposes. Their desired properties may vary depending on their purpose, but all of them exhibit some common similarities:

- should emit only the radiation required for its medical purpose – other radiation emitted from the medical radioisotope will unnecessarily increase the radiation dose (Section 2.3.4) to the patient and the personel,
- should have $T_{1/2}$ which corresponds to the medical purpose and procedure,
- should easily build stable complexes with desired radiotracers (Section 2.3.2),
- should decay to stable or very long-lived isotope (otherwise the patient receives additional dose),
- should have a feasible, cost-effective, and safe production route.

Production of medical radioisotopes

As mentioned in Sections 2.1.3 and 2.1.4, radioactive isotopes can be produced in various nuclear reactions during the irradiation of stable matter (targets) with the flux of particles. This is achieved with the use of different machines which provide intensive flux to produce sufficient activity of the radioisotope.

One of such machine is a nuclear reactor where fuel rods with fissile elements (such as ^{235}U or ^{239}Pu) produce a cloud of neutrons via the controlled consecutive fissions (chain reaction). These neutrons are usually thermalized in water to the energy of tens of meV[12]. Placing the target in the reactor exposes it to the neutron flux of typically 10^{14} s^{-1}cm^{-2} which, in the case of thermal neutrons, activates the targets via (n,γ) reactions, producing neutron-rich radioisotopes. Alternatively, a radioisotope of interest can be selected from a mass distribution of fission products (for example, the yield of ^{235}U+n fission fragments is shown in Figure 2.14).

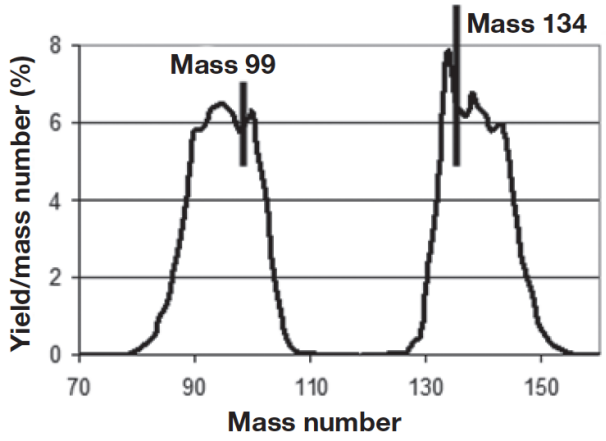

FIGURE 2.14: The yield of ^{235}U+n fission fragments as a function of mass (figure taken from [36]). Marked masses represent the process leading to the production of ^{99}Mo/^{99m}Tc generator.

[12]Since neutrons have no electrical charge, they can enter a nucleus also at thermal energies and induce a nuclear reaction with high cross-section. However, reactions induced by fast neutrons are also utilized.

Two masses (99 and 134) marked in the figure correspond to the products of the medically interesting reaction:

$$^{235}\mathrm{U} + \mathrm{n} \rightarrow {}^{99}\mathrm{Mo} + {}^{134}\mathrm{Sn} + 3 \cdot \mathrm{n}$$

as ^{99}Mo ($T_{1/2}$ = 2.7 d) decays to $^{99\mathrm{m}}$Tc ($T_{1/2}$ = 6.0 h) commonly used in SPECT imaging technique (see Section 2.3.3). The first ^{99}Mo/$^{99\mathrm{m}}$Tc generator system was introduced at the Brookhaven National Laboratory in 1957 [37]. In principle, the "mother" radioisotope loaded onto the generator constantly produces the final radioisotope, which can be repetitively eluted (with chromatographic techniques, distillation or phase partitioning). This solution allows the production of the medical radioisotopes conveniently on site, without the need of the reactor or the cyclotrons at spot.

However, most medical radioisotopes do not have a convenient generator system, and cyclotrons are being installed near medical centers to provide the daily supply of short-lived radioisotopes. Cyclotrons are much more compacted, easier to manage, and cheaper than the reactors [38]. The simplified principle of operation of the cyclotron is shown in Figure 2.15 and consists of the following steps:

1. the ion source generates positively or negatively charged ions and injects them inside the cyclotron (under vacuum),
2. ions are accelerated between two electrodes ("dees") by the voltage and move in the circular orbit inside the cyclotron magnetic field,
3. when the desired energy is reached, the beam is extracted (for example with the deflecting electrode), transported in vacuum and focalized on a production target directly[13], resulting in the irradiation discussed in Section 2.1.4.

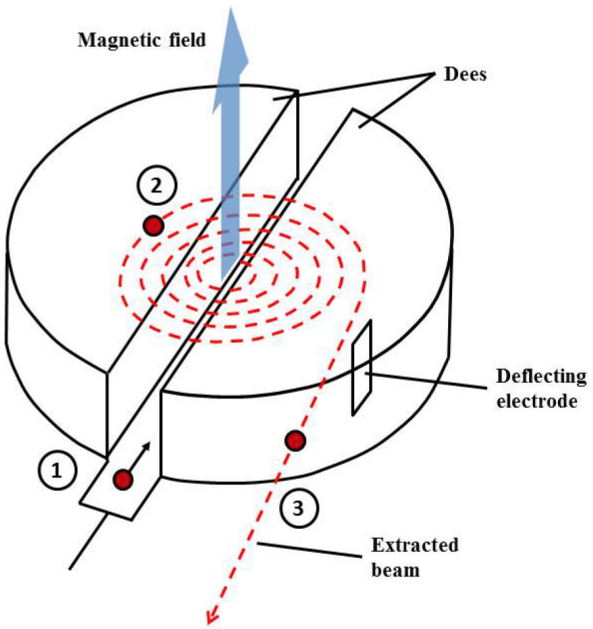

FIGURE 2.15: The simplified cyclotron principle [36].

Typical projectiles accelerated in the cyclotrons for the production of medical radioisotopes are not heavier than α particles. This is because the range of heavier nuclei is shorter (compared to light projectiles in the same material), and would yield lower activity (Equation 2.22). The energy range of accelerated particles varies usually between 10 MeV and

[13] Depending on the facility, the target can be also placed inside the cyclotron for the irradiation.

80 MeV, and should be adjusted in order to satisfy the nuclear reaction of interest and reduce the contribution of other reactions which may yield radioactive impurities (see Section 2.3.2 and Figure 2.5).

Another device to accelerate charged particles is a Linear Accelerator (LINAC). Here, particles are accelerated with the electric field, as they pass through the hollow tubes in the straight line. LINACs usually offer higher beam intensity compared to the cyclotrons. However, they are also more expensive, making cyclotrons more attractive for the production of medical radioisotopes.

Recently also (γ,n) reactions are gaining popularity (despite a low cross-section associated to photonuclear reactions) due to the developments of γ beams of satisfactory intensities. The modern γ facilities offers an attractive production routes of radioisotopes that cannot be easily produced by other means (such as ^{225}Ac, ^{67}Cu, or ^{47}Sc).

Targetry

Targets with specific nucleus are essential to satisfy the nuclear reaction during the irradiation. In particular, the isotopically enriched targets (with the increased abundance of the isotope of interest) can be chosen in the cases where the desired radioisotope is formed on low-abundant or radioactive isotope.

Targets used in nuclear physics experiments have different form (solid, liquid, gaseous, elemental or as compounds) depending on the chemical properties of the element used for reaction. Their thickness varies from from a few $\mu g/cm^2$ (targets used for the fundamental research in nuclear physics) up to a few hundred mg/cm^2 (targets used for the research and/or production of the medical radioisotopes). The challenges posed to a cyclotron-irradiated target are following:

- its thickness must correspond to the energy range favouring the reaction of interest and reducing the production of contaminants (see Figure 2.5),
- it should have uniform thickness distribution to prevent the appearance of hot spots during the irradiation,
- it should have high chemical purity to limit the production of unwanted radionuclides,
- it should be durable enough to withstand the mechanical operations (mounting and dismounting) and the heat deposited during the irradiation (see Section 2.2.2),
- it must be adjusted to the capabilities of the set-up at given facility,
- its composition should allow a feasible post-irradiation extraction chemistry (in the case of the production of medical radioisotopes),
- it should allow high efficiency material recovery after the irradiation (in the case of the production of medical radioisotopes with the isotopically enriched target material).

The target design and preparation is a difficult task, and many characteristics in physics, chemistry and engineering go into its design and preparation (summarized in details in [39]). In the case of solid targets, the main preparation techniques include:

- mechanical reshaping – which include tablet pressing (a powder is formed into a pellet with the use of pressing device), and metal rolling (material is reshaped using a rolling mill),
- electrodeposition – an electrolyte containing the target material is made and allows target material to be deposited on one of the electrodes thanks to the applied voltage,
- sedimentation – material prepared in the form of suspension is precipitated on a substrate mounted at the bottom of the precipitation vessel,
- melting – the target material is melted (for example on a hot plate) and distributed on the support.

The targets produced in these ways might have different thicknesses (d [m]) and densities, depending on the parameters used for the preparation. For example, target preparation with use of mechanical press from same amount of material (number of atoms, N_{stab}) can result with pellets of various thickness (in linear units) depending on the force applied. However, the induced activity will be almost the same due to the same amount of material irradiated. This is why, when describing the thickness of the target, it is better to use areal density (x [mg/cm^2]), as shown in Equation 2.28.

Processing of activated targets

After the irradiation of the target, the desired radioisotope must be isolated (from the bulk target) and purified (from co-produced radioisotopes of other elements). The separation procedure must meet the following requirements:

- it must be very precise, as in usual irradiation only a few nanomoles of desired radioisotope are produced in a typical milligrams of bulk material,
- in the case of short-lived products – it must be relatively fast in order to save the decreasing radioactivity,
- it should allow the feasible labelling of radiotracers (see Section 2.3.2),
- in the case of the irradiation of isotopically enriched target material – it should allow for an efficient material recovery.

Several techniques can be employed to separate radioisotope from the target (summarized in [36]). In case of solid targets, the common and often effective method is to dissolve the target and extract the radioisotope through the selective ion exchange process. The separation is performed for example with the use of ion-exchange columns or chromatography systems. In other cases, more sophisticated methods must be use, like a mass separation employed for example in [40] for the terbium production. The separated radioisotope can be then sampled and used in the further processing.

2.3.2 Radiotracers

Even if the radioisotope emits the radiation of diagnostic or therapeutic relevance, it must be guided to reach the place in the human body where it can play its medical role. Usually, this requires a biologically active molecule (biomolecule) which guides the radioisotope to the location for imaging or tumor to kill. Biomolecule and radioisotope are connected with the bifunctional linker and form a radiotracer[14], as shown in Figure 2.16.

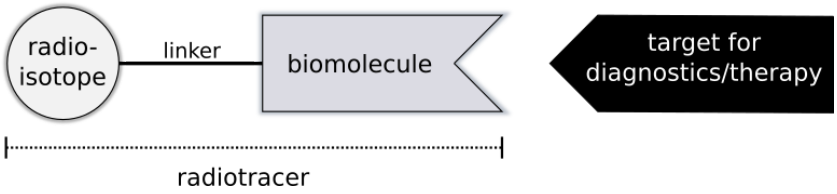

FIGURE 2.16: Principle of typical radiotracer, labeled with radioisotope and targeting uniquely the medically relevant structure in the human body.

The biomolecule determines the biodistribution (in vivo distribution) and physiological behaviour of the radiotracer. It should have high affinity to the structure of interest in the human body (for example: investigated tissue or tumor cells), which ensures the selective concentrations and prolonged retention of the radiotracer in the region of interest. Therefore

[14]Radiotracers are sometimes called "radiopharmaceuticals", however they are given in such small concentrations that they do not elicit any pharmacological response as regular pharmaceuticals, hence the name "radiotracers" for disambiguation [37].

each radiotracer is dedicated for its unique purpose (the vast list of known radiotracers and their applications can be found in multiple papers, including [41]).

The radioisotope can be attached to the biomolecule in different chemical reactions (not discussed here) which vary depending on the nature of radioisotope, biomolecule, and selected linker. In practice, these reactions are performed in an authomatic synthesis modules (a system of storage vials, connected by tubes and valves) where each step of the reaction is controlled by the computer.

Along with the radioisotope of interest, all other radioisotopes of the same element will chelate the radiotracer. Therefore it is important to keep co-produced radioactive impurities at minimum level (activity $< 1\%$). This standard is required for a radiotracer in order to be used safely in humans. Other requirements include: radiochemical impurity, chemical purity, isotopic purity, specific activity, total activity, pH, and sterility. Validated radiotracers are then used for diagnostic purposes (see Section 2.3.3), in about 95% of cases, and for therapy (see Section 2.3.4) in the remainder [37].

2.3.3 Medical imaging with radioisotopes

SPECT

SPECT (Single-Photon Emission Computed Tomography) is a worldwide gold standard technique used in medical imaging for quantitative in vivo measurements of radiotracer emitting γ radiation. SPECT principles and various applications were presented in many papers, including IAEA reports [42, 43].

Briefly, the radioactive tracer (see Section 2.3.2) is injected into the patient, and emits γ radiation which can escape the human body. The photons are then detected with a gamma camera, a matrix of small scintillation crystals, in one position (planar imaging) or at several angles (SPECT). In the first case, map of activity observed on the detector corresponds directly to the activity distribution in the patient (as collimators removes almost all photons non-perpendicular to the detector plane). In the latter, a computer applies different tomographic reconstruction algorithms to compile a 3D distribution model based on collected images.

Obviously, some photons will be attenuated in the human body, and others will scatter (see Section 2.2.3), which will reduce the image quality and introduce the noise. Therefore the photon emitted from the radioisotope should have around 100–200 keV to escape the human body, reduce the contribution of Compton effect, and produce photoelectric effect in crystal. Today, radioisotopes exhibiting this property, and used in SPECT, include mainly: ^{67}Ga, ^{99m}Tc, ^{123}I, ^{201}Tl, used usually in MBq quantities. In particular, ^{99m}Tc produced via the generator system has become the most widely used radionuclide in nuclear medicine, accounting for as much as 85% of all diagnostic procedures [37].

PET

PET (Positron Emission Tomography) is another well-known diagnostic technique. It allows quantitative in vivo measurements of the distribution of administered positron-emitting radioisotopes in human body. Its principle and numerous applications were summarized recently by IAEA [36, 44] and EANM [45, 46].

In short, the β^+ radioactive tracer (see Section 2.3.2) is injected into the patient, and the annihilation of the positron produces two 511 keV energy photons (see Section 2.2.2), which are emitted in opposite directions and can escape the human body. These photons are then detected in coincidence by parallel rings of scintillation crystals surrounding the patient[15]. Two detected photons of the right energy allow to assume that the positron emitter is located somewhere in between, defining a Line Of Response (LOR). In the first approximation, the

[15]J-PET group from Jagiellonian University in Cracov introduced an alternative detector based on inexpensive plastic scintillators. The innovative arrangement of long scintillator strips in J-PET detector opens promising perspectives for the cost effective construction of the whole-body PET scanner, as well as construction of MR and CT compatible PET inserts. J-PET tomograph and its medical applications were recently reported in [47].

intersection of multiple LOR provides the distribution of the tracer (although in practice many additional corrections are applied).

To satisfy the PET acquisition requirements, the radioisotope must exhibit a high probability of β^+ decay of possibly the lowest average energy (because high energy would allow the positron to travel further before annihilating hence blurring the image). Today, the most common PET radioisotopes are: ^{11}C, ^{13}N, ^{15}O, ^{18}F, ^{68}Ga, and ^{82}Rb, used mostly in MBq quantities. Additionally, radioisotopes that undergoes β^+ and IT can be employed in coincidence PET technique (see Appendix B).

2.3.4 Radionuclide therapy

As described in Section 2.2, the destructive nature of radiation comes with the ability to deposit energy in the matter and ionize it. The energy deposited in the process per unit mass of the medium is defined as radiation dose. While very high amount of radiation damages nonliving and living matter alike, the complexity of the latter shows more subtle response even at lower doses. Radiobiology (which is a very broad field and will not be discussed here in details) studies these effects, and results are applied in radiotherapy (radiation therapy).

The aim of radiotherapy is to kill tumor cells or ease cancer symptoms while preserving the healthy tissues. The radiotherapy may include radionuclide therapy or external beam therapy, and is often accompanied by other procedures (like surgery, chemotherapy, or hyperthermia) to improve the overall effect of the treatment [13]. The surgery and the external beam therapy focus on killing the primary site of cancer while the radionuclide therapy and chemotherapy aim to kill metastases. The detailed terminology, procedures, and advancements in radiotherapy were recently summarized by IAEA [48, 49] and EANM [50].

One important quantity which should be mentioned is LET (Linear Energy Transfer). In contrast to the stopping-power (energy loss by a charged particle – Section 2.2.1), LET focuses on the energy absorbed by the medium as the radiation traverses it. If this energy is used, directly or indirectly, to induce double-strand DNA break then the cell is likely to enter the apoptosis pathway, leading to its death. In the case of radionuclide therapy, to ensure that this process happens in the tumor cells and has a therapeutic effect, two conditions must be met:

- the radioisotope must emit a radiation with optimal LET, preferably around 100 keV/µm, which ensures high but local dose distribution, spearing the healthy tissue around tumor,
- the radiotracer must be very selective to lead the radioisotope preferably exclusively to the tumor, where it attaches to the cell membrane or enters it.

In practice, radiotheraphy requires radioisotopes with usually longer half-lives (up to few days) and of higher activity (order of GBq) compared to nuclear imaging. Their radiation must have range adapted to the size of the tumor (or the observed metastases) and the selectivity of the radiotracer:

- low energy Auger electrons – with the range up to tens of nanometers (in water) and thus suitable for the radiotracers targeting the cell nucleus,
- α particles – with the typical range around 10 µm (in water) corresponding to the size of a cell, suitable for the radiotracers docking in the cancer cells' membrane,
- β^- particles – with the range up to 12 mm (in water), employed in cases of bigger metastases where the cross-fire effect allows to deposit the dose in deeply located cancer cells that could not have been reached by the radiotracers.

Today, the list of therapeutical radioisotopes include: ^{67}Cu, ^{89}Sr, ^{90}Y, ^{131}I, ^{149}Tb, ^{153}Sm, ^{177}Lu, ^{188}Re, ^{211}At, ^{223}Ra, and ^{225}Ac. In particular, most commonly used radiopharmaceuticals for radionuclide therapy are: ^{89}Sr-chloride, ^{90}Y-microspheres, ^{90}Y-octreotide, ^{131}I-iodide, ^{131}I-MIBG, and ^{153}Sm-EDTMP [51]. Recently, Lutathera (^{177}Lu-DOTATATE) is also becoming popular in medical practice [52].

2.3.5 Theranostics

In 1993, the study was performed to merge therapeutic function of ^{90}Y with diagnostic capabilities of ^{86}Y [53]. Later, this approach was named "theranostics". In general, the theranostic pairs are the radioisotopes of the same or very similar element from a chemical point of view so they can be bonded with the same biologically active molecule (in different required doses). One theranostic partner is emitting γ or β^+ radiation used for imaging, while the second partner is β^-, Auger or α emitter used for the cancer treatment. Both radioisotopes can be used simultaneously for monitoring the therapy course, or separately, to provide important dosimetric and toxicological information.

So far, there are a lot of possible theranostic matched pairs, from which most are of the different chemical element [54, 55]. This is a drawback as for example diagnostic ^{68}Ga and therapeutic ^{177}La have similar yet not the same chemistry, which translates to slightly different labeling conditions which eventually means troubles with the automatization of the process. Additionally, it is not clear if different elements have exactly the same biodistribution so the dose predicted with imaging radioisotope might not reflect the actual dose delivered with therapeutic agent. The solution is to use monoelement theranostic radioisotopes, from which one of the most promising are the one of terbium (^{149}Tb as α emitter, ^{152}Tb as β^+ emitter, ^{155}Tb as γ emitter and ^{161}Tb as β^- emitter) but their effective production and chemical separation can be difficult or challenging [40, 56–62]. An interesting theranostics alternative are the radioisotopes of copper (^{64}Cu as β^+, β^-, and Auger electron emitter, as well as ^{67}Cu as β^- and γ emitter) discussed recently in [63–67], and the radioisotopes of scandium (studied in this work and discussed in Section 4.3).

Chapter 3

Experimental procedures

This chapter describes the experimental procedures, data acquisition, and data analysis adopted in this work. The results from all conducted experiments (Chapter 4) are obtained with the use of the methodology presented here.

3.1 Cyclotrons and irradiations

In this work, the production of medical isotopes is studied with the use of three cyclotrons: GE PETtrace in Heavy Ion Laboratory (HIL) in Warsaw, C70 in Accelerator for Research in Radiochemistry and Oncology at Nantes Atlantic (ARRONAX), and C30 in National Centre for Nuclear Research (NCNR) in Świerk. These machines are shown in Figure 3.1, and their beam parameters are given in Table 3.1 (energies and intensities shown are upper limits).

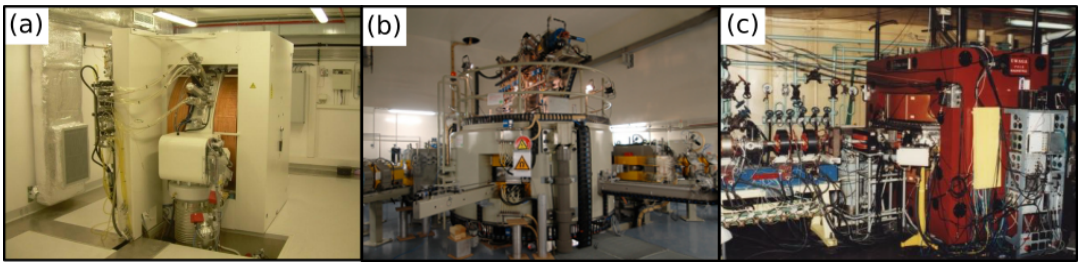

FIGURE 3.1: Photos of the cyclotrons employed in this work: (a) GE PETtrace in Heavy Ion Laboratory, (b) C70 in ARRONAX, (c) C30 in National Centre for Nuclear Research.

Beams from these machines were extracted to irradiate various targets. The targets were prepared separately for each experiment to study the σ or TTY of production routes of different medical radioisotopes. However, these values depend not only on the target but also on the energy of the accelerated particles. The energy value is provided in each experiment

TABLE 3.1: Beams parameters available at the employed cyclotrons.

	PETtrace HIL	**C70 ARRONAX**	**C30 NCNR**
proton (H^+)	16.5 MeV, 80 µA	70 MeV, 375 µA	28.7 MeV, 50 nA
deuteron (D^+)	8.4 MeV, 60 µA	35 MeV, 50 µA	
proton (HH^+)		35 MeV, 50 µA	
α particle (He^{+2})		67.4 MeV, 70 µA	
reference	[68]	[69]	[70]

by the cyclotron operators but it has been also verified experimentally (see Section 3.3.3). Similarly, the beam current (see Section 2.1.4) is also provided by the online measurement with the Faraday Cup. However, the target geometry or the focalization of the beam might cause part of the flux not to hit the target, therefore each target was equipped with thin monitor foils. The methodology described in Section 3.3.2 shows the method of the beam current calculation based on the activation of monitor foils.

The targets were mounted on the dedicated stations (the target surface is perpendicular to the beam), in which the energy of the accelerated projectiles was reduced by the following factors:

- station in HIL (Figure 3.2a) – a station with helium cooling, where the energy of the beam is degraded by 25 µm havar cyclotron window and 1 cm of air,
- NICE2 station, ARRONAX (Figure 3.2b) – a station with air cooling, installed after 50 µm kapton cyclotron window and 7 cm air,
- vacuum chamber, ARRONAX (Figure 3.2c) – a station connected directly to vacuum of the cyclotron (no energy degradation),
- station in NCNR (Figure 3.2d) – a station installed after 90 µm Al cyclotron window and 8 cm air.

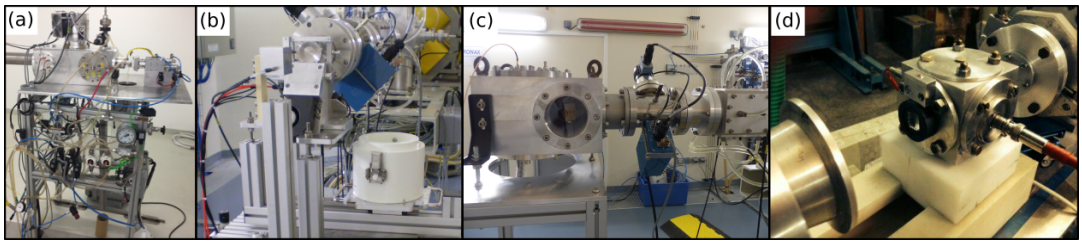

FIGURE 3.2: Photos of the stations holding the targets during the irradiations: (a) station in HIL, (b) NICE2 in ARRONAX, (c) vaccum chamber in ARRONAX, (d) station in NCNR.

Typical irradiation of targets in this work lasted from 10 minutes to few hours with no more than 0.5 µA beam intensity[1]. The targets were left for cooling for at least 1 h to allow the decay of inessential, short lived radioisotopes (produced in the target and in the irradiation station) hence reducing the radiation dose to the personel. Then, targets were transported to the acquisition room to measure the induced activity with HPGe detectors.

3.2 HPGe γ spectroscopy

3.2.1 Principle of semiconductor detectors

The radiation detectors have many applications, including the quantification of radioactive materials present in the irradiated target. For this particular purpose, the commonly used detector type is a semiconductor. Detectors more effective for other purposes are: gaseous ionization detectors and scintillators (summarized in recent IAEA handbook [36]). However, since most radioisotopes emit characteristic γ radiation (see Section 2.1.2) of different energies with known intensities, it is possible to distinguish between several possible radioisotopes present in the sample. The semiconductor detector is most suitable for this task thanks to its high energy resolution when properly cooled [71] and therefore it was used in this study.

The idea of semiconductor detectors is to use interaction of γ radiation (Section 2.2.3) with the semiconductor crystal, where the electrons are lifted from the valence band into the

[1] Even though the higher beam current was possible in certain cases, it would induce more activity (Equations 2.21 and 2.22) which would not be possible to measure with the detectors employed in this work (see Section 3.2.3).

conduction band, and then transported and amplified, resulting in observable charge. The typically cylindrical crystal is kept at around 80 K with the use of liquid nitrogen. The low temperature prevents the elevation of electrons to the conduction band though the thermic movement, allowing precise measurements. The crystals used in this work are HPGe (High Purity Germanium), however other types are commercially available.

In the ideal case, γ quanta enters the crystal volume, and transfers all its energy to an electron through the photoelectric effect[2]. The electron excites other electrons (Section 2.2.2), lifting them to the conduction band. The number of electrons in the conduction band is therefore related to the γ quanta energy. Produced signal is amplified and reaches the analog-digital converter, where it is registered in the analyser's arbitrary channel, proportional to the energy. If γ quanta of the same energy will reach the detector again, it will register another count in the same channel, producing the γ peak (photopeak), and ultimately plotting a histogram of various detected energies of γ radiation called "γ spectrum".

It is also possible that γ radiation will interact with an electron through Compton effect, yielding signals of lower energies (depending on the scattering angle). This produces "Compton background" for each photopeak as shown in Figure 3.3. For example, despite that the radioactive source, ^{137}Cs, emits only one γ line of 662 keV, multiple other energies are measured because of the Compton scattering and the radiation background.

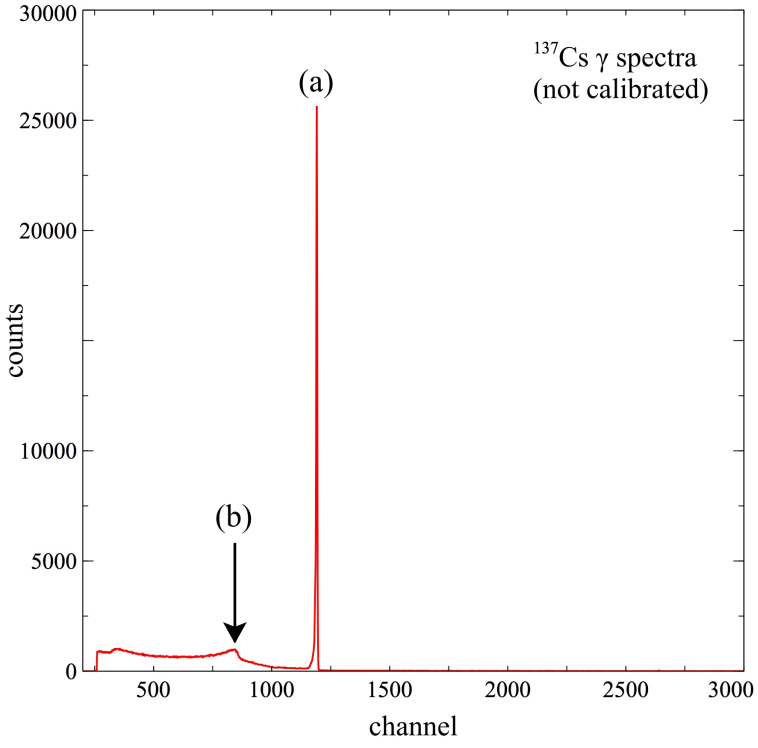

FIGURE 3.3: Simple example of the ^{137}Cs γ spectrum collected with HPGe detector: (a) photopeak of 662 keV, (b) maximum Compton scattering at 476 keV (scattering of 662 keV photon at 180°).

Even though ^{137}Cs always emits exactly 662 keV, its photopeak spreads to several channels which translates to the typical energy resolution of few keV (for semiconductor detectors). This happens mainly because the whole process of signal formation is subjected to statistical fluctuations. Additionally, during the signal formation (which might take up to few microseconds), the detector is not able to process another signal. If too much γ rays are entering the crystal, some of them are lost in the time overlap. This translates to increased dead time of the measurement, which, in practice, should be kept below 10% of the real measurement time. In this study, a pulser was employed to validate the dead time correction for the measurement time provided by the acquisition system.

[2]The binding energy of electron (~eV) is negligible compared to the photon energy (keV – MeV).

Occasionally, two γ quanta emitted in quick succession might be seen as one larger energy deposited in the detector. This coincidence results in a formation of the summation peak – a peak on the spectrum corresponding to the sum of the energies of two characteristic γ lines.

The γ quanta of energy $E_\gamma \geq 1022$ keV might also produce a positron-electron pair inside the detector. The positron annihilates with an electron (which are very abundant) and two 511 keV photons are released back to the system. This process is fast enough to be detected in the coincidence with initial photon, producing a peak of the energy E_γ. However, when one or two annihilation photons escape the detector, the observed peaks have the energy of $E_\gamma - 511$ keV (single escape peak) and $E_\gamma - 1022$ keV (double escape peak), respectively.

3.2.2 Detector calibrations

Energy calibration

In order to collect experimental data and identify various radioisotopes based on their characteristic γ lines, an energy scale in γ spectra is required. Calibration is possible based on the measurements of the certified radiation sources which emits the γ radiation of known energies. For example, in a particular case of the γ spectrum (Figure 3.3) of ^{137}Cs radiation source, the peak at the channel 1191 (where the maximum of photopeak is located) corresponds to photons of 662 keV energy.

Registration of photopeaks of energies E_γ (from different calibration sources) at channels C allows to find the channel-to-energy relationship for the given detector set-up (usually a linear function is sufficient):

$$E_\gamma = b_0 + b_1 \cdot C \tag{3.1}$$

where: E_γ – energy of γ quanta [keV], C – channel number, b_0 – intercept coefficient [keV], b_1 – slope coefficient [keV/channel].

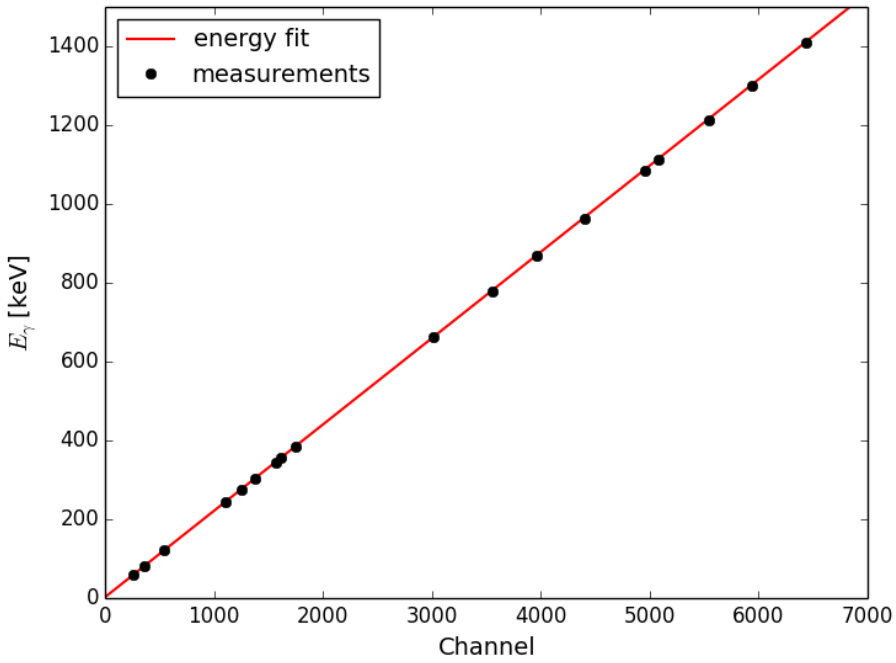

FIGURE 3.4: Example of energy calibration curve provided by TUKAN 8k software after the measurements of decays (IT) of ^{133}Ba, ^{137}Cs, ^{152}Eu, and ^{241}Am calibration sources with CANBERRA HPGe detector at HIL (see Section 3.2.3).

Example of the energy calibration for the HPGe detector at HIL (see Section 3.2.3) is shown in Figure 3.4. The valid energy calibration allows for the proper identification of radioisotopes as shown in Figure C.12.

Efficiency calibration

During a typical measurement in this work, the irradiated target was placed in front of HPGe detector. Radioisotopes inside the target emit characteristic γ radiation in full solid angle and only part of them reaches the Ge crystal, however, some without interacting with it (in particular, low-energy photons might be attenuated in the detector cap, and high-energy photons tend to escape the Ge crystal if it is not thick enough). Even if they do interact, it may be via Compton scattering which will not contribute to the signal measured in photopeak, and will produce a Compton background instead (as shown in Figure 3.3). Therefore, each photon of energy E_γ emitted from the source has a certain probability of being detected in the photopeak by the detector at given geometry (source-detector distance and source geometry). This probability is called detector efficiency, ϵ, and is obtained by measuring the calibration source of known activity A_{cal}. Once placed in fixed geometry, calibration source emits one or several γ quanta, yielding several photopeaks in collected γ spectrum. The number of counts, $N_{dec,obs}$, in each photopeak of different energy, E_γ, is then used to calculate efficiency at this energy (by solving Equation 3.7 for ϵ) as the activity of the source is known as well as the branching ratio associated to each γ line:

$$\epsilon = \frac{N_{dec,obs} \cdot \lambda}{A_{cal} \cdot I_\gamma \cdot \left(1 - \exp(-\lambda \cdot t_{mes})\right)} \tag{3.2}$$

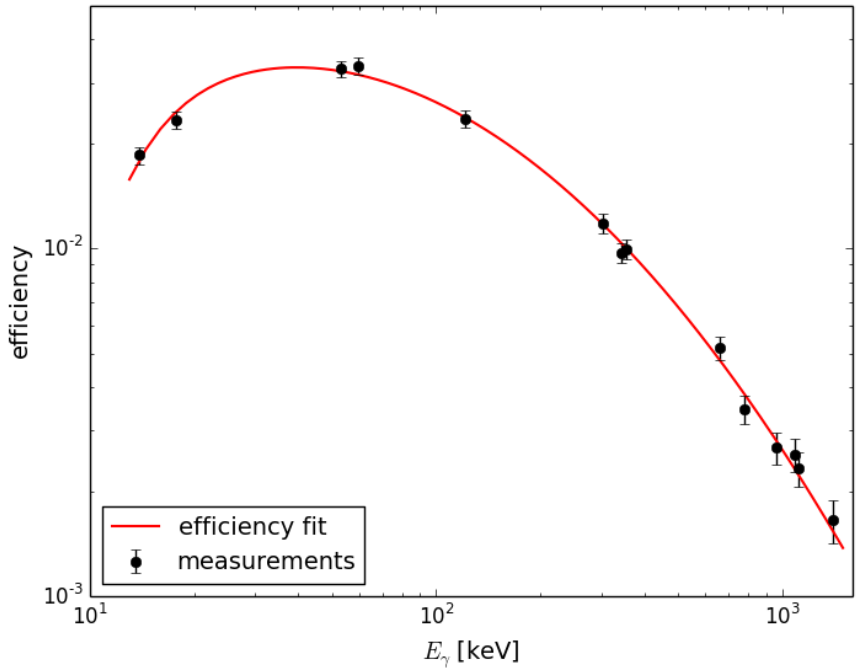

FIGURE 3.5: Example of efficiency calibration curve (Equation 3.3) of CANBERRA HPGe detector at HIL (see Section 3.2.3) at geometry 5.5 cm. The calibration sources include ^{133}Ba, ^{137}Cs, ^{152}Eu, and ^{241}Am.

An example of efficiency calibration measurements at different energies is shown in Figure 3.5. To interpolate these values for every energy E_γ [keV], a fit is performed. In this work, the following formula was used:

$$\epsilon(E_\gamma) = 10^{c_0+c_1\cdot\log(E_\gamma)+c_2\cdot\log^2(E_\gamma)+c_3/{E_\gamma}^3} \tag{3.3}$$

where: c_i – i-th calibration coefficient. The calibration function is purely empirical and several other functions are available which may better reflect certain energy ranges [71].

3.2.3 HPGe detectors employed in this work

The γ radiation from produced radioisotopes was measured after each experiment with the use of the following HPGe detectors (detectors with the bigger crystal have higher efficiency particularly at high γ energies, and detectors with special windows have higher efficiency for the detection of low-energy photons, like X-rays):

- EG&G ORTEC, model: GEM, HPGe 70.1 mm × 69.8 mm, 60% relative efficiency (at HIL),
- CANBERRA, model: BE2825, thickness: 25.5 mm, active area: 2800 mm^2, with 0.6 mm thick Carbon Epoxy window (at HIL),
- CANBERRA vertical detector with 20% relative efficiency (at ARRONAX),
- EG&G ORTEC, model: GMX-25190-p, 56.8 mm × 70.0 mm, with a 0.5 mm thick Be window (at NCNR).

CANBERRA detector at ARRONAX is shown in Figure 3.6 as an example of HPGe detectors used in this work. In this set-up, two geometries are available: close one (3.6c) where the sample is placed on top of the detector head, and far one (3.6d) located 19 cm above the detector. The efficiency is higher at close geometry, however far geometry is used in the case of high activity measurements in order to keep the dead time below 10%. At HIL, available geometries varied from 5.5 cm to 86 cm.

All detectors were equipped with with low-background lead shielding to reduce the contribution of the background γ radiation on the measured spectra. Additional few millimetres of Sn-Cu (at HIL) or Cu (at ARRONAX) is used to eliminate around 97% of the Pb fluorescence X-ray peaks caused by the sample radiation on the lead shielding. Data were collected and analyzed using NCNR TUKAN 8k system (at HIL), ORTEC LVis system and JF Computing Services FitzPeaks Software (at ARRONAX), and CANBERRA Gamma Acquisition & Analysis V1.4 system (at NCNR).

The detectors at HIL and at NCNR were calibrated with ^{133}Ba, ^{137}Cs, ^{152}Eu, and ^{241}Am calibration sources made by NCNR POLATOM. Calibration sources at ARRONAX, ^{57}Co, ^{60}Co and ^{152}Eu, were provided by LEA-CERCA. Nuclear data of these calibration sources are given in Table 3.2.

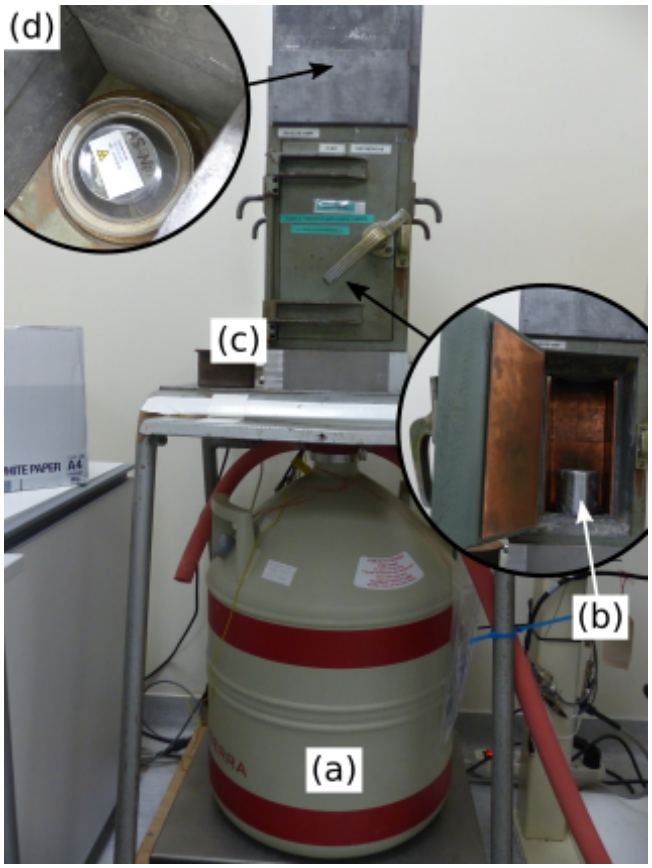

FIGURE 3.6: CANBERRA HPGe detector at ARRONAX: (a) cryostat with the liquid nitrogen, (b) head of HPGe crystal (shielded), (c) thick lead shielding and position for close geometry, (d) far geometry position (behind shielding) with placed radioactive source.

TABLE 3.2: Characteristics of radioisotopes employed as calibration sources in this work (data from [72]).

Isotope	$T_{1/2}$	**Main γ lines** [keV] **(intensity)**
^{57}Co	271.7 d	14.4 (9.16%), 122.1 (85.6%), 136.5 (10.7%)
^{60}Co	5.27 y	1173.2 (99.85%), 1332.5 (99.98%)
^{133}Ba	10.55 y	81.0 (32.9%), 276.4 (7.16%), 302.9 (18.34%), 356.0 (62.05%), 383.8 (8.94%)
^{137}Cs	30.08 y	661.7 (85.1%)
^{152}Eu	13.52 y	121.8 (28.53%), 244.7 (7.55%), 964.1 (14.51%), 1085.8 (10.11%), 1112.1 (13.67%), 1408.0 (20.87%)
^{241}Am	432.6 y	59.4 (35.9%)

3.3 Data analysis

3.3.1 Spectra analysis

Activity calculation

If the sample of total activity $A(t)$ is measured for the time t_{mes} then N_{dec} of them will decay (see Equation 2.4):

$$N_{dec} = \int_0^{t_{mes}} A(t)\,\mathrm{d}t \tag{3.4}$$

However, only fraction of them ($N_{dec,obs}$) will be registered in photopeak (see Section 3.2.2) due to the detector efficiency ϵ, and intensity I_γ of the emitted γ quanta:

$$N_{dec,obs} = N_{dec} \cdot \epsilon \cdot I_\gamma \tag{3.5}$$

$N_{dec,obs}$ is typically obtained by fitting a Gaussian function to the photopeak of interest, and integrating it over the energy with the subtraction of background noise (this procedure is usually done by the software provided with the acquisition system). The radioisotope also decays during the measurement (Equation 2.5) therefore:

$$N_{dec,obs} = \epsilon \cdot I_\gamma \cdot \int_0^{t_{mes}} A(t)\,\mathrm{d}t = \epsilon \cdot I_\gamma \cdot \int_0^{t_{mes}} A_0 \cdot \exp(-\lambda \cdot t)\,\mathrm{d}t \tag{3.6}$$

where A_0 is the activity of the radioisotope at the beginning of the measurement. The solution of this equation allows to calculate the activity at the beginning of the measurement (A_0) of the radioisotope based on $N_{dec,obs}$ counts in its photopeak (of given intensity and efficiency for detection) measured during the time t_{mes}:

$$A_0 = \frac{N_{dec,obs} \cdot \lambda}{\epsilon \cdot I_\gamma \cdot \left(1 - \exp(-\lambda \cdot t_{mes})\right)} \tag{3.7}$$

If such measurement of A_0 was performed Δt after the irradiation, it is possible to calculate activity at the EOB (A_{EOB}) of the given radioisotope by solving Equation 2.5:

$$A_{EOB} = A_0 \cdot \exp(\lambda \cdot \Delta t) \tag{3.8}$$

The uncertainty of such value is propagated from the uncertainties of $N_{dec,obs}$ (value given by software during after the Gaussian fit), and of ϵ at given energy. The final A_{EOB} is then an average from A_{EOB} values calculated with multiple measurements at different times after EOB. The uncertainty of final A_{EOB} is calculated based on the standard deviation between these measurements and their uncertainties.

In the case of radioisotopes of activity $A_{0,2}$ (at the beginning of the measurement) forming during the measurement via the decay of "mother" of activity $A_{0,1}$ (see Section 2.1.2), the evolution of "daughter" activity, $A_2(t)$, in Equation 3.6 is given by Equation 2.7 which results in corrected activity:

$$\begin{aligned} A_{0,2} = {} & \frac{N_{dec,obs} \cdot \lambda_2}{\epsilon \cdot I_\gamma \cdot \left(1 - \exp(-\lambda_2 \cdot t_{mes})\right)} - \frac{\lambda_2}{1 - \exp(-\lambda_2 \cdot t_{mes})} \cdot A_{0,1} \cdot \\ & \cdot \left(\frac{\lambda_2}{\lambda_1 \cdot (\lambda_2 - \lambda_1)} \cdot \left(1 - \exp(-\lambda_1 \cdot t_{mes})\right) - \frac{1}{\lambda_2 - \lambda_1} \cdot \left(1 - \exp(-\lambda_2 \cdot t_{mes})\right) \right) \end{aligned} \tag{3.9}$$

where $N_{dec,obs}$ is the number of counts in "daughter" photopeak, and $A_{0,1}$ is known from the same measurement and calculation based on Equation 3.7. Several such $A_{0,2}$ measurements after EOB might be used for fit of Equation 2.7 to experimental points and find $A_{EOB,2}$.

Minimum Detectable Activity

Sometimes the measured radioisotopes emits γ lines of low intensities, or the measured radioactive source contains very low amount of radioisotope of interest. Then, if the background is not completely eliminated, the desired photopeak is not visible on a spectrum.

In these cases, it is only possible to calculate the Minimum Detectable Activity (MDA). It is an estimation of the activity required to identify a radiation source with an amount of statistical certainty. At 95% confidence level, it is estimated as [73]:

$$MDA[\mathrm{Bq}] = \frac{\left(2.71 + 4.65 \cdot \sqrt{N_{bg}}\right) \cdot \lambda[\mathrm{s}^{-1}]}{\epsilon \cdot I_\gamma \cdot \left(1 - \exp(-\lambda \cdot t_{mes})\right)} \tag{3.10}$$

where: N_{bg} is the number of background counts in the energy region of expected photopeak, and ϵ is the detector efficiency at this energy and employed geometry of the measurement. In general, smaller MDA characterizes better detectors or better measuring set-ups (or lower background), and translates to upper limit of undetected activity of the radioisotope.

Experimental σ and TTY

In some experiments, the measured activities A_{EOB} are induced by the projectiles of energy E (Section 3.3.3) impinging on thin foils. To estimate the probability of their production, foils can be measured with HPGe detector to find A_{EOB} of produced radioisotopes. Then, Equation 2.21 can be solved for σ to calculate the cross-section based on the estimated I (Section 3.3.2):

$$\sigma(E)[\mathrm{mb}] = \frac{A_{EOB}[\mathrm{MBq}] \cdot M[\mathrm{u}] \cdot Z_p \cdot e}{H \cdot N_A \cdot I[\mu\mathrm{A}] \cdot \rho[\mathrm{g/cm^3}] \cdot d[\mu\mathrm{m}] \cdot \left(1 - \exp\left(-\lambda[\mathrm{s}^{-1}] \cdot t_{irr}[\mathrm{s}]\right)\right) \cdot 10^{-43}} \tag{3.11}$$

For higher beam energies, an additional foil, catcher, is installed after each foil (as shown in Figure 4.2), and later measured in the same way. The catcher stops the recoiled nuclei after the nuclear reaction and so collects some of the products during the irradiation. Therefore, the activity measured in the catcher is added to activity measured in the respective foil and then used to calculate σ.

In the case when the A_{EOB} is induced in thick targets by projectiles of energy E, the experimental value of TY or TTY can be obtained from equations from Section 2.1.4:

$$TYY(E)[\mathrm{MBq/\mu Ah}] = \frac{A_{EOB}[\mathrm{MBq}]}{I[\mu\mathrm{A}] \cdot \tau[\mathrm{h}] \cdot \left(1 - \exp\left(-\lambda[\mathrm{s}^{-1}] \cdot t_{irr}[\mathrm{s}]\right)\right)} \tag{3.12}$$

and compared to theoretical predictions from Equation 2.35. If the radioisotopes are formed directly and indirectly in thin or thick targets (Section 2.1.4), Equations 2.38 or 2.39 are used instead to determine σ or TTY.

3.3.2 Beam current monitoring

The beam current is monitored with use of the monitoring foils (see Table 3.3) placed in front of target. The energy of the projectile is degraded by roughly 1% in such foils and thus is not detrimental for the production yield. At the same time, the activity induced in monitor foil with well-known cross-section provides information about the beam current (flux of particles) impinging on the target. During the target preparation, a special care is taken to ensure the same area of monitor foil and production target is seen from the beam side so that the same particle flux passes through both materials (in certain cases, an additional catcher foil must be also installed).

In practice, activated monitor foil is measured in the same way as activated target, with the use of HPGe detector (Section 3.2.3), to calculate A_{EOB} of the monitor radioisotope. Several monitor reactions are recommended by IAEA [74, 75], from which a suitable one must be chosen, with sufficient cross-section value at energy corresponding to the energy and type

TABLE 3.3: Monitor foils and recommended cross-sections employed in this work at HIL, ARRONAX, and NCNR to calculate proton (p), deuteron (d), and α-particle beam current.

Foil, thickness	**Product, $T_{1/2}$**	**Main γ lines [keV] (intensity)** [72]	**Beams, energy**	**Cross-section**
^{nat}Cu, 11 µm	^{62}Zn 9.2 h	40.9 (25.2%), 507.6 (14.8%), 548.4 (15.3%), 596.6 (26.0%)	p 15.3 MeV (HIL) p 33.0 MeV (ARRONAX) p 28.7 MeV (NCNR)	Figure C.1
	^{63}Zn 33.3 h	669.6 (8.2%), 962.1 (6.5%)	p 15.3 MeV (HIL) p 33.0 MeV (ARRONAX) p 28.7 MeV (NCNR)	Figure C.2
	^{65}Zn 244 d	1115.5 (50.04%)	p 15.3 MeV (HIL) p 33.0 MeV (ARRONAX) p 28.7 MeV (NCNR)	Figure C.3
			d 7.5 MeV (HIL)	Figure C.4
^{nat}Ti, 11.2 µm	^{48}V 16.0 d	983.5 (99.98%), 1312.1 (98.2%)	p 15.3 MeV (HIL)	Figure C.5
^{nat}Ni, 8.5–10 µm	^{57}Ni 35.6 h	127.2 (16.7%), 1377.6 (81.7%), 1919.5 (12.3%)	p 33.0 MeV (ARRONAX) p 28.7 MeV (NCNR)	Figure C.6
	^{56}Co 77.3 d	846.8 (99.94%), 1037.8 (14.05%), 1238.3 (66.64%), 1771.4 (15.41%), 2598.5 (16.97%)	d 7.5 MeV (HIL)	Figure C.7
	^{58}Co 70.7 d	810.8 (99.45%)	d 20.0 MeV (ARRONAX)	Figure C.8
	^{61}Cu 3.33 h	283.0 (12.2%), 656.0 (10.8%)	d 7.5 MeV (HIL)	Figure C.9
^{nat}Al, 10 µm	^{24}Na 15.0 h	1368.6 (100%), 2754.0 (99.9%)	α 67.4 MeV (ARRONAX)	Figure C.10

of the employed projectile. Monitor foils used in this work are summarized in Table 3.3 with the recommended cross-section reference on corresponding figures in Appendix C.

After the measurements of A_{EOB} of monitor radioisotopes, Equation 2.21 is solved for I to calculate the beam current based on the recommended cross-sections σ_M for reaction induced by the projectiles of energy E (Section 3.3.3) impinging on monitor foil:

$$I[\mu A] = \frac{A_{EOB}[\mathrm{MBq}] \cdot M[\mathrm{u}] \cdot Z_p \cdot e}{H \cdot N_A \cdot \sigma_M(E)[\mathrm{mb}] \cdot \rho[\mathrm{g/cm^3}] \cdot d[\mu\mathrm{m}] \cdot (1 - \exp(-\lambda[\mathrm{s^{-1}}] \cdot t_{irr}[\mathrm{s}])) \cdot 10^{-43}} \tag{3.13}$$

This approach was used in each experiment to calculate the beam current I used to irradiate the target. In the case of experiments with more than one monitor foil, or with several monitor radioisotopes produced, the averaged beam current was calculated (its uncertainty was estimated based on the uncertainty of beam current calculated from each isotope, and the standard deviation between them). Usually, average beam current measured with the monitor foils was consistent with the Faraday's Cup measurements. If not, intensity from the monitor foil was used in further analysis (required in particular in Equation 3.11 to calculate σ, and in Equation 3.12 to calculate TTY).

3.3.3 Beam energy verification

As shown in [76], monitor foils can also be used to verify the beam energy irradiating the target. If more than one monitor radioisotope is produced (either in the same foil or by using more than one monitor foil) then the activity EOB ($A_{EOB,i}$) of each i-th radioisotope (with the decay constant of λ_i) is produced in corresponding foil (of thickness x_i and molar mass M_i) and with reaction cross-section (σ_i). This relation is given by Equation 2.21 which can be solved for σ_i. For each pair of monitor radioisotopes, for example, $i = 1$ and $i = 2$, the cross-section ratio (r_σ) is defined and calculated as:

$$r_\sigma = \frac{\sigma_1}{\sigma_2} = \frac{A_{EOB,1}}{A_{EOB,2}} \cdot \frac{M_1 \cdot x_2}{M_2 \cdot x_1} \cdot \frac{1 - \exp(-\lambda_2 \cdot t_{irr})}{1 - \exp(-\lambda_1 \cdot t_{irr})} \tag{3.14}$$

Firstly, this is independent of beam intensity I and therefore removes one possible variable in case of doubts. Secondly, it can be compared with expected values of $r_\sigma(E)$ calculated for every energy based on the recommended cross-section values [74, 75]. The projectile energy impinging on the monitor foil is assumed to be the value where measured and expected cross-section ratio match.

Example of beam energy verification is shown in Figure 3.7 that comes from one of irradiation of $^{\mathrm{nat}}$Ti and $^{\mathrm{nat}}$Cu foils with proton beam at HIL (see Table 3.3). The difference of energy impinging on first and second monitor foil were 0.1 MeV which was assumed to be negligible in this analysis. After the irradiation, r_σ for the following pairs were calculated: ^{48}V/^{62}Zn, ^{62}Zn/^{65}Zn, and ^{62}Zn/^{63}Zn, marked as points on lower part of the plot[3]. Compared to the expected cross-section ratio marked as solid lines, the average proton beam energy is located at 15.3 MeV, indicated by the left vertical dashed line.

This approach is consistent with parallel analysis method shown on upper part of Figure 3.7. Here, solid lines represent the values of beam current that would have been calculated based on A_{EOB} of employed monitor radioisotopes (Equation 3.13) for different recommended cross-section values (σ_M) corresponding to different projectile energies. Then, for every energy, the standard deviation between all currents is calculated and plotted as bold solid line STD. Since STD is calculated based on the same A_{EOB} values, it is clear that it points toward the same beam energy, 15.3(1) MeV.

The methodology for the energy verification described here was employed in all experiments in this work to verify the beam energy provided by the cyclotron supplier. Usually, two values matched well within the error limit. However, discrepancy were observed in the case of targets irradiated on the PETtrace station installed at HIL (Section 3.1). The nominal

[3] Technically, there are three more pairs of these radioisotopes but their cross-section ratio is almost constant throughout the investigated energy range and thus making the precise energy estimation impossible.

proton energy from PETtrace machine is 16.5 MeV (Table 3.1), which translates to 16.1 MeV impinging on the target (marked as indicated by the right vertical dashed line) after passing through havar and air. At the moment, the reason for this discrepancy is unknown but the experimental value of 15.3(1) MeV was adopted as the proton energy irradiating the targets at PETtrace station at HIL.

In each experiment, the beam energy is adopted and then re-calculated (as discussed in Section 2.2.1) to the energy impinging on each subsequent element of the irradiated target with the use of SRIM software [32]. The propagation of uncertainty of beam energy (estimated from cross-section ratio method or provided by the laboratory team) and energy straggling are also simulated with SRIM.

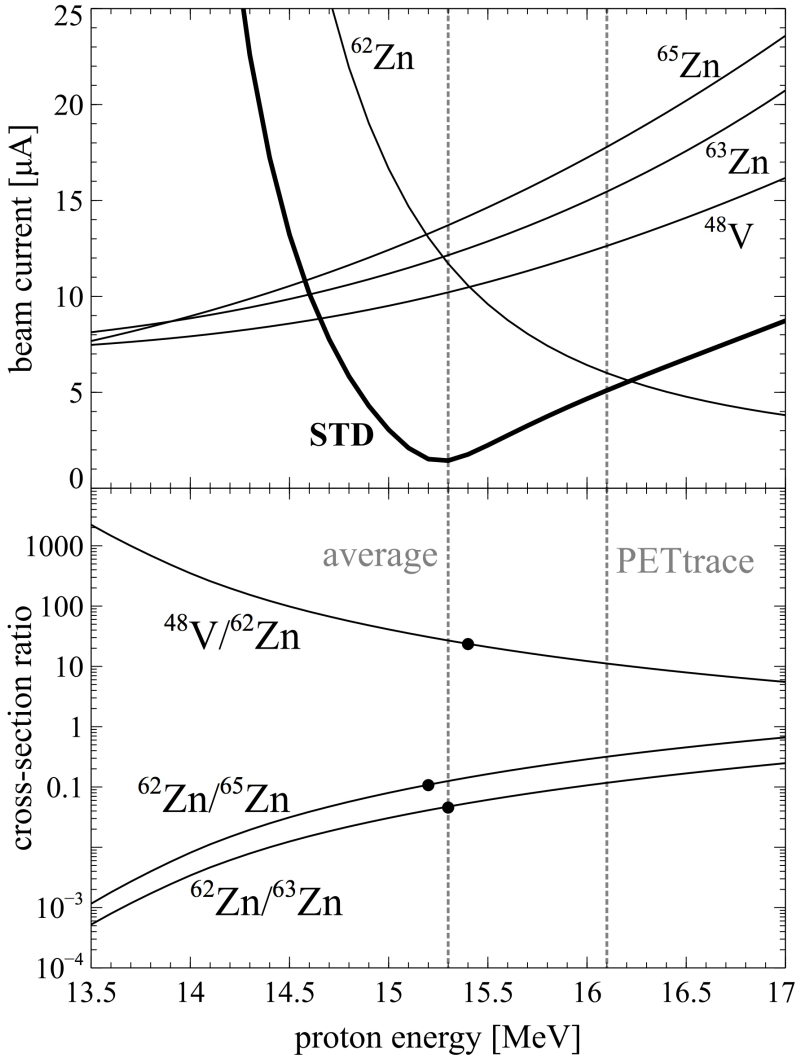

FIGURE 3.7: Analysis of PETtrace proton beam energy (station at HIL) with the use of activity induced in ^{nat}Cu and ^{nat}Ti monitor foils (see Table 3.3). Upper part: values of estimated beam currents, and the standard deviation (STD) between them assuming different PETtrace energy. Lower part: expected (lines) and measured (points) cross-section ratios. Both approaches indicate the proton energy of 15.3(1) MeV impinging on the monitor foil.

Chapter 4

Projects and experiments

This chapter focuses on five uncommon or emerging medical radioisotopes: ^{97}Ru, ^{105}Rh, and $^{43,44g,m,47}Sc$. In particular, their innovative production is discussed based on the performed experiments and the results of the analysis. The measured data included the cross-section of ^{97}Ru and ^{105}Rh production. In the case of $^{43,44g,m,47}Sc$ radioisotopes, Thick Target Yields data was measured and employed for the reconstruction of the excitation functions.

4.1 ^{97}Ru production with α beam

4.1.1 Introduction

The ^{97}Ru radioisotope was first acknowledged as medically interesting in 1970 [77] and is even studied in recent measurements [78, 79]. It has a half-life of 2.9 d allowing non-local production and emits low-energy high-intensity γ line (216 keV, 86%) suitable for prolonged SPECT examinations. It also introduces no additional dose from β^+ as it decays only via EC. It has a theranostic matched pair – ^{103}Ru ($T_{1/2}$ = 39.26 d) that decays to the short-lived Auger emitter ^{103m}Rh ($T_{1/2}$ = 56.12 min), a promising γ-free therapeutic agent. Ruthenium itself has a rich chemistry associated with its various oxidation states (II, III, IV and VIII) and forms more stable compounds compared to the SPECT-standard ^{99m}Tc [80]. Many radioactive Ru-labeled compounds have been studied and found applications as summarized recently in [81], in particular as the chemotherapy agents [82, 83].

Due to these interesting characteristics, many studies on production of ^{97}Ru have been conducted. The reactor route via ^{96}Ru(n,γ) reaction [77] yields very low specific activity which may limit its use for some applications such as molecular imaging. To obtain high specific activity product, one can use charged projectile from accelerators. In the case of cyclotron routes, the first and most used reaction is ^{103}Rh(p,spall) with 200 MeV proton beam and natural rhodium target, as suggested in [84]. While producing high amount of activity of no-carrier-added ^{97}Ru, this method requires high-energy protons and no details about the impurity levels were reported. Another reaction route is the ^{103}Rh(p,x) reaction using 60 MeV proton beam [85]. The ^{97}Ru production yield is very high but accompanied by Tc radioactive impurities which are difficult to discard even after the chemical separation step. A feasible production is the ^{99}Tc(p,3n) reaction suggested in [86] and studied later up to 100 MeV of proton energy [80, 87, 88] as it produces significant amounts of ^{97}Ru with very small amount of radioactive impurities. However, the availability of ^{99}Tc radioactive target is an issue. Later, experimental excitation functions were reported for ^{nat}Ag(p,x) up to 80 MeV of proton energy [89] and for ^{nat}Pd(p,x) up to 70 MeV [90]. These two production routes have much smaller cross-section, hence ^{97}Ru production would require long irradiation time and would contain a substantial amount of radioactive impurities. In the case of deuteron beam, the available reaction ^{96}Ru(d,x) (studied in [91] and partially in this work, see Figure 4.10) is favorable but would produce very low specific activity as the target material is an isotope of the nuclide of interest. Some groups have also investigated more exotic projectiles: ^{nat}Mo(^{3}He,x) [92], ^{93}Nb(^{7}Li,3n) [93] and ^{89}Y(^{12}C,p3n) [78, 94]. In these cases, after chemical separation, low level of radioactive impurities can be achieved but the availability of these beams is scarce making these processes not suitable to launched clinical trials. Finally, the cross-sections for α-induced reactions on Mo were reported in [95]. Additionally, ^{nat}Mo(α,x) production and impurities up to 40 MeV were thoroughly studied in [79, 96].

TABLE 4.1: Nuclear data [72] and production routes of the radioisotopes studied in this work ("tot" indicates production of radionuclide directly and via decay of short-lived metastable state).

Isotope	$T_{1/2}$	**Decay (%)**	**Main γ lines [keV] (%)**	**Contributing reactions**	**Q-value [MeV]**
^{97}Ru	2.83 d	EC (100)	215.7 (85.8), 324.5 (10.8)	^{94}Mo(α,n)^{97}Ru	−7.9
				^{95}Mo(α,2n)^{97}Ru	−15.3
				^{96}Mo(α,3n)^{97}Ru	−24.5
				^{97}Mo(α,4n)^{97}Ru	−31.3
				^{98}Mo(α,5n)^{97}Ru	−41.6
				^{100}Mo(α,7n)^{97}Ru	−54.1
^{89g}Zr	78.4 h	β^+ (23), EC (77)	909.0 (100)	^{92}Mo(α,x)^{89tot}Zr	−16.7
				^{94}Mo(α,x)^{89tot}Zr	−14.0
				^{95}Mo(α,x)^{89tot}Zr	−21.4
				^{96}Mo(α,x)^{89tot}Zr	−30.6
				^{97}Mo(α,x)^{89tot}Zr	−37.4
				^{98}Mo(α,x)^{89tot}Zr	−46.0
				^{100}Mo(α,x)^{89tot}Zr	−60.2
				^{92}Mo(α,x)^{89tot}Nb→^{89tot}Zr	−21.1
				^{94}Mo(α,x)^{89tot}Nb→^{89tot}Zr	−38.9
				^{95}Mo(α,x)^{89tot}Nb→^{89tot}Zr	−46.2
				^{96}Mo(α,x)^{89tot}Nb→^{89tot}Zr	−55.4
				^{97}Mo(α,x)^{89tot}Nb→^{89tot}Zr	−62.2
				^{98}Mo(α,x)^{89tot}Nb→^{89tot}Zr	−70.9
				^{100}Mo(α,x)^{89tot}Nb→^{89tot}Zr	−85.1
^{95g}Tc	20.0 h	EC (100)	765.8 (93.8)	^{92}Mo(α,n)^{95g}Tc	−5.7
				^{94}Mo(α,x)^{95g}Tc	−14.9
				^{95}Mo(α,x)^{95g}Tc	−22.3
				^{96}Mo(α,x)^{95g}Tc	−31.4
				^{97}Mo(α,x)^{95g}Tc	−38.3
				^{98}Mo(α,x)^{95g}Tc	−46.9
				^{100}Mo(α,x)^{95g}Tc	−61.1
				^{92}Mo(α,n)^{95}Ru→^{95g}Tc	−9.0
				^{94}Mo(α,3n)^{95}Ru→^{95g}Tc	−26.7
				^{95}Mo(α,4n)^{95}Ru→^{95g}Tc	−34.1
				^{96}Mo(α,5n)^{95}Ru→^{95g}Tc	−43.3
				^{97}Mo(α,6n)^{95}Ru→^{95g}Tc	−50.1
				^{98}Mo(α,7n)^{95}Ru→^{95g}Tc	−58.7
				^{100}Mo(α,9n)^{95}Ru→^{95g}Tc	−73.0
^{96g}Tc	4.28 d	EC (100)	778.2 (100), 812.6 (82), 849.9 (98), 1127.0 (15.2)	^{94}Mo(α,x)^{96g}Tc	−13.3
				^{95}Mo(α,x)^{96g}Tc	−14.4
				^{96}Mo(α,x)^{96g}Tc	−23.7
				^{97}Mo(α,x)^{96g}Tc	−30.4
				^{98}Mo(α,x)^{96g}Tc	−39.0
				^{100}Mo(α,x)^{96g}Tc	−53.3
^{99}Mo	65.9 h	β^- (100)	140.5 (89.43), 739.5 (12.13)	^{97}Mo(α,2p)^{99}Mo	−13.7
				^{98}Mo(α,x)^{99}Mo	−14.7
				^{100}Mo(α,x)^{99}Mo	−8.3

In this work, the optimization of ^{nat}Mo(α,x)^{97}Ru production route was studied at ARRONAX and extend the available cross-section data to higher projectile energy in coherence with commercially available cyclotrons, which are able to deliver up to about 70 MeV α beam. The coproduction of radioactive impurities (listed in Table 4.1) via ^{nat}Mo(α,x) reactions was also reported, and the possible commercial production of ^{97}Ru with the ^{nat}Mo target was explored. Part of the results of these studies has also been published in [97].

4.1.2 Targets

Three experiments were performed at ARRONAX. The stacked-foils targets were irradiated in vacuum with an α beam of 67.4(5) MeV for about 1 h with beam currents of 40–60 nA. A typical stacked-foil target consisted of an Al monitor foil in front, followed by the set of multiple ^{nat}Mo foils (around 10 µm thick each and natural abundance listed in Table C.1 in Appendix C) and Al degraders (with thickness from 50 to 500 µm), arranged alternately. The order of the foils in the stacks were planned so that each ^{nat}Mo foil is activated with a various energy, all covering the energy range from 40 to 67 MeV in about 3 MeV intervals. Other ^{nat}Al foils were used as catchers of the recoil atoms (this was necessary due to the high energy of α particles), and an additional ^{nat}Ni foil was used as catcher for the ^{nat}Al monitor in front of the stack. A set-up used for the stacked-foils irradiation at ARRONAX is shown in Figure 4.1 and the scheme of a target in Figure 4.2. After the preparation, the target was installed on ARRONAX station (Figure 3.2c).

All foils with a purity of 99% for Al and 99.9% for ^{nat}Mo were purchased from the GoodFellow company. Each foil was weighed before irradiation using an precise scale (10^{-5} g) and scanned for area determination, allowing the precise thickness calculation (assuming the homogeneity over the whole surface).

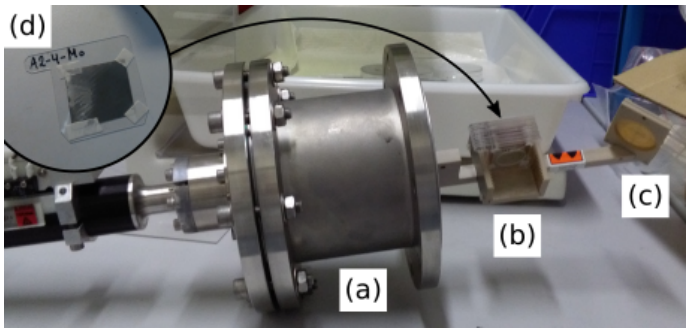

FIGURE 4.1: Photo of the set-up used for the stacked-foils irradiation: (a) holding arm, (b) stack of foils, (c) aluminum foil used for the beam focalization, (d) one of ^{nat}Mo foils from the stack.

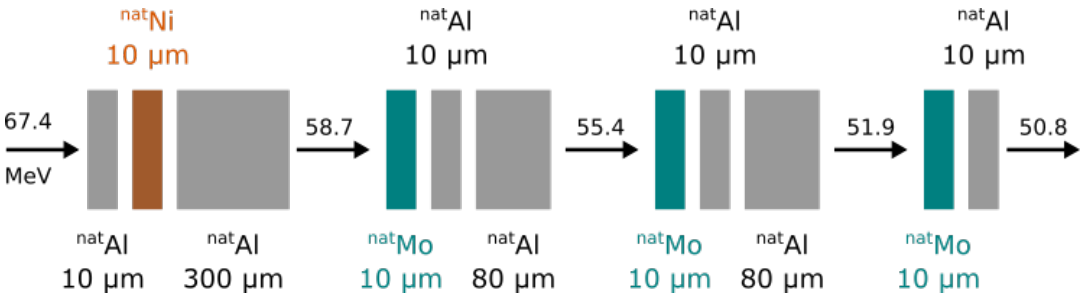

FIGURE 4.2: Stacked-foils scheme used to study ^{nat}Mo(α,x) cross-sections at energies 58.7, 55.4, and 51.9 MeV. ^{nat}Ni foil works as catcher for first ^{nat}Al monitor.

4.1.3 Experimental results

Irradiated stacked-foils (with corresponding catchers) were measured at ARRONAX as discussed in Section 3.2. One of the measured γ spectrum is shown in Figure C.11 (Appendix C). ^{97}Ru is observed, along with radioactive species: ^{89g}Zr, ^{95g}Tc, ^{96g}Tc, and ^{99}Mo. The contributing reactions forming these radioisotopes are listed in Table 4.1 and were taken into account when calculating the expected values based on TENDL [24]. The experimental data are also compared with previous experiments reported in literature [79, 95, 96]. Measured cross-section values are listed in Table C.5 (with corresponding energy uncertainties, not visible on the graphs).

In the case of ^{97}Ru production (Figure 4.3), the measurements are in line with the previously reported data at lower projectile energies. Compared to the experimental data, TENDL shows similar structure but underestimates the cross-section by about 30 mb in the region 20→40 MeV. The subsequent fall of the excitation function and a bump seem to be shifted by 5–10 MeV with respect to the experimental data.

The ^{89g}Zr excitation function (Figure 4.4) is measured for the first time. The predictions of TENDL shows a similar trend as the measurements but slightly shifted toward lower projectile energies (5 MeV).

For ^{95g}Tc (Figure 4.5), the obtained cross-section values are consistent with the previously measured data at lower projectile energies. The shape of TENDL calculations seems to be the same as obtained in the measurements, but again a shift in energy is observed. This shift is probably related to the code since 3 different sets of data acquired at different time, different laboratories and overlapping energy range are consistent with each other and shows the same shift with respect to TENDL.

The experimental data describes well the excitation function for ^{96tot}Tc (Figure 4.6). Additionally, the measurements from this work preserve the trend of the ones reported earlier for lower projectile energies. No shift with respect to the TENDL calculations is observed, contrary to the previous reactions.

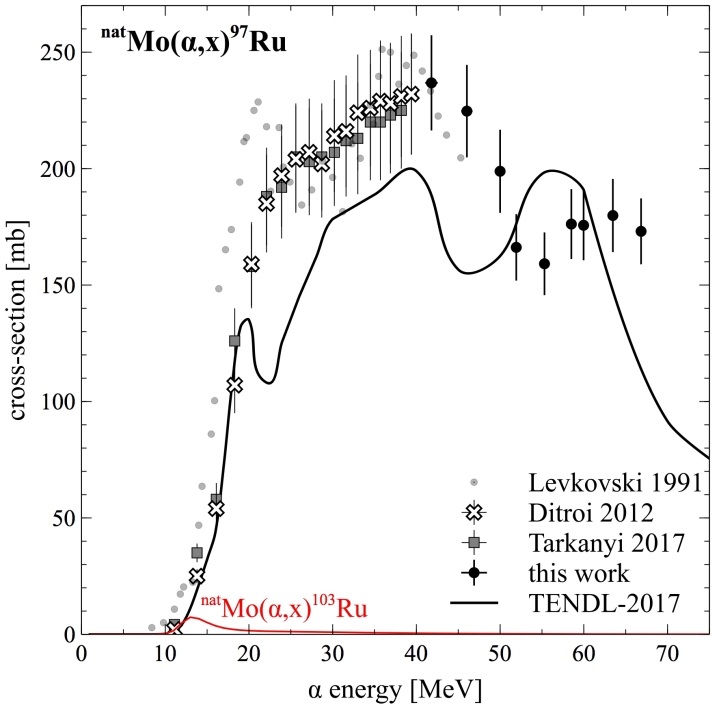

FIGURE 4.3: Measured cross-section for ^{nat}Mo(α,x)^{97}Ru reaction compared with the literature data [79, 95, 96]. The coproduction of ^{103}Ru via ^{100}Mo(α,n)^{103}Ru and ^{100}Mo(α,p)^{103}Tc→^{103}Ru reactions was not observed in the investigated energy range but the total cross-section for ^{103}Ru production is plotted from TENDL (red line).

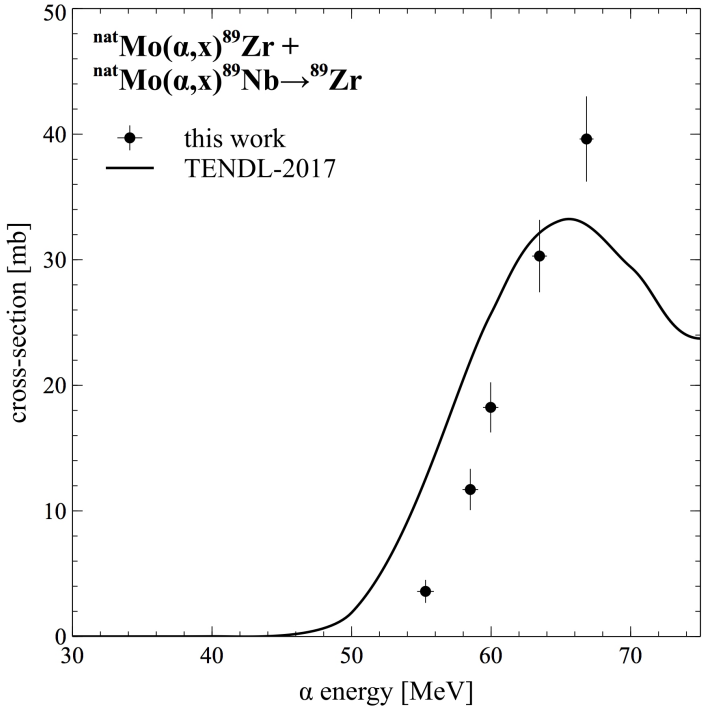

FIGURE 4.4: Measured cross-section for ^{nat}Mo(α,x)^{89g}Zr reaction.

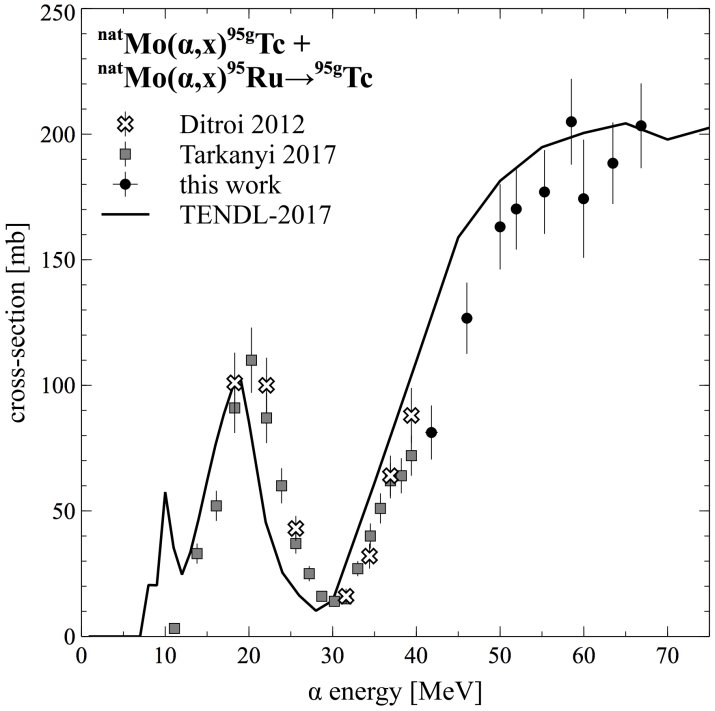

FIGURE 4.5: Measured cross-section for ^{nat}Mo(α,x)^{95g}Tc reaction compared with the literature [79, 96].

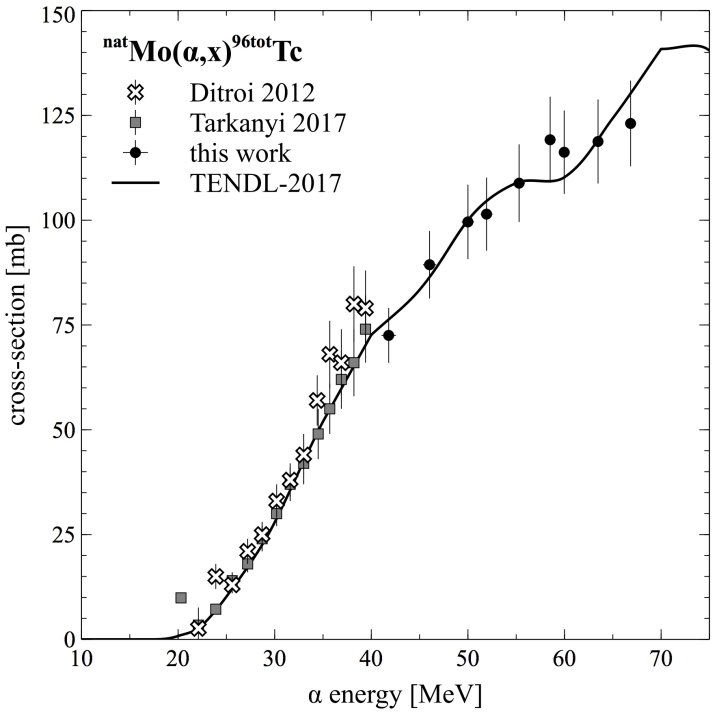

FIGURE 4.6: Measured cumulative cross-section for ^{nat}Mo(α,x)^{96m}Tc and ^{nat}Mo(α,x)^{96g}Tc reactions compared with the literature [79, 96].

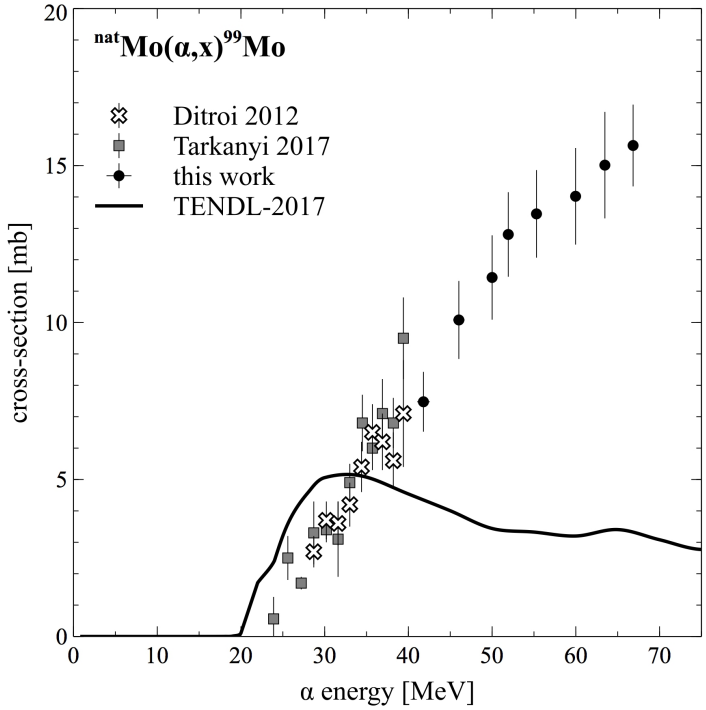

FIGURE 4.7: Measured cross-section for ^{nat}Mo(α,x)^{99}Mo reaction compared with the literature [79, 96].

All experimental cross-sections data for ^{99}Mo production (Figure 4.7) are consistent. The results from this work show a continuous rise of the excitation function up to the maximum energy of these measurements. This is in obvious contrast to TENDL which predicts a maximum at around 30 MeV and then a decrease of the excitation function. A slight shift between TENDL and experimental results is observed at low projectile energies.

4.1.4 Discussion

Cross-section data measured in this work are in line with the existing data at low energies for all radionuclides under investigation. These data were used to calculate production yields of each observed radioisotope using Equation 2.35 and the RYC software (see Appendix A). The *TTY* curve for ^{97}Ru is shown in Figure 4.8. These values were used to estimate the possible production of ^{97}Ru with ^{nat}Mo target and α particles two energies: 30 MeV and 70 MeV, which are the most common in commercially available cyclotrons. The ^{97}Ru production yields are 3.5 MBq/µAh and 20 MBq/µAh respectively. Although the yield is almost 6 times larger at 70 MeV than at 30 MeV, the latter energy of α beam is more common in current cyclotron facilities and is more suitable for the production of other emerging medical radioisotopes like ^{211}At or ^{43}Sc. At the same time, the production route with the α beam of the energy of 70 MeV yields more radioactive impurities and stable Ru isotopes, resulting in lower specific activity.

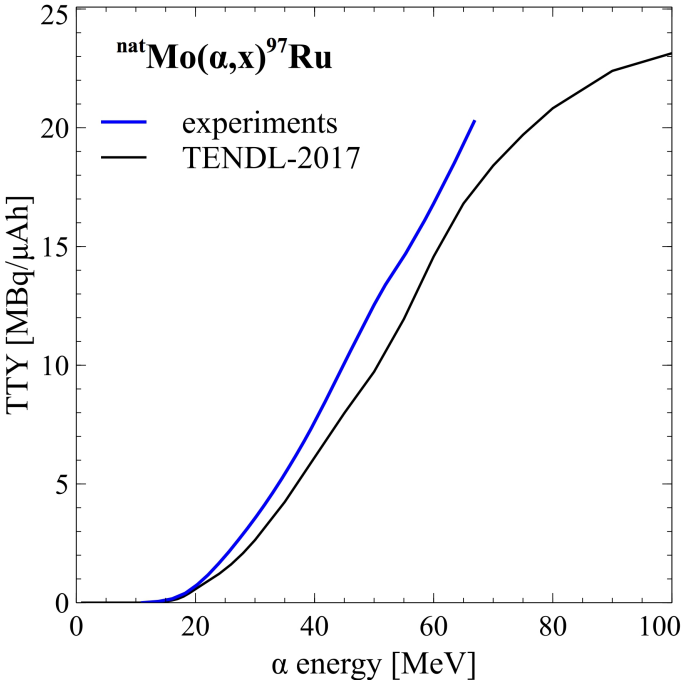

FIGURE 4.8: *TTY* of ^{nat}Mo(α,x)^{97}Ru reaction. The experimental curve (blue) is calculated using the cross-section from this work (above 40 MeV) and the data provided in [79, 96] below 40 MeV.

Table 4.2 shows the parameters for the possible production of 50 MBq as this amount was proven SPECT-applicable in several clinical trials [98]. The yield and the number of produced stable Ru atoms (^{96}Ru, ^{98}Ru, ^{99}Ru, ^{100}Ru, ^{101}Ru, ^{102}Ru) based on the TENDL cross-sections were also calculated in order to estimate the specific activity, SA, of ^{97}Ru. The SA presented here assumes 100% successful chemical extraction of Ru isotopes from Mo target at EOB and hence is just an estimation used to compare different production routes. For the completeness of this study, the alternative production of ^{97}Ru with the use of 100% enriched ^{95}Mo and ^{96}Mo targets and α beams of 30→15 MeV and 67→15 MeV respectively.

It is worth mentioning that from the diagnostics point of view, the most dangerous impurity is ^{103}Ru. It is the only other radioactive Ru element with long half-life ($T_{1/2}$ = 39.26 d),

TABLE 4.2: Estimation of ^{97}Ru activity produced with α beam on molybdenum targets compared with the production route with proton beam and rhodium and technetium targets. The list of radioactive impurities is narrowed down to the most intensive long-lived ones.

Projectile	α particle				proton	
Energy range	30→15 MeV		67→15 MeV		60→45 MeV	50→25 MeV
Target	^{nat}Mo	^{95}Mo (100%)	^{nat}Mo	^{95}Mo (100%)	^{nat}Rh	^{99}Tc
Thickness	100 µm	100 µm	530 µm	530 µm	1.7 mm	2.8 g/cm^2
^{97}Ru yield	3.5 MBq/µAh	14 MBq/µAh	20 MBq/µAh	31 MBq/µAh	40 MBq/µAh	260 MBq/µAh
Specific activity	9 kCi/mmol	36 kCi/mmol	11 kCi/mmol	17 kCi/mmol	3.2 kCi/mmol	11 kCi/mmol
Irradiation	1 h, 15 µA	1 h, 15 µA	1 h, 2.5 µA	1 h, 2.5 µA	1 h, 1.3 µA	1 h, 0.2 µA
Activity EOB	50 MBq (1.4 mCi)	200 MBq (5.4 mCi)	50 MBq (1.4 mCi)	80 MBq (2.2 mCi)	50 MBq (1.4 mCi)	50 MBq (1.4 mCi)
Relative activity at EOB ^{97}Ru	100	100	100	100	100	100
^{89g}Zr			3	0.04		
^{95g}Tc	95	10^{-3}	200	150		200
^{96g}Tc	4	0.2	25	34		60
^{103}Ru	0.12		0.2			
^{99g}Rh					67	
^{100}Rh					2000	
^{100}Pd					250	
Reference	[79, 96]	TENDL	[79, 96] this work	TENDL	[85]	[80]

which will contribute to the patient's dose via β^- decay, high intensity γ line, and Auger electrons from its daughter (^{103m}Rh). During the irradiation of ^{nat}Mo with α beam it can be only formed via ^{100}Mo(α,x) reactions marked as the red line in Figure 4.3. Its contribution is negligible in the investigated energy range (67→40 MeV). For the estimation of thick target yields (Table 4.2), its contribution was calculated considering measured data [79, 96] at lower energies where the main production of ^{103}Ru occurs.

For the completeness of this analysis, Table 4.2 shows also the production of ^{97}Ru with two other promising routes via ^{103}Rh(p,x) and ^{99}Tc(p,3n) reactions with the projectiles and energies available in the commercial cyclotrons. The first production route offers more activity of ^{97}Ru with the use of natural target, however the contribution of co-produced radioactive impurities is higher and the specific activity is lower. Very high activity, purity, and specific activity can be obtained with the use of the second reaction, ^{99}Tc(p,3n), which however requires also radioactive ^{99}Tc target. The energy window employed in this production route should be adjusted to the amount of the available technetium material.

4.1.5 Summary

This work extended the available cross-section data of selected ^{nat}Mo(α,x) reactions up to 70 MeV. The reported measurements preserve well the trend of the cross-section values reported previously below 40 MeV and are consistent in overlapping energy ranges. A reasonable agreement with TENDL predictions is observed however in certain cases the shift of 5-10 MeV is visible with respect to the experimental data.

The production of medically interesting ^{97}Ru was proposed with α beam and ^{nat}Mo target for the projectile energy ranges of 30→15 MeV or 67→15 MeV. The only dangerous radioisotopic impurity that could not be chemically separated would be ^{103}Ru, produced however in negligible amounts. Results from this work indicate that a single 1 h production run with few μA α beam should satisfy the need of SPECT imaging for one patient. Several doses could be produced with longer irradiations with higher beam intensities or by using enriched ^{95,96}Mo targets which would substantially increase the production efficiency.

Further chemical separation would be required to extract Ru element from Mo target and separate it from formed radioactive and stable elements of Tc, Nb and Zr. This can be done for example with either the solvent extraction or distillation methods with an efficiency better than 80% [92]. The specific activity should also be considered in further chemical research as each production route form additional stable atoms of Ru, which would chelate the labelling compound.

4.2 ^{105}Rh production with deuteron beam

4.2.1 Introduction

The radioisotope ^{105}Rh ($T_{1/2}$ = 35.4 h) is an emitter of soft β^- particles of weighted average energy of 150 keV. The mean range of emitted particles in the water is 0.76 mm making ^{105}Rh suitable for labelling monoclonal antibody fragments and accurately delivering the radiation dose to small tumours [99]. The advantage of ^{105}Rh is formation of kinetically inert complexes [100, 101], which are very stable in vivo, contrary to ^{131}I (which 8 day half-life may be too long and labeled molecules may dehalogenate in vivo [102]). For example, preclinical studies on ^{105}Rh-EDTMP reported rapid blood clearance and selective uptake in the bone, offering promising treatment of pain related to bone metastases [103]. Many possible complexes of ^{105}Rh has also been summarized in [100]. Moreover, ^{105}Rh demonstrates low energy γ emission (of 319 keV with 19% intensity) which is appropriate for imaging the distribution of the radionuclide in the human body and dose estimations [103].

Today, the ^{105}Rh radioisotope can be produced with high specific activity via (n,γ) reaction on highly enriched ^{104}Ru target followed by the subsequent β^- decay of the ^{105}Ru. The one day irradiation of 100 mg of ^{104}Ru target in the reactor with the neutron flux of 4×10^{14} s^{-1} produces around 5.3 GBq (on natural target) or 27 GBq (on 99% enriched target) at EOB, suitable for chemical and clinical investigations [102]. The separation of ^{105}Rh from Ru target can be then done via RuO_4 distillation [102] or based on MgO absorption [104].

The production of ^{105}Rh via ^{nat}Pd(p,x) reaction was proposed in [105, 106] with the cross-sections verified up to 80 MeV proton energy [107, 108]. The estimated yield of ^{105}Rh production at 16 MeV is around 2 MBq/µAh. To compare it with the reactor route, one day of irradiation of natural target with 60 µA (equivalent of 4×10^{14} s^{-1} flux) would produce around 3 GBq. The produced activity is comparable to reactor route and could be doubled with the use of a proton beam of 30 MeV. The use of deuteron beam and ^{nat}Pd(d,x)^{105}Rh reaction would also increase the activity by the factor of about 2 if the beam of the same energy is available (cross-section reported in [109]).

In this work, an alternative production route was proposed and studied at ARRONAX. Namely, the ^{nat}Ru(d,x) reactions for which the excitation function for ^{105}Rh and other radioisotopes (listed in Table 4.3) have been measured. The possible commercial production of ^{105}Rh with ruthenium targets is discussed. This production route was also employed in 2013 for labelling studies in Institute of Nuclear Chemistry and Technology in Warsaw, Poland [110].

4.2.2 Targets

Two runs were performed at ARRONAX, irradiating stacked-foils targets in vacuum with deuteron beam of energy below 18 MeV for about 1 h with beam current of 100 nA. The methodology of target preparation was similar to the one described earlier, in previous experiment (Section 4.1.2). The ^{nat}Ru of purity 99.9% was purchased from the GoodFellow company in the form of thin ruthenium layer (0.1 µm) deposited on Al support (25 µm)[1]. Additional Al foils (with thickness from 50 to 300 µm) were arranged alternately for the energy degradation, as shown in Figure 4.9. The natural abundance of ruthenium is shown in Table C.2 (Appendix C). After the preparation, the targets were installed at the ARRONAX station from Figure 3.2c.

Contrary to the previous experiment, deuteron beam used here was of much lower energy. Additionally, the 25 µm Al support of each ^{nat}Ru worked as catcher hence additional ones were not needed. No recoiled nuclei from the ^{nat}Ni monitor were observed on first ^{nat}Ru foil.

Because of the 25 µm Al support, it was not possible to measure the precise thickness of ^{nat}Ru deposition with the measurement of foils' surface and mass. An attempt was made

[1]The only available thicker targets have a thickness above 1 mm allowing the *TTY* measurements and potential large-scale production. However, 1 mm target of ^{nat}Ru would stop 18 MeV deuteron beam completely therefore it could not be employed in the cross-section measurements in this work.

TABLE 4.3: Nuclear data [72] of ^{105}Rh, radioactive contaminants, and their production routes studied in this work, below 18 MeV ("tot" indicates production of radionuclide directly and via decay of short-lived metastable states).

Isotope	$T_{1/2}$	**Decay (%)**	**Main γ lines [keV] (%)**	**Contributing reactions**	**Q-value [MeV]**
^{105}Rh	35.4 h	β^- (100)	306.1 (5.1), 318.9 (19.1)	^{104}Ru(d,n)^{105tot}Rh	4.8
				^{104}Ru(d,p)^{105}Ru→^{105tot}Rh	3.4
^{97}Ru	2.83 d	EC (100)	215.7 (85.8), 324.5 (10.8)	^{96}Ru(d,p)^{97}Ru	5.9
				^{96}Ru(d,n)^{97tot}Rh→^{97}Ru	1.6
				^{98}Ru(d,x)^{97}Ru	−3.9
				^{98}Ru(d,3n)^{97tot}Rh→^{97}Ru	−16.7
				^{99}Ru(d,x)^{97}Ru	−11.4
^{99g}Rh	16.1 d	β^+ (4), EC (96)	89.8 (33.4), 353.1 (34.5), 528.2 (37.9)	^{98}Ru(d,n)^{99g}Rh	2.4
				^{99}Ru(d,2n)^{99g}Rh	−5.1
				^{100}Ru(d,3n)^{99g}Rh	−14.8
^{99m}Rh	4.7 h	β^+ (6), EC (94)	340.8 (72.0), 617.8 (12.3), 1261.2 (11.4)	^{98}Ru(d,n)^{99m}Rh	2.4
				^{99}Ru(d,2n)^{99m}Rh	−5.1
				^{100}Ru(d,3n)^{99m}Rh	−14.8
^{100g}Rh	20.8 h	β^+ (4), EC (96)	446.2 (12.0), 539.5 (80.6), 822.7 (21.1), 1107.2 (13.6), 1362.2 (15.4), 1553.3 (20.7), 1929.8 (11.6), 2376.0 (32.6)	^{99}Ru(d,n)^{100tot}Rh	3.0
				^{100}Ru(d,2n)^{100tot}Rh	−6.6
				^{101}Ru(d,3n)^{100tot}Rh	−13.4
^{101m}Rh	4.34 d	EC (92.8), IT (7.2)	306.9 (81.0)	^{100}Ru(d,n)^{101m}Rh	3.1
				^{101}Ru(d,2n)^{101m}Rh	−3.7
				^{102}Ru(d,3n)^{101m}Rh	−12.9
^{103}Ru	39.2 d	β^- (100)	497.1 (91.0)	^{104}Ru(d,x)^{103}Ru	−2.6
				^{102}Ru(d,p)^{103}Ru	4.0
^{105}Ru	4.44 h	β^- (100)	316.4 (11.1), 469.3 (17.5), 724.3 (47.3)	^{104}Ru(d,p)^{105}Ru	3.4

to verify it with the use of the Scanning Electron Microscope at ARRONAX. Some inhomogeneity regions were observed, however the scan of all irradiated foils, inch by inch, for the measurement of precise thickness map was not possible due to the timing limitations. Therefore the thickness provided by the supplier (with 20% uncertainty) was adopted.

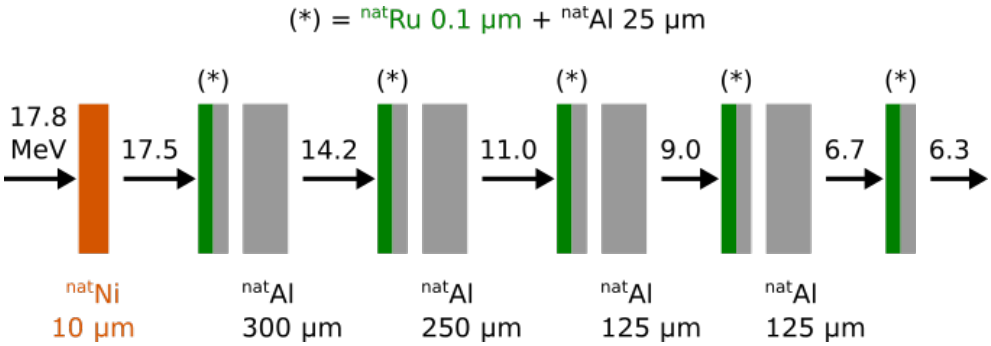

FIGURE 4.9: Stacked-foils design used to study ^{nat}Ru(d,x) cross-sections at energies 17.5, 14.2, 11.0, 9.0, 6.7, and 3.8 MeV. ^{nat}Ru is deposited on Al support. ^{nat}Ni foil is used as monitor.

4.2.3 Experimental results

Measurements and evaluations

The irradiated foils were measured at ARRONAX. ^{105}Rh was observed along with other radioactive species that will act as impurities: ^{97}Ru, ^{99g}Rh, ^{99m}Rh, and ^{100g}Rh, ^{101m}Rh, ^{103}Ru, and ^{105}Ru. The contributing reactions forming these radioisotopes are shown in Table 4.3 and were taken into account when calculating the expected values based on TENDL [24]. Experimental results are compared with the only one literature data [91] available for some of the investigated reactions. The results are shown in following figures and the values are listed in Table C.6. All measured cross-sections have almost 25% uncertainty due to two main factors:

- 20% uncertainty of Ru thickness (inhomogeneity of deposition, see Section 4.2.2),
- 5–20% uncertainty of gaussian fit of the small photopeaks caused by low produced activity (coming from the very thin Ru layer available, 0.1 µm).

In certain cases, no photopeak was visible even after 24 h measurement, and thus some cross-section data were not obtained.

The ^{97}Ru radioisotope is formed directly and indirectly via the decays of two "mother" nuclides: ^{97g,m}Rh. However, their half-lives are relatively short (30.7 min and 46.2 min respectively) and their measurement was not possible thus the cross-section reported here is the cumulative one (Figure 4.10). These results are in the agreement with the measurements reported in [91] and withTENDL predictions.

In the case of other observed radioisotopes: ^{99g}Rh (Figure 4.11), ^{99m}Rh (Figure 4.12), ^{100g}Rh (Figure 4.13), and ^{101m}Rh (Figure 4.14), their formation is only direct. TENDL predictions are higher by a factor of about 2 than the measured cross-section values although experimental data seem to preserve the behaviour of TENDL excitation functions. No other experimental data are available for the comparison.

The only available cross-section data [91] for ^{nat}Ru(d,x)^{103}Ru reaction provides almost exactly 2 times higher values than data from this work (Figure 4.15). The discrepancy may be related to the calibration issue in [91], where 497 keV γ line was compared with 511 keV γ line from ^{22}Na source without accounting for 200% intensity from annihilation. Applying this correction would place all experimental results and TENDL predictions within the error limit.

Finally, the ^{105}Ru radioisotope is formed uniquely on ^{104}Ru. The measurements confirm the shape of excitation function from TENDL which however provides around 30% lower values above 10 MeV.

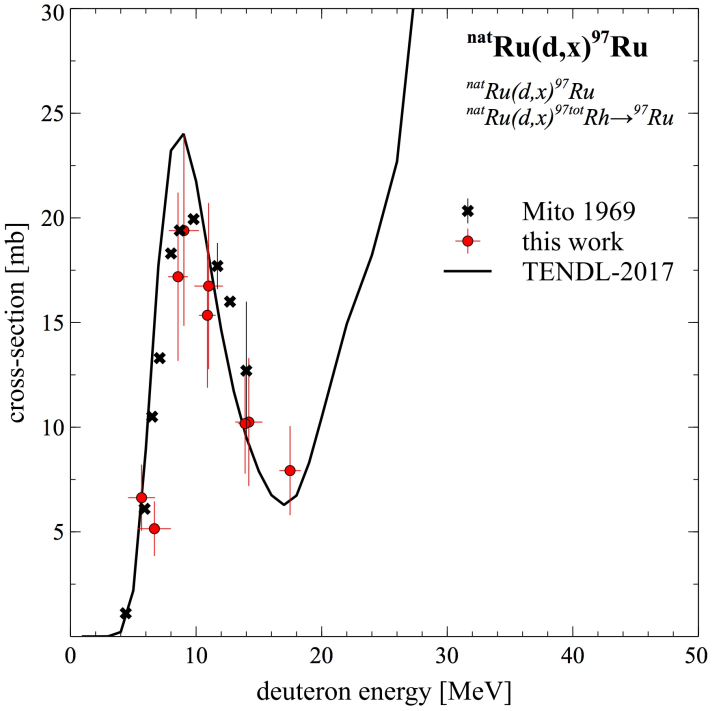

FIGURE 4.10: Measured cross-section for ^{nat}Ru(d,x)^{97}Ru reaction compared with the literature data [91] and TENDL predictions [24].

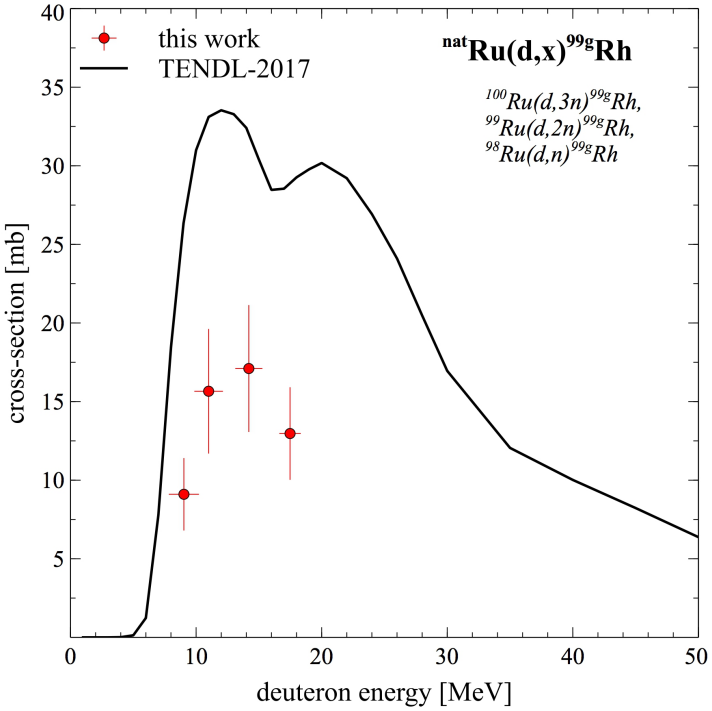

FIGURE 4.11: Measured cross-section for ^{nat}Ru(d,x)^{99g}Rh reaction compared with TENDL predictions [24].

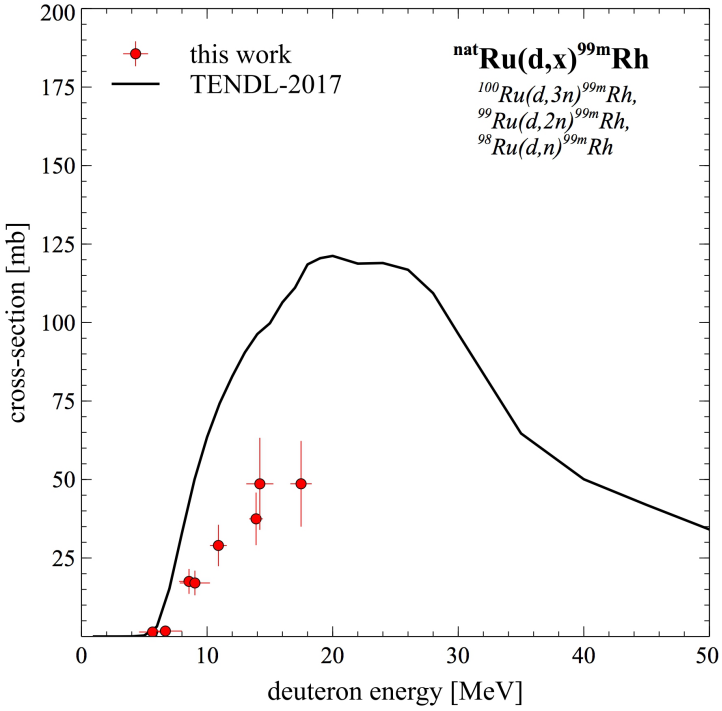

FIGURE 4.12: Measured cross-section for ^{nat}Ru(d,x)^{99m}Rh reaction compared with TENDL predictions [24].

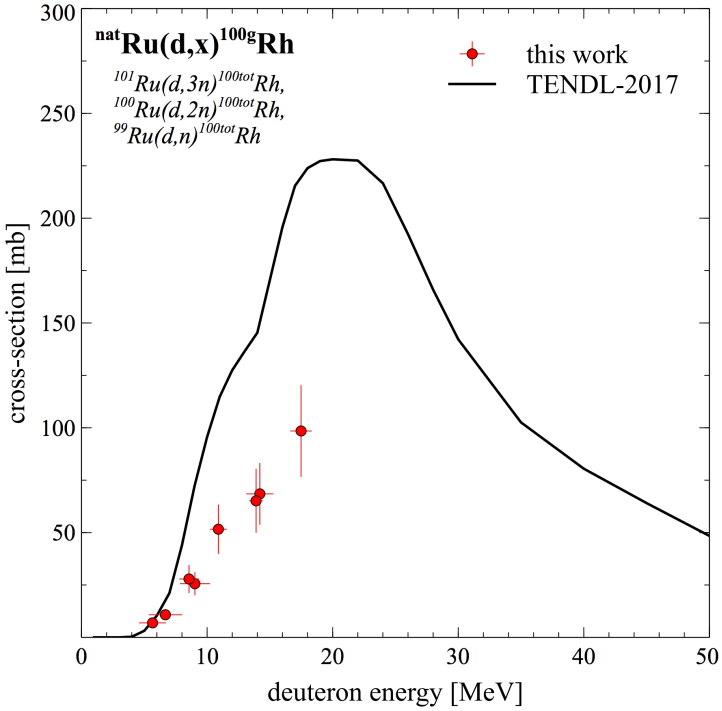

FIGURE 4.13: Measured cross-section for ^{nat}Ru(d,x)^{100g}Rh reaction compared with TENDL predictions [24].

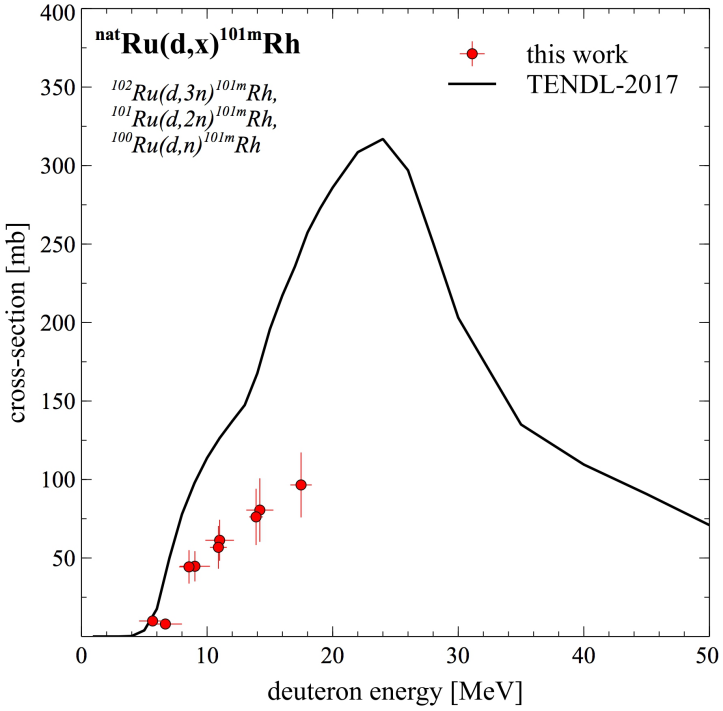

FIGURE 4.14: Measured cross-section for ^{nat}Ru(d,x)^{101m}Rh reaction compared with TENDL predictions [24].

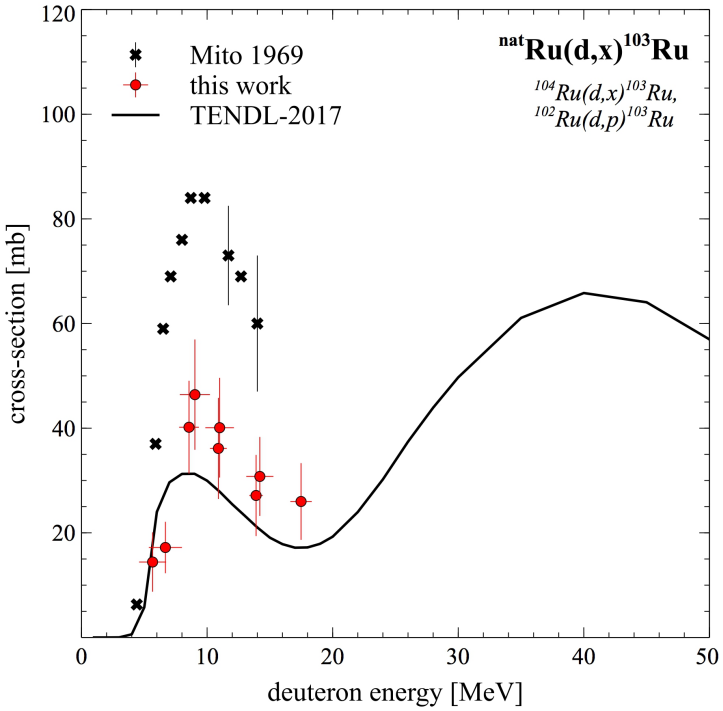

FIGURE 4.15: Measured cross-section for ^{nat}Ru(d,x)^{103}Ru reaction compared with the literature data [91] and TENDL predictions [24].

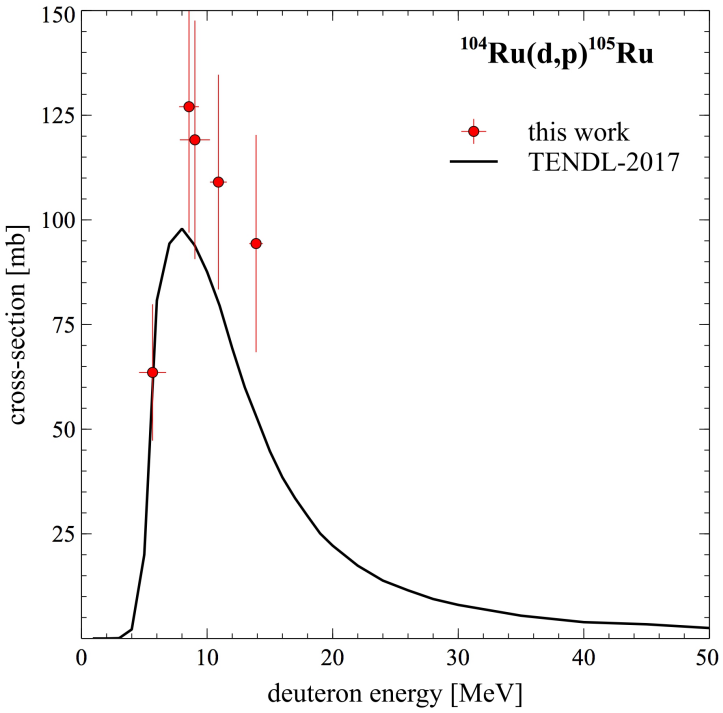

FIGURE 4.16: Measured cross-section for ^{104}Ru(d,p)^{105}Ru reaction compared with TENDL predictions [24].

Analysis of ^{105}Rh formation

The ^{105}Rh is produced in several ways but only on ^{104}Ru and always partially through the 100% IT decay of isomeric state ^{105m}Rh ($T_{1/2}$ = 42.9 s). The direct production of ground state and through metastable state is not distinguished here, due to very short half-life of the isomer, therefore all cross-section indicates the total production, ^{105tot}Rh. Additionally, ^{105tot}Rh is formed through the decay of co-produced ^{105}Ru ($T_{1/2}$ = 4.44 h). Assuming $T_{1/2}(^{105}\text{Ru}) << T_{1/2}(^{105}\text{Rh})$, the ^{105}Ru can be treated as "compound nucleus", and the cross-section for ^{104}Ru(d,x)^{105tot}Rh reaction (σ_{tot}) is a sum of cross-section for ^{104}Ru(d,n)^{105tot}Rh reaction (σ_{Rh}) and ^{104}Ru(d,n)^{105}Ru reaction (σ_{Ru}), as given by Equation 2.21:

$$A_{EOB,Rh} = H \cdot \frac{N_A}{M} \cdot \frac{I}{Z_p \cdot e} \cdot x \cdot \underbrace{(\sigma_{Rh} + \sigma_{Ru})}_{\sigma_{tot}} \cdot (1 - \exp(-\lambda \cdot t_{irr})) \tag{4.1}$$

where $A_{EOB,Rh}$ is activity EOB of ^{105}Rh measured at least 3 d after EOB, allowing the complete decay of ^{105}Ru, and recalculated for EOB.

This approach assumes that $A_{EOB,Rh}$ comes from direct ^{105}Rh formation and from "immediate" ^{105}Ru decay during and after EOB. Cross-section for ^{104}Ru(d,x)^{105tot}Rh calculated in this way, σ_{tot}, is shown in Figure 4.17. The cross-section from TENDL presented on the plot is also a sum of two cross-sections and shows a relatively good agreement with the measurements from this work, preserving the shape of excitation function but providing about 30% lower values above the projectile energy of 10 MeV. There is no other reported experimental data for this excitation function. Nevertheless, cross-section for ^{104}Ru(d,p)^{105}Ru reaction reported in [91] is based on the measurements of ^{105}Rh activity. In the article, there is no remark on direct ^{105}Rh formation hence the data presented in [91] might be in fact σ_{tot} as discussed here. Therefore they are presented in Figure 4.17, instead of in Figure 4.16, where they would be about 2 times above measurements obtained in this work and predictions of TENDL.

However the methodology described above is a simplification and after EOB the ^{105}Rh radioisotope is formed in "mother-daughter" decay of ^{105}Ru. Knowing the activity EOB of

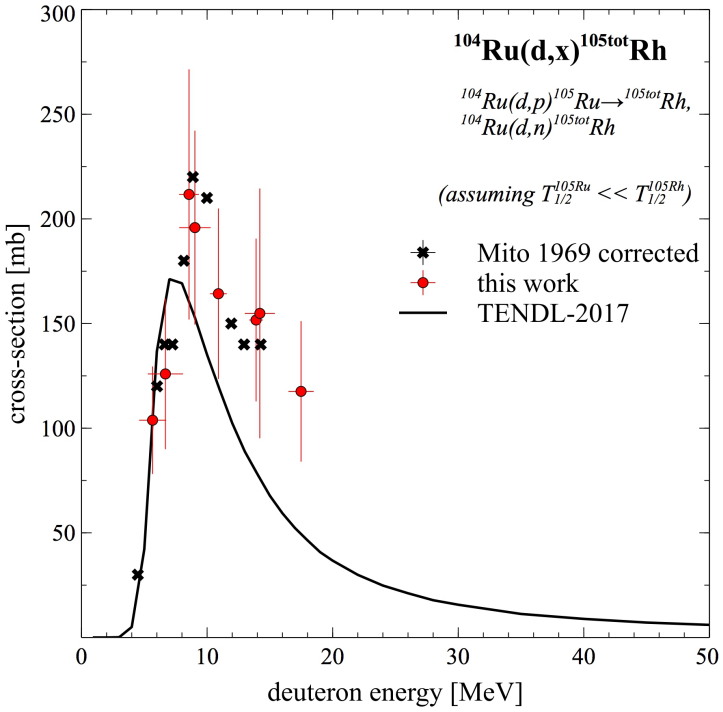

FIGURE 4.17: Measured cross-section for ^{104}Ru(d,x)^{105tot}Rh reaction compared with the corrected data from the literature [91] and with TENDL predictions [24].

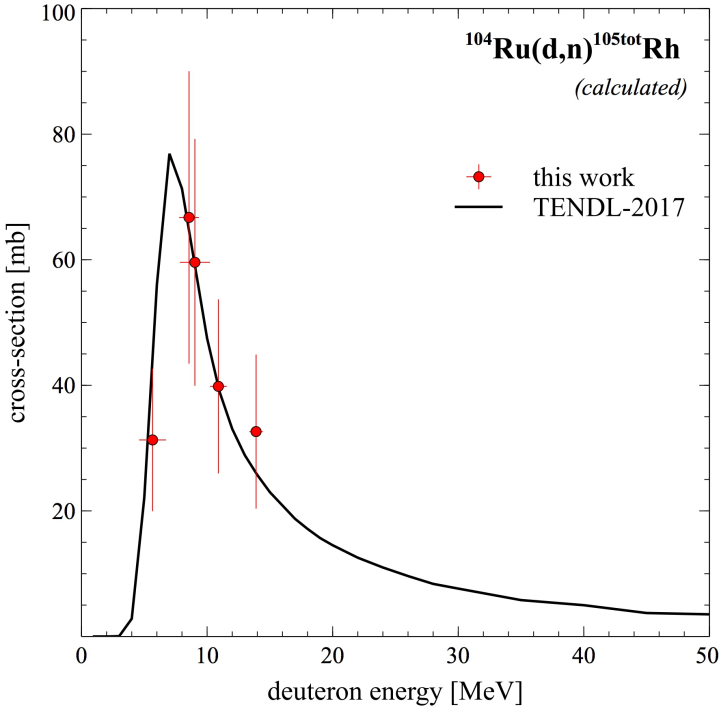

FIGURE 4.18: Calculated cross-section for ^{104}Ru(d,n)^{105tot}Rh reaction compared with TENDL predictions [24].

^{105}Ru it is then possible to calculate the activity EOB of ^{105}Rh produced only during irradiation, $A^{dir}_{EOB,Rh}$ (by solving Equation 2.7 for $A_2(t=0)$). This activity is formed only during the irradiation but still some of it is produced through the decays of ^{105}Ru which is also forming and decaying before EOB, and therefore is given by Equation 2.38:

$$A^{dir}_{EOB,Rh} = H \cdot \frac{N_A}{M} \cdot \frac{I}{Z_p \cdot e} \cdot x \cdot \Big((\sigma_{Rh} + \frac{\lambda_{Rh}}{\lambda_{Ru} - \lambda_{Rh}} \cdot \sigma_{Ru}) \cdot (1 - \exp(-\lambda_{Rh} \cdot t_{irr})) - \\ - \frac{\lambda_{Rh}}{\lambda_{Ru} - \lambda_{Rh}} \cdot \sigma_{Ru} \cdot (1 - \exp(-\lambda_{Ru} \cdot t_{irr})) \Big) \tag{4.2}$$

where $\lambda_{Rh,Ru}$ are the decay constants of ^{105}Rh and ^{105}Ru respectively. Given the measured σ_{Ru} (five experimental points, Figure 4.16) and $A^{dir}_{EOB,Rh}$ calculated as above, the direct production cross-section of ^{104}Ru(d,n)^{105tot}Rh was calculated (Figure 4.18). The results show very good agreement with TENDL which indicates that 30% shift observed for cumulative production of ^{105tot}Rh (Figure 4.17) is related to shift present in ^{105}Ru excitation function (Figure 4.16). It is also worth mentioning that Equation 4.2 transforms to Equation 4.1 in limit $\lambda_{Ru} \to \infty$ reflecting the assumption $T_{1/2}(^{105}\text{Ru}) << T_{1/2}(^{105}\text{Rh})$ which confirms the validity of ^{105}Rh calculations.

4.2.4 Discussion

The measured cross-sections were used to calculate production yields of each observed radioisotope. The TTY curve for direct and indirect production of ^{105}Rh on natural target is shown in Figure 4.19 (the yield is 5 times higher for 99% enriched target). This yield is calculated based on cumulative cross-section for the formation of ^{105}Rh and ^{105}Ru which decays to ^{105}Rh. All obtained yields were used to estimate the possible production of ^{105}Rh with ^{nat}Ru and enriched ^{104}Ru targets, as shown in Table 4.4, for the same beam flux and irradiation time as used in the case of the reactor route. For the estimation of contribution of ^{103}Ru in enriched target, cross-section from TENDL was employed. This is because ^{103}Rh is produced on enriched target only via ^{104}Ru(d,x) reactions and the experimental cross-section from this work is for ^{104}Ru(d,x)^{103}Ru (Figure 4.15).

As mentioned in [102], the activation of 100 mg enriched target with the same flux of neutrons produces around 27 GBq of ^{105}Rh after one day of irradiation (the activities of co-produced radioisotopes were not reported). Hence, the activation of 200 mg of enriched ^{104}Ru would produce around 54 GBq of ^{105}Rh. The activity produced with the use of the deuteron beam of the same flux provides around 43 GBq with almost no contribution of radioactive impurities. Assuming the standard size of the beam of 1 cm^2, the deuteron route requires 350 mg target material to cover the energy range 17.5→5 MeV. If the beam intensity of 100 µA is available, the same activity could be produced in 14→7 MeV energy range with 200 mg material. Further decrease of the required mass of the target would be achieved with better focalisation of the deuteron beam. For more detailed comparison, the parameters of given cyclotrons and reactors should be taken into account. However, it is clear that both routes produce the similar activity of ^{105}Rh with comparable amounts of enriched target material.

For the reactor route, the details of SA calculations are not specified in [102] but the value of around 3.3 kCi/mmol is expected after one day activation of enriched ^{104}Ru followed by 48 h cooling time and 50% chemical separation efficiency. The main factor lowering SA discussed in the article is the contribution of Ru leftovers which would compete with ^{105}Rh in labelling process. In estimations presented here, it is assumed that the same fraction of Ru would be left from 350 mg target, and the same cooling time and chemical separation would be applied to 43 GBq of ^{105}Rh. The specific activity in these conditions would reach roughly 2.6 kCi/mmol though it might be lower due to concentration of other metal ions which depends on the chemical separation method. However, it is safe to assume that ^{105}Rh productions with neutron or deuteron projectiles provide similar specific activity.

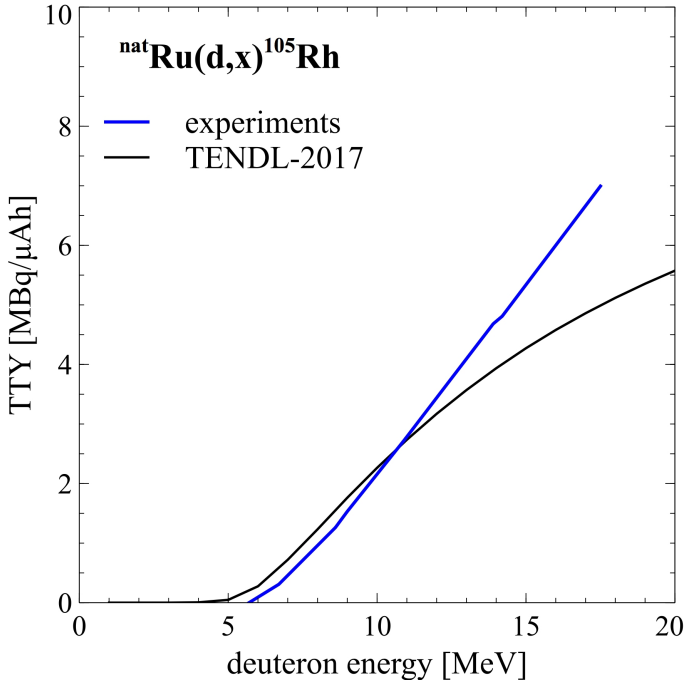

FIGURE 4.19: *TTY* of ^{nat}Ru(d,x)^{105}Rh calculated from the measured cross-section. The yield takes into account the indirect production of ^{105}Ru and decay to ^{105}Rh.

TABLE 4.4: Estimation of ^{105}Ru activity and long-lived impurities produced with deuteron beam on ruthenium targets activated in the same conditions as in the reactor. (*) indicates the estimation based on TENDL cross-section.

Deuteron energy		17.5 → 5 MeV	
Target		^{nat}Ru	^{104}Ru (99%)
Thickness		350 mg/cm^2	350 mg/cm^2
^{105}Rh yield		7 MBq/μAh	37 MBq/μAh
Irradiation		1 d, 60 μA	1 d, 60 μA
Activity EOB		8 GBq	43 GBq
Relative activity at EOB	^{105}Ru	100	100
	^{97}Ru	25	
	^{99g}Rh	5	
	^{99m}Rh	310	
	^{100g}Rh	290	
	^{101m}Rh	90	
	^{103}Ru	6	0.13 (*)

4.2.5 Summary

This work experimentally verified and re-evaluated previous data on ^{105}Rh formation via ^{104}Ru(d,n) reaction up to 17.5 MeV. Additionally, data on ^{nat}Ru(d,x) reactions were studied for the first time although the measurements have around 25% uncertainty and thus should be redone in the future to get better precision.

The activation of enriched ^{104}Ru with the same flux of neutron and deuteron beams was also discussed. Both routes yield GBq quantities of ^{105}Rh in one day irradiation. Deuterons provide around 1.5 times more activity and similar specific activity but require around 2–3 times more target material. The estimation of specific activity should be verified by the chemical study.

4.3 Production of Sc radioisotopes with proton and deuteron beams

4.3.1 Introduction

Interest and applications of scandium radioisotopes

Recently there is a growing interest in three scandium radioisotopes, ^{43}Sc, ^{44g,m}Sc and ^{47}Sc, in the nuclear medicine field (their properties are shown in Table 4.5, along with the investigated production routes and observed coproduced radioactive impurities). They have been proven to be an interesting alternative to currently used radioisotopes, both for therapy and diagnostics. In spite of poorer positron tomography resolution [111] with the use of these radioisotopes, their production using a single facility and subsequent distribution to hospitals not possessing a cyclotron or radiopharmaceutical synthesis equipment may be attractive.

Both positron emitters ^{43}Sc and ^{44g}Sc are promising PET radioisotopes that can compete with commonly used ^{68}Ga [111–115]. The additional γ quanta from ^{44g}Sc is a disadvantage as it introduces additional dose to the patient. However, as shown by XEMIS group [116–118] and suggested in [119, 120], the γ photon from ^{44g}Sc can be used in coincidence with β^+ decay for imaging, lowering the required activity and thus reducing the overall dose (see Appendix B). A metastable state, ^{44m}Sc, has relatively long $T_{1/2}$, and decays mainly by a low energy IT to the ground state, and thus can be used as long-lived in vivo ^{44m}Sc/^{44g}Sc generator for the prolonged examinations or studies of long metabolic processes [121–124].

Meanwhile, ^{47}Sc is a low-energy β^- emitter suitable for targeted radiotherapy and SPECT imaging [125], which is emphasized also within IAEA Coordinated Research Project [126]. As mentioned in [127, 128], this radioisotope can form a matched pair with diagnostic scandium radioisotopes. It can also be used instead of the therapeutic ^{177}Lu as they share similar chemistry [129].

The general interest of scandium radioisotopes was also stressed recently in [130]. It is not only related to their convenient physical properties, but also to the feasible chemistry that has been reported mainly for the labeling of DOTA-peptides along with the stability and biodistribution studies [112, 113, 121–123, 131–140].

Availability of scandium radioisotopes

The production of scandium radioisotopes with the use of cyclotrons has been presented in numerous papers with the use of proton [113, 127, 132, 133, 136–139, 141–146], deuteron [121–124, 147] and α particle beams [147–151] with calcium and potassium targets. The reaction with potassium nuclei requires α beam and generates lower activities [150]. Therefore, typically calcium in the form of CaO or $CaCO_3$ targets is used. CaO or $CaCO_3$ can be later easily dissolved for the chemical separation [113, 121, 123, 131–134, 136–140]. In this work, these data is complemented by the *TTY* measurements and study of production optimization with the use of natural and enriched $CaCO_3$ and TiO_2 targets irradiated by proton (HIL, ARRONAX, NCNR) and deuteron (HIL) beams (see Table 3.1). All observed radioisotopes

TABLE 4.5: Nuclear data [72] of medically interesting scandium radioisotopes, their radioactive impurities, and main production routes with proton and deuteron beams observed in this work.

Isotope	$T_{1/2}$	**Decay (%)**	**Main γ lines** [keV] **(intensity %)**	**Contributing reactions**	**Q-value** [MeV]
^{43}Sc	3.89 h	β^+ (88), EC (12)	373 (22.5)	^{43}Ca(p,n)^{43}Sc	−3.0
				^{44}Ca(p,2n)^{43}Sc	−14.1
				^{46}Ti(p,α)^{43}Sc	−3.1
				^{47}Ti(p,n+α)^{43}Sc	−1.2
				^{42}Ca(d,n)^{43}Sc	2.7
^{44g}Sc	3.97 h	β^+ (94.3), EC (5.7)	1157 (99.9)	^{44}Ca(p,n)^{44g}Sc	−4.4
				^{48}Ti(p,n+α)^{44g}Sc	−1.4
				^{43}Ca(d,n)^{44g}Sc	4.5
^{44m}Sc	58.6 h	IT (99), EC (1)	271 (86.7), 1002 (1.2), 1126 (1.2), 1157 (1.2)	^{44}Ca(p,n)^{44m}Sc	−4.7
				^{48}Ti(p,n+α)^{44m}Sc	−1.4
				^{43}Ca(d,n)^{44m}Sc	4.2
^{46}Sc	83.8 d	β^- (100)	159 (68.3)	^{48}Ca(p,3n)^{46}Sc	−1.9
				^{47}Ti(p,2p)^{46}Sc	−1.0
^{47}Sc	3.35 d	β^- (100)	159 (68.3)	^{48}Ca(p,2n)^{47}Sc	−8.7
				^{48}Ti(p,2p)^{47}Sc	−1.1
				^{46}Ca(d,n)^{47}Sc	6.3
^{48}Sc	43.7 h	β^- (100)	175 (7.5), 984 (100), 1038 (97.6), 1213 (2.4), 1312 (100)	^{48}Ca(p,n)^{48}Sc	−5.0
				^{49}Ti(p,2p)^{48}Sc	−1.1
				^{48}Ca(d,2n)^{48}Sc	−2.7
^{47}Ca	4.54 d	β^- (100)	489 (5.9), 808 (5.9), 1297 (67.0)	^{48}Ca(p,3n)^{46}Sc	−1.9
^{43}K	22.3 h	β^- (100)	143 (2.6), 305 (90.9), 476 (4.1), 769 (1.5)	^{44}Ca(p,2p)^{43}K	−1.2
^{48}V	16.0 d	β^+ (50), EC (50)	944 (7.9), 984 (100), 1312 (98.2), 2240 (2.3)	^{48}Ti(p,n)^{48}V	−4.8

and their production channels are listed in Table 4.5. Part of this work has also been published in [152].

As studied in above-mentioned references, ^{43}Sc can be obtained via ^{40}Ca(α,p) reaction[2] at 30 MeV projectile energy impinging on ^{nat}Ca or $^{nat}CaCO_3$ targets. These production routes provide very high yields (up to around 210 and 90 MBq/μAh respectively) and very good purity thanks to high natural abundance of ^{40}Ca. The 4 h irradiation of $^{nat}CaCO_3$ with alpha beam of the 25 μA intensity and in the energy range 20→0 MeV would produce around 6 GBq ^{43}Sc with negligible contamination of ^{44g}Sc and ^{47}Sc at the level of 0.03%. However, α beam is not commonly available hence the interest of proton or deuteron induced reaction is discussed in this work.

In the case of ^{44g}Sc, its production is possible with the highly enriched ^{41}KCl and $^{42}CaCO_3$ targets via α beam bombardment. The yield reaches up to 60 MBq/μAh but radioactive impurities are at the level of 15% even with the optimized energy range. More attractive solution is the deuteron induced reaction, ^{44}Ca(d,2n). On enriched calcium carbonate target, TTY is about 700 MBq/μAh at 15 MeV, followed by around 1% of radioactive impurities. In this work, a similarly attractive solution with the use of proton beam is discussed.

Alternatively, ^{44g}Sc can be obtained from ^{44}Ti/^{44g}Sc generator ($T_{1/2}$ = 59.1 y [72]) as pointed in [134, 135, 153, 154] and summarized recently in [155]. Currently, such generator is available in Mainz, with 185 MBq ^{44}Ti and the possibility to extract 97% ^{44g}Sc in 20 mL solution [153].

So far, yield of ^{47}Sc production with the use of accelerators was studied in [156] via ^{48}Ca(p,2n) reaction. This work verifies this data and discuss the possible cyclotron production of ^{47}Sc with respect to more common reactor route. The latter was presented in number of papers for fast or slow neutron reactions [125, 127, 157–161] together with (γ,p) reactions [162–164]. In both cases, high activity of ^{47}Sc can be produced with the use of ^{46}Ca or ^{48}Ti targets respectively. However, these routes requires dedicated facilities. At the same time, α particle induced reaction even on enriched ^{44}Ca targets has much too low yields for practical application [150, 151].

4.3.2 Targets

Targets in a form of pellets were prepared from the natural or enriched target material, $CaCO_3$ or TiO_2 (see Tables C.3 and C.4 in Appendix C). The reason to use carbonate and oxide was the commercial availability of enriched material, required to satisfy the nuclear reaction of interest. The details of calcium targets production at HIL were published in [165].

Briefly, targets in form of self-supporting pellet (Figure 4.20a) with thickness of up to ~300 mg/cm^2 were prepared by pressing the $CaCO_3$ or TiO_2 powder placed in a die with ~40 kN. The thickness of each prepared target was calculated based on the expected beam energy on the target (Section 3.3.3) and desired optimal energy range (Figure 2.5).

To economize, the enriched material was mixed with graphite in mass proportions varying from 10% to 25% for $CaCO_3$ (Figure 4.20b) and 20% for TiO_2. This method allows the production of thin as well as thick targets with low amount of expensive enriched material, while preserving the total thickness of the target, needed to ensure the required decrease in the projectile energy. In the first approximation, graphite admixture works as "transparent solvent" for the beam, simply lowering the TTY proportionally to carbon contribution. The values of TTY obtained in such targets were then recalculated for hypothetical pure $CaCO_3$ by simple multiplication. Additionally, the values were also corrected for the difference between $\mathrm{d}E/\mathrm{d}x$ of mixed and pure target (calculated with SRIM [32]).

The use of additional graphite (thermal conductor) introduces a better heat transfer within the irradiating target, allowing the use of higher beam currents. However, it limits the access of the acid which is used to dissolve the target in post-irradiation processing thus sometimes the mechanical smashing was required to access the inner parts of the activated material. To overcome this difficulty, a new method of target preparation was introduced, namely a separately prepared carbonate pellet was inserted into the graphite pocket and pressed together, creating integrated target (Figure 4.20c).

[2] Reaction ^{40}Ca(α,n)^{43}Ti→^{43}Sc is predicted to have a considerably lower cross-section compared to ^{40}Ca(α,p)^{43}Sc [24].

The homogenous mixing and the pocket approaches were verified with $^{nat}CaCO_3$ targets. The results were consistent with the data obtained with the pure $^{nat}CaCO_3$. All targets were installed in the similar holder dedicated for the irradiation station employed (Figure 3.2) – an example holder for HIL PETtrace station is shown in Figure 4.20d.

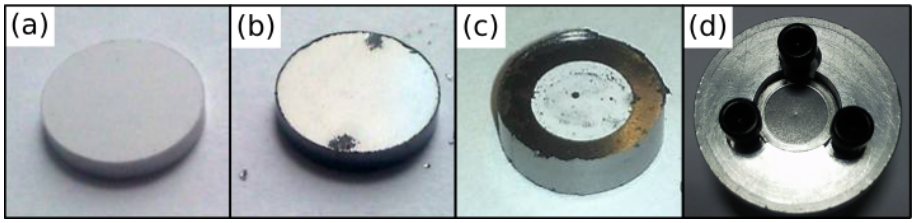

FIGURE 4.20: Photo of $CaCO_3$ targets employed in this work: (a) pure pellet, (b) mixed with graphite, (c) in graphite pocket, (d) installed on irradiation station at PETtrace HIL (courtesy of Anna Stolarz).

In a number of irradiations with such targets, additional ^{nat}Cu, ^{nat}Ni or ^{nat}Ti foils were added in front of each target (depending on the beam energy, as discussed in Table 3.3). The typical scheme of the target is shown in Figure 4.21. In some cases, to measure *TTY* at other energies, additional ^{nat}Al foils were placed to degrade the beam energy in front of the carbonate material.

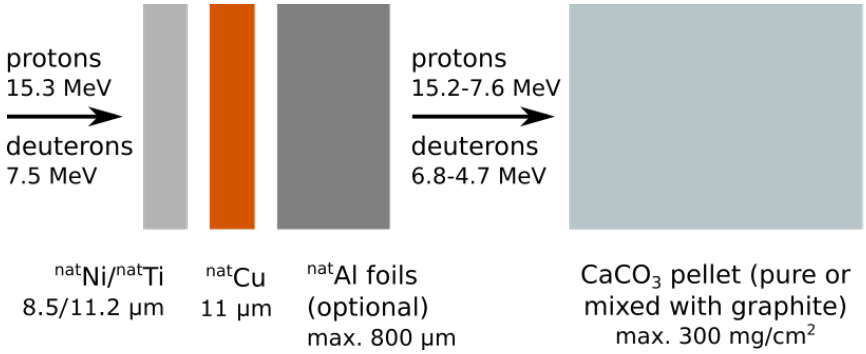

FIGURE 4.21: Typical calcium carbonate target scheme for the irradiation at PETtrace station at HIL.

4.3.3 Experimental results and discussion

Production of ^{43}Sc radioisotope

In this work, two ways of producing ^{43}Sc on natural and enriched calcium carbonate targets were investigated:

- *TTY* of $^{43}Ca(p,n)$ reaction with the use of 16 MeV proton beam from PETtrace cyclotron at HIL and 30 MeV proton beam from C30 cyclotron at NCNR (the energy was reduced to 17 MeV with the use of aluminium foils to simulate the PETtrace energy),
- *TTY* of $^{42}Ca(d,n)$ reaction with the use of 8 MeV deuteron beam from PETtrace cyclotron at HIL.

The Thick Target Yields for various proton and deuteron bombarding energies are presented in Tables C.7 and C.8 (Appendix C), and compared with theoretical values in Figure 4.22 (recalculated for the maximal available enrichment).

In the case of proton-induced reaction, the *TTY* measurements from this work correspond to *TTY* values calculated with the use of reported cross-section data [145, 166], and are lower that the predictions of EMPIRE and TENDL by a factor of 2 around 10 MeV projectile energy. The *TTY* values of $^{43}Ca(p,n)$ reaction are reported up to 17 MeV because ^{43}Sc observed in the targets irradiated with the protons of higher energy came also from $^{44}Ca(p,2n)$

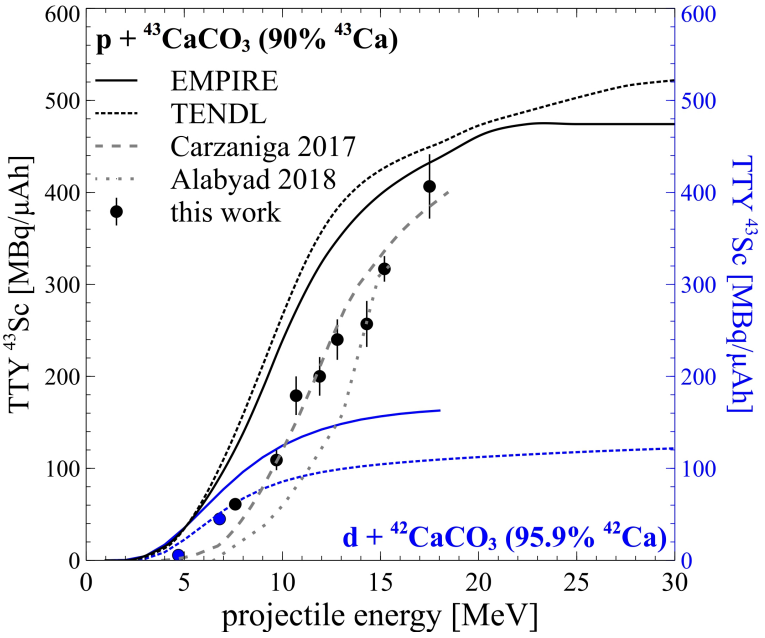

FIGURE 4.22: *TTY* of ^{43}Sc produced by deuterons (blue) impinging on an isotopically enriched $^{42}CaCO_3$ target, and protons (black) impinging on enriched $^{43}CaCO_3$ (experimental data is recalculated for 95.9% enrichment for deuterons and 90% for protons). Literature data is taken from [145, 166].

TABLE 4.6: Measured activity EOB of ^{43}Sc and radioactive impurities produced with proton and deuteron beams on enriched calcium carbonate targets (experimental values were recalculated for the maximal available enrichment).

Projectile		proton	deuteron
Energy range		15.2→0 MeV	6.8→0 MeV
Target (enrichment)		$^{43}CaCO_3$ (90%)	$^{42}CaCO_3$ (95.9%)
Irradiation		4 h, 1 μA	4 h, 1 μA
A_{EOB} **^{43}Sc**		910(40) MBq	129(11) MBq
Relative activity at EOB	^{43}Sc	100	100
	^{44g}Sc	12.0(1.5)	0.25(16)
	^{44m}Sc	0.95(12)	0.0054(19)
	^{47}Sc	0.0131(17)	0.0019(2)
	^{48}Sc	0.025(3)	0.06(2)
	^{47}Ca	$3.3(5) \times 10^{-4}$	

reaction. In the case of deuteron beam, two performed measurements reflects the predictions of TENDL rather than EMPIRE, the latter giving overestimated values.

Evidently, deuterons with energies of around 7 MeV produce only half of the possible ^{43}Sc activity in this reaction. A deuteron energy of 15 MeV would double the ^{43}Sc production yield. The (p,n) reaction on presently available $^{43}CaCO_3$ targets (enriched to 90% with 4.44% ^{44}Ca content) gives a much higher *TTY* value.

The EOB activities and produced radioactive impurities for 15.2→0 MeV proton energy and 6.8→0 MeV deuteron energy ranges are given in Table 4.6 (the values were calculated with the use of *TTY* measurements of all radioisotopic contaminants). Reasonable sample intensities and acceptable isotopic purity would be obtained in reactions induced by 15 MeV deuterons with isotopically enriched $^{42}CaCO_3$ targets, and with higher beam current. The proton irradiation of $^{43}CaCO_3$, although with substantially higher efficiency than the deuteron route, leads to samples with about 12% of ^{44g}Sc impurity with the presently available enriched targets (see Table C.3 in Appendix C).

Production of ^{44g,m}Sc radioisotopes

In this work, the production of ^{44g,m}Sc was investigated via the ^{44}Ca(p,n) reaction with all three cyclotrons (Table 3.1) up to the projectile energy of 30 MeV. The target nucleus is the most abundant Ca isotope, besides ^{40}Ca (which irradiation by protons produces only short lived products), and at least few times more abundant than other calcium isotopes that could be used for the production of ^{44g,m}Sc. Hence even the natural target can be used for the preliminary research of production of relatively pure ^{44g}Sc (see Table 4.7). Spectrum of γ ray emitted from $^{nat}CaCO_3$ irradiated with proton beam from PETtrace at HIL confirms small contribution of radioactive impurities (Figure C.12 in Appendix C). In this case, the largest impurity is ^{43}Sc at the level of around 3%.

However, for the large-scale production, the enriched $^{44}CaCO_3$ (94.8%) target is required. *TTY* measurements of ^{44g,m}Sc are shown in Figure 4.23 and values are listed in Table C.7 in Appendix C. The results presented in this work are in agreement with *TTY* calculated with the use of cross-section reported in [145], and with estimations of EMPIRE and TENDL. These yields are sufficient to produce GBq quantities in a 4 h irradiation in PETtrace cyclotron (see Table 4.7).

TABLE 4.7: Activity EOB of ^{44g}Sc and radioactive impurities produced with proton beam with natural and enriched $CaCO_3$ targets.

Projectile		proton	proton
Energy range		15.2→0 MeV	15.2→0 MeV
Target (enrichment)		$^{nat}CaCO_3$	$^{44}CaCO_3$ (94.8%)
Irradiation		4 h, 1 µA	4 h, 1 µA
A_{EOB} **^{44g}Sc**		50(2) MBq	2240(80) MBq
Relative activity at EOB	^{43}Sc	3.0(2)	0.0049(6)
	^{44g}Sc	100	100
	^{44m}Sc	0.62(3)	0.62(3)
	^{47}Sc	0.56(7)	0.0033(4)
	^{48}Sc	1.1(1)	0.0063(8)
	^{47}Ca	0.014(2)	$8.4(1) \times 10^{-5}$

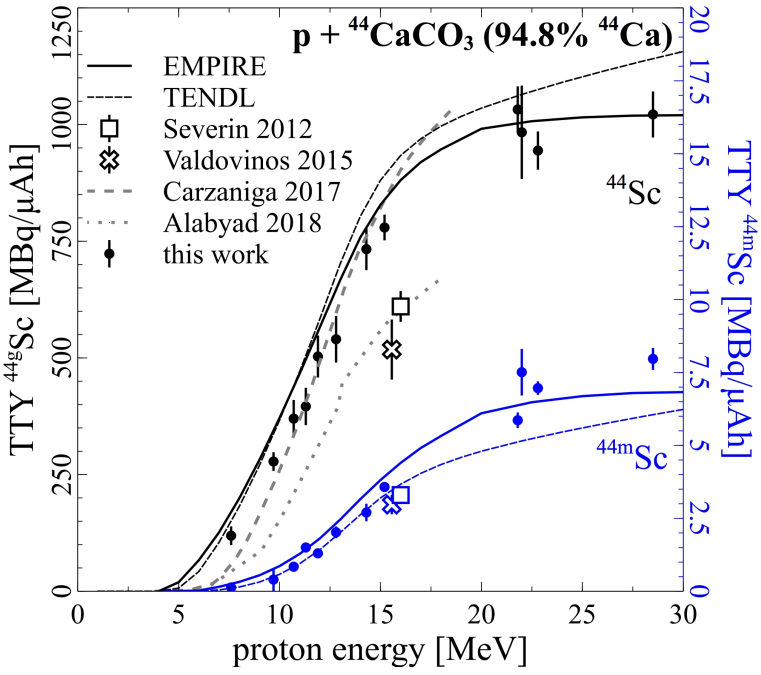

FIGURE 4.23: Comparison of ^{44g}Sc (black) and ^{44m}Sc (blue) *TTY* for a proton beam impinging on enriched $^{44}CaCO_3$ (experimental data is recalculated for 94.8% enrichment). Literature data is taken from [136, 138, 145, 166].

Measurements of ^{44g,m}Sc production yields reported in [136, 138] were obtained with Ca metalic targets, and were recalculated for $CaCO_3$ taking into account the difference in molar mass and stopping-power. The absolute values of *TTY* from these references were converted to $CaCO_3$ target equivalents, multiplying them by a factor 0.36[3]. After such a conversion, the metallic target data are about 30% lower than those obtained in this work. This discrepancy is probably due to the partial flux losses of proton beam in the Wisconsin experiments.

Additionally, a high spin ^{44m}Sc isomer with a 2.4 d half-life is suitable for an in vivo ^{44m}Sc/^{44g}Sc generator. The feasibility of the production of such generator was presented in [121–124]. Proposed reaction, ^{44}Ca(d,n), was motivated by the higher ^{44m}Sc/^{44g}Sc cross-section ratio in comparison with proton induced reactions on the same target. Similarly, this ratio is even higher for the α-induced reaction, ^{42}Ca(α,2n), due to higher momentum transfer to CN [150]. In the case of proton induced reaction, the isomeric ratio is lower, and mainly ground state is populated. Therefore, in the case of ^{44m}Sc/^{44g}Sc generator production with proton beam, the equilibrium between ^{44m}Sc and ^{44g}Sc activities required for the generator is reached 40 h after EOB. For the same beam current, deuteron and α particle routes reach it sooner, and with higher generator activity, as shown in Figure 4.24.

However, it is not clear which route is the best for large scale production of ^{44m}Sc/^{44g}Sc generator. The enriched ^{42}Ca target for the α particle irradiations is about 4 times more expensive than the ^{44}Ca for deuteron and proton induced reactions. On the other hand, to generate the same ^{44m}Sc activity a much thicker target is necessary for deuterons and protons which compensates for the price difference but leads to a higher contribution of radioactive impurities [123, 150]. Additionally, proton beam from the commercially available cyclotrons can reach higher intensity than deuteron or α particle, resulting in proportionally higher activity of ^{44m}Sc (if the cooling conditions for these samples are good).

[3]This factor is estimated as the ratio of Ca and $CaCO_3$ atomic masses, 40/100, multiplied by the ratio of the 16 MeV protons stopping-powers, 0.023/0.026, in these materials.

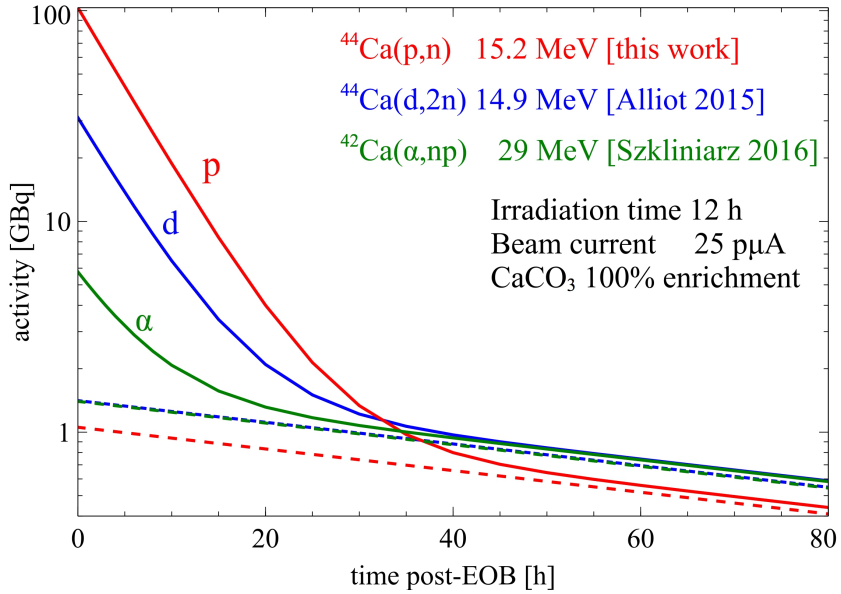

FIGURE 4.24: Activity of ^{44g}Sc (solid line) and ^{44m}Sc (dashed line) produced with protons (this work), deuterons [123], and α particle [150] beams for ^{44m}Sc/^{44g}Sc in-vivo generator.

Production of ^{47}Sc radioisotope

In this work, the production of ^{47}Sc was studied in two routes: ^{48}Ca(p,2n) on calcium carbonate targets (irradiated in HIL, ARRONAX, and NCNR), and ^{48}Ti(p,2p) on titanium oxide targets (irradiated in ARRONAX and NCNR).

The first reaction requires the use of enriched target which would nevertheless lead to the co-production of two undesired radioisotopes: ^{46}Sc and ^{48}Sc. As shown in Figure 4.25, the excitation functions for ^{48}Ca(p,xn) reactions have intersection regions and there is a relatively small energy range (22.8→17.1 MeV) optimal for ^{47}Sc production which has been investigated in this work. Two sets of proton energy ranges were used to irradiate $CaCO_3$ targets:

- E→17.1 MeV where $E > 21$ MeV,
- E→E_{thr} where $E \leq 15.2$ MeV and $E_{thr} = 8.9$ MeV.

Measured yields were added to calculate TTY for energies E above 15.2 MeV:

$$TTY(E) = TTY_{exp}(15.2) + TY_{\text{TENDL}}(17.1 \rightarrow 15.2) + TY_{exp}(E \rightarrow 17.1) \tag{4.3}$$

Here, $TTY_{exp}(15.2)$ and $TY_{exp}(E \rightarrow 17.1)$ are measured yields, and $TY_{\text{TENDL}}(17.1 \rightarrow 15.2)$ is yield calculated from TENDL cross-section. These results are shown in Figures 4.26, 4.27, and 4.28, as well as in Table C.7 (in Appendix C). Similar recalculation for TTY was applied for TY measured in [156] and shown in mentioned figures. Both data sets are consistent and confirm the predictions of TENDL and EMPIRE. The only exception is ^{48}Sc, which yield reported in [156] was found to be more than a factor 1.4 lower than determined in the present work (the reason for this discrepancy is unknown).

Measured TTY indicates that with 22.8→17.1 MeV proton energy range impinging on highly enriched $^{48}CaCO_3$ targets, almost 0.5 GBq can be produced in one 8 h run with 1 μA beam current (Table 4.8). The produced radioactivity will be contaminated with no more than 0.07% of long-lived ^{46}Sc (calculated with MDA, see Section 3.3.1) but also with 26% of ^{48}Sc. Unless the mass separation is available, the contribution of ^{48}Sc can be reduced by cooling time, thanks to the shorter half-life of ^{48}Sc and additional production of ^{47}Sc from co-produced "mother" ^{47}Ca. Assuming that 380 h cooling time is applied to the $^{48}CaCO_3$ sample irradiated with a 1 μA proton beam, the ^{47}Sc activity is 26 MBq with 1% contribution of ^{48}Sc. Similarly, a cooling time of 120 h leads to 210 MBq of ^{47}Sc with 10% of ^{48}Sc.

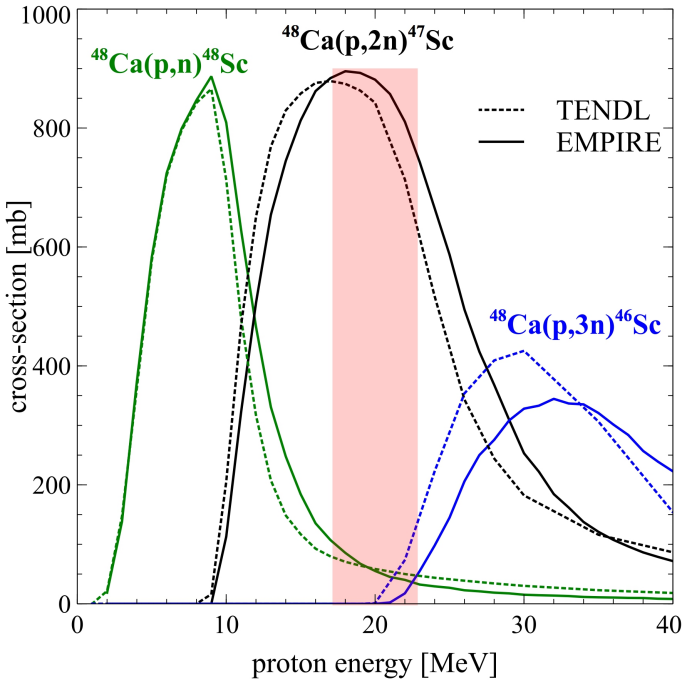

FIGURE 4.25: Cross-sections for ^{48}Ca(p,xn) reactions from TENDL [24] and EMPIRE [25]. Red area indicates the optimal energy range (22.8→17.1 MeV) for ^{47}Sc production.

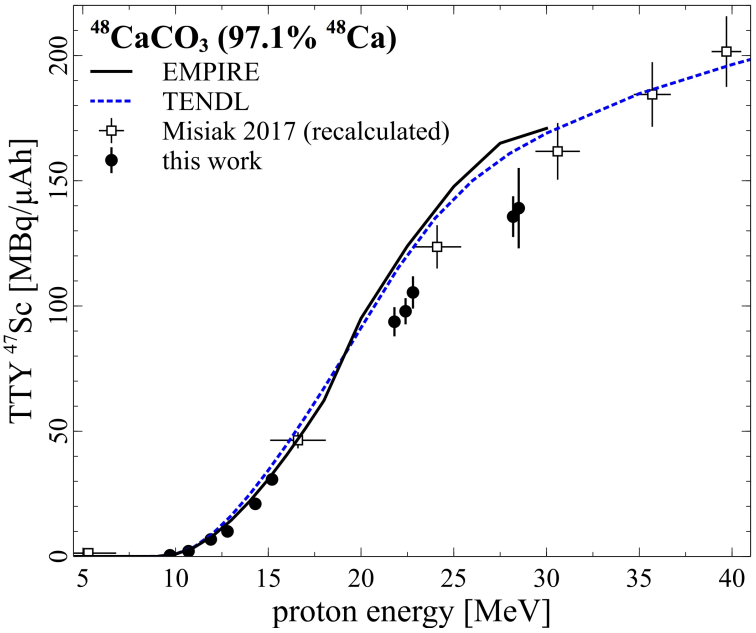

FIGURE 4.26: Comparison of ^{47}Sc *TTY* for a proton beam impinging on enriched $^{48}CaCO_3$ (experimental data is recalculated for 97.1% enrichment). Literature data is taken from [156].

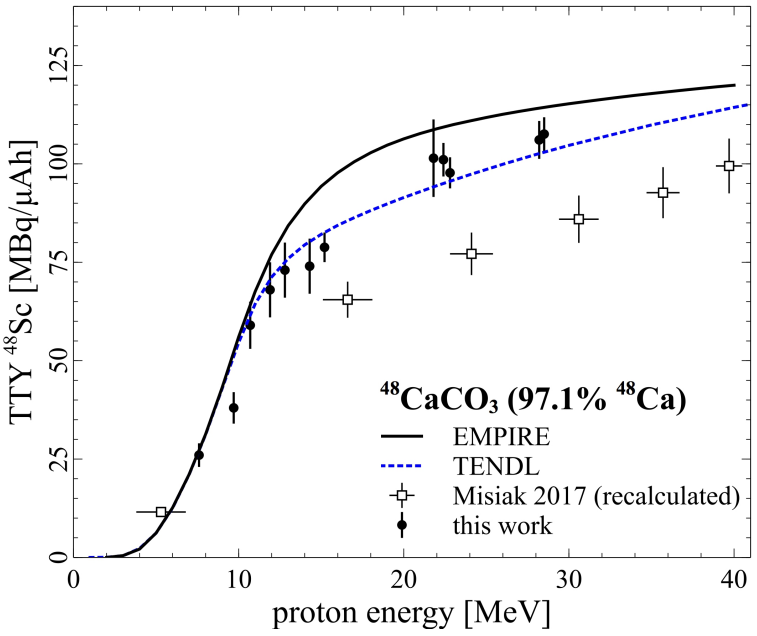

FIGURE 4.27: Comparison of ^{48}Sc *TTY* for a proton beam impinging on enriched $^{48}CaCO_3$ (experimental data is recalculated for 97.1% enrichment). Literature data is taken from [156].

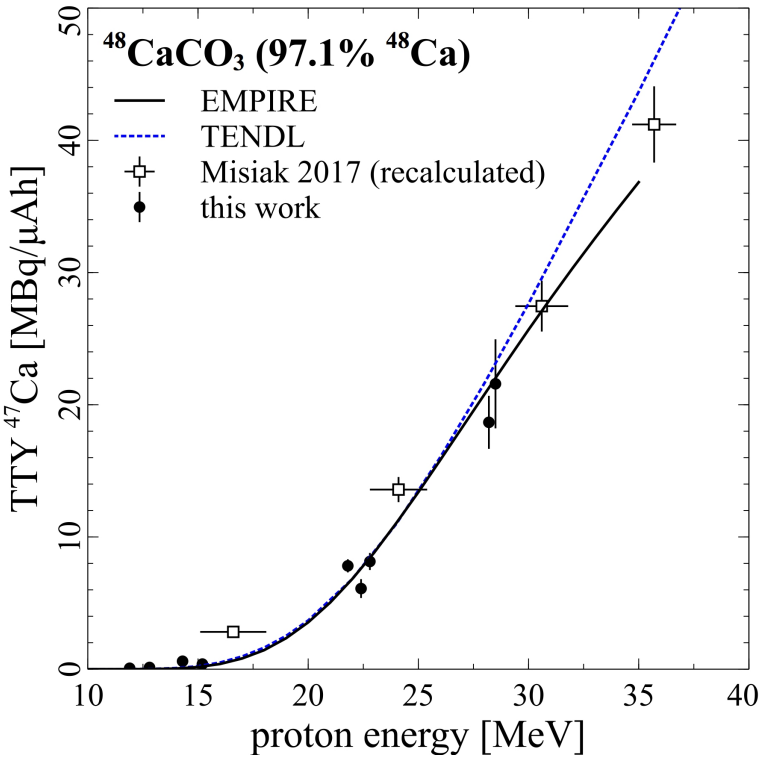

FIGURE 4.28: Comparison of ^{47}Ca *TTY* for a proton beam impinging on enriched $^{48}CaCO_3$ (experimental data is recalculated for 97.1% enrichment). Literature data is taken from [156].

TABLE 4.8: ^{47}Sc and radioactive impurities produced with proton beam on $CaCO_3$ and TiO_2 targets. Value with (*) is calculated from Minimum Detectable Activity.

Projectile		proton	proton	
Energy range		22.8→17.1 MeV	28.0→18.3 MeV	
Target		$^{48}CaCO_3$ (97.1%)	$^{48}TiO_2$ (99.6%)	
Irradiation		8 h, 1 µA	8 h, 1 µA	
Activity ^{47}Sc		at EOB: 420(40) MBq	at EOB: 20(4) MBq	40 h later: 14(3) MBq
Relative activity at EOB	^{43}Sc	0.25(40)	4.3(12)	0.0048(14)
	^{44g}Sc	0.106(13)	170(40)	71(19)
	^{44m}Sc	0.0077(9)	80(20)	66(18)
	^{46}Sc	<0.07 (*)	0.033(9)	0.046(12)
	^{47}Sc	100	100	100
	^{48}Sc	26(3)	0.08(2)	0.058(15)
	^{47}Ca	13.0(1.6)		
	^{43}K	$9.6(1.3) \times 10^{-4}$		
	^{48}V		190(50)	250(60)

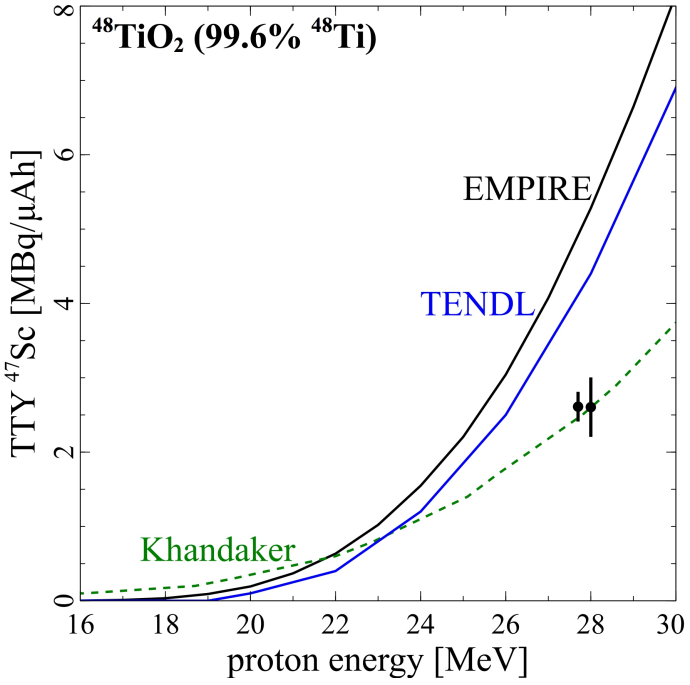

FIGURE 4.29: *TTY* of ^{48}Ti(p,2p)^{47}Sc reaction measured with $^{48}TiO_2$ target (experimental data is recalculated for 99.6% enrichment). Dashed line is calculated based on cross-section data from [141].

Alternatively, a relatively cheap $^{48}TiO_2$ enriched target was used to study the second production route, via ^{48}Ti(p,2p). Two experiments were performed, in ARRONAX and in NCNR, to verify the *TTY* shown in Figure 4.29. The results are around 2 times lower than the prediction of EMPIRE and TENDL, but they confirm the *TTY* calculated from cross-section reported in [141].

Table 4.8 shows the produced activity and measured radioactive impurities. At EOB, the strongest scandium impurity corresponds to ^{44g}Sc, at the level of 170%, produced in seven reaction paths [167]. It can be calculated that even the 40 h cooling time after EOB does not reduce impurities to the acceptable level while preserving the reasonable amount of ^{47}Sc (thus the mass separation is required to achieve sufficient purity). Meanwhile, the high activity of ^{48}V can be separated by the chemical means. Other radioisotopes were also expected: products of mainly ^{50}Ti(p,2p)^{49}Sc and ^{49}Ti(p,n)^{49}V reactions, however first one emits 0.05% intensity γ lines, while the second none at all, thus they were not observed.

4.3.4 Summary

The production of ^{43}Sc is the most cost-effective with the use of ^{nat}Ca targets and α beam. Deuteron beam provides comparably high yield with less than 1% radioactive contaminants but the expensive enriched ^{42}Ca target is required. The proton induced reaction on ^{43}Ca yields too high radioactive impurity level.

The most efficient way of direct ^{44g}Sc production leads via ^{44}Ca(p,n) reaction at 15 MeV projectile energy or ^{44}Ca(d,2n) reaction also at 15 MeV on enriched targets, both with very high yield and purity. For research purposes with lower activities, even the irradiation of natural target with proton beam can be considered. Alternative route with the use of α beam and enriched ^{42}Ca targets exhibit lower yield and more contaminants. Higher energies of proton or deuteron beam increase the yield but also increase the contribution of impurities.

The cyclotron production of ^{47}Sc in quantities useful for the medical procedures is still possible with the use of proton beam and enriched ^{48}Ca and ^{48}Ti targets. However, the mass separation must be considered to reduce the high contribution of other observed scandium impurities. For now, the direct production of ^{47}Sc seems more effective with the neutron induced reactions.

4.4 Reconstruction of scandium production cross-sections

4.4.1 Introduction

Pervious sections described σ measurements and TTY calculations (Sections 4.1, 4.2), or direct measurements of TTY (Section 4.3). As discussed previously, the cross-section measurements requires the use of thin target (in which the energy loss of the projectile is negligible as compared to the evolution of the cross-section). At the same time, the study of production yields demands thick targets (with thickness covering the projectile energy range for maximal up to reaction threshold). However, production of thin, homogeneous, self-supporting targets (in the order of $1\,\mathrm{mg/cm^2}$) might not feasible in certain cases which means that only TTY can be measured.

This problem is addressed by attempting to reconstruct reaction cross-section based on the measured TTY. For this purpose, TTY data were employed for the following reactions (see Table 4.5): ^{43}Ca(p,n)^{43}Sc, ^{44}Ca(p,n)^{44g}Sc, ^{44}Ca(p,n)^{44m}Sc, ^{48}Ca(p,2n)^{47}Sc, and ^{48}Ca(p,n)^{48}Sc. Other yields reported in this work do not have enough experimental points required for further analysis. Similar attempt has already been proposed in [168] for the study of ^{34m}Cl production. This approach is verified for above-mentioned reactions while employing different, straight-forward numerical algorithm. Part of this project has also been published recently in [169].

4.4.2 Reconstruction methodology

TTY and σ values are related as shown in Equation 2.35. This work is an attempt to solve this equation to obtain the energy dependence of the cross-section basing on the measured $TTY(E)$ values for different projectile energies E (see Table C.7 in Appendix C). These data are supported by an assumption $TTY(E_{thr}) = 0$, where E_{thr} denotes the energy threshold for this reaction.

The crucial factor is the choice of the function $TTY_{fit}(E)$ used to describe the TTY energy dependence. The number of parameters of the function used to fit the data should be restricted, as the number of the experimental data points is usually limited. Therefore, a simple shape is proposed:

$$TTY_{fit}(E) = a_0 + \frac{a_1 \cdot a_3}{2} \cdot \left(\sqrt{\pi} \cdot (a_2 - E_{thr}) \cdot \right. \\ \left. \cdot \operatorname{erf}\left(\frac{E - a_2}{a_1} \right) - a_1 \cdot \exp\left(\frac{-(E - a_2)^2}{{a_1}^2} \right) \right) \tag{4.4}$$

which is fitted to experimental TTY data with least square method and fulfils several important criteria. This function is monotonically increasing, as $TTY(E)$ should be. Most importantly, its derivative is a modified q-Weibull distribution [170]:

$$\frac{\mathrm{d}TTY_{fit}(E)}{\mathrm{d}E} = \max\left[0;\ a_3 \cdot (E - E_{thr}) \cdot \exp\left(\frac{-(E - a_2)^2}{{a_1}^2} \right)\right] \tag{4.5}$$

which reflects the general shape of the (p,n) and (p,2n) excitation functions studied in this work. The request $TTY(E_{thr}) = 0$ provides a condition:

$$a_0 = \frac{{a_1}^2}{a_3} \cdot \exp\left(\frac{-(a_2 - E)^2}{{a_1}^2} \right) \tag{4.6}$$

and limits the number of TTY_{fit} parameters to three: a_1, a_2 and a_3. Once those parameters are obtained, the cross-section values, $\sigma(E)$ [mb], can be estimated for any energy E [MeV] as:

$$\sigma(E) = \frac{\tau[\mathrm{h}] \cdot Z_p \cdot e[\mathrm{C}] \cdot M[\mathrm{u}]}{N_A \cdot H} \cdot \frac{\mathrm{d}TTY_{fit}(E)}{\mathrm{d}E} \left[\frac{\mathrm{MBq}}{\mu\mathrm{A} \cdot \mathrm{h} \cdot \mathrm{MeV}} \right] \cdot \frac{\mathrm{d}E}{\mathrm{d}x} \left[\frac{\mathrm{MeV}}{\mathrm{mg/cm^2}} \right] \cdot 10^{42} \tag{4.7}$$

In the case of this study, $\mathrm{d}E/\mathrm{d}x$ values correspond to the energy loss in calcium carbonate (provided by SRIM software [32]), $M = 100$ u to address the mass of $CaCO_3$, and H is the level of enrichment of employed material. The 95% confidence band for $TTY_{fit}(E)$ fit was also calculated and propagated to the reconstructed cross-section based on the fit covariance matrix. All calculations were done in `Python` programming language (version 2.7) [171].

Alternatively, [168] reconstructed cross-section after fitting the TTY curve by calculating target yields (TY) for thicknesses corresponding to 0.1 MeV projectile energy loss each 1 MeV and multiplied them by projectile range. This method assumes the constant stopping-power in each layer. This simplification was not necessary in the approach described in this work.

4.4.3 Results

Figures 4.30, 4.31, 4.32, 4.33, and 4.34 show TTY data and the reconstructed cross-sections for ^{43}Ca(p,n)^{43}Sc, ^{44}Ca(p,n)^{44g}Sc, ^{44}Ca(p,n)^{44m}Sc, ^{48}Ca(p,2n)^{47}Sc, and ^{48}Ca(p,n)^{48}Sc reactions. The fit parameters are shown in Table C.10 while the reconstructed cross-section values are listed in Table C.9 (Appendix). Results are compared with the experimental cross-section data reported in [95, 133, 145, 146, 166, 172–176], with the recommended values from [177], with the predictions of EMPIRE [25] evaporation code (version 3.2.2 Malta), and with the TENDL cross-section library [24]. All reconstructions exhibit a similar shape to the model predictions and measured cross-section values, indicating the relevance of modified q-Weibull distribution in estimating the global shape of the (p,n) and (p,2n) excitation functions.

The reconstruction approach from [168] resulted in similar cross-section values (marked as black dashed lines on cross-section plots) with visible correction near the threshold in ^{44m}Sc case (Figure 4.32) but also with the discontinuity fragments due to numerical approach. Since the mentioned paper does not provide the recommended TTY_{fit} function, the one described here was adopted (Equation 4.4).

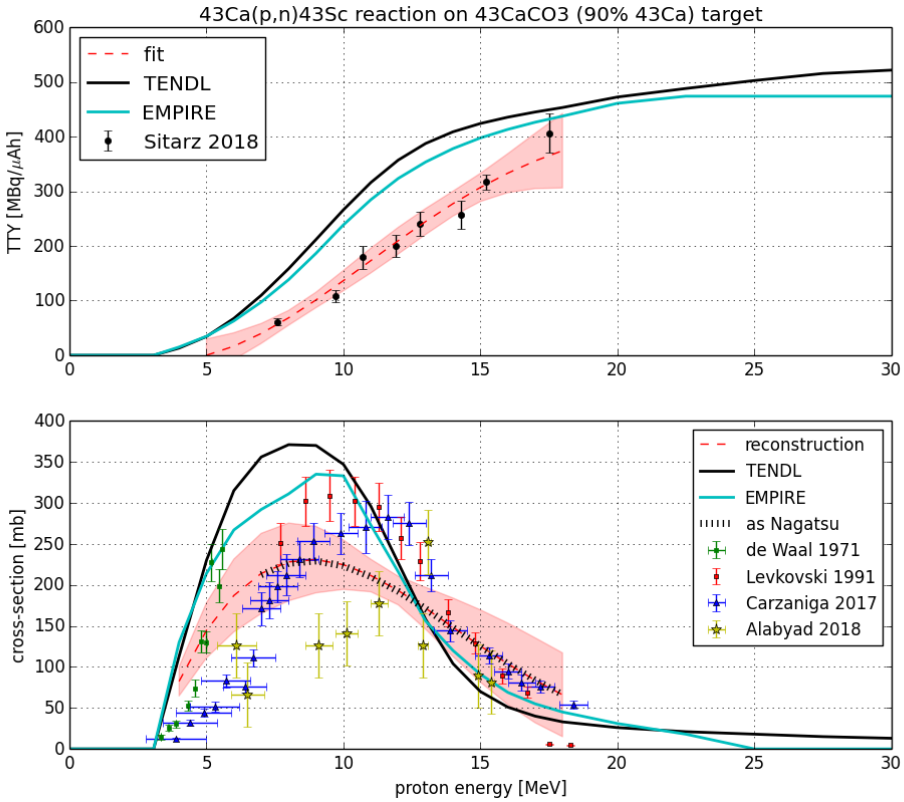

FIGURE 4.30: ^{43}Ca(p,n)^{43}Sc reconstruction (bottom) based on TTY_{fit} (top). The cross-section data is taken from [95, 145, 166, 176].

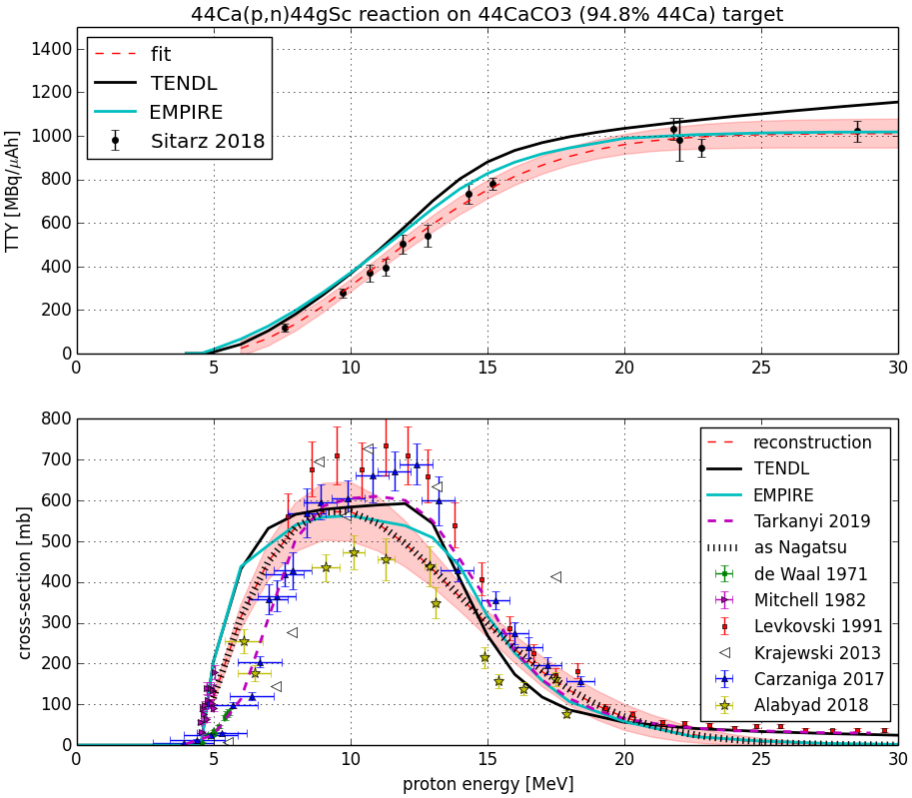

FIGURE 4.31: ^{44}Ca(p,n)^{44g}Sc reconstruction (bottom) based on TTY_{fit} (top). Cross-section data is taken from [95, 133, 145, 166, 173, 176, 177].

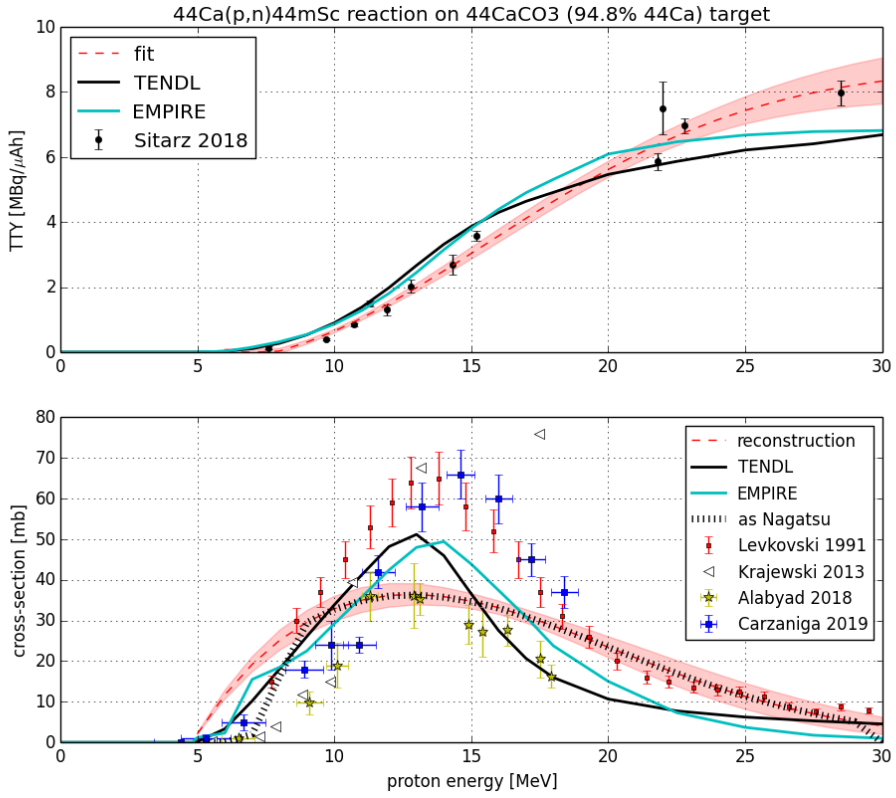

FIGURE 4.32: ^{44}Ca(p,n)^{44m}Sc reconstruction (bottom) based on TTY_{fit} (top). Cross-section data is taken from [95, 133, 146, 166].

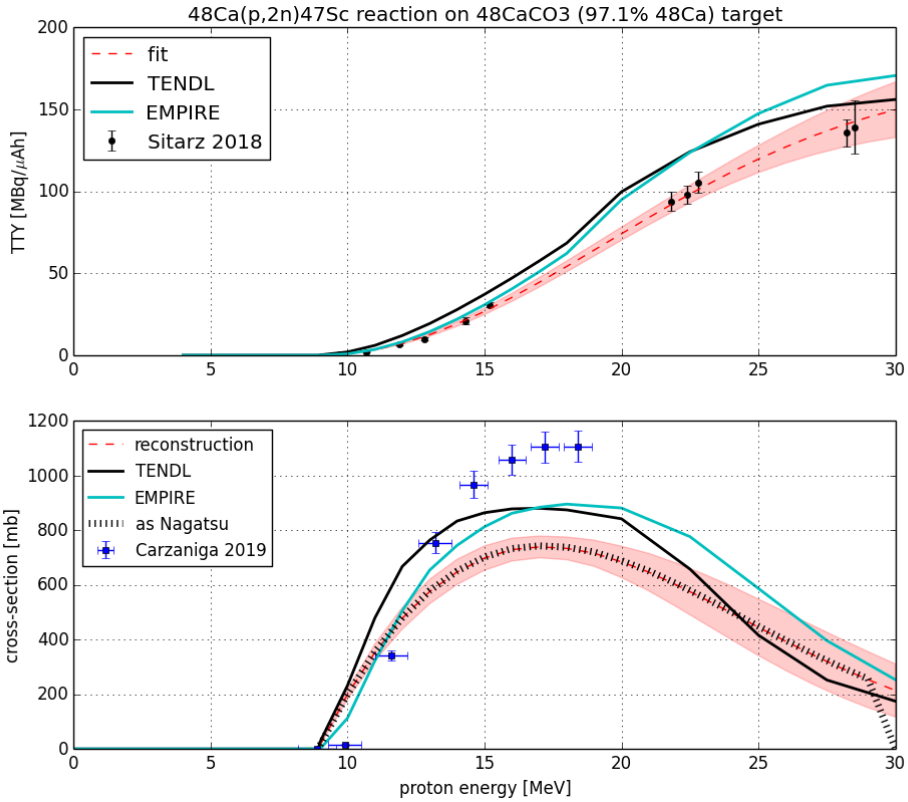

FIGURE 4.33: ^{48}Ca(p,2n)^{47}Sc reconstruction (bottom) based on TTY_{fit} (top). Cross-section data is taken from [146].

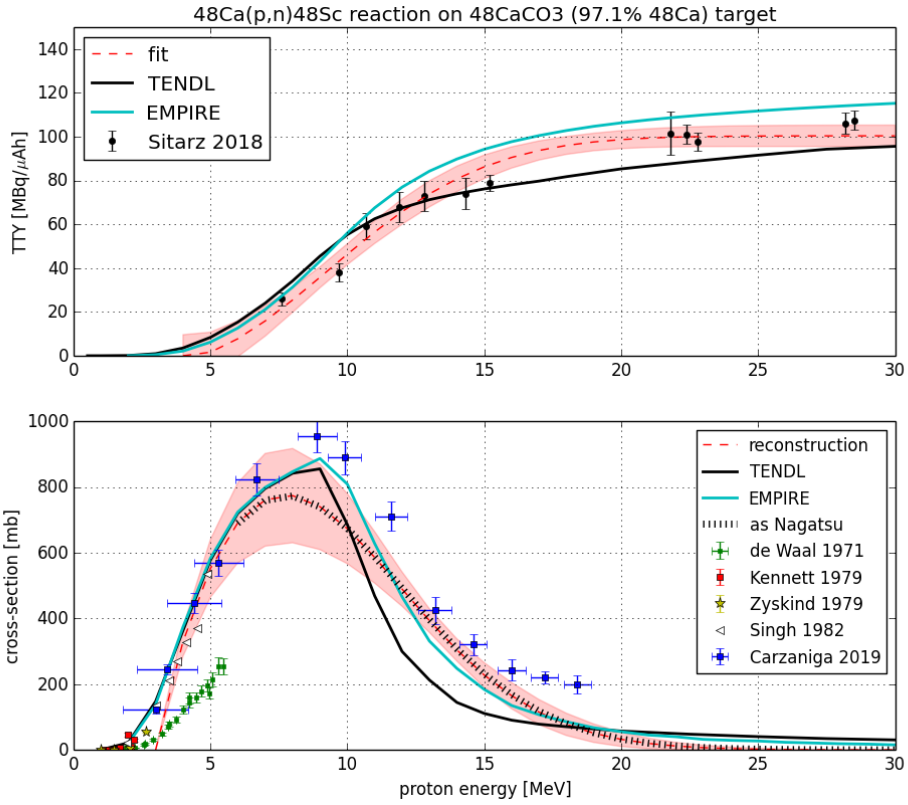

FIGURE 4.34: ^{48}Ca(p,n)^{48}Sc reconstruction (bottom) based on TTY_{fit} (top) with arbitrary E_{thr} = 3.0 MeV. Cross-section data is taken from [146, 172, 174–176]. The results from [172, 174, 175] are averaged.

In the case of ^{43}Sc data (Figure 4.30) the recent experimental results [166] are significantly lower than other measurements (by a factor of 2 around 10 MeV proton energy). The experimental results on TTY are quite linear in the measured proton energy range and do not reach the expected saturation, so the resulting excitation function is relatively flat and does not reproduce any of previous measurements, in particular the results reported in [166] around 10 MeV proton energy, and overestimates the cross-section values around the threshold. This reaction might require further validation, also by the extension of *TTY* measurements up to 30 MeV proton energy.

The general agreement is observed for ^{44g}Sc (Figure 4.31), both with the theoretical models and experimental results, although again the data in [166] are lower than measurements. More discrepancies are observed in the case of ^{44m}Sc (Figure 4.32). The excitation function obtained from *TTY* measurements does not show the peak seen in the experiments and in model calculations and overestimates the values near the reaction threshold. The problem with this reconstruction might be related to the offset of *TTY* data as only in the case of ^{44m}Sc, TTY values are below model predictions at low energies and above them at higher energies, which causes the reconstructed excitation function to be flatter.

For ^{47}Sc (Figure 4.33), the shape of reconstruction reflects the shape predicted by both model calculations. While results from this work provide about 10% lower values compared to the models, recent measurements [146] indicate similar values at low energies but about 20% higher values at maximum.

Finally, the arbitrary value of E_{thr} = 3.0 MeV was adopted as a parameter for ^{48}Sc fit (Figure 4.34) to satisfy the visible and significant *TTY* build-up at this energy rather than the actual threshold (0.51 MeV). It might be explained by the fact, that the shape of the function used for the fit does not describe adequately the behavior of the cross-section at energies so below the Coulomb barrier. Since the cross-section values deeply below the Coulomb barrier are very small, they do not contribute significantly to the *TTY* values. The extracted cross-section values are in line with the data in [172] at lower energies, and in [146] at higher energies.

4.4.4 Summary

The method described here is the first attempt to estimate cross-section based on *TTY* measurements. This method is based on fitting a function with three free parameters to *TTY* data points and using its analytical derivative to obtain cross-section. The fitting requires the knowledge of the reaction threshold and sufficient number of experimental points to represent the shape of *TTY* curve, including the saturation region. The numerical approach presented here is simplified yet fast and easy to implement in a programming language.

The presented method was employed to obtain estimation of ^{43}Ca(p,n)^{43}Sc, ^{44}Ca(p,n)^{44g}Sc, ^{44}Ca(p,n)^{44m}Sc, ^{48}Ca(p,2n)^{47}Sc, and ^{48}Ca(p,n)^{48}Sc reaction cross-sections. The general agreement between reconstruction and experimental data was observed. However, the method would need development in the future, especially to improve the reconstruction near the reaction threshold.

Chapter 5

Conclusions and summary

This thesis presented possible production routes of ^{97}Ru, ^{105}Rh, and ^{43,44g,m,47}Sc medical radioisotopes with the use of cyclotrons. Excitation functions and Thick Target Yields data were measured, calculated, or reconstructed for the production of above-mentioned radioisotopes. Results were used to estimate the conditions for the large-scale activity production and the contribution of radioactive contaminants. The results were also compared with other reported data and various production routes.

It has been shown that, in most cases, the conditions can be optimized so that one irradiation with the beam from commercially available cyclotrons and targets can yield up to a several tens radioisotopically pure patient doses. In other cases, especially when it comes to neutron-rich isotopes (for example therapeutic ^{47}Sc), the efficient production might require another approaches, for example with the use of the reactors.

The conclusions from this work give a good insight into the accessibility of studied radioisotopes for the next steps of researches, namely: chemical separation and recovery of the target material, labelling of biologically active molecules, *in vitro* and *in vivo* studies (biodistribution, imaging quality or therapeutic effect), pre-clinical and clinical trials, and ultimately leading to the production of the effective radiopharmaceutical.

However, one should also remember that further research on discussed (as well as other) medical radioisotopes should be justified. It is true that ^{105}Rh can be employed for the treatment of bone metastases but so can many other radioisotopes, in particular calcium homologues. In most cases, it is more convenient to use conventional ^{99m}Tc instead of ^{97}Ru in SPECT technique. The radioisotope of ^{44g}Sc is very attractive for $\beta^+\gamma$ coincidence PET proof-of-concept but different candidates may be in order for the clinical practice.

In conclusion, results from this thesis prove that cyclotrons open many possibilities for the efficient production of innovative medical radioisotopes. In the "nuclear medicine clock", the cyclotrons are clearly a very important gear. All the more reason to use it rationally.

Appendix A

Radionuclide Yield Calculator

A.1 About RYC

Radionuclide Yield Calculator (RYC) is a GUI software developed during this thesis. It is dedicated to radioisotope production with the use of the cyclotron. It calculates the yield, activity and number of nuclei of any isotope for various production conditions based on the provided excitation function. It was written in `Python` programming language (version 2.7) [171] using the `TKinter` module and compiled with `PyInstaller` (version 3.4) [178]. It also uses `SRIM module` [32] to calculate the stopping-power of the projectiles. The main features of RYC include:

- fit different functions to the cross-section data,
- import TENDL cross-section [24],
- calculate *TTY* or production rate of stable nuclei,
- calculate activity at EOB and the number of produced nuclei,
- search the radioactive impurities.

RYC is available for free on the ARRONAX website (`http://www.cyclotron-nantes.fr/spip.php?article372`) and is distributed under the Creative Commons Attribution-NoDerivatives 4.0 International License[1]. This software was also introduced in [97].

A.2 Requirements and installation

RYC is distributed in `RYC.zip` archive which includes several files, taking around 60 Mb once extracted:

- `RYC.exe` – main program file, executable on Windows 64-bit OS,
- `Manual.pdf` and `Manual_short.pdf` – detailed and concise versions of the RYC manual (the detailed version include troubleshooting),
- `LICENSE.txt` – details of Creative Commons license,
- `SRModule.exe` (`SRIM Module`), `SCOEF03.dat`, `SNUC03.dat`, `VERSION` and `SR.IN` – SRIM software files, necessary to calculate stopping-power and ultimately *TTY* (these files must be kept in the same directory as `RYC.exe`),

After extraction of `zip` archive, RYC is launched by executing `RYC.exe` file and presents GUI as seen in Figure A.1. The program automatically communicates with other files when needed and this does not require the user's intervention. In particular, the installation of SRIM software is not required.

To use the `import` function in `TENDL` cross-section input, internet connection is required, as RYC communicates with TENDL website. Alternatively, `TENDL-archive.zip` can be downloaded separately, extracted, and placed in the same directory as `RYC.exe`. It contains over

[1] To view a copy of this license, visit `http://creativecommons.org/licenses/by-nd/4.0/` or send a letter to Creative Commons, PO Box 1866, Mountain View, CA 94042, USA.

350 000 `txt` files with TENDL cross-section (version 2015) on stable nuclei. Files take around 0.5 Gb but offer a solution to import cross-section to RYC without the need of the internet connection.

A.3 Layout and use

RYC main window (Figure A.1) allows for step-by-step introduction of irradiation conditions to calculate *TTY* for the radioisotope of interest. Additional options are provided under `File` and `Edit` menus.

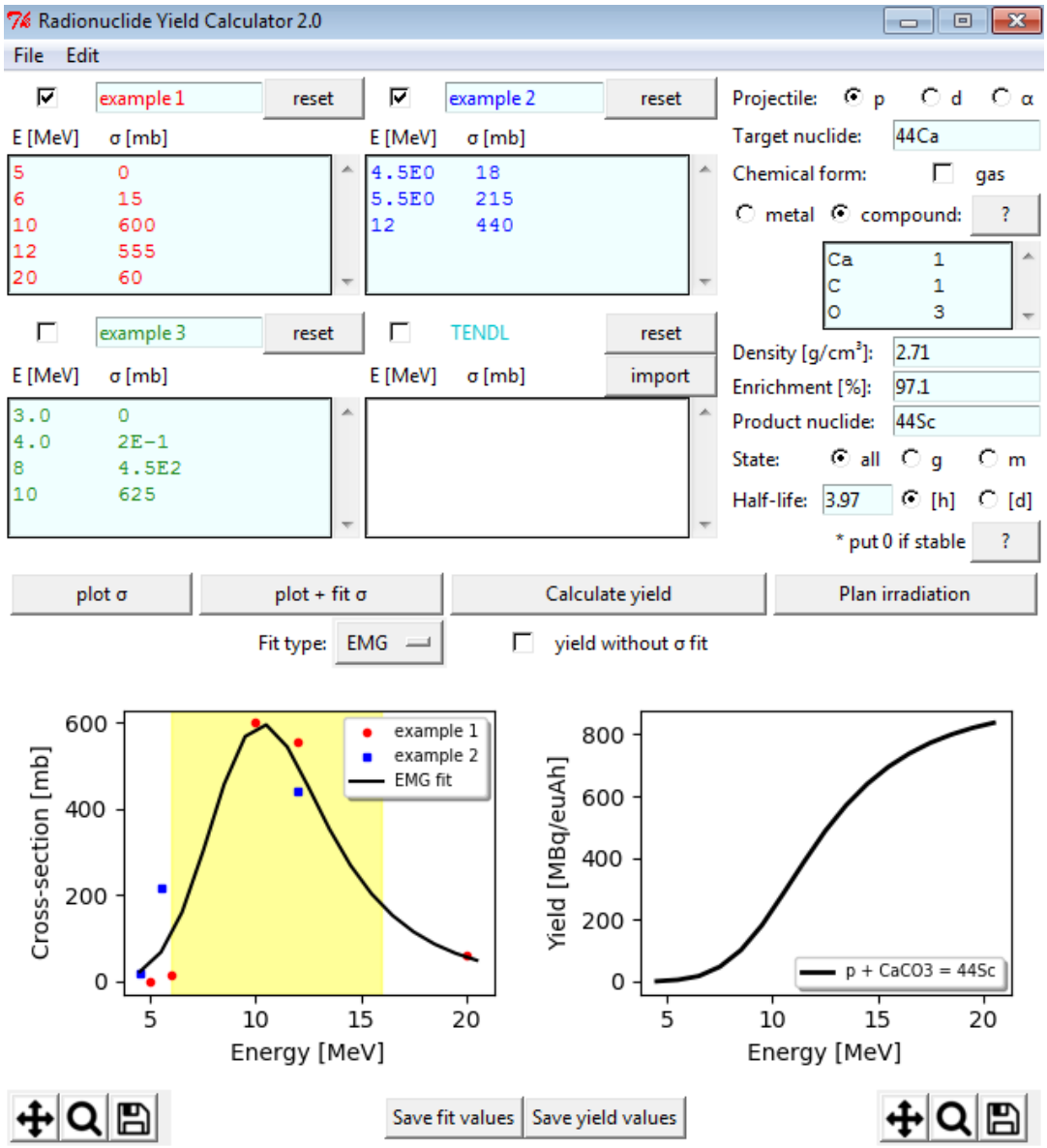

FIGURE A.1: Main window of Radionuclide Yield Calculator, used to introduce target and product parameters, and calculate production yield.

Cross-section inputs introduce excitation function of the nuclear reaction used to produce the isotope of interest. The user is asked to provide at least one set of cross-section values (E [MeV] and corresponding σ [mb] per row). Up to three sets can be provided at once. Additionally, `import` command places cross-section values in `TENDL` section if the `Projectile`, `Target nuclide`, `Product nuclide`, and its `State` are specified (on the right).

Selected cross-section data sets can be then plotted with `plot σ` command on the left graph. The `plot + fit σ` command additionally fits the function declared in `Fit type` to the data. The possible fit functions include: EMG distribution, GGD (generalized error version), modified q-Weibull distribution, and polynomial of degrees from 3 to 6.

Before calculating the production yield, RYC requires to define the following irradiation parameters:

- `Projectile` – proton (p), deuteron (d), or α particle,
- `Target nuclide` – written as mass number and element symbol,
- `Chemical form` – `metal` or `compound` target (the stoichiometry of the latter should be defined in the dedicated section below),
- `Density` – the density of the target material,
- `Enrichment` – the abundance of the target nuclide in target material,
- `Product nuclide` – written as mass number and element symbol,
- `State` – parameter of the produced isotope: ground (g), metastable (m), or all,
- `Half-life` – the half-life of the product in hours [h] or days [d].

The `Calculate yield` command uses the defined parameters, communicates with `SRIM Module` to obtain stopping-power in the target, calculates *TTY* [MBq/μAh] (Equation 2.35) for various projectile energies *E* [MeV] with the Simpson's algorithm, and plots it on the right graph. If the user marks `yield without σ fit` option, *TTY* will be calculated based on one selected cross-section data set, without the fit.

Having obtained *TTY*, user can estimate the expected activity of radioisotope with `Plan irradiation`. This command opens the separate window (Figure A.2) to provide irradiation parameters: beam current (`I`), irradiation time (`t`), and energy range in the target material (from `max` to `min`). The `Calculate` comand gives the values of activity produced at the end of such irradiation (`EOB`) and the `thickness` of the described target required to satisfy the declared energy range. The possible isotopic contaminants produced during such irradiation can be listed with `Check impurities` command (this uses TENDL cross-section).

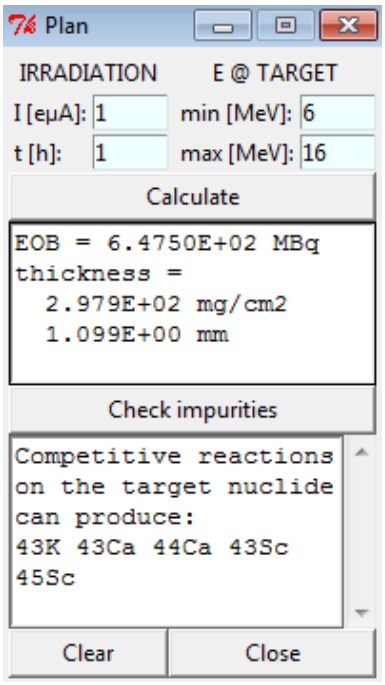

FIGURE A.2: RYC window used for the calculation of produced activity and radioactive impurities.

The same procedures can be performed for the stable nuclei by using `Half-life` $= 0$. Then, TTY_0 is calculated in the rate of produced nuclei $[(\mu A \cdot h)^{-1}]$ (Equation 2.42) and number of produced nuclei is printed instead of activity (calculated without the decay correction, as in Equation 2.43).

A.4 RYC verification

The validation of RYC was performed using data from the literature. Figure A.3 shows *TTY* for three reactions on elemental targets: ^{127}I(p,3n)^{125}Xe, ^{64}Ni(d,2n)^{64}Cu, and ^{209}Bi(α,2n)^{211}At. Red points correspond to the values calculated with RYC based on cross-section published by IAEA [179, 180], and black lines represent the data calculated separately by IAEA based on the same cross-section. As can be seen, for the 3 types of projectiles and for the different target masses, a very good agreement is obtained.

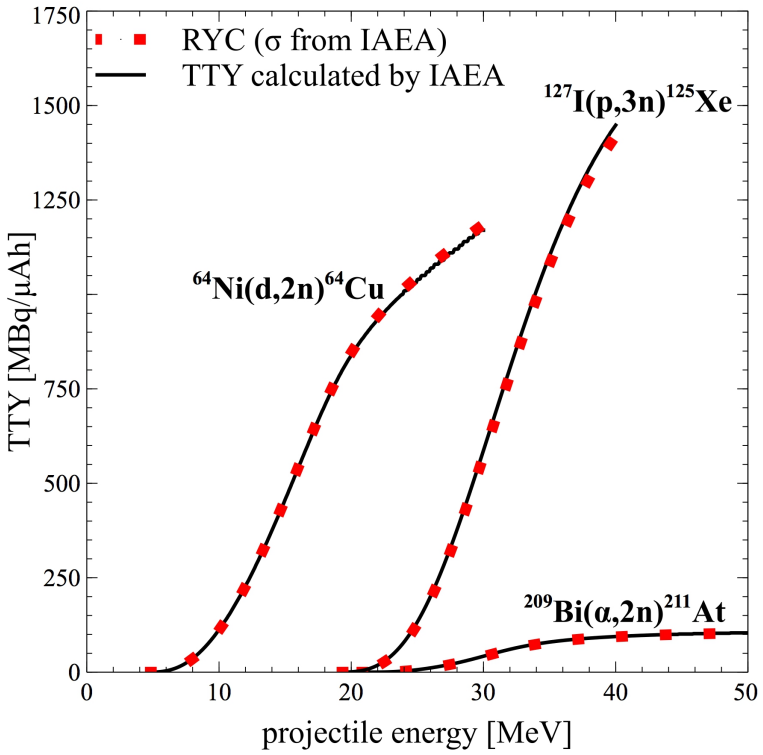

FIGURE A.3: Comparison between *TTY* calculated with RYC (points) and by IAEA (lines) [179, 180] based on the same cross-section values.

Appendix B

$\beta^+\gamma$ coincidence PET

B.1 Introduction

During the recent years, we have witnessed birth and steady development of a new extension of PET imaging (see Section 2.3.3), namely a $\beta^+\gamma$ coincidence technique [116, 119, 120, 181–187]. Compared to the classical PET, it offers better spatial resolution [116, 187, 188] or, alternatively, provides the same image quality with less radioactivity.

In principle, $\beta^+\gamma$ coincidence PET uses a β^+ source that also emits γ quanta (sometimes called "third γ")[1]. Assuming that the β^+ and the third γ are emitted at the same location, the position of the radioisotope is then obtained by the intersection of the arrival direction of the third γ with the conventional Line Of Response, LOR (Figure B.1). The localization via direction cone implies the Compton scattering of the third γ and detection of the scattered photon in the photoelectric interaction. This favours the third γ of high energy, around 1 MeV. While it would give additional radiation dose to the patient, the precision of the $\beta^+\gamma$ PET is supposed to allow the administration of lower activities, significantly reducing the overall dose.

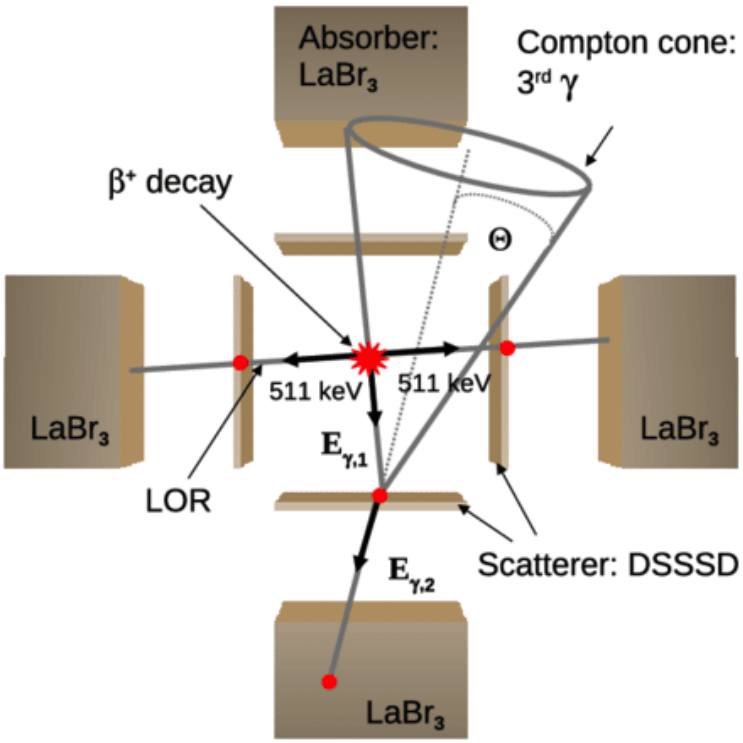

FIGURE B.1: Principle of $\beta^+\gamma$ coincidence PET (for details see [119]).

[1] The the third γ should be emitted from the radioisotope up to few nanoseconds after the β^+ decay to assure that the acquisition system recognizes it as a coincident event.

TABLE B.1: Properties of radioisotopes suitable for $\beta^+\gamma$ PET (nuclear data from [72]). The radioisotope ^{44g}Sc is discussed in Section 4.3.

Isotope	$T_{1/2}$	**Decay (%)**	**Main γ lines [keV] (intensity; delay)**
^{10}C	19.3 s	β^+ (99.9), EC (0.1)	718.4 (100%; 0.71 ns)
^{14}O	70.6 s	β^+ (99.9), EC (0.1)	2312.6 (99.4%; 68 fs)
^{22}Na	2.6 y	β^+ (90), EC (10)	1274.5 (99%; 3.6 ps)
^{34m}Cl	32 min	β^+ (54.3), EC (1.1), IT (44.6)	146.4 keV (40.5%; IT), 1176.6 (14.1%; 136 fs), 2127.5 (42.8%; 318 fs), 3304.0 (12.3%; 136 fs)
^{44g}Sc	3.9 h	β^+ (94.3), EC (5.7)	1157.0 (99.9%; 2.61 ps)
^{48}V	16.0 d	β^+ (49.9), EC (50.1)	983.5 (100%; 4.04 ps), 1312.1 (97.5%; 0.76 ps)
^{52m}Mn	21 min	β^+ (97), EC (1), IT (2)	1434.1 (98.3%; 0.783 ps)
^{55}Co	17.5 h	β^+ (76), EC (24)	477.2 (20.2%; 37.9 ps), 931.1 (75%; 8 ps), 1408.4 (16.9%; 37.9 ps)
^{60}Cu	24 min	β^+ (93), EC (7)	826.1 (22%; 0.59 ps), 1332.5 (88%; 0.735 ps)
^{66}Ga	9.49 h	β^+ (56), EC (44)	1039.2 (37%; 1.68 ps), 2752 (23%; not found)
^{69}Ge	39 h	β^+ (24), EC (76)	574.2 (13.3%; 1.7 ps), 872.1 (11.9%; 0.25 ps), 1107 (36%; 0.222 ps)
^{72}As	26 h	β^+ (86), EC (14)	834.0 (80%; 3.35 ps)
^{76}Br	16.2 h	β^+ (55.6), EC (44.4)	559.1 (74.0%; 12.3 ps), 657.0 (15.9%; 11 ps), 1853.7 (14.7%; not found)
^{82g}Rb	1.3 min	β^+ (95), EC (5)	776.5 (13%; 4.45 ps)
^{86g}Y	14.7 h	β^+ (31.9), EC (68.1)	443.1 (16.9%; 5 ns), 627.7 (32.6%; 0.9 ps), 703.3 (15.4%; 5 ns), 777.4 (22.4%; 0.386 ps), 1076.6 (82.5%; 1.46 ps), 1153.1 (30.5%; 1.73 ps), 1920.7 (20.8%; not found)
^{94m}Tc	52 min	β^+ (72), EC (28)	871.1 (94%; 2.77 ps)
^{110m}In	69.1 min	β^+ (61.2), EC (38.8)	657.8 (97.7%; 5.42 ps)
^{124}I	4.2 d	β^+ (22.7), EC (77.3)	602.7 (62.9%, 6.2 ps), 722.7 (10.4%; 1.04 ps), 1691.0 (11.2%; 0.17 ps)

In the study of $\beta^+\gamma$ coincidence PET with the use of XEMIS and XEMIS2 detectors [116–118, 188], ^{44g}Sc was used as the $\beta^+\gamma$ emitter. It has a half-life suitable for medical practice ($T_{1/2}$ = 3.9 h) and emits only one, high-intensity γ-line with sufficient energy (1157 keV, 99%), which makes ^{44g}Sc the undoubtedly most useful radioisotope for $\beta^+\gamma$ PET proof of concept (recommended in [119, 120]). Its possible production routes were presented in Section 4.3. However, scandium, as every other element, has certain limitations and in some cases it might be necessary to consider other radioisotopes. They must have sufficient β^+ branching ratio, high energy and intensity of third γ, lack of additional intense γ lines, applicable $T_{1/2}$ and feasible production route. Radioisotopes satisfying these criteria (or most of them) are listed in Table B.1 and discussed in this Appendix, along with their possible production and applications so far[2].

Additionally, it is also possible to imagine an approach in which LOR is reconstructed with two (or more) γ-rays emitted from the nucleus, forcing the reconstruction based on three complete Compton events. There are radioisotopes that satisfy this criterion, with three high-intensity γ lines: ^{94g}Tc ($T_{1/2}$ = 4.9 h), ^{96}Tc ($T_{1/2}$ = 4.3 d), ^{108}In ($T_{1/2}$ = 58 min), ^{110g}In ($T_{1/2}$ = 4.9 h) and ^{206}Bi ($T_{1/2}$ = 6.2 d), the latter being already an attractive biological tracer [189–191]. However, this imaging method would require more activity compared to the $\beta^+\gamma$ coincidence and is not discussed further here.

There is also a similar PET technique which utilizes a rare three γ quanta emission from the orto-positronium annihilation, investigated in [192–194] as well as by J-PET group [195, 196]. This method can be applied with all β^+ radionuclides and is not discussed further here.

B.2 Medical radioisotopes for $\beta^+\gamma$ PET

B.2.1 Promising candidates for $\beta^+\gamma$ PET

^{48}V

^{48}V radioisotope is well-known only as a monitor for beam current measurements [179]. It emits two high-intensity γ lines and has a β^+ branching ratio of only 50%. However, it has the longest half-life (16 d) among all discussed $\beta^+\gamma$ candidates, suitable for the studies of slow metabolic processes and for the labelling of organic compounds [197]. The prospects of ^{48}V were recently reminded in [198] as it is already finding applications as a tracer in biological actions in plants [199], in material science [200] or in the renal artery brachytherapy [201]. As suggested in [181] it is also a promising candidate for coincidence PET.

As summarized in [179], the cross-section for ^{48}V production via ^{nat}Ti(p,x), ^{nat}Ti(d,x) and ^{nat}Ti(^{3}He,x) are well measured. Alternatively, favorable reported α-induced reactions include ^{nat}Ti(α,x) [202–205] and ^{nat}Sc(α,n) [95, 206–208]. However, the most interesting seems to be the ^{nat}Ti(p,x) as the major contribution comes from ^{48}Ti(p,n) reaction suitable for the energy of the commonly available cyclotrons and the target nuclide has high natural abundance [209]. With 16 MeV beam and 1 μAh irradiation of ^{nat}Ti target, almost 20 MBq of ^{48}V can be produced. Unless the enriched ^{48}Ti material is used, the ^{nat}Sc(α,n) route will produce much less radioactive vanadium impurities (in particular, no long-lived ^{49}V will be formed) but the ^{48}V production yield will also be lower, by the factor of 20 for 30 MeV α-beam (energy commonly used for ^{211}At or ^{43}Sc production).

^{55}Co

^{55}Co has been acknowledged as "the emerging PET radionuclide" in [210] as it features high β^+ branching ratio, half-life of 17.5 hfavouring the studies of slow biological process and feasible labeling with different complexes as well as satisfactory biodistribution [211–215]. Numerous applications of ^{55}Co (summarized in [210]) include: the lung cancer detection [216], the renal imaging [217] and the neuro-imaging [218–222]. These procedures can be also performed with $\beta^+\gamma$ coincidence PET [181] as ^{55}Co emits one high-intensity high-energy γ line (931 keV, 75%). Additionally, there is a theranostic matched pair with Auger-emitter ^{58m}Co ($T_{1/2}$ = 9.1 h).

[2]The short version of this Appendix was also published as an overview [REF].

The production routes of ^{55}Co have been thoroughly studied via different nuclear reactions, for which the cross-section and thick target yield data are very well reported. The most promising ones are: ^{56}Fe(p,2n) [95, 223–228], ^{58}Ni(p,α) [95, 213, 229–236] and ^{54}Fe(d,n) [212, 236–244]. In each case, special care should be taken to avoid the co-production of long-lived radioactive impurities of ^{56}Co ($T_{1/2}$ = 77.2 d) and ^{57}Co ($T_{1/2}$ = 271.7 d) as they emit high intensity γ lines which unnecessarily increase the dose.

The first production route, ^{56}Fe(p,2n), is feasible with ^{nat}Fe but the energy exiting the target should be around 20 MeV to reduce the formation of ^{56}Co via ^{56}Fe(p,n). With 30 MeV proton beam and 1 μAh irradiation, produced activity is around 100 MBq, with less than 1% ^{56}Co. In the case of ^{58}Ni(p,α), proton energy less than 16 MeV is recommended to avoid the formation of ^{56}Co and ^{57}Co. With 1 μAh beam and thick ^{nat}Ni target, around 10 MBq of ^{55}Co can be produced, with less than 1% ^{57}Co. The third reaction, ^{54}Fe(d,n), requires enriched target (to produce sufficient quantities as well as avoid the co-production of impurities) available commercially at the levels higher than 95%, in the form of metal (^{54}Fe) or oxide ($^{54}Fe_2O_3$). With the metal target and 1 μAh irradiation of 8 or 15 MeV deuteron beam, up to 20 MBq or 40 MBq of ^{55}Co respectively can be produced, with negligible amount of ^{56}Co and ^{57}Co.

^{60}Cu

^{60}Cu is a short-lived ($T_{1/2}$ = 24 min) β^+ emitter with additional γ line making it suitable for $\beta^+\gamma$ coincidence PET [181]. So far, it has only been used in standard PET technique along with the labeling studies of ^{60}Cu-ATSM for tumor hypoxia imaging [245–250]. It also has a theranostic matched pair, ^{67}Cu as a β^- emitter for targeted radionuclide therapy.

The most commonly used production route of ^{60}Cu is via ^{60}Ni(p,n) or ^{nat}Ni(p,x) reactions (used in above-mentioned papers). The corresponding cross-sections have been already well reported [95, 229, 233, 235, 251–254]. Irradiations of thick ^{nat}Ni targets with proton beam of 16 MeV and 1 μA for 20 minutes, followed by 1 h post-irradiation processing time, are sufficient to achieve up to 100 MBq, with around 4% of ^{61}Cu ($T_{1/2}$ = 3.34 h). The radioactive impurity can be eliminated by using the commercially available 99% ^{60}Ni enrichment which would also increase the ^{60}Cu production by the factor of 4.

Another production of ^{60}Cu was suggested in [255] via ^{nat}Co(α,3n) reaction although the reported contribution of ^{61}Cu radioactive impurity was too high to consider this route in practice. More attractive alternative is ^{nat}Co(^{3}He,2n) as recommended in [256]. The measured cross-section indicates that if the ^{3}He beam of around 30 MeV is available, a short irradiation of 20 minutes and 1 μA followed by 1 h processing time would produce 60 MBq of ^{60}Cu with around 2% of ^{61}Cu radioactive impurity.

Alternative reaction, ^{58}Ni(α,x)^{60}Cu, has not yet been verified for practical purposes. The experimental cross-section [95, 257, 258] indicate the optimal beam energy range 40→20 MeV to irradiate the ^{nat}Ni target but compared to the ^{60}Ni(p,n) route, it produces 5 times less activity of ^{60}Cu and 4 times more ^{61}Cu.

^{66}Ga

The radioisotope of ^{66}Ga already has multiple applications and it has been widely used as PET radioisotope. Labelled with albumin colloids from commercially available kits designed for ^{99m}Tc, ^{66}Ga was successfully used in the imaging of the lymphatic transport [259]. The feasible ^{66}Ga labelling and purification was also reported for: ^{66}Ga-DOTA-Tyr3-octreotide and ^{66}Ga-DOTA-biotin [260], the blood cells [261, 262] and ^{66}Ga-deferoxamine-folate for in vivo and in vitro imaging [263–265]. Additionally, the most abundant β^+ particles (51.5%) emitted by ^{66}Ga has a uniquely high energy (4.2 MeV), which allowed the use of ^{66}Ga-DOTATOC for both PET imaging and radiotherapy [266]. Finally, ^{66}Ga emits high-energy γ line making it appropriate for $\beta^+\gamma$ coincidence PET. However, it also emits many low-intensity (no more than 4%) but high-energy γ lines (up to 4 MeV) and one 2752 keV (23%) γ line that will introduce noise in the imaging and dose to the patient.

The method of choice to produce ^{66}Ga is via ^{66}Zn(p,n) reaction. For this reaction, several production data were investigated (cross-section in [95, 267–274], thick target yield in

[252, 260, 269, 270, 272, 275–277]). This reaction was also summarized and re-evaluated with ALICE/ASH 0.1 and TALYS-1.2 codes in [278]. The natural abundance of ^{66}Zn is quite low but a feasible method was reported for the preparation and recovery of the enriched target [277]. Around 200 mg/cm^2 of Zn target is enough for the optimal production of ^{66}Ga with the 15 MeV proton beam. The reported yields were around 500 MBq/μAh for 99% enriched target or 130 MBq/μAh for the natural one. In the latter case, the reactions on other Zn isotopes, in particular ^{67}Zn(p,n) and ^{68}Zn(p,n), will form the radioactive impurities of ^{67}Ga ($T_{1/2}$ = 3.3 d) and ^{68}Ga ($T_{1/2}$ = 68 min) at the level below 1% at EOB. The optimal post-irradiation processing of Zn targets and ^{66}Ga separation was found to be a cation-exchange chromatography and/or liquid-liquid extraction method [260, 277].

Alternative approach leads via ^{63}Cu(α,n) reaction for which the excitation function was thoroughly investigated using ^{63}Cu targets [95, 279–289] and ^{nat}Cu targets [283, 290–296]. This reaction is also a monitor reaction for beam current measurements [179]. Unless the enriched target is available, the ^{67}Ga impurity formation on ^{65}Cu can be reduced with lower energy beam. For example, 17.5 MeV was reported to produce on thick ^{nat}Cu target is about 19 MBq/μAh (while the *TTY* calculated from the averaged experimental cross-section is 21 MBq/μAh) and about 0.5% of ^{67}Ga at EOB [259]. With 30 MeV, both ^{66}Ga yield and ^{67}Ga contribution increase by about a factor of 2 [284]. Although the separation of ^{66}Ga from irradiated Cu was developed [259, 297], the previous production with protons and Zn seems more efficient.

^{72}As

In the nuclear medicine, another popular PET radioisotope, ^{72}As, can be considered in the $\beta^+\gamma$ coincidence PET thanks to its additional γ line. It has proven its favourable physical and chemical properties in labelling and preclinical studies [298–301]. Furthermore, it has a therapeutic matched pair in the form of the β^- emitting ^{77}As that has been studied with the ^{72}As in preclinical and clinical research [301, 302]. Arsenic itself, in the form of the arsenic trioxide, is a popular anticancer drug [303], successfully used recently in the clinical treatment of the acute promyelocytic leukemia [304, 305].

There are many methods for the production of ^{72}As. The direct ones were summarized and re-evaluated with ALICE/ASH and TALYS-1.4 in [306]. Among them, the optimal one is ^{72}Ge(p,n) reaction, studied on metallic and oxide targets [95, 301, 307–310]. This production route requires enriched target as irradiation of ^{nat}Ge produces too much radioactive impurities of As. Based on reported experimental cross-section data, the calculated ^{72}As yield in the energy range 16→6 MeV is almost 300 MBq/μAh for 100% enriched ^{72}Ge, followed by 0.2% of ^{71}As radioactive impurity at EOB. The feasible irradiation using a medical cyclotron and a post-irradiation separation has also been reported [301].

However, much more attention is paid to the generator ^{72}Se/^{72}As due to its convenient half-life of 8.4 d. Many practical extraction methods for this generator have already been reported [300, 311–318]. According to the literature, the best method for the production of ^{72}Se/^{72}As is via ^{70}Ge(α,2n) reaction [95, 149, 311, 314, 318–322]. Different irradiation conditions have been used but the available cross-section data indicates the optimal energy 40→25 MeV that produces around 0.9 MBq/μAh of ^{72}Se on ^{nat}Ge target (poor heat conductivity of GeO_2 makes it unfit for the α beam irradiations) with about 20% of radioactive impurity ^{75}Se that decays to stable ^{75}As. The 6 h irradiation with 40 μA would result in 200 MBq of ^{72}Se/^{72}As, from which almost 100 MBq of ^{72}As could be extracted each day during the following week. The yield of ^{72}Se can be also increased about 2 times if the enriched ^{70}Ge targets are used [318] which also eliminates ^{75}Se.

Other production method for ^{72}Se/^{72}As generator require the 100 MeV proton beam. The ^{nat}Br(p,x) reaction reported higher yield and introduced NaBr target but also produced very high amount of radioactive impurity of ^{75}Se [315]. The ^{nat}As(p,4n) reaction [323, 324] was reported satisfactory with long irradiation of high beam intensity and lower ^{75}Se contamination compared to α production route.

^{76}Br

The radioisotope of ^{76}Br emits a large number of γ rays, from which the most intensive (559 keV, 74%) makes ^{76}Br a possible $\beta^+\gamma$ candidate (as suggested in [119, 120, 184, 187]) whose coincidence PET imaging and appropriate corrections have been already investigated [184]. There are two factors limiting the possible interest in ^{76}Br: the γ line used for the coincidence has quite low energy and other γ lines contribute to the dose. However, the labelling chemistry of bromine is similar to that of iodine, which is relatively well investigated [325] and might render ^{76}Br worth considering. So far, it has been successfully used to study dopamine receptors associated with the diagnosis of schizophrenia [326, 327], as the amino acid tracer [328], as the monitor for corticotropin-releasing hormone [329], as the bromo analog marker to diagnose heart disease [330], for the labelling of mouse epidermal growth factor [331] and to study the tumor angiogenesis by labeling a human antibody [332]. Additionally, ^{76}Br was used to verify the thymidine analogue, BUdR, as the tumor cell proliferation imaging agent [333].

As summarized in [334], the most feasible method for production of ^{76}Br is via ^{76}Se(p,n) reaction for which the cross-section [95, 334–336] and experimental yields [337, 338] are well measured. The excitation function was also summarized and reevaluated in [278]. However, the favourable cross-section requires in this case an enriched target due to the low abundance of ^{76}Se. The literature indicates that around 360 MBq/μA of ^{76}Br can be produced by the irradiation of the commercially available 97% enriched metal target with the proton beam of energy 15→8 MeV. The radioactive impurity of ^{77}Br was observed at the level below 2% and originated from ^{77}Se impurity in the target. Alternatively, to optimize the routine and economic production, the $Cu_2{}^{76}Se$ powder can be prepared, yielding up to 70 MBq/μAh after around 1 h separation (thermal chromatography in conjunction with dry distillation with 70% separation efficiency) and almost full target recovery procedure [338]. Another production method is ^{75}As(^{3}He,2n)^{76}Br reaction with 30 MeV beam used in [330] although no physical yield data is available, similarly to no cross-section measurements.

Meanwhile, it is also possible to produce the generator ^{76}Kr/^{76}Br ($T_{1/2}$ = 14.8 h) that requires dedicated yet simple separation set-up [339]. The first possible reaction, ^{nat}Br(p,xn)^{76}Kr, was used in [331, 340]. The measured cross-section [339, 341–346] are relatively low and 7 h long cooling-time is suggested to avoid the contamination of ^{77}Kr/^{77}Br, effectively yielding about 20 MBq/μAh of extracted ^{76}Br from NaBr target irradiated with 60 MeV beam. Without the cooling time, the contribution of the impurity greatly exceeds the activity of ^{76}Kr/^{76}Br. Alternative reaction, ^{nat}Se(^{3}He,xn)^{76}Kr, results in considerably lower yields [340].

B.2.2 Possible candidates for $\beta^+\gamma$ PET

^{34m}Cl

Compared to above-mentioned radioisotopes, ^{34m}Cl is less popular in the nuclear medicine field. However, it was recognized as potential PET radionuclide [347, 348] and has already been used to label dopamine D1 agonists [349, 350]. The first factor limiting its popularity is the number of high-intensity γ lines increasing the dose. While they might be used in coincidence for the $\beta^+\gamma$ imaging, other radioisotopes discussed here offer better physical properties for this purpose.

The second limiting factor is the difficult production of ^{34m}Cl. The reaction on chlorine, ^{nat}Cl(p,x) studied in [351] at 68 MeV, reaches very high yield but have very low specific activity. The practical, no-carrier-added production leads via ^{nat}S(α,x) which requires about 65 MeV beam according to measured and estimated cross-section [168, 352, 353]. The saturation of the thick target irradiation results in radio-contaminant-free 1500 MBq/μA ^{34m}Cl [168, 354, 355]. A feasible production chain was also developed, consisting of the 80% effective separation using heated water and HPLC pump [355]. The other α-induced reaction, ^{nat}P(α,n), was found to have much lower yield [353, 354]. Alternative production via ^{34}S(p,x) or ^{34}S(d,x) reactions [354, 356] require enriched sulphur targets and face the problem of poor thermal properties of its compounds [357]. The solution for the facilities with no α beam was presented in [357, 358] with the deuteron beam of 8 MeV, highly enriched ^{36}Ar target and the average yield of 65 MBq/μA of radionuclidically pure ^{34m}Cl.

^{52m}Mn

The recent advancements in hybrid MRI induced the interest in ^{52g}Mn radioisotope. It was suggested as the tracer of Mn^{+2} ions [359] that serve as the T1 relaxation agent in the Manganese-Enhanced Magnetic Resonance Imaging (MEMRI) [360–365]. However, in the light of the reported risk regarding the use of the bulk manganese [366], the use of ^{52g}Mn in conventional PET/MRI was suggested [367] to obtain analogous data with lower biological toxicity. Many reactions for its production are reported in the literature, from which the most commonly used is ^{nat}Cr(p,x)^{52tot}Mn. Its feasibility, from target preparation to chemical separation, was well reported [368]. Recently also other cross-sections have been reevaluated: ^{52}Cr(p,n), ^{52}Cr(d,2n) and ^{51}V(α,n) [369]. Along with the ground state ^{52g}Mn, the metastable level ^{52m}Mn is formed, which has very high β^+ branching ratio and emits only one, high-energy and high-intensity γ line (1434 keV, 98%). Since the $\beta^+\gamma$ coincidence imaging requires less activity, the toxicity of manganese in PET/MRI could be further reduced with the use of ^{52m}Mn (already suggested for $\beta^+\gamma$ coincidence PET in [181]). However, it should be noted that significant modifications might be required for PET hardware to permit the acquisition in the presence of a strong magnetic field and radiofrequency pulses [10].

The short half-life (21 min) of ^{52m}Mn radioisotope makes its direct production doubtful, especially since it is not possible to avoid the co-formation of ^{52g}Mn (which will be a radioactive impurity for $\beta^+\gamma$ PET). However, it is possible to produce a generator, ^{52g}Fe/^{52m}Mn, since ^{52g}Fe decays in 100% to ^{52m}Mn. However, the co-produced ^{52m}Fe ($T_{1/2}$ = 46 s) decays in 100% to ^{52g}Mn so it should be taken into account by managing the post-irradiation separation, rapidly removing ^{52g}Mn and then waiting for ^{52m}Mn to be formed from the decays of ^{52g}Fe.

The possible production routes for ^{52g}Fe/^{52m}Mn generator have been summarized in [370, 371]. According to the literature, the first reasonable option is to irradiate thick ^{nat}Mn target with protons of energy from 40-50 to 60-75 MeV. This procedure is routinely used in Brookhaven Linac Isotope Producer. Up to 22 MBq/μAh of ^{52g}Fe/^{52m}Mn was reached, with no more than 1% of ^{55}Fe ($T_{1/2}$ = 2.74 y) radioactive contaminant. Alternatively, the ^{nat}Ni(p,spall) reaction can be employed with the calculated thick target yield of 450 MBq/μAh of ^{52g}Fe/^{52m}Mn at 1000 MeV (based on cross-section data reported in [372]) and measured 2.5 MBq/μAh at 200 MeV [370] but the thorough verification of radioactive impurities is yet required. Another production route via ^{52}Cr(^{3}He,3n) reaction was well developed in [373, 374] although the reported thick target yield is lower, 1.9 MBq/μAh at 45 MeV. Finally, the cross-section for ^{50}Cr(α,2n) reaction was also studied [95] and its yield verified [374] but the cross-section seems too low for the practical application.

^{69}Ge

The "unravelled potential of ^{69}Ge" [375] is mainly related to the common interest shifted on a different germanium isotope (namely, the ^{68}Ge/^{68}Ga generator, summarized in [376, 377]). However, its physical properties make it a potential PET agent, also for the $\beta^+\gamma$ coincidence, and its chemistry is already well developed for the purpose of the mentioned generator. So far, it was only used to label nanoparticles for successful in vivo PET/MRI imaging [378]. Due to its long half-life, it can be also considered for immunoPET studies and antibody labelling.

The production of the potentially applicable amounts of ^{69}Ge was not yet investigated but the verified possible nuclear reactions include: ^{69,nat}Ga(p,n) [95, 379–382], ^{nat}Ga(d,x) [381], ^{66,67,68,nat}Zn(α,x) [95, 383–386] and ^{69}Ga(α,x) [95, 387, 388]. The proton induced reaction seems the most cost-efficient and available for small cyclotrons: 16 MeV beam interacting on a thick ^{nat}Ga target would produce around 110 MBq/μAh. However, no cross-section data is available to estimate the co-production of radioactive impurity of ^{71}Ge. The measurement is challenging due to no γ emission but important as ^{71}Ge is the long-lived Auger-emitter which would contribute to the dose.

^{82g}Rb

An interesting case, ^{82g}Rb, emits β^+ radiation (branching = 95%) followed by only one low-intensity γ line (777 keV, 15%). Still, it was introduced as the $\beta^+\gamma$ PET candidate [119, 120] but due to its very short half-life it can be considered only with the generator (for repetitive, short studies). Its metastable state, ^{82g}Rb ($T_{1/2}$ = 6.47 h), cannot be used as such because it decays in 100% to ^{82}Kr. Instead, it is already used in PET [389, 390] but due to the multiple accompanying γ rays, ^{82m}Rb is not recommended for the coincidence imaging.

The radioisotope of ^{82}Sr ($T_{1/2}$ = 25.4 d) however decays in 100% by EC to ^{82g}Rb and the generator ^{82}Sr/^{82g}Rb has already gained incredible popularity. It is widely used to diagnose cardiovascular disease (a leading cause of death in modern industrialized countries) in myocardial perfusion imaging [391–400]. It provides significantly better precision compared to ^{201}Tl SPECT [393] and presents less radiation exposure for patients compared to ^{99m}Tc scan [398]. Many studies have also been performed on the elution system and the optimized chemical separation [391, 392, 394, 396, 398, 401–404].

The method of choice for ^{82}Sr/^{82g}Rb generator production is the (p,4n) reaction on ^{85}Rb which benefits from high natural abundance. This method was studied multiple times and is most often employed for large-scale production [402, 403, 405–410], although, as summarized in [411], significant discrepancies still exist. For the proton energy of 70-60 MeV (with 40 MeV exiting from the thick Rb or RbCl target), the ^{82}Sr/^{82g}Rb production yields of 8-13 MBq/μAh were reported. The observed long-lived radioactive impurity of ^{85}Sr was below 1%. As the typical generator activity used for clinical studies reaches 4 GBq [394], the typical irradiation lasts for few days and requires high beam current.

Suggested alternative productions include: ^{nat}Kr(α,xn) and ^{nat}Kr(^{3}He,xn) [412, 413] as well as ^{nat}Mo(p,spall) [414, 415]. However they have lower yields and high contribution of the ^{83}Sr impurity. Significantly higher activity and purity was reported with ^{84}Sr(p,x) reaction but it requires highly enriched strontium target [416].

^{86g}Y

The potential of ^{86g}Y lies within its theranostic matched pair [417–419], the β^- emitter ^{90}Y available from the long-lived ^{90}Sr/^{90}Y generator system, which is a versatile therapy agent (as reviewed in [420]). However, the emission of multiple intensive, dose-contributing γ rays from ^{86g}Y and the recent development of the ^{90}Y imaging with the bremsstrahlung photons (summarized in [421]) might render the matched pair obsolete. Still, many radiochemical and in vivo PET imaging studies were performed with ^{86g}Y (summarized in [422]) and its dominating γ line (1077 keV, 83%) was recognized for the $\beta^+\gamma$ coincidence PET [119, 120, 182, 185–187]. In fact, the coincidence imaging and appropriate corrections for this radioisotope have been already investigated [182, 185, 186].

Several methods of ^{86g}Y production were investigated (in each, the co-produced ^{86m}Y decays in 99% with $T_{1/2}$ = 47.4 min to ^{86g}Y). As reviewed in [423], the most commonly used is ^{86}Sr(p,n) reaction, for which the excitation function has been also re-evaluated with nuclear codes in [278]. It requires about 14 MeV as higher energies increase the percentage of the contaminants. The reported irradiation of around 200 mg/cm^2 of the commercially available 95% enriched $^{86}SrCO_3$ target yields about 150 MBq/μAh with less than 3% of radioactive impurities [424–430]. For comparison, around 10 MBq of ^{86g}Y is enough for in vivo mice studies [431, 432].

About 6 times higher yield with less radioactive impurities can be achieved with the ^{86}Zr/^{86g}Y generator produced in the irradiation of natural yttrium target with the proton energy range of 70→45 MeV [433]. However, this method requires high energy proton beam and the efficient separation method (also reported). Other alternative production methods include: ^{88}Sr(p,3n) [434] and ^{nat}Sr(d,x) [435]. The cross-sections have been measured also for the reactions: ^{85}Rb(α,3n) [95, 436–438] and ^{nat}Rb(^{3}He,x) [424]. However, these processes are less cost-effective and are of minor interest for the large-scale production.

^{94m}Tc

Despite the clear dominance of ^{99m}Tc in nuclear medicine for SPECT imaging, other technetium radioisotope, ^{94m}Tc, is of a potential interest as a PET quantification of ^{99m}Tc-labelled radiopharmaceuticals [439, 440] due to the same chemistry of both isotopes. It decays completely to ^{94}Mo and emits one high-intensity high-energy γ line making it suitable for $\beta^+\gamma$ coincidence imaging [119, 120, 181]. The feasibility of standard in vivo PET studies has been already reported [441–443].

The method of choice for the ^{94m}Tc production is the bombardment of ^{94}Mo with medium energy proton beam [439, 444–448]. The commercially available enrichment of about 95% is available in MoO_3 powder form. The irradiation with the optimal energy range of 13→8 MeV produces about 2 GBq/μAh ^{94m}Tc with about 8% of ^{94g}Tc impurity (the irradiation of natural target produces additional technetium impurities at the level unattractive for practical use). A 1 h irradiation with 4 μA beam followed by 0.5 h thermochromatographic separation with 90% efficiency results in 1300 MBq $^{94m}TcO_4^-$, ready for medical application [445]. Other purification and target recovery methods were also investigated (summarized in [446]). Also, [449] invented the feasible production on liquid ^{nat}Mo, providing a potential feasible automatization yet reducing the ^{94m}Tc yield. It is also possible to remove the ^{94g}Tc impurity by producing ^{94}Ru/^{94m}Tc generator via ^{92}Mo(α,2n)^{94}Ru [450, 451] with however about 10 times lower effective yield compared to ^{94}Mo(p,n)^{94m}Tc. The direct ^{94m}Tc production with the use of ^{93}Nb(^{3}He,2n) (yields: [452]), ^{93}Nb(α,3n) (cross-section: [453, 454]) and ^{92}Mo(α,np) (yields: [451]) also showed too small high spin to low spin formation ratio.

^{110m}In

So far, the radioisotope of ^{110m}In has not drawn a lot of attention in the nuclear medicine field. However, as confirmed by in vivo clinical studies, it provides 3 times better resolution than the typical ^{111}In SPECT [455] which opens the possibilities for the detection of small tumors with indium-labelled radiopharmaceuticals. This might be important in the light of an emerging radioisotope ^{114m}In [180], an Auger emitter with almost instant β^- emissions (from its short-lived daughter), whose therapeutic properties are expected [456]. Additionally, ^{110m}In emits medium-energy but high-intensity γ line which could be potentially interesting for $\beta^+\gamma$ coincidence PET.

Several cross-sections measurements are available, suggesting the potential ^{110m}In production options (summarized recently in [457]). The studied excitation functions include ^{110,111,112,nat}Cd(p,x) [457–467], ^{110,112}Cd(d,x) [457, 468], ^{nat}Cd(α,x) [469], ^{107,109,nat}Ag(α,x) [279, 457, 467, 470–472] and ^{109}Ag(^{3}He,2n) [457]. The direct production of ^{110m}In always leads to the co-formation of the radioactive impurity ^{110g}In but the higher isomeric ratio can be achieved with lower projectile energies. The recommended reaction, ^{110}Cd(p,n), at 15 MeV energy (available in commonly used machines) and with electroplated ^{nat}Cd target [473] yields 160 MBq/μAh of ^{110m}In with around 3% of ^{110g}In and 6% of ^{111g}In radioactive impurities [473, 474]. The use of the enriched ^{110}Cd would increase the yield and reduce the activity of ^{111g}In.

Meanwhile, ^{110m}In without ^{110g}In contribution can be obtained with the use of generator ^{110}Sn/^{110m}In although all production routes require high-energy beams. The literature agrees that the optimal production is achieved via ^{nat}In(p,x) reaction yielding about 400 MBq/μAh of ^{110}Sn at 75 MeV on 5 mm thick target [457, 475].

^{124}I

A textbook medical radionuclide ^{124}I has relatively low β^+ branching ratio and the medium-intensive medium-energy γ line but was still suggested as $\beta^+\gamma$ PET candidate [119, 120, 181, 183, 187] and the corrections for its coincidence imaging have also been investigated [183]. This is mainly because it is the only isotope of iodine suitable for PET that can be paired with the strategic therapeutical ^{131}I [417] commonly used for the treatment of hyperthyroidism and thyroid cancer (overviewed in [476, 477]). Furthermore, ^{124}I itself has already been used for the imaging of tissue proliferation [478–480] and for multiple in vivo cancer imaging

[481–483] including thyroid [484–488]. It is also considered as a potential Auger-emitter for the radiotherapy [489].

The methods for production of ^{124}I were thoroughly studied by many groups with the use of protons, deuterons and α-particles (summarized in [423, 490]). As one of the "emerging isotopes", its production cross-sections are also collected in IAEA database [180]. The most typical ^{124}I production method is the ^{124}Te(p,n) reaction [491–496] suitable for popular small cyclotrons but requiring the enriched target material (which is crucial to increase the yield and to reduce the radioactive impurities). Recent thick target yield measurements [494] indicate that the irradiation of the commercially available $^{124}TeO_2$ targets (99.9% ^{124}Te) with the energy range of 14→7 MeV produces around 21 MBq/μAh of ^{124}I with around 0.03% of radioactive impurities of ^{125}I and ^{126}I, followed by the dry distillation. As investigated in [495], the synthesis of Al_2Te_3 target provides the yield of about 9 MBq/μAh but allows to use the high beam currents and increases the target recovery (98%). Basically, a few hour run with around 20 μA is enough to produce several 50 MBq batches used for the imaging [488]. Similar yield can be achieved with ^{124}Te(d,2n) around 15 MeV [496–500] yet with higher contribution of radioactive impurities. The reaction ^{125}Te(p,2n) provides up to 100 MBq/μAh but requires higher energy, 22→14 MeV [501, 502]. The alternative production with α beam and natural or enriched antimony target has considerably lower yield and complexed target processing [503–505].

B.2.3 Other $\beta^+\gamma$ radioisotopes

Online monitors

There are two very short-lived $\beta^+\gamma$ emitters suitable for in vivo PET imaging during hadron therapy [119, 120, 181], namely: ^{10}C ($T_{1/2}$ = 19.3 s) and ^{14}O ($T_{1/2}$ = 70.6 s). They are formed via the fragmentation of the high energy heavy ions or different nuclear reactions induced by the high energy projectiles on ^{12}C, ^{14}N, ^{16}O nuclides which are immensely abundant in the organic compounds. During the charged-particle therapy, the beam energy is much higher than the thresholds for these reactions. Therefore the beam, apart from the delivery of the radiation dose to cancerous tumors, produces ^{10}C and ^{14}O allowing the visualization of the treatment (in particular the measurement of the range) with the online acquisition system.

PET scans has already been reported for the mentioned radionuclides [506–509]. However, good time resolution is required as many 511 keV γ quanta can be expected from co-produced ^{15}O (^{10}C and ^{14}O have much lower probability for reactions) [508, 510, 511]. Also, as discussed in [512], the online PET is actually a posteriori control and the imaging of prompt-gamma might be utilized instead, if the collimated machines are installed. Therefore, the method with $\beta^+\gamma$ coincidence PET can be considered for online treatment monitoring in the cases where the lower statistic is expected.

It is worth mentioning that the ^{10}C production with 11 MeV proton beam on enriched $^{10}B_2O_3$ target was also introduced [513]. It is followed by the immediate flow-through chemistry processing for human inhalation of $^{10}CO_2$ for the blood flow imaging with PET.

Calibration source

^{22}Na is a common calibration source, used even in the recent PET research [509]. It has a very long half-life of 2.6 years and high β^+ branching ratio, making it a convenient β^+ emitter for the repetitive calibrations. ^{22}Na also emits 1274.5 keV γ line that was used as a trigger during the calibration of liquid argon detector [514]. Being already recognized as the $\beta^+\gamma$ PET candidate [119, 120, 181], ^{22}Na can be therefore considered as a calibration source for $\beta^+\gamma$ coincidence PET.

^{22}Na sources can be bought from the different suppliers or even produced on the site (as summarized in [515]). In the case of the common cyclotrons with the proton beam of about 16 MeV, the most promising route is via ^{22}Ne(p,n). The ^{nat}Ne gas target (with 9% abundance of ^{22}Ne) produces around 30 kBq with 1 μAh irradiation in 15→6 MeV energy range [515]. The same production of ^{22}Na and the design of ^{nat}Ne gas target was recently well reported in [516]. Meanwhile, for cyclotrons with higher proton energy, the ^{nat}Al target

can be used instead. The irradiation with the beam energy range of 70→25 MeV or 600→400 MeV would give the yields of 6 kBq/μAh and 6 MBq/μAh respectively ([515], calculated from cross-section in [517]). The purification of the irradiated Al target and the preparation of ^{22}Na source with the use of ISOLDE mass separator in CERN was described in [518]. Today, the only large-scale production is performed with the use of 70 MeV proton cyclotron by iThemba LABS in South Africa.

Appendix C

Supplementary data

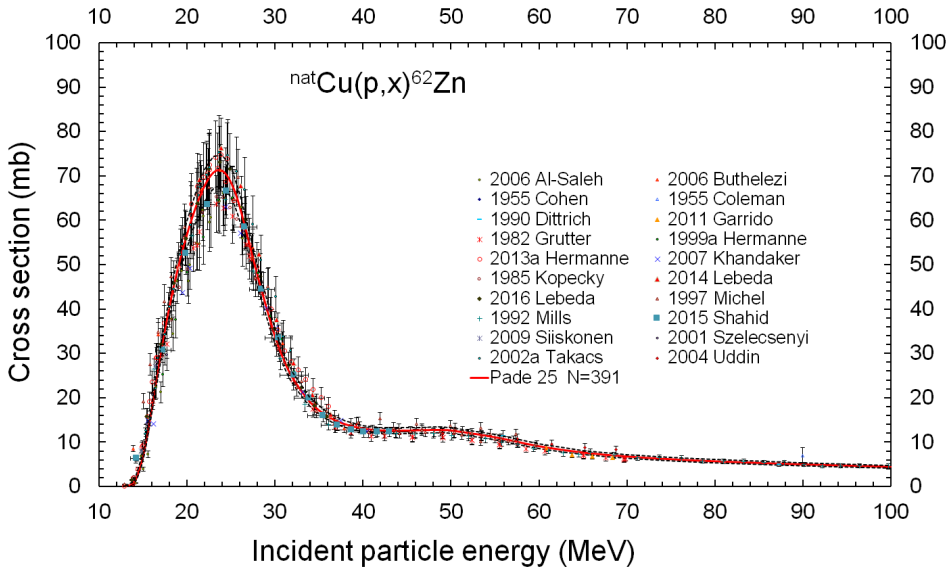

FIGURE C.1: Monitor cross-section: $^{nat}Cu(p,x)^{62}Zn$ [74, 75].

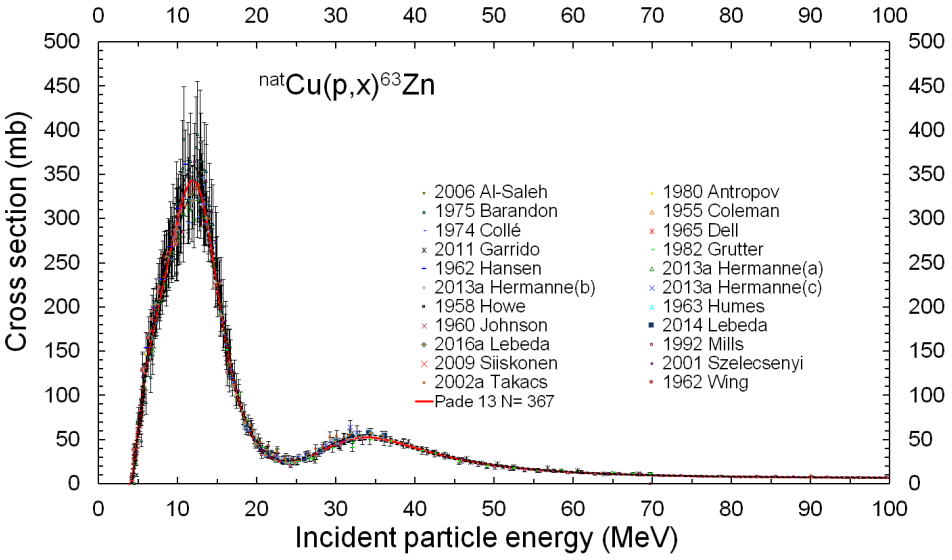

FIGURE C.2: Monitor cross-section: $^{nat}Cu(p,x)^{63}Zn$ [74, 75].

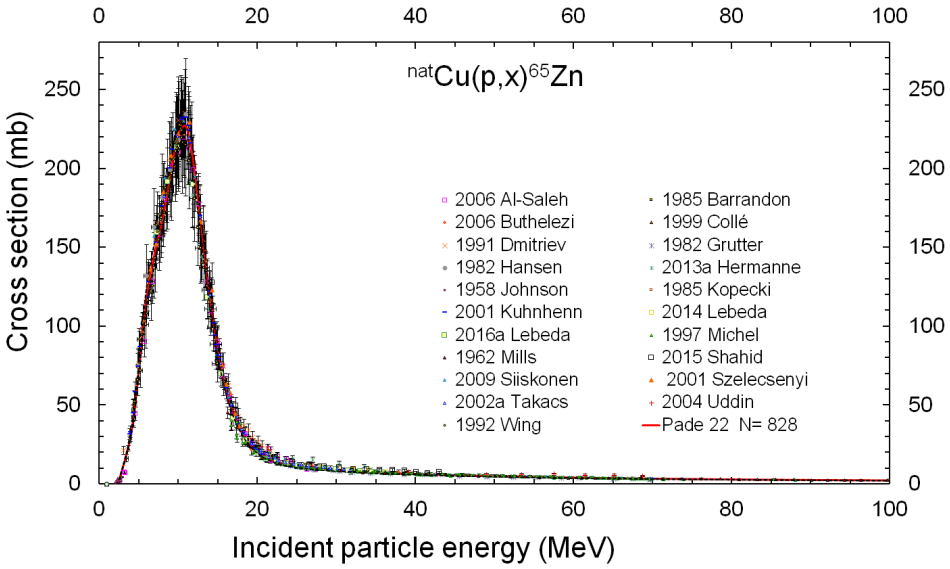

FIGURE C.3: Monitor cross-section: $^{nat}Cu(p,x)^{65}Zn$ [74, 75].

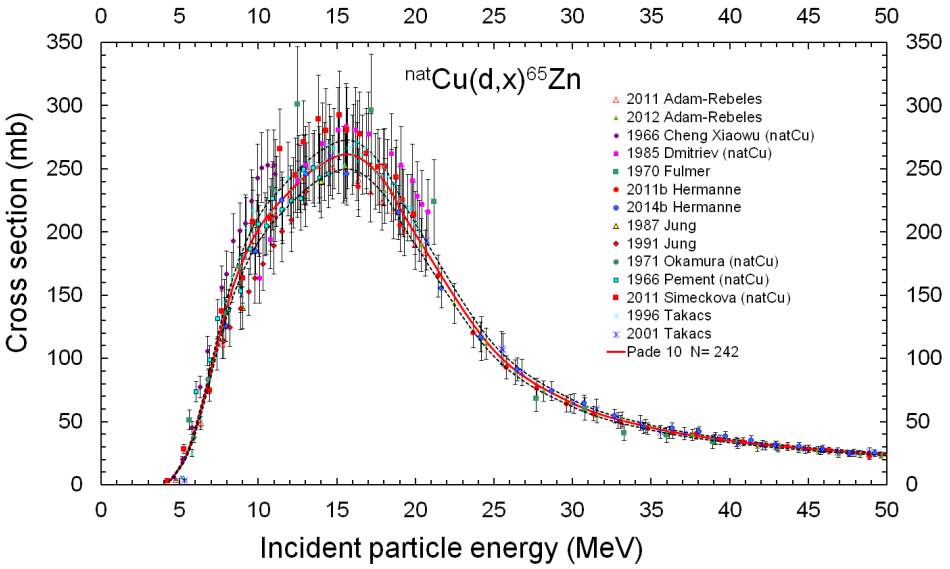

FIGURE C.4: Monitor cross-section: $^{nat}Cu(d,x)^{65}Zn$ [74, 75].

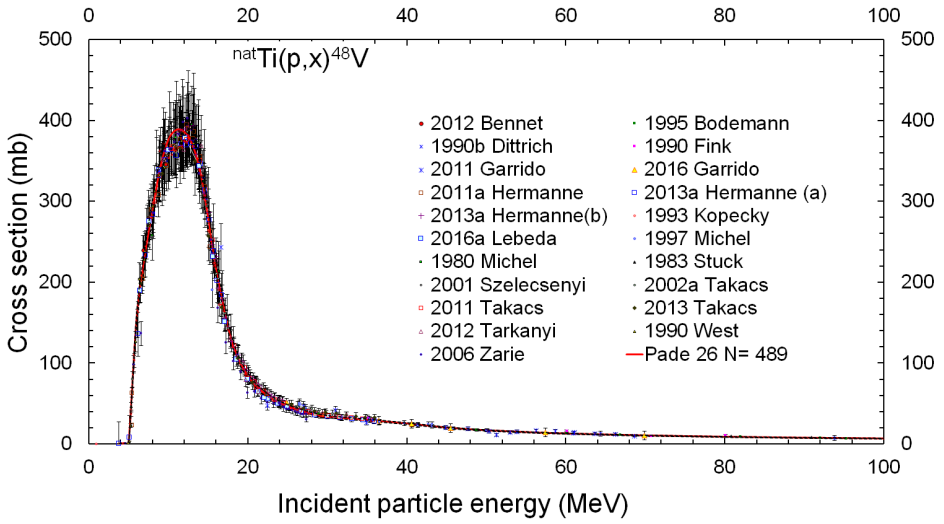

FIGURE C.5: Monitor cross-section: ^{nat}Ti(p,x)^{48}V [74, 75].

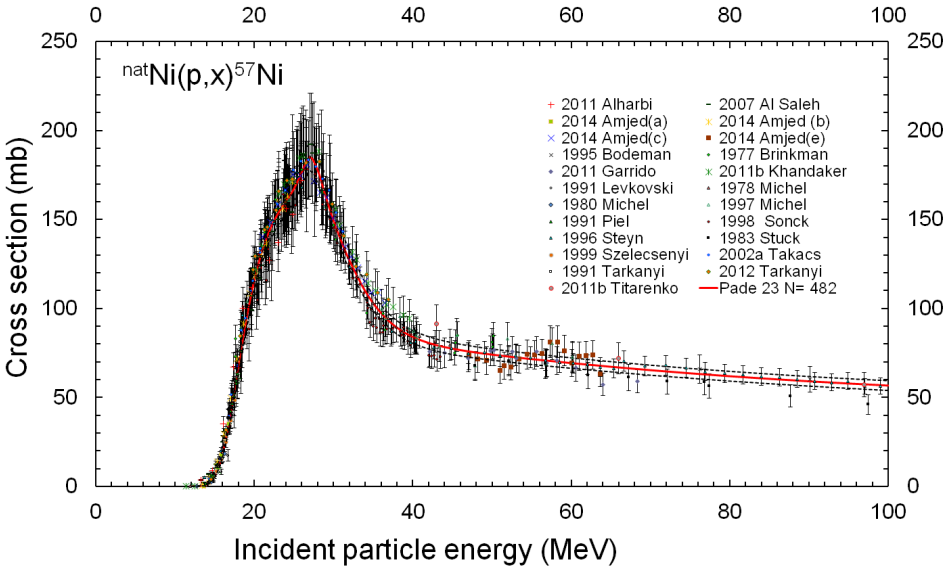

FIGURE C.6: Monitor cross-section: ^{nat}Ni(p,x)^{57}Ni [74, 75].

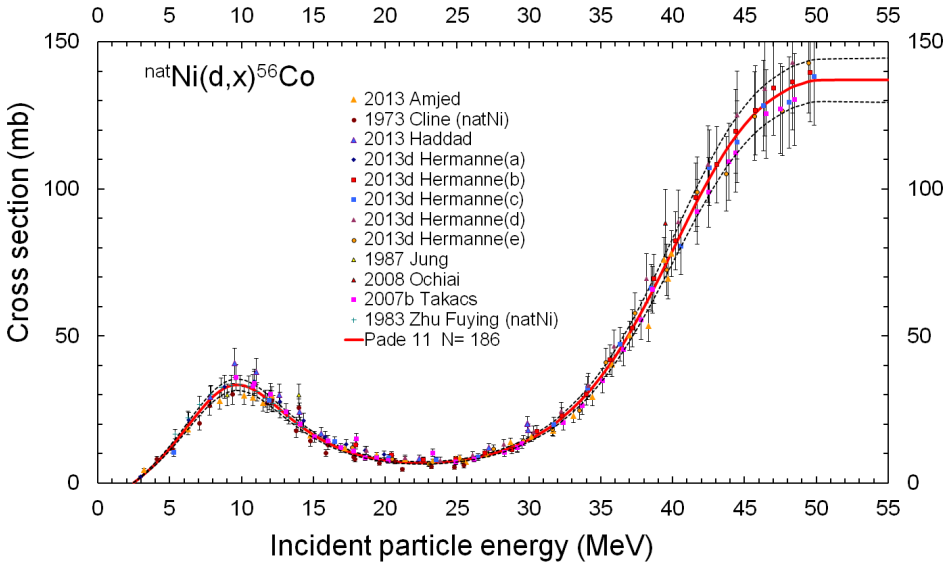

FIGURE C.7: Monitor cross-section: ^{nat}Ni(d,x)^{56}Co [74, 75].

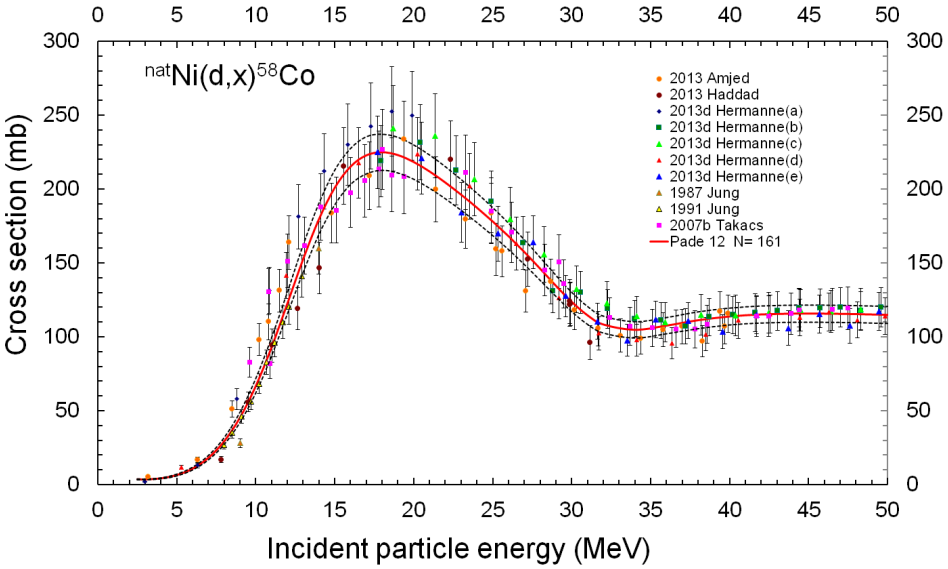

FIGURE C.8: Monitor cross-section: ^{nat}Ni(d,x)^{58}Co [74, 75].

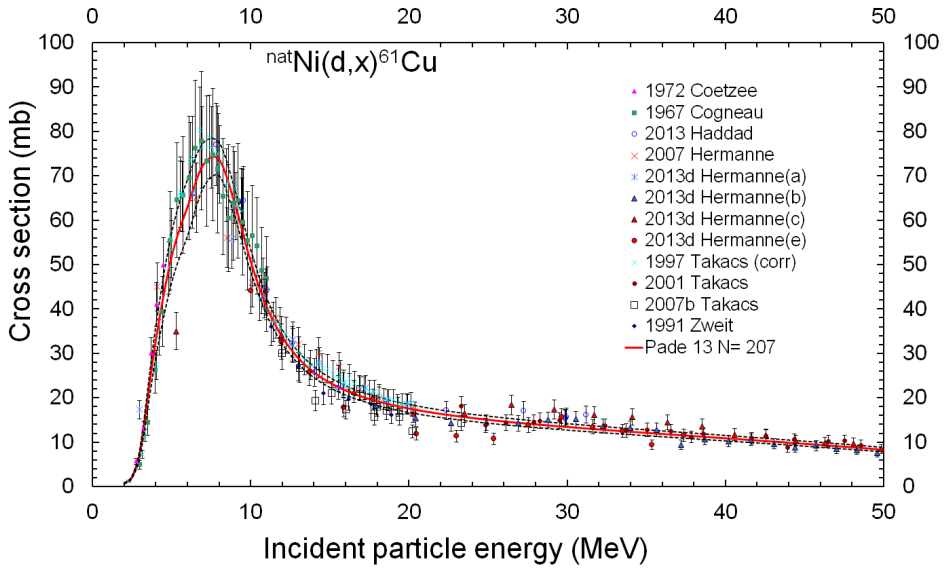

FIGURE C.9: Monitor cross-section: ^{nat}Ni(d,x)^{61}Cu [74, 75].

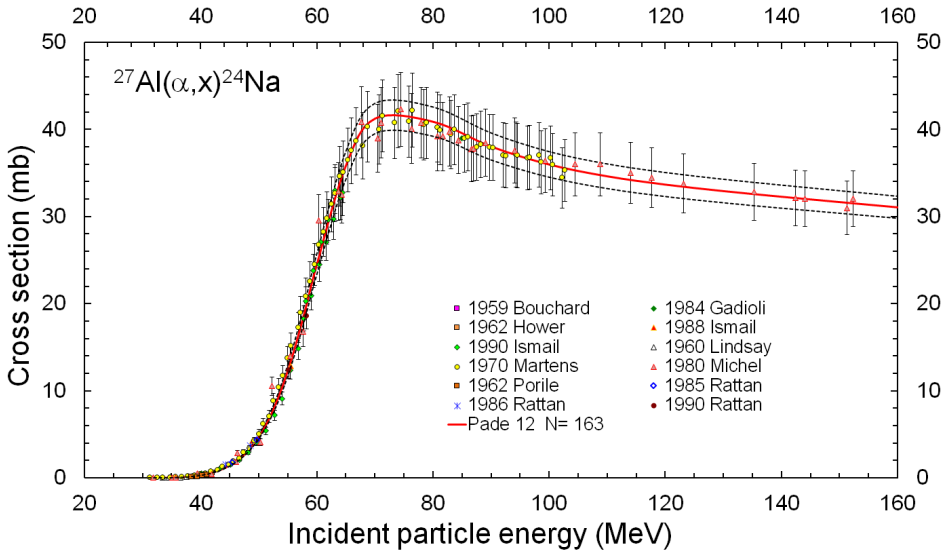

FIGURE C.10: Monitor cross-section: ^{27}Al(α,x)^{24}Na [74, 75].

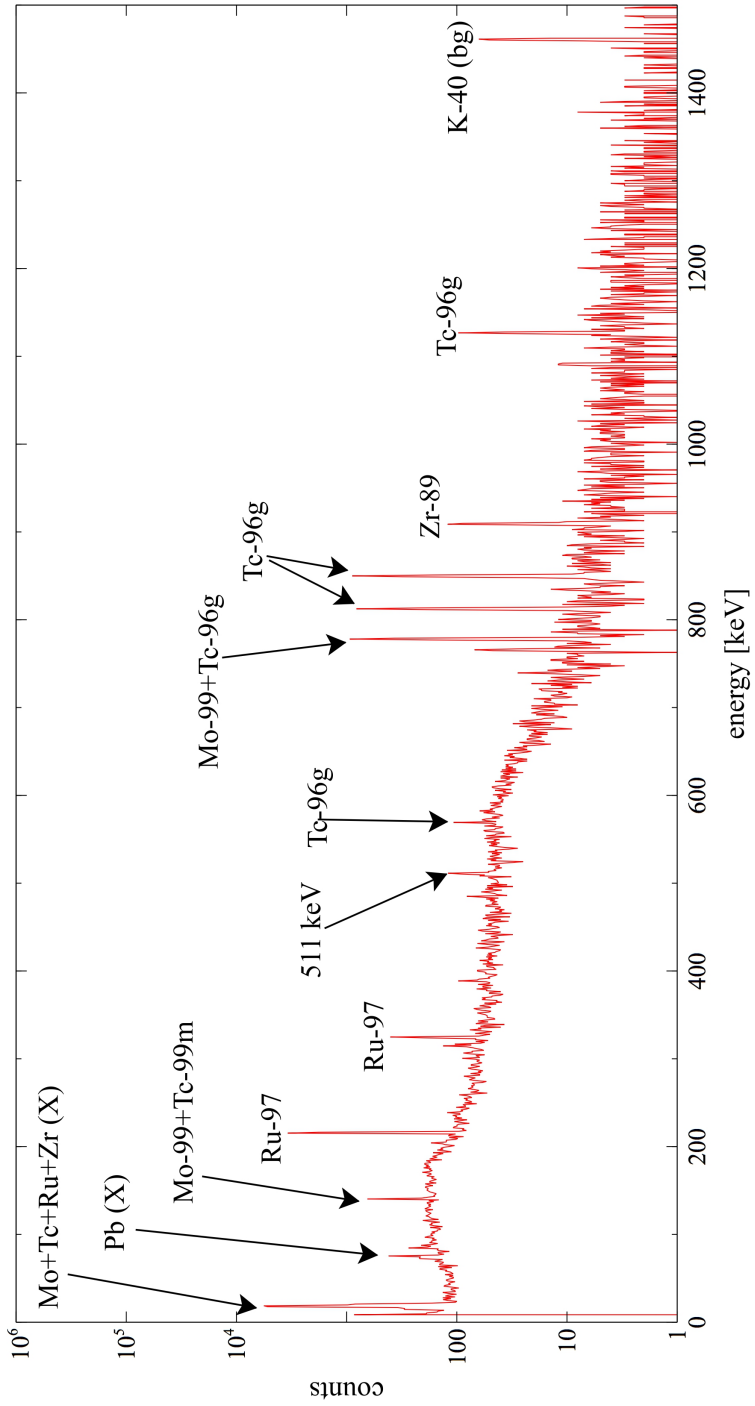

FIGURE C.11: Spectrum of 10 µm ^{nat}Mo foil irradiated for 1 h with α beam of 60.0 MeV and 60 nA. Spectrum was collected 6.7 d after EOB with HPGe at ARRONAX (Section 3.2.3) during 2.2 h in geometry 19 cm (with dead time below 1%).

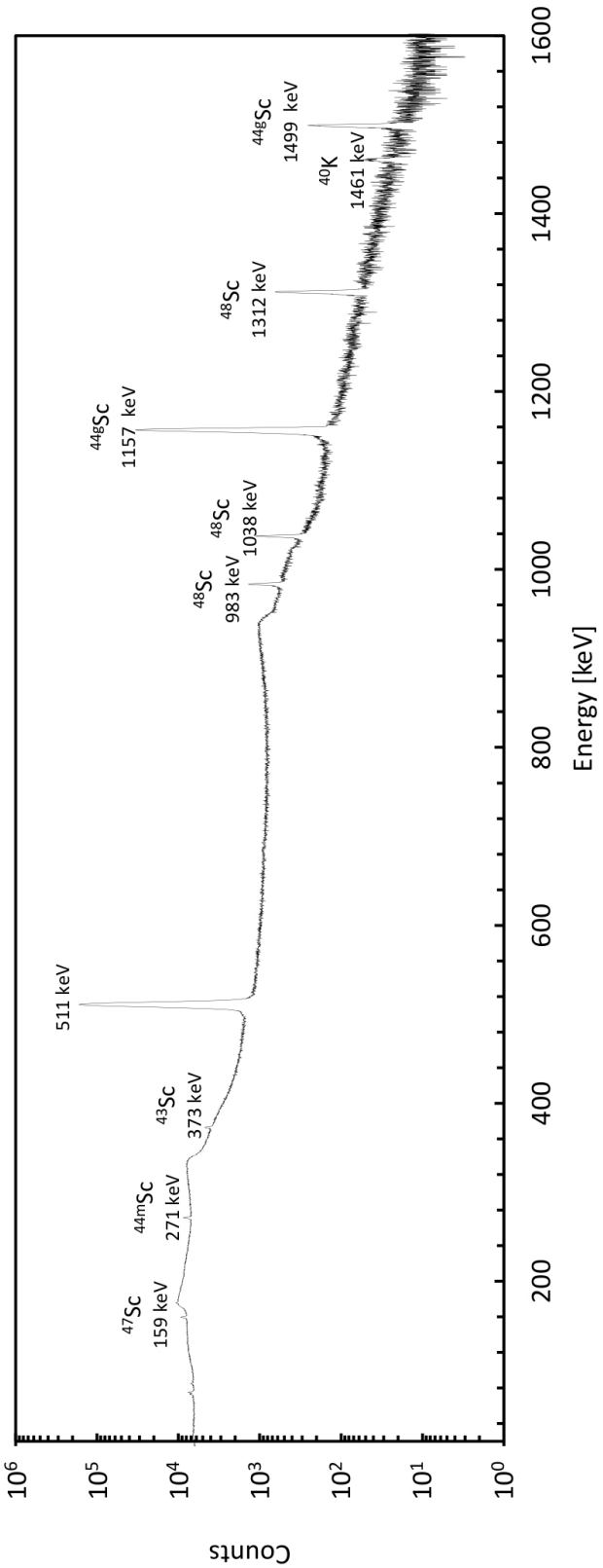

FIGURE C.12: Spectrum of 75% $^{nat}CaCO_3$ mixed with 25% graphite target irradiated during 0.42 h with proton beam in energy range 15.2→3.0 MeV and intensity of 210 nA. Spectrum was collected 5.2 h after EOB with EG&G ORTEC HPGe (Section 3.2.3) in geometry 30 cm during 1.2 h with dead time 8.4% (courtesy of Katarzyna Szkliniarz).

TABLE C.1: Isotopic composition [%] of natural molybdenum targets.

	^{92}Mo	**^{94}Mo**	**^{95}Mo**	**^{96}Mo**	**^{97}Mo**	**^{98}Mo**	**^{100}Mo**
^{nat}Mo	14.53	9.15	15.84	16.67	9.60	24.39	9.82

TABLE C.2: Isotopic composition [%] of natural ruthenium targets.

	^{96}Ru	**^{98}Ru**	**^{99}Ru**	**^{100}Ru**	**^{101}Ru**	**^{102}Ru**	**^{104}Ru**
^{nat}Ru	5.54	1.87	12.76	12.60	17.06	31.55	18.62

TABLE C.3: Isotopic composition [%] of natural and commercially available enriched calcium carbonate targets (ISOFLEX, USA). Materials marked with (*) were employed in this work.

	^{40}Ca	**^{42}Ca**	**^{43}Ca**	**^{44}Ca**	**^{46}Ca**	**^{48}Ca**
^{nat}Ca (*)	**96.94**	0.647	0.135	2.086	0.004	0.187
^{42}Ca (*)	29.9	**68**	0.4	1.5	<0.01	0.2
^{42}Ca	3.24	**95.9**	0.13	0.7	<0.01	0.03
^{43}Ca (*)	23.8	1.0	**62.2**	12.8	<0.01	0.2
^{43}Ca	5.3	0.18	**90**	4.44	<0.01	0.08
^{44}Ca (*)	5.03	0.1	<0.01	**94.8**	<0.01	<0.05
^{48}Ca (*)	27.9	0.3	0.1	2.2	<0.1	**69.2**
^{48}Ca	2.72	0.2	0.01	0.15	<0.01	**97.1**

TABLE C.4: Isotopic composition [%] of natural and enriched titanium dioxide targets. The isotopes with the quoted enrichment values are available from ISOFLEX, USA. Both materials were employed.

	^{46}Ti	**^{47}Ti**	**^{48}Ti**	**^{49}Ti**	**^{50}Ti**
^{nat}Ti	8.25	7.44	73.72	5.41	5.18
^{48}Ti	0.09	0.1	99.63	0.12	0.06

TABLE C.5: Observed cross-sections for ^{nat}Mo(α,x) reactions.

E [MeV]	^{nat}Mo(α,x) cross-section [mb]				
	^{97}Ru	^{89g}Zr	^{95g}Tc	^{96tot}Tc	^{99}Mo
41.80(75)	237(20)		81(11)	73(7)	7.5(1.0)
46.03(68)	225(20)		127(14)	89(8)	10.1(1.2)
50.00(64)	199(18)		163(17)	100(9)	11.4(1.3)
51.93(62)	166(14)		170(16)	101(9)	12.8(1.3)
55.30(60)	159(13)	3.6(9)	177(17)	109(9)	13.5(1.4)
58.51(56)	176(15)	11.7(1.6)	205(17)	119(10)	
59.97(55)	176(15)	18(2)	174(24)	116(10)	14.0(1.5)
63.47(53)	180(16)	30(3)	188(16)	118(10)	15.0(1.7)
66.84(50)	173(14)	40(3)	203(17)	122(10)	15.6(1.3)

TABLE C.6: Observed cross-sections for deuteron-induced reactions on ^{104,nat}Ru and calculated values for ^{104}Ru(d,n)^{105tot}Rh direct reaction ("tot" indicates production of radionuclide directly and via decay of short-lived metastable states).

E [MeV]	^{nat}Ru(d,x) cross-section data [mb]						^{104}Ru(d,x)^{105tot}Rh data [mb]	^{104}Ru(d,p)^{105}Ru data [mb]	^{104}Ru(d,n)^{105tot}Rh calculation [mb]
	^{97}Ru	^{99g}Rh	^{99m}Rh	^{100g}Rh	^{101m}Rh	^{103}Ru			
5.7(1.1)	6.6(1.6)		1.4(4)	6.9(1.8)	10(3)	14(6)	104(26)	64(16)	31(11)
6.68(1.32)	5.1(1.3)		1.7(5)	11(2)	7.9(1.9)	17(5)	126(36)		
8.6(0.8)	17.2(4.0)		18(4)	29(7)	44(11)	40(9)	212(60)	127(30)	67(23)
9.0(1.2)	19.4(4.5)	9.1(2.3)	17(4)	26(6)	45(10)	46(11)	196(46)	119(28)	60(20)
10.9(0.67)	15.3(3.5)		30(7)	52(12)	57(14)	36(10)	164(41)	109(26)	40(14)
11.00(1.14)	16.7(4.0)	15.7(4.0)			61(13)	40(10)			
13.9(0.5)	10.2(2.4)		37(8)	65(15)	76(18)	27(8)	152(39)	94(26)	33(12)
14.2(1.1)	10.2(3.1)	17.1(4.0)	49(15)	68(15)	81(20)	31(8)	155(60)		
17.5(0.9)	7.9(2.1)	13.0(2.9)	49(14)	98(22)	97(21)	26(7)	116(34)		

TABLE C.7: *TTY* of radioisotopes formed during irradiation of thick $CaCO_3$ targets with proton beam for the production of medical scandium radioisotopes (measured data are recalculated for the maximum commercially available enrichment). In some targets, not all radioisotopes were observed due to the use of enriched target material and unobservable amounts of impurities produced.

Isotope	^{43}Sc	^{44g}Sc	^{44m}Sc	^{47}Sc	^{48}Sc	^{47}Ca
Target	$^{43}CaCO_3$ (90%)	$^{44}CaCO_3$ (94.8%)	$^{44}CaCO_3$ (94.8%)	$^{48}CaCO_3$ (97.1%)	$^{48}CaCO_3$ (97.1%)	$^{48}CaCO_3$ (97.1%)
***E* [MeV]**	**Thick Target Yield [MBq/μAh]**					
7.6	61(6)	120(20)	0.13(50)		26(3)	
9.7	109(11)	280(20)	0.40(40)	0.47(5)	38(4)	
10.7	180(20)	370(40)	0.84(5)	2.1(2)	59(6)	
11.3		400(40)	1.5(1)			
11.9	200(20)	500(50)	1.3(2)	6.8(8)	68(7)	0.070(7)
12.8	240(20)	540(50)	2.0(2)	10(1)	73(7)	0.13(1)
14.3	260(30)	730(50)	2.7(3)	21(2)	74(7)	0.60(6)
15.2	317(14)	780(30)	3.6(1)	31(2)	79(4)	0.39(14)
17.5	410(40)					
21.8		1030(50)	5.9(3)	94(6)	101(10)	7.8(5)
22.0		980(100)	7.5(8)			
22.4				98(5)	101(4)	6.1(7)
22.8		940(40)	7.0(2)	105(6)	98(4)	8.1(6)
28.2				136(8)	106(5)	17(2)
28.5		1020(50)	8.0(4)	139(16)	108(4)	22(3)

TABLE C.8: *TTY* of radioisotopes formed during irradiation of thick $CaCO_3$ targets with deuteron beam for the production of medical scandium radioisotopes (measured data are recalculated for the maximum commercially available enrichment).

Isotope	^{43}Sc	^{44g}Sc	^{44m}Sc	^{47}Sc	^{48}Sc
Target	$^{42}CaCO_3$ (95.9%)				
***E* [MeV]**	**Thick Target Yield [MBq/μAh]**				
4.7	5.6(8)	0.014(6)	$1.6(7) \times 10^{-4}$	$6.9(7) \times 10^{-5}$	$1.3(5) \times 10^{-4}$
6.8	45(4)	0.11(7)	$1.8(6) \times 10^{-3}$	$6.3(5) \times 10^{-4}$	0.020(8)

TABLE C.9: Reconstructed cross-section values, σ [mb], for different proton energy E [MeV] (for details see Section 4.4).

E	^{43}Ca(p,n)^{43}Sc Figure 4.30	^{44}Ca(p,n)^{44g}Sc Figure 4.31	^{44}Ca(p,n)^{44m}Sc Figure 4.32	^{48}Ca(p,2n)^{47}Sc Figure 4.33	^{48}Ca(p,n)^{48}Sc Figure 4.34
5	145(20)	115(6)	2.11(8)	0	552(48)
6	187(26)	314(13)	11.7(5)	0	692(66)
7	214(29)	450(20)	19.2(8)	0	761(77)
8	228(28)	534(26)	25.1(1.1)	0	744(78)
9	231(24)	572(31)	29.6(1.3)	14.2(6)	740(71)
10	225(18)	572(32)	32.9(1.4)	199(7)	674(58)
11	211(12)	543(30)	35.0(1.4)	353(14)	586(43)
12	193(10)	493(25)	36.2(1.3)	478(18)	490(29)
13	172(15)	431(19)	36.4(1.2)	576(20)	393(20)
14	148(21)	363(15)	35.9(1.0)	647(20)	304(18)
15	125(26)	297(14)	34.7(8)	698(20)	228(21)
16	140(29)	235(15)	33.1(7)	729(19)	164(22)
17	84(30)	180(16)	31.0(7)	739(18)	115(21)
18	66(30)	134(16)	28.7(8)	734(18)	78(19)
19		97(16)	26.1(1.0)	716(21)	51(15)
20		68(14)	23.4(1.1)	684(26)	32(12)
21		47(12)	20.8(1.3)	647(31)	20(9)
22		31(10)	18.2(1.4)	600(35)	12(6)
23		20(7)	15.7(1.4)	550(40)	7(4)
24		13(6)	13.5(1.4)	499(43)	4(3)
25		8(4)	11.3(1.4)	445(46)	2.0(1.6)
26		5(3)	9.5(1.4)	393(47)	1.0(9)
27		2.8(1.8)	7.8(1.3)	343(48)	0.5(5)
28		1.5(1.1)	6.4(1.2)	297(47)	0.3(3)
29		0.8(7)	5.1(1.1)	253(45)	0.12(16)
30		0.4(4)	4.0(9)	213(43)	0.05(8)

TABLE C.10: Parameters of the TTY_{fit} obtained with least square method for different nuclear reactions and the χ^2/dof values for each fit. Parameter a_0 is calculated from a_1, a_2, a_3, and E_{thr} (for details see Section 4.4).

parameter	^{43}Ca(p,n)^{43}Sc Figure 4.30	^{44}Ca(p,n)^{44g}Sc Figure 4.31	^{44}Ca(p,n)^{44m}Sc Figure 4.32	^{48}Ca(p,2n)^{47}Sc Figure 4.33	^{48}Ca(p,n)^{48}Sc Figure 4.34
E_{thr} [MeV]	3.07	4.54	4.81	8.93	theory: 0.51 adopted: 3.0
a_1 [MeV]	10(2)	8.8(6)	13.7(7)	14.7(9)	8.0(8)
a_2 [MeV]	4.5(6)	4.8(1.0)	7.0(1)	9.05(0.14)	4.2(7)
a_3 [MBq/µA/h/MeV^2]	7.1(9)	24.5(1.2)	0.075(3)	1.57(6)	2.5(2)
a_0 [MBq/µA/h]	348	952	6.82	169	79.4
χ^2/dof	1.30	0.57	6.11	1.05	1.79

List of Abbreviations

ARRONAX	**A**ccelerator for **R**esearch in **R**adiochemistry and **O**ncology at **N**antes **A**tlantique
CN	**C**ompound **N**ucleus
CT	**C**omputed **T**omography
dof	**d**egrees **o**f **f**reedom
EANM	**E**uropean **A**ssociation of **N**uclear **M**edicine
EC	**E**lectron **C**apture
EMG	**E**xperimentally **M**odified **G**aussian
EOB	**E**nd **O**f **B**ombardment
GGD	**G**eneralized **G**aussian **D**istribution
GUI	**G**raphical **U**ser **I**nterface
HIL	**H**eavy **I**on **L**aboratory
HPGe	**H**yper-**P**ure **Ge**rmanium
IAEA	**I**nternational **A**tomic **E**nergy **A**gency
IT	**I**someric **T**ransition
LET	**L**inear **E**nergy **T**ransfer
LINAC	**Lin**ear Energy **Ac**celerator
LOR	**L**ine **O**f **R**esponse
MDA	**M**inimum **D**etectable **A**ctivity
MEMRI	**M**anganese-**E**nhanced **M**agnetic **R**esonance **I**maging
MRI	**M**agnetic **R**esonance **I**maging
NCNR	**N**ational **C**entre for **N**uclear **R**esearch
OS	**O**perating **S**ystem
PET	**P**ositron **E**mission **T**omography
QCD	**Q**uantum **C**hromo**d**ynamics
RYC	**R**adionuclide **Y**ield **C**alculator
SA	**S**pecific **A**ctivity
SPECT	**S**ingle-**P**hoton **E**mission **C**omputed **T**omography
STD	**St**andard **D**eviation
TENDL	**T**ALYS-based **E**valuated **N**uclear **D**ata **L**ibrary
TTY	**T**hick **T**arget **Y**ield
TY	**T**arget **Y**ield

List of Symbols

a_i	i-th coefficient of TTY_{fit}	
A	atomic mass number	
A_0	activity at the beginning of measurement	[Bq]
A_{cal}	activity of calibration source	[Bq]
$A_{EOB}(t_{irr})$	activity at EOB after t_{irr} irradiation	[Bq]
$A_i(t)$	activity of radioisotope i at time t	[Bq]
A_{sat}	saturation activity	[Bq/A]
b_i	i-th coefficient (energy calibration)	
c_i	i-th coefficient (efficiency calibration)	
C	number of analyser's channel	
d	thickness, range of projectile	[cm]
$\mathrm{d}E/\mathrm{d}x$	stopping-power	$[\mathrm{MeV} \cdot (\mathrm{g/cm^2})^{-1}]$
E	projectile energy	[MeV]
E_{max}	maximal/initial energy of the projectile	[MeV]
E_{thr}	reaction threshold energy	[MeV]
E_0	energy of the projectile leaving the target	[MeV]
E_γ	energy of γ quanta	[keV]
f_p	flux	$[\mathrm{s^{-1}}]$
f_s	flux per surface unit	$[\mathrm{s^{-1} \cdot cm^{-2}}]$
F_e	electromagnetic force	[N]
H	target enrichment	
I	beam current (intensity)	[A = "eA"]
I_{av}	average ionization potential	[eV]
I_{par}	particle beam current	["pA"]
I_γ	γ decay intensity	
k	wavenumber	$[\mathrm{m^{-1}}]$
L	angular momentum	$[\hbar]$
m	mass	[g]
M	molar mass	[g/mol]
MDA	Minimum Detectable Activity	[Bq]
n_i	number of nuclei i per unit mass	$[\mathrm{g^{-1}}]$
n_e	number of electrons per unit mass	$[\mathrm{g^{-1}}]$

N	number of neutrons	
N_{bg}	number of background counts	
N_{dec}	number of decays	
$N_{dec,obs}$	number of observed decays	
$N_i(t)$	number of nuclei i at moment t	
$N_i(t_{irr})$	number of nuclei i after t_{irr} irradiation	
N_{stab}	number of stable nuclei in target	
$\mathcal{N}$	number of nuclei per unit area	$[\mathrm{cm}^{-2}]$
P	probability	
q	electrical charge	[C]
Q	reaction Q-value	[MeV]
r	distance of interaction	[fm]
$\vec{r}$	position	[m]
$r_\sigma(E)$	cross-section ratio	
R	rate of nuclear reactions	$[\mathrm{s}^{-1}]$
S	area	$[\mathrm{cm}^2]$
SA	specific activity	[Bq/mol]
t	time	[s]
t_{irr}	irradiation time	[s]
t_{mes}	time of the measurement	[s]
Δt	time between EOB and measurement	[s]
$T_{1/2}$	half-life	[s]
TY	Target Yield (production yield)	$[\mathrm{Bq} \cdot (\mathrm{A} \cdot \mathrm{s})^{-1}]$
TTY	Thick Target Yield (production yield)	$[\mathrm{Bq} \cdot (\mathrm{A} \cdot \mathrm{s})^{-1}]$
TTY_{fit}	Thick Target Yield (fit function)	$[\mathrm{Bq} \cdot (\mathrm{A} \cdot \mathrm{s})^{-1}]$
TTY_0	production rate of stable product	$[(\mathrm{A} \cdot \mathrm{s})^{-1}]$
v_p	speed of projectile	[m/s]
V	interaction potential	[MeV]
$W(t)$	amount of isotopes at time t	[mol]
x	thickness, range of projectile	$[\mathrm{g/cm}^2]$
X	isotope (ground state)	
X^*	isotope (excited state)	
Z	atomic number	
Z_p	atomic number of the projectile	
Z_t	atomic number of the target material	
$\epsilon(E_\gamma)$	detector efficiency	
θ	scattering angle	[rad]
λ	decay probability (decay constant)	$[\mathrm{s}^{-1}]$
ρ	density	$[\mathrm{g/cm}^3]$

σ	reaction cross-section	[mb = 10^{-27} cm^2]
σ_M	monitor reaction cross-section	[mb = 10^{-27} cm^2]
τ	mean life-time	[s]
χ^2	Pearson's chi-squared variable	
ψ	wave function	
Ω	solid angle	[sr]

Physical Constants

Avogadro's constant	N_A	$= 6.022\,140\,86 \times 10^{23}\ \mathrm{mol}^{-1}$
elementary charge	e	$= 1.602\,176\,62 \times 10^{-19}\ \mathrm{C}$
mass of electron	m_e	$= 0.510\,998\,946\,1\ \mathrm{MeV/c^2}$
mass of neutron	m_n	$= 939.565\,413\,3\ \mathrm{MeV/c^2}$
mass of proton	m_p	$= 938.272\,081\,3\ \mathrm{MeV/c^2}$
Planck's constant (reduced)	$\hbar$	$= 6.582\,119\,514 \times 10^{-16}\ \mathrm{eV \cdot s}$
speed of light	c	$= 2.997\,924\,58 \times 10^{8}\ \mathrm{m/s}$

List of Figures

List of Tables

Bibliography

[1] Popper, K.R. *The Open Society and Its Enemies*. Vol. 1. London: Routledge, 1945.

[2] Gill, M., Livens, F., and Peakman, A. "Chapter 9 - Nuclear Fission". In: *Future Energy*. Ed. by Trevor M. Letcher. 2nd ed. Boston: Elsevier, 2014, pp. 181 –198. DOI: 10.1016/B978-0-08-099424-6.00009-0.

[3] Carlson, S. "A Glance At The History Of Nuclear Medicine". In: *Acta Oncologica* 34.8 (1995), pp. 1095–1102. DOI: 10.3109/02841869509127236.

[4] Jaszczak, R.J. "The early years of single photon emission computed tomography (SPECT): an anthology of selected reminiscences". In: *Physics in Medicine and Biology* 51.13 (2006), R99–R115. DOI: 10.1088/0031-9155/51/13/R07.

[5] Editors of Encylopaedia Britannica. *Nuclear Medicine*. URL: https://www.britannica.com/science/nuclear-medicine (visited on 03/25/2019).

[6] World Health Organization. *Cancer*. URL: https://www.who.int/news-room/fact-sheets/detail/cancer (visited on 03/25/2019).

[7] World Nuclear Association. *Radioisotopes in Medicine*. URL: http://www.world-nuclear.org/information-library/non-power-nuclear-applications/radioisotopes-research/radioisotopes-in-medicine.aspx (visited on 03/25/2019).

[8] International Atomic Energy Agency. *Research Reactor Database*. URL: https://nucleus.iaea.org/RRDB/Content/Util/IsoTopes.aspx (visited on 03/25/2019).

[9] Paul-Emmanuel Goethals. *A directory covering over 1,200 medical cyclotrons worldwide*. URL: https://www.linkedin.com/pulse/directory-covering-over-1200-medical-cyclotrons-goethals (visited on 03/25/2019).

[10] Disselhorst, J.A., Bezrukov, I., Kolb, A., Parl, C., and Pichler, B.J. "Principles of PET/MR Imaging". In: *Journal of Nuclear Medicine* 55 (2004), 2S.

[11] Broski, S.M., Goenka, A.H., Kemp, B.J., and Johnson, G.B. "Clinical PET/MRI: 2018 Update". In: *American Journal of Roentgenology* 211.2 (2018), pp. 295–313. DOI: 10.2214/AJR.18.20001.

[12] Buck, A.K., Herrmann, K., Stargardt, T., Dechow, T., Joachim Krause, B., and Schreyögg, J. "Economic Evaluation of PET and PET/CT in Oncology: Evidence and Methodologic Approaches". In: *Journal of Nuclear Medicine Technology* 38.1 (Mar. 2010), pp. 6–17. DOI: 10.2967/jnmt.108.059584.

[13] Arruebo, M., Vilaboa, N., Sáez-Gutierrez, B., Lambea, J., Tres, A., Valladares, M., and González-Fernández, Á. "Assessment of the Evolution of Cancer Treatment Therapies". In: *Cancers* 3.3 (2011), pp. 3279–3330. DOI: 10.3390/cancers3033279.

[14] Modo, M. and Bulte, J. *Design and Applications of Nanoparticles in Biomedical Imaging*. Springer International Publishing, 2017. DOI: 10.1007/978-3-319-42169-8.

[15] Vouche, M., Vanderlinden, B., Delatte, P., Lemort, M., Hendlisz, A., Deleporte, A., Guiot, T., Garcia, C., and Flamen, P. "New Imaging Techniques for ^{90}Y Microsphere Radioembolization". In: *Journal of Nuclear Medicine & Radiation Therapy* 2.1 (2011), pp. 1–12. DOI: 10.4172/2155-9619.1000113.

[16] Navarro-Teulon, I., Lozza, C., Pèlegrin, A., Vivès, E., and Pouget, J.-P. "General overview of radioimmunotherapy of solid tumors". In: *Immunotherapy* 5.5 (2013), pp. 467–487. DOI: 10.2217/imt.13.34.

[17] Bayat Mokhtari, R., Homayouni, T.S., Baluch, N., Morgatskaya, E., Kumar, S., Das, B., and Yeger, H. "Combination therapy in combating cancer". In: *Oncotarget* 8.23 (2017), pp. 38022–38043. DOI: 10.18632/oncotarget.16723.

[18] Qaim, S. "Nuclear data for medical applications: An overview of present status and future needs". In: *EPJ Web of Conferences* 146 (Jan. 2017), p. 08001. DOI: 10.1051/epjconf/201714608001.

[19] *Nuclear Data for the Production of Therapeutic Radionuclides*. Technical Reports Series 473. Vienna: International Atomic Energy Agency, 2012. ISBN: 978-92-0-115010-3. URL: https://www.iaea.org/publications/8522/nuclear-data-for-the-production-of-therapeutic-radionuclides.

[20] Cancer Research UK. *Worldwide cancer statistics*. URL: https://www.cancerresearchuk.org/health-professional/cancer-statistics/worldwide-cancer (visited on 03/25/2019).

[21] Ishii, N., Aoki, S., and Hatsuda, T. "Nuclear force from lattice QCD". In: *Physical review letters* 99 (July 2007), p. 022001. DOI: 10.1103/PHYSREVLETT.99.022001.

[22] Choppin, G., Liljenzin, J.-O., Rydberg, J., and Ekberg, C. *Radiochemistry and Nuclear Chemistry*. 4th ed. Springer International Publishing, 2013. ISBN: 978-0-12-405897-2. DOI: 10.1016/C2011-0-07260-5.

[23] National Nuclear Data Center. *Interactive Chart of Nuclides*. URL: https://www.nndc.bnl.gov/nudat2/ (visited on 04/07/2019).

[24] Koning, A.J. and Rochman, D. "Modern Nuclear Data Evaluation with The TALYS Code System". In: *Nuclear Data Sheets* 113 (2012), pp. 2841–2934. DOI: 10.1016/j.nds.2012.11.002.

[25] Herman, M., Capote, R., Carlson, B.V., Obložinský, P., Sin, M., Trkov, A., Wienke, H., and Zerkin, V. "EMPIRE: Nuclear Reaction Model Code System for Data Evaluation". In: *Nuclear Data Sheets* 108.12 (2007). Special Issue on Evaluations of Neutron Cross Sections, pp. 2655 –2715. DOI: 10.1016/j.nds.2007.11.003.

[26] Koning, A.J., Hilaire, S., and Duijvestijn, M.C. "TALYS: Comprehensive Nuclear Reaction Modeling". In: *AIP Conference Proceedings* 769.1 (2005), pp. 1154–1159. DOI: 10.1063/1.1945212.

[27] Bertulani, C.A. "Nuclear Reactions". In: *eprint arXiv:0908.3275*. Aug. 2009. URL: https://arxiv.org/abs/0908.3275.

[28] Choppin, G.., Rydberg, J., and Liljenzin, J.-O. *Radiochemistry and Nuclear Chemistry*. Elsevier Science, 2001. ISBN: 9780080515663.

[29] Lebeda, O. and Pruszyński, M. "New measurement of excitation functions for (p,x) reactions on ^{nat}Mo with special regard to the formation of ^{95m}Tc, $^{96m+g}$Tc, ^{99m}Tc and ^{99}Mo". In: *Applied Radiation and Isotopes* 68 (Dec. 2010), pp. 2355–2365. DOI: 10.1016/j.apradiso.2010.05.011.

[30] Qaim, S., Sudar, S., Scholten, B., Koning, A., and Coenen, H.H. "Evaluation of excitation functions of ^{100}Mo(p,d+pn)^{99}Mo and ^{100}Mo(p,2n)^{99m}Tc reactions: Estimation of long-lived Tc-impurity and its implication on the specific activity of cyclotron-produced ^{99m}Tc". In: *Applied Radiation and Isotopes* 85 (Jan. 2014), pp. 101–113. DOI: 10.1016/j.apradiso.2013.10.004.

[31] S. Naeem Ahmed. "Interaction of radiation with matter". In: *Physics and Engineering of Radiation Detection*. Ed. by Naeem Ahmed, S. 2nd ed. Elsevier, 2015, pp. 65 –155. ISBN: 978-0-12-801363-2. DOI: 10.1016/B978-0-12-801363-2.00002-4.

[32] Ziegler, J.F., Ziegler, M.D., and Biersack, J.P. *SRIM Code, Version 2008.04*. URL: http://www.srim.org/ (visited on 01/21/2019).

[33] Cirrone, P., Cuttone, G., Lojacono, P.A., Nigro, S., Mongelli, V., Patti, I., Privitera, G., Raffaele, L., Rifuggiato, D., Sabini, M.G., Salamone, V., Spatola, C., and Valastro, L. "A 62 MeV proton beam for the treatment of ocular melanoma at Laboratori Nazionali del Sud-INFN". In: *IEEE Transactions on Nuclear Science* 51 (July 2004), pp. 860 –865. DOI: 10.1109/TNS.2004.829535.

[34] Hubbell, J.H., Gimm, H.A., and Øverbø, I. "Pair, Triplet, and Total Atomic Cross Sections (and Mass Attenuation Coefficients) for 1 MeV-100 GeV Photons in Elements Z=1 to 100". In: *Journal of Physical and Chemical Reference Data* 9.4 (1980), pp. 1023–1148. DOI: 10.1063/1.555629.

[35] Krause, M.O. "Rearrangement of Inner Shell Ionized Atoms". In: *Journal de Physique Colloques* 32.C4 (1971), pp. 67 –75. DOI: 10.1051/jphyscol:1971415.

[36] *Nuclear Medicine Physics*. Non-serial Publications. Vienna: International Atomic Energy Agency, 2015. ISBN: 978-92-0-143810-2. URL: https://www.iaea.org/publications/10368/nuclear-medicine-physics.

[37] *Cyclotron Produced Radionuclides: Principles and Practice*. Technical Reports Series 465. Vienna: International Atomic Energy Agency, 2009. ISBN: 978-92-0-100208-2. URL: https://www.iaea.org/publications/7849/cyclotron-produced-radionuclides-principles-and-practice.

[38] CBC News. *FAQ: Cyclotrons*. URL: https://www.cbc.ca/news/technology/faq-cyclotrons-1.789206 (visited on 03/08/2019).

[39] Stolarz, A. "Target preparation for research with charged projectiles". In: *Journal of Radioanalytical and Nuclear Chemistry* 299.2 (2014), pp. 913–931. DOI: 10.1007/s10967-013-2652-2.

[40] van der Meulen, N.P., Vermeulen, C., Köster, U., Johnston, K., Haller, S., Schibli, R., Türler, A., and Müller, C. "The use of ^{149}Tb and ^{152}Tb in preclinical investigations: an update on its mass separation and subsequent application for imaging and therapy". In: *Radiotherapy & Oncology* 118.S1 (2016), S106.

[41] "Chapter 1 - Radiopharmaceuticals". In: *Nuclear Medicine*. Ed. by Ziessman, H.A., O'Malley, J.P., and Thrall, J.H. 4th ed. Philadelphia: W.B. Saunders, 2014, pp. 1–15. ISBN: 978-0-323-08299-0. DOI: 10.1016/B978-0-323-08299-0.00001-8.

[42] *Clinical Applications of SPECT/CT: New Hybrid Nuclear Medicine Imaging System*. TECDOC Series 1597. Vienna: International Atomic Energy Agency, 2008. ISBN: 978-92-0-107108-8. URL: https://www.iaea.org/publications/7928/clinical-applications-of-spect/ct-new-hybrid-nuclear-medicine-imaging-system.

[43] *Quality Assurance for SPECT Systems*. Human Health Series 6. Vienna: International Atomic Energy Agency, 2009. ISBN: 978-92-0-103709-1. URL: https://www.iaea.org/publications/8119/quality-assurance-for-spect-systems.

[44] *A Guide to Clinical PET in Oncology: Improving Clinical Management of Cancer Patients*. TECDOC Series 1605. Vienna: International Atomic Energy Agency, 2008. ISBN: 978-92-0-110608-7. URL: https://www.iaea.org/publications/8015/a-guide-to-clinical-pet-in-oncology-improving-clinical-management-of-cancer-patients.

[45] Hogg, P. and Testanera, G., eds. *Principles and Practice of PET/CT Part 1*. A Technologist's Guide. Vienna: European Association of Nuclear Medicine, 2010. URL: https://www.eanm.org/publications/technologists-guide/principles-practice-petct-part-1/.

[46] Testanera, G. and van den Broek, W.J.M., eds. *Principles and Practice of PET/CT Part 2*. A Technologist's Guide. Vienna: European Association of Nuclear Medicine, 2011. URL: https://www.eanm.org/publications/technologists-guide/principles-practice-petct-part-2/.

[47] Moskal, P., Kisielewska, D., Curceanu, C., Czerwiński, E., Dulski, K., Gajos, A., Gorgol, M., Hiesmayr, B., Jasińska, B., Kacprzak, K., Kapłon, Ł., Korcyl, G., Kowalski, P., Krzemień, W., Kozik, Y., Kubicz, E., Mohammed, M., Niedźwiecki, Sz., Pałka, M., Pawlik-Niedźwiecka, M., Raczyński, L., Raj, J., Sharma, S., Shivani, Shopa, R.Y., Silarski, M., Skurzok, M., Stępień, E., Wiślicki, W., and Zgardzińska, B. "Feasibility study of the positronium imaging with the J-PET tomograph". In: *Physics in Medicine and Biology* 64.5 (2019), p. 055017. DOI: 10.1088/1361-6560/aafe20.

[48] *Radiation Oncology Physics*. Non-serial Publications. Vienna: International Atomic Energy Agency, 2005. ISBN: 92-0-107304-6. URL: https://www.iaea.org/publications/7086/radiation-oncology-physics.

[49] *Nuclear Medicine Resources Manual*. Non-serial Publications. Vienna: International Atomic Energy Agency, 2006. ISBN: 92-0-107504-9. URL: https://www.iaea.org/publications/7038/nuclear-medicine-resources-manual.

[50] Rep, S., Santos, A., and Testanera, G., eds. *Radiation Protection and Dose Optimisation*. A Technologist's Guide. Vienna: European Association of Nuclear Medicine, 2016. ISBN: 978-3-902785-12-1. URL: https://www.eanm.org/publications/technologists-guide/radiation-protection-dose-optimisation/.

[51] Ersahin, D., Doddamane, I., and Cheng, D. "Targeted Radionuclide Therapy". In: *Cancers* 3.4 (2011), pp. 3838–3855. DOI: 10.3390/cancers3043838.

[52] European Medicines Agency. *Lutathera*. URL: https://www.ema.europa.eu/en/medicines/human/EPAR/lutathera (visited on 06/16/2019).

[53] Herzog, H., Rösch, F., Stöcklin, G., Lueders, C., Qaim, S.M., and Feinendegen, L.E. "Measurement of Pharmacokinetics of Yttrium-86 Radiopharmaceuticals with PET and Radiation Dose Calculation of Analogous Yttrium-90 Radiotherapeutics". In: *Journal of Nuclear Medicine* 34.12 (1993), pp. 2222–2226.

[54] Rösch, F. and Baum, R.P. "Generator-based PET radiopharmaceuticals for molecular imaging of tumours: on the way to theranostics". In: *Dalton Transactions* 40 (Mar. 2011), pp. 6104–6111. DOI: 10.1039/c0dt01504k.

[55] Srivastava, S.C. "A Bridge not too Far: Personalized Medicine with the use of Theragnostic Radiopharmaceuticals". In: *Journal of Postgraduate Medicine, Education and Research* 47.1 (2013), pp. 31–46. DOI: 10.5005/jp-journals-10028-1054.

[56] Müller, C., Zhernosekov, K., Köster, U., Johnston, K., Dorrer, H., Hohn, A., van der Walt, N.T., Türler, A., and Schibli, R. "A Unique Matched Quadruplet of Terbium Radioisotopes for PET and SPECT and for α- and β^- -Radionuclide Therapy: An In Vivo Proof-of-Concept Study with a New Receptor-Targeted Folate Derivative". In: *Journal of Nuclear Medicine* 53.12 (2012), p. 1951.

[57] Engle, J.W., Mashnik, S.G., Parker, L.A., Jackman, K.R., Bitteker, L.J., Ullmann, J.L., Gulley, M.S., Pillai, C., John, K.D., Birnbaum, E.R., and Nortier, F.M. "Nuclear excitation functions from 40 to 200 MeV proton irradiation of terbium". In: *Nuclear Instruments and Methods in Physics Research Section B: Beam Interactions with Materials and Atoms* 366 (2016), p. 206.

[58] Vermeulen, C., Steyn, G.F., Szelecsényi, F., Kovács, Z., Suzuki, K., Nagatsu, K., Fukumura, T., Hohn, A., and van der Walt, T.N. "Cross sections of proton-induced reactions on ^{nat}Gd with special emphasis on the production possibilities of ^{152}Tb and ^{155}Tb". In: *Nuclear Instruments and Methods in Physics Research Section B: Beam Interactions with Materials and Atoms* 275 (2012), p. 24.

[59] Tárkányi, F., Takács, S., Ditrói, F., Csikai, J., Hermanne, A., and Ignatyuk, A.V. "Activation cross-sections of deuteron induced reactions on ^{nat}Gd up to 50 MeV". In: *Applied Radiation and Isotopes* 83 (2014), p. 25.

[60] Sarkar, S., Allen, B., Imam, S., Goozee, G., Leigh, J., and Meriaty, H. "Production and Separation of Terbium-149,152 for Targeted Cancer Therapy". In: *Second international conference on isotopes. Conference proceedings*. Ed. by C.J. Hardy. 1991.

[61] Allen, B.J., Goozee, G., Sarkar, S., Beyer, G., Morel, C., and Byrne, A.P. "Production of terbium-152 by heavy ion reactions and proton induced spallation". In: *Applied Radiation and Isotopes* 54 (2001), p. 53.

[62] Formento Cavaier, R., Haddad, F., Sounalet, T., Stora, T., Zahi, I., and MEDICIS-PROMED collaboration. "Terbium Radionuclides for Theranostics Applications: A Focus On MEDICIS-PROMED". In: *Physics Procedia* 90 (2017), p. 157.

[63] Jalilian, A.R. and Osso Jr, J. "The current status and future of theranostic Copper-64 radiopharmaceuticals". In: *Iranian Journal of Nuclear Medicine* 25.1 (2017), pp. 1–10.

[64] Boschi, A., Martini, P., Janevik-Ivanovska, E., and Duatti, A. "The emerging role of copper-64 radiopharmaceuticals as cancer theranostics". In: *Drug Discovery Today* 23.8 (2018), pp. 1489–1501. DOI: 10.1016/j.drudis.2018.04.002.

[65] Gutfilen, B., Al Souza, S., and Valentini, G. "Copper-64: a real theranostic agent". In: *Drug Design, Development and Therapy* 12 (2018), pp. 3235–3245. DOI: 10.2147/DDDT.S170879.

[66] Pupillo, G., Sounalet, T., Michel, N., Mou, L., Esposito, J., and Haddad, F. "New production cross sections for the theranostic radionuclide ^{67}Cu". In: *Nuclear Instruments and Methods in Physics Research Section B: Beam Interactions with Materials and Atoms* 415 (2018), pp. 41 –47. DOI: 10.1016/j.nimb.2017.10.022.

[67] Bailey, D., Schembri, G., Willowson, K., Hedt, A., Lengyelova, E., and Harris, M. "A Novel Theranostic Trial Design Using ^{64}Cu/^{67}Cu with Fully 3D Pre-Treatment Dosimetry". In: *Journal of Nuclear Medicine* 60.supplement 1 (2019), p. 204.

[68] Choiński, J., Jastrzębski, J., Kilian, K., Mazur, I., Napiorkowski, P.J., Pękal, A., and Szczepaniak, D. "The Radiopharmaceuticals Production and Research Centre established by the Heavy Ion Laboratory of the University of Warsaw". In: *EPJ Web of Conferences* 66 (2014), p. 10003. DOI: 10.1051/epjconf/20146610003.

[69] Poirier, F., Girault, S., Auduc, S., Huet, C., Mace, E., Delvaux, J.L., and Haddad, F. "The C70 ARRONAX and Beam Lines Status". In: *Conference Proceedings* C110904 (2011), pp. 2661–2663.

[70] Marti, F. "Cyclotrons and their applications. Proceedings, 16th International Conference, Cyclotrons 2001, East Lansing, USA, May 13-17, 2001". In: *AIP Conference Proceedings* 600 (2001), p. 513.

[71] Debertin, K. and Helmer, R.G. *Gamma- and X-ray spectrometry with semiconductor detectors*. Netherlands: Elsevier, 1988. ISBN: 978-0444871077.

[72] International Atomic Energy Agency. *Live Chart of Nuclides*. URL: https://www-nds.iaea.org/relnsd/vcharthtml/VChartHTML.html (visited on 01/21/2019).

[73] Knoll, G.F. *Radiation Detection and Measurement*. 4th ed. New York: Wiley, 2010. ISBN: 978-0-470-13148-0.

[74] International Atomic Energy Agency. *Monitor Reactions*. URL: https://www-nds.iaea.org/medical/monitor_reactions.html (visited on 01/21/2019).

[75] Hermanne, A., Ignatyuk, A.V., Capote, R., Carlson, B.V., Engle, J.W., Kellett, M.A., Kibédi, T., Kim, G., Kondev, F.G., Hussain, M., Lebeda, O., Luca, A., Nagai, Y., Naik, H., Nichols, A.L., Nortier, F.M., Suryanarayana, S.V., Takács, S., Tárk'anyi, F.T., and Verpelli, M. "Reference Cross Sections for Charged-particle Monitor Reactions". In: *Nuclear Data Sheets* 148 (2018). Special Issue on Nuclear Reaction Data, pp. 338 –382. DOI: 10.1016/j.nds.2018.02.009.

[76] Piel, H., Qaim, S.M., and Stöcklin, G. "Excitation Functions of (p,xn)-Reactions on ^{nat}Ni and Highly Enriched ^{62}Ni: Possibility of Production of Medically Important Radioisotope ^{62}Cu at a Small Cyclotron". In: *Radiochimica Acta* 57.1 (1992), pp. 1–6. DOI: 10.1524/ract.1992.57.1.1.

[77] Subramanian, G., McAfee, J.G., and Poggenburg, J.K. "Ruthenium-97: A preliminary evaluation of a new radionuclide for use in nuclear medicine". In: *Journal of Nuclear Medicine* 11 (1970), p. 365.

[78] Maiti, M. and Lahiri, S. "Measurement of yield of residues produced in ^{12}C+^{nat}Y reaction and subsequent separation of ^{97}Ru from Y target using cation exchange resin". In: *Radiochimica Acta* 103 (2015), pp. 7–13.

[79] Tárkányi, F., Hermanne, A., Ditrói, F., Takács, S., and Ignatyuk, A. "Investigation of activation cross section data of alpha particle induced nuclear reaction on molybdenum up to 40 MeV: Review of production routes of medically relevant ^{97,103}Ru". In: *Nuclear Instruments and Methods in Physics Research Section B: Beam Interactions with Materials and Atoms* 399 (2017), pp. 83–100.

[80] Zaitseva, N.G., Stegailov, V.I., Khalkin, V.A., Shakun, N.G., and Shishlyannikow, P.T.; Bukow, K.G. "Metal Technetium Target and Target Chemistry for the Production of ^{97}Ru via the ^{99}Tc(p,3n)^{97}Ru Reaction." In: *Applied Radiation and Isotopes* 47 (1996), pp. 145–151.

[81] Mukhopadhyay, B. and Mukhopadhyay, K. "Applications of the Carrier Free Radioisotopes of Second Transition Series Elements in the Field of Nuclear Medicine". In: *Journal of Nuclear Medicine and Radiation Therapy* 2 (2011), p. 1000115.

[82] Shao, H.S., Meinken, G.E., Srivastava, S.C., Slosman, D., Sacker, D.F., Sore, P., and Brill, A.B. "In vitro and in vivo characterization of ruthenium bleomycin compared to cobalt- and copper-bleomycin". In: *Journal of Nuclear Medicine* 27 (1986), p. 1044.

[83] Clarke, M.J. "Ruthenium in Cancer Chemotherapy". In: *Platinum Metals Review* 32 (1988), p. 198.

[84] Ku, T.H., Richards, P., Srivastava, S.C., Prach, T., and Stang, L.G.Jr. "Production of ruthenium-97 for medical applications". In: *Proceedings of the 2nd International Congress of the World Federation of Nuclear Medicine and Biology, Washington, DC, USA,* 1979.

[85] Lagunas-Solar, M.C., Avila, M.J., Navarro, N.L., and Johnson, P.C. "Cyclotron Production of No-carrier-added ^{97}Ru by Proton Bombardment of ^{103}Rh Targets". In: *Applied Radiation and Isotopes* 34 (1983), pp. 915–922.

[86] Lebowitz, E., Kinsley, M., Klotz, P., Bachsmith, C., Ansari, A., and Richards, P.; Atkins, H.L. "Development of ^{97}Ru and ^{67}Cu for medical use". In: *Journal of Nuclear Medicine* 15 (1974), p. 511.

[87] Zaitseva, N.G., Rurarz, E., Vobecký, M., Hwan, K.H., Nowak, K., Téthal, T., Khalkin, V.A., and Popinenkova, L.M. "Excitation function and yield for ^{97}Ru production in ^{99}Tc(p,3n)^{97}Ru reaction in 20–100 MeV proton energy range". In: *Radiochimica Acta* 56 (1992), pp. 59–68.

[88] Dmitriev, S.N., Zaitseva, N.G., Starodub, G.Y., Maslov, O.D., Shishkin, S.V., and Shishkina, T.V. "High-purity radionuclide production: Material, construction, target chemistry for ^{26}Al, ^{97}Ru, ^{178}W, ^{235}Np, ^{236,237}Pu". In: *Nuclear Instruments and Methods in Physics Research Section A: Accelerators, Spectrometers, Detectors and Associated Equipment* 397 (1997), pp. 125–130.

[89] Uddin, M.S., Hagiwara, M., Baba, M., and Tárkányi, F. "Experimental studies on excitation functions of the proton-induced activation reactions on silver". In: *Applied Radiation and Isotopes* 62 (2005), pp. 533–540.

[90] Ditrói, F., Tárkányi, F., Takács, S., Mahunka, I., Csikai, J., Hermanne, A., Uddin, M.S., Hagiwara, M., Baba, M., Ido, T., Shubin, Y., and Dityuk, A.I. "Measurement of activation cross sections of the proton induced nuclear reactions on palladium". In: *Journal of Radioanalytical and Nuclear Chemistry* 272 (2007), 231–235.

[91] Mito, A., Komura, K., Mitsugashira, T., and Otozai, K. "Excitation functions for the (d, p) reactions on ^{96}Ru, ^{102}Ru and ^{104}Ru". In: *Nuclear Physics A* 129 (1969), pp. 165–171.

[92] Comparetto, G. and Qaim, S. "A Comparative Study of the Production of Short-Lived Neutron Deficient Isotopes ^{94,95,97}Ru in α- and ^{3}He-Particle Induced Nuclear Reactions on Natural Molybdenum". In: *Radiochimica Acta* 27 (1980), pp. 177–180.

[93] Maiti, M. and Lahiri, S. "Production and separation of ^{97}Ru from ^{7}Li activated natural niobium". In: *Radiochimica Acta* 99 (2011), pp. 359–364.

[94] Maiti, M. "Production and separation of ^{97}Ru and coproduced ^{95}Tc from ^{12}C-induced reaction on yttrium target". In: *Radiochimica Acta* 101 (2013), 437–444.

[95] Levkovskij, V.N. *Cross-section of medium mass nuclide activation (A=40-100) by medium energy protons and alpha-particles (E=10-50 MeV)*. Moscow: Inter-Vesi, 1991.

[96] Ditrói, F., Hermanne, A., Tárkányi, F., Takács, S., and Ignatyuk, A.V. "Investigation of the α-particle induced nuclear reactions on natural molybdenum". In: *Nuclear Instruments and Methods in Physics Research Section B: Beam Interactions with Materials and Atoms* 285 (2012), pp. 125–141.

[97] Sitarz, M., Nigron, E., Guertin, A., Haddad, F., and Matulewicz, T. "New Cross-Sections for ^{nat}Mo(α,x) Reactions and Medical ^{97}Ru Production Estimations with Radionuclide Yield Calculator". In: *Instruments* 3.1 (Jan. 2019), p. 7. DOI: 10.3390/instruments3010007.

[98] Zanzi, I., Srivastava, S.C., Meinken, G.E., Robeson, W., Mausner, L.F., Fairchild, R.G., and Margouleff, D. "A New Cholescintigraphic Agent: Ruthenium-97-DISIDA". In: *Nuclear Medicine and Biology* 16 (1989), pp. 397–403.

[99] Brooks, R.C., Carnochan, P., Vollano, J.F., Powell, N.A., Zweit, J., Sosabowski, J.K., Martellucci, S., Darkes, M.C., Fricker, S.P., and Murrer, B.A. "Metal complexes of bleomycin: evaluation of [Rh-105]–bleomycin for use in targeted radiotherapy". In: *Nuclear Medicine and Biology* 26.4 (1999), pp. 421–430.

[100] Jurisson, S.S., Ketring, A.L., and Volkert, W.A. "Rhodium-105 complexes as potential radiotherapeutic agents". In: *Transition Metal Chemistry* 22 (1997), p. 315.

[101] Carroll, V., Demoin, D.W., Hoffman, T.J., and Jurisson, S.S. "Inorganic chemistry in nuclear imaging and radiotherapy: current and future directions". In: *Radiochimica Acta* 100.8–9 (2012), p. 653.

[102] Grazman, B. and Troutner, B.E. "^{105}Rh as a Potential Radiotherapeutic Agent". In: *Applied Radiation and Isotopes* 39.3 (1988), p. 257.

[103] Ando, A., Ando, I., Tonami, N., Kinuya, S., Okamoto, N., Sugimoto, M., Fukuda, N., and Matsumoto, S. "Production of ^{105}Rh-EDTMP and its bone accumulation". In: *Applied Radiation and Isotopes* 52 (2000), p. 211.

[104] Jia, W., Ma, D., Volkert, E.W., Ketring, A.R., Ehrhardt, G.J., and Jurisson, S.S. "Production of No-Carrier-Added ^{105}Rh from Neutron Irradiated Ruthenium Target". In: *Platinum Metals Review* 44.2 (2000), p. 50.

[105] Khandaker, M.U., Kim, K., Lee, M., Cho, Y.-S, Lee, Y.-O., and Kim, G. "Cyclotron production of the ^{105}Rh radionuclide from natural palladium". In: *Transactions of the Korean Nuclear Society Spring Meeting (Gyeongju, Korea, May 29-30, 2008)*. 2008, p. 147.

[106] Khandaker, M.U., Kim, K, and Kim, G. "Production parameters of the therapeutic ^{105}Rh radionuclide using medium energy cyclotron". In: *Pramana* 79.2 (2012), p. 243.

[107] Khandaker, M.U., Kim, K., Kim, G., and Otuka, N. "Cyclotron production of the 105,106mAg, 100,101Pd, 100,101m,105Rh radionuclides by natPd(p,x) nuclear processes". In: *Nuclear Instruments and Methods in Physics Research Section B: Beam Interactions with Materials and Atoms* 268 (2010), p. 2303.

[108] Tárkányi, F., Ditrói, F., Takács, S., Csikai, J., Hermanne, A., Uddind, S., and Baba, M. "Activation cross sections of proton induced nuclear reactions on palladium up to 80 MeV". In: *Applied Radiation and Isotopes* 114 (2016), p. 128.

[109] Ditrói, F., Tárkányi, F., Takács, S., Hermanne, A., Ignatyuk, A.V., and Baba, M. "Activation cross-sections of deuteron induced reactions on natural palladium". In: *Nuclear Instruments and Methods in Physics Research Section B: Beam Interactions with Materials and Atoms* 270 (2012), p. 61.

[110] Krajewski, S. "Metaloorganiczne i chelatowe kompleksy $^{105/103m}$Rh jako potencjalne prekursory radiofarmaceutyków terapeutycznych". PhD thesis. Institute of Nuclear Chemistry and Technology, 2013.

[111] Bunka, M., Müller, C., Vermeulen, C., Haller, S., Türler, A., Schibli, R., and van der Meulen, N.P. "Imaging quality of ^{44}Sc in comparison with five other PET radionuclides using Derenzo phantoms and preclinical PET". In: *Applied Radiation and Isotopes* 110 (2016), p. 129.

[112] Koumarianou, E., Pawlak, D., Korsak, A., and Mikołajczak, R. "Comparison of receptor affinity of ^{nat}Sc-DOTA-TATE versus ^{nat}Ga-DOTA-TATE". In: *Nuclear Medicine Review* 14.2 (2011), p. 85.

[113] Domnanich, K.A., Müller, C., Farkas, R., Schmid, R.M., Ponsard, B., Schibli, R., Türler, A., and van der Meulen, N.P. "^{44}Sc for labeling of DOTA- and NODAGA-functionalized peptides: preclinical in vitro and in vivo investigations". In: *EJNMMI Radiopharmacy and Chemistry* 1 (2016), p. 8.

[114] Walczak, R., Krajewski, S., Szkliniarz, K., Sitarz, M., Abbas, K., Choiński, J., Jakubowski, A., Jastrzębski, J., Majkowska, A., Simonelli, F., Stolarz, A., Trzcińska, A., Zipper, W., and Bilewicz, A. "Cyclotron production of ^{43}Sc for PET imaging". In: *EJNMMI Physics* 2 (2015), p. 33. DOI: 10.1186/s40658-015-0136-x.

[115] Domnanich, K.A., Eichler, R., Müller, C., Jordi, S., Yakusheva, V., Braccini, S., Behe, M., Schibli, R., Türler, A., and van der Meulen, N.P. "Production and separation of ^{43}Sc for radiopharmaceutical purposes". In: *EJNMMI Radiopharmacy and Chemistry* 2 (2017), p. 14.

[116] Grignon, C., Barbet, J., Bardiès, M., Carlier, T., Chatal, J.F., Couturier, O., Cussonneau, J.P., Faivre, A., Ferrer, L., Girault, S., Haruyama, T., Le Ray, P., Luqiun, L., Lupone, S., Métivier, V., Morteau, E., Servagent, N., and Thers, D. "Nuclear medical imaging using $\beta^+\gamma$ coincidence from ^{44}Sc radio-nuclide with liquid xenon as detection medium". In: *Nuclear Instruments and Methods in Physics Research Section A: Accelerators, Spectrometers, Detectors and Associated Equipment* 571 (2007), p. 142.

[117] Cussonneau, J.P., Abaline, J.M., Acounis, S., Beaupère, N., Beney, J.L., Bert, J., Bouvier, S., Briend, P., Butterworth, J., Carlier, T., Chanal, H., Cherel, M., Dahoumane, M., Diglio, S., Gallego-Manzano, L., Giovagnoli, D., Idier, J., Kraeber-Bodere, F., Lefebvre, F., Lemaire, O., Le Ray, P., Manen, S., Masbou, J., Mathez, H., Morteau, E., Pillet, N., Royer, L., Staempflin, M., Stutzmann, J.S., Vandaele, R., Virone, L., Visvikis, D., Xing, Y., Zhu, Y., and Thers, D. "3γ Medical Imaging with a Liquid Xenon Compton Camera and ^{44}Sc Radionuclide". In: *Acta Physica Polonica B* 48.10 (2017), p. 1661.

[118] Gallego Manzano, L., Abaline, J.M., Acounis, S., Beaupère, N., Beney, J.L., Bert, J., Bouvier, S., Briend, P., Butterworth, J., Carlier, T., Chanal, H., Cherel, M., Cussonneau, J.P., Dahoumane, M., Diglio, S., Giovagnoli, D., Idier, J., Kraeber-Bodere, F., Lefevre, F., Lemaire, O., Le Ray, P., Manen, S., Masbou, J., Mathez, H., Morteau, E., Pillet, N., Royer, L., Staempflin, M., Stutzmann, J.S., Vandaele, R., Virone, L., Visvikis, D., Xing, Y., Zhu, Y., and Thers, D. "XEMIS2: A liquid xenon detector for small animal medical imaging". In: *Nuclear Instruments and Methods in Physics Research Section A: Accelerators, Spectrometers, Detectors and Associated Equipment* 912 (2018), p. 329.

[119] Lang, C., Habs, D., Parodi, K., and Thirolf, P.G. "Sub-millimeter nuclear medical imaging with reduced dose application in positron emission tomography using β^+ γ coincidences". In: *Journal of Instrumentation* 9 (2013), P01008.

[120] Thirolf, P.G., Lang, C., and Parodi, K. "Perspectives for highly-sensitive PET-based medical imaging using $\beta^+\gamma$ coincidences". In: *Acta Physica Polonica A* 127.5 (2015), p. 1441.

[121] Huclier-Markai, S., Kerdjoudj, R., Alliot, C., Bonraisin, A.C., Michel, N., Haddad, F., and Barbet, J. "Optimization of reaction conditions for the radiolabeling of DOTA and DOTA-peptide with $^{44m/44}$Sc and experimental evidence of the feasibility of an in vivo PET generator". In: *Nuclear Medicine and Biology* 41 (2014), e36.

[122] Alliot, C., Audouin, N., Barbet, J., Bonraisin, A.C., Bossé, V., Bourdeau, C., Bourgeois, M., Duchemin, C., Guertin, A., Haddad, F., Huclier-Markai, S., Kerdjoudj, R., Laizé, J., Métivier, V., Michel, N., Mokili, M., Pageau, M., and Vidal, A. "Is there an interest to use deuteron beams to produce non-conventional radionuclides?" In: *Frontiers in Medicine* 2 (2015), p. 31. DOI: 10.3389/fmed.2015.00031.

[123] Alliot, C., Kerdjoudj, R., Michel, N., Haddad, F., and Huclier-Markai, S. "Cyclotron production of high purity ^{44m,44}Sc with deuterons from $^{44}CaCO_3$ targets". In: *Nuclear Medicine and Biology* 42 (2015), p. 524.

[124] Duchemin, C., Guertin, A., Haddad, F., Michel, N., and Métivier, V. "Production of scandium-44m and scandium-44g with deuterons on calcium-44: cross section measurements and production yield calculations". In: *Physics in Medicine and Biology* 60 (2015), p. 6847. DOI: 10.1088/0031-9155/60/17/6847.

[125] Domnanich, K.A., Müller, C., Benešová, M., Dressler, R., Haller, S., Köster, U., Ponsard, B., Schibli, R., Türler, A., and van der Meulen, N.P. "^{47}Sc as useful β^- emitter for the radiotheragnostic paradigm: a comparative study of feasible production routes". In: *EJNMMI Radiopharmacy and Chemistry* 2 (2017), p. 5.

[126] International Atomic Energy Agency. *Therapeutic Radiopharmaceuticals Labelled with New Emerging Radionuclides (^{67}Cu, ^{186}Re, ^{47}Sc)*. URL: https://www.iaea.org/projects/crp/f22053 (visited on 05/02/2019).

[127] Müller, C., Bunka, M., Haller, S., Köster, U., Groehn, V., Bernhardt, P., van der Meulen, N.P., Türler, A., and Schibli, R. "Promising prospects for ^{44}Sc-/^{47}Sc-based theragnostics: application of ^{47}Sc for radionuclide tumor therapy in mice". In: *Journal of Nuclear Medicine* 55 (2014), p. 1658.

[128] Müller, C., Domnanich, K.A., Umbricht, C.A., and van der Meulen, N.P. "Scandium and terbium radionuclides for radiotheranostics: current state of development towards clinical application". In: *British Journal of Radiology* 91 (2018), p. 20180074.

[129] Umbricht, C.A., Benešová, M., Schmid, R.M., Türler, A., Schibli R., van der Meulen, N.P., and Müller, C. "^{44}Sc-PSMA-617 for radiotheragnostics in tandem with ^{177}Lu-PSMA-617-preclinical investigations in comparison with ^{68}Ga-PSMA-11 and ^{68}Ga-PSMA-617". In: *EJNMMI Research* 7.1 (2017), p. 9.

[130] Huclier-Markai, S., Alliot, C., Kerdjoudj, R., Mougin-Degraef, M., Chouin, N., and Haddad, F. "Promising Scandium Radionuclides for Nuclear Medicine: A Review on the Production and Chemistry up to In Vivo Proofs of Concept". In: *Cancer Biotherapy and Radiopharmaceuticals* 33.8 (2018), p. 316.

[131] Cydzik, I., Seweryn, K., Abbas, K., Simonell, F., Bulgheroni, A., and Kasperek, A. "Labelling of DOTATATE with cyclotron produced ^{44}Sc and ^{43}Sc". In: *The Quarterly Journal of Nuclear Medicine and Molecular Imaging* 56 (2012), p. 33.

[132] Krajewski, S., Cydzik, I., Abbas, K., Bulgheroni, A., Simonell, F., Majkowska-Pilip, A., and Bilewicz, A. "Simple procedure of DOTATATE labelling with cyclotron produced ^{44}Sc and ^{43}Sc". In: *Nuclear Medicine Review* 15 (2012), A27.

[133] Krajewski, S., Cydzik, I., Abbas, K., Bulgheroni, A., Simonell, F., Holzwarth, U., and Bilewicz, A. "Cyclotron production of ^{44}Sc for clinical application". In: *Radiochimica Acta* 101 (2013), p. 333.

[134] Pruszyński, M., Majkowska-Pilip, A., Loktionova, N.S., Eppard, E., and Rösch, F. "Radiolabeling of DOTATOC with the long-lived positron emitter ^{44}Sc". In: *Applied Radiation and Isotopes* 70 (2012), p. 974.

[135] Roesch, F. "Scandium-44: Benefits of a Long-Lived PET Radionuclide Available from the ^{44}Ti/^{44}Sc Generator System". In: *Current Radiopharmaceuticals* 5 (2012), p. 187.

[136] Severin, G.W., Engle, J.W., Valdovinos, H.F., Barnhart, T.E., and Nickels, R.J. "Cyclotron produced ^{44g}Sc from natural calcium". In: *Applied Radiation and Isotopes* 70 (2012), p. 1526.

[137] Müller, C., Bunka, M., Reber, J., Fischer, C., Zhernosekov, K., Türler, A., and Schibli, R. "Promises of cyclotron-produced ^{44}Sc as a diagnostic match for trivalent β^-emitters: in vitro and in vivo study of a ^{44}Sc-DOTA-folate conjugate". In: *Journal of Nuclear Medicine* 54 (2013), p. 2168.

[138] Valdovinos, H.F., Hernandez, R., Barnhart, T.E., Graves, S., Cai, W., and Nickles, R.J. "Separation of cyclotron-produced ^{44}Sc from a natural calcium target using a dipentyl pentylphosphonate functionalized extraction resin". In: *Applied Radiation and Isotopes* 95 (2015), p. 23.

[139] van der Meulen, N.P., Bunka, M., Domnanich, K.A., Müller, C., Haller, S., Vermeulen, C., Türler, A., and Schibli, R. "Cyclotron production of ^{44}Sc: from bench to bedside". In: *Nuclear Medicine and Biology* 42 (2015), p. 745.

[140] Kilian, K., Cheda, Ł., Sitarz, M., Szkliniarz, K., Choiński, J., and Stolarz, A. "Separation of ^{44}Sc from Natural Calcium Carbonate Targets for Synthesis of ^{44}Sc-DOTATATE". In: *Molecules* 23 (2018), p. 1787.

[141] Khandaker, M.U., Kim, K., Lee, M.W., Kim, K.S., Kim, G.N., Cho, Y.S., and Lee, Y.O. "Investigations of the ^{nat}Ti(p,x)^{43,44m,44g,46,47,48}Sc,^{48}V nuclear processes up to 40 MeV". In: *Applied Radiation and Isotopes* 67 (2009), p. 1348.

[142] Hernandez, R., Valdovinos, H.F., Yang, Y., Chakravarty, R., Hong, H., Barnhart, T.E., and Cai, W. "^{44}Sc: an attractive isotope for peptide-based PET imaging". In: *Molecular Pharmaceutics* 11 (2014), p. 2954.

[143] Hoehr, C., Oehlke, E., Bénard, F., Lee, C.J., Hou, X., Badesso, B., Ferguson, S., Miao, Q., Yang, H., Buckley, K., Hanemaayer, V., Zeisler, S., Ruth, T., Celler, A., and Schaffer, P. "^{44g}Sc production using a water target on a 13 MeV cyclotron". In: *Nuclear Medicine and Biology* 41 (2014), p. 401.

[144] Singh, A., Baum, R., Klette, I., van der Meulen, N., Müller, C., Türler, A., and Schibli, R. "Scandium-44 DOTATOC PET/CT: first in-human molecular imaging of neuroendocrine tumors and possible perspectives for theranostics". In: *Journal of Nuclear Medicine* 56.S3 (2015), p. 267.

[145] Carzaniga, T.S., Auger, M., Braccini, S., Bunka, M., Ereditato, A., Nesteruk, K.P., Scampoli, P., Türler, A., and van der Meulen, N. "Measurement of ^{43}Sc and ^{44}Sc production cross-section with an 18 MeV medical PET cyclotron". In: *Applied Radiation and Isotopes* 129 (2017), p. 96.

[146] Carzaniga, T.S. and Braccini, S. "Cross-section measurement of ^{44m}Sc, ^{47}Sc, ^{48}Sc and ^{47}Ca for an optimized ^{47}Sc production with an 18 MeV medical PET cyclotron". In: *Applied Radiation and Isotopes* 143 (2019), pp. 18 –23. DOI: 10.1016/j.apradiso.2018.10.015.

[147] Kuhn, S., Spahn, I., Scholten, B., Hermanne, A., and Coenen, H.H. "Production of the medically interesting radioisotopes ^{44,44m}Sc and their radioactive by-products via deuteron and alpha particle induced nuclear reactions on natural Ca and K". In: *Journal of Labelled Compounds and Radiopharmaceuticals* 56 (2013), S232.

[148] Coenen, H.H., Kuhn, S., and Spahn, I. "Development of the non-standard PET radionuclides ^{43,44g}Sc and ^{45}Ti". In: *Nuclear Medicine and Biology* 41 (2014), p. 647.

[149] Szkliniarz, K., Jastrzębski, J., Bilewicz, A., Chajduk, E., Choiński, J., Jakubowski, A., Janiszewska, Ł., Leszczuk, E., Łyczko, M., Sitarz, M., Stolarz, A., Trzcińska, A., Wąs, B., and Zipper, W. "Medical radioisotopes produced using the alpha particle beam from the Warsaw heavy ion cyclotron". In: *Acta Physica Polonica A* 127.5 (2015), p. 1471.

[150] Szkliniarz, K., Sitarz, M., Walczak, R., Jastrzębski, J., Bilewicz, A., Choiński, J., Jakubowski, A., Majkowska, A., Stolarz, A., Trzcińska, A., and Zipper, W. "Production of medical Sc radioisotopes with an alpha particle beam". In: *Applied Radiation and Isotopes* 118 (2016), p. 182.

[151] Minegishi, K., Nagatsu, K., Fukada, M., Suzuki, H., Ohya, T., and Zhang, M.-R. "Production of scandium-43 and -47 from a powdery calcium oxide target via the $^{nat/44}$Ca(α,x)-channel". In: *Applied Radiation and Isotopes* 116 (2016), p. 8.

[152] Sitarz, M., Szkliniarz, K., Jastrzębski, J., Choiński, J., Guertin, A., Haddad, F., Jakubowski, A., Kapinos, K., Kisieliński, M., Majkowska, A., Nigron, E., Rostampour, M., Stolarz, A., Trzcińska, A., Walczak, R., Wojtkowska, J., Zipper, W., and Bilewicz, A. "Production of Sc medical radioisotopes with proton and deuteron beams". In: *Applied Radiation and Isotopes* 142 (Dec. 2018), pp. 104–112.

[153] Filosofov, D.V., Loktionova, N.S., and Rösch, F. "A ^{44}Ti/^{44}Sc radionuclide generator for potential nuclear-medical application of ^{44}Sc-based PET-radiopharmaceuticals". In: *Radiochimica Acta* 98 (2010), p. 149.

[154] Pruszyński, M., Loktionova, N., Filosofov, D., and Rösch, F. "Post-elution processing of Ti-44/Sc-44 generator-derived Sc-44 for clinical application". In: *Applied Radiation and Isotopes* 68 (2010), p. 1636.

[155] Hassan, H.E., Al-Abyad, M., and Mohamed., G.Y. "Production of ^{44}Ti→^{44}Sc Generator in Comparison with Direct Routes by Cyclotrons: Cross Section Evaluation Using Nuclear Models Codes." In: *Arab Journal of Nuclear Sciences and Applications* 51.1 (2017), p. 57.

[156] Misiak, R., Walczak, R., Wąs, B., Bartyzel, M., Mietelski, J.W., and Bilewicz, A. "47Sc production development by cyclotron irradiation of 48Ca". In: *Journal of Radioanalytical and Nuclear Chemistry* 313.2 (2017), pp. 429–434. DOI: 10.1007/s10967-017-5321-z.

[157] Kolsky, K.L., Joshi, V., Mausner, L.F., and Srivastava, S.C. "Radiochemical purification of no-carrier-added scandium-47 for radioimmunotherapy". In: *Applied Radiation and Isotopes* 49 (1998), p. 1541.

[158] Mausner, L.F., Kolsky, K.L., Joshi, V., and Srivastava, S.C. "Radionuclide development at BNL for nuclear medicine therapy". In: *Applied Radiation and Isotopes* 49 (1998), p. 285.

[159] Majkowska-Pilip, A. and Bilewicz, A. "Macrocyclic complexes of scandium radionuclides as precursors for diagnostic and therapeutic radiopharmaceuticals". In: *Journal of Inorganic Biochemistry* 105.2 (2011), p. 313.

[160] Bartoś, B., Majkowska, A., Kasperek, A., Krajewski, S., Bilewicz, A. "New separation method of no-carrier-added ^{47}Sc from titanium targets". In: *Radiochimica Acta* 100 (2012), p. 457.

[161] Połosak, M., Piotrowska, A., Krajewski, S., and Bilewicz, A. "Stability of ^{47}Sc-complexes with acyclic polyamino-polycarboxylate ligands". In: *Journal of Radioanalytical and Nuclear Chemistry* 295.3 (2013), p. 1867.

[162] Habs, D. and Köster, U. "Production of medical radioisotopes with high specific activity in photonuclear reactions with γ-beams of high intensity and large brilliance". In: *Applied Physics B* 103 (2 Aug. 2011), pp. 501–519. DOI: 10.1007/s00340-010-4278-1.

[163] Mamtimin, M., Harmon, F., and Starovoitova, V. "Sc-47 production from titanium targets using electron linacs". In: *Applied Radiation and Isotopes* 102 (2015), p. 1.

[164] Rotsch, D.A., Brown, M.A., Nolen, J.A., Brossard, T., Henning, W.F., Chemerisov, S.D., Gromov, R.G., and Greene, J. "Electron linear accelerator production and purification of scandium-47 from titanium dioxide target". In: *Applied Radiation and Isotopes* 131 (2018), p. 77.

[165] Stolarz, A., Kowalska, J.A., Jastrzębski, J., Choiński, J., Sitarz, M., Szkliniarz, K., Trzcińska, A., and Zipper, W. "Targets for production of the medical radioisotopes with alpha and proton or deuteron beams". In: *AIP Conference Proceedings* 1962.1 (2018), p. 020004. DOI: 10.1063/1.5035517.

[166] Alabyad, M., Mohamed, G.Y., Hassan, H.E., Takács, S., and Ditrói, F. "Experimental measurements and theoretical calculations for proton, deuteron and α-particle induced nuclear reactions on calcium: special relevance to the production of ^{43,44}Sc". In: *Journal of Radioanalytical and Nuclear Chemistry* 316.1 (2018), pp. 119–128. DOI: 10.1007/s10967-018-5733-4.

[167] Soppera, N., Dupont, E., and Bossant, M., *JANIS Book of Proton-Induced Cross-Sections. OECD NEA Data Bank*. URL: https://www-nds.iaea.org/medical/monitor_reactions.html (visited on 08/21/2018).

[168] Nagatsu, K., Fukumura, T., Takei, M., Szelecsényi, F., Kovács, Z., and Suzuki, K. "Measurement of thick target yields of the $^{nat}S(\alpha,x)^{34m}Cl$ nuclear reaction and estimation of its excitation function up to 70 MeV". In: *Nuclear Instruments and Methods in Physics Research Section B: Beam Interactions with Materials and Atoms* 266 (2008), p. 709.

[169] Sitarz, M., Jastrzębski, J., Haddad, F., Matulewicz, T., Szkliniarz, K., and Zipper, W. "Can We Extract Production Cross-Sections from Thick Target Yield Measurements? A Case Study Using Scandium Radioisotopes". In: *Instruments* 3.2 (2019), p. 29. DOI: 10.3390/instruments3020029.

[170] Jose, K.K. and Naik, S.R. "On the q-Weibull Distribution and Its Applications". In: *Communications in Statistics - Theory and Methods* 38.6 (2009), pp. 912–926. DOI: 10.1080/03610920802322474.

[171] Python Software Foundation. *Python Programming Language, Version 2.7. 2010*. URL: https://www.python.org (visited on 01/21/2019).

[172] Singh, G., Kailas, S., Saini, S., Chatterjee, A., Balakrishnan, M., and Mehta, M.K. "Reaction $^{48}Ca(p,n)^{48}Sc$ from E(p) = 1.885 to 5.1 MeV". In: *Pramana* 19.6 (1982), p. 565.

[173] Mitchell, L.W., Anderson, M.R., Kennett, S.R., and Sargood, D.G. "Cross-sections and thermonuclear reaction rates for $^{42}Ca(p,\gamma)^{43}Sc$, $^{44}Ca(p,\gamma)^{45}Sc$, $^{44}Ca(p,n)^{44}Sc$ and $^{45}Sc(p,n)^{45}Ti$". In: *Nuclear Physics A* 380 (1982), p. 318.

[174] Zyskind, J.L., Davidson, J.M., Esat, M.T., Spear, R.H., Shapiro, M.H., Fowler, W.A., and Barnes, C.A. "Cross Section Measurements and Thermonuclear Reaction Rates for $^{48}Ca(p,\gamma)^{49}Sc$ and $^{48}Ca(p,n)^{48}Sc$". In: *Nuclear Physics A* 315 (1979), p. 430.

[175] Kennett, S.R., Switkowski, Z.E., Paine, B.M., and Sargood, D.G. "Yield Measurements in the Reactions $^{48}Ca(p,\gamma)^{49}Sc$ and $^{48}Ca(p,n)^{48}Sc$". In: *Journal of Physics G* 5 (1979), p. 339.

[176] de Waal, T.J., Peisach, M., and Pretorius, R. "Activation cross sections for proton-induced reactions on calcium isotopes up to 5.6 MeV". In: *Journal of Inorganic and Nuclear Chemistry* 33 (1971), p. 2783.

[177] Tárkányi, F.T., Ignatyuk, A.V., Hermanne, A., Capote, R., Carlson, B.V., Engle, J.W., Kellett, M.A., Kibédi, T., Kim, G.N., Kondev, F.G., Hussain, M., Lebeda, O., Luca, A., Nagai, Y., Naik, H., Nichols, A.L., Nortier, F.M., Suryanarayana, S.V., Takács, S., and Verpelli, M. "Recommended nuclear data for medical radioisotope production: diagnostic positron emitters". In: *Journal of Radioanalytical and Nuclear Chemistry* 319.2 (2019), pp. 533–666. DOI: 10.1007/s10967-018-6380-5.

[178] D. Cortesi. *PyInstaller Documentation, Release 3.4. 2018*. URL: https://www.pyinstaller.org/documentation.html (visited on 01/21/2019).

[179] International Atomic Energy Agency. *Charged-Particle cross Section Database for Medical Radioisotope Production: Diagnostic Radioisotopes and Monitor Reactions*. URL: https://www-nds.iaea.org/medical (visited on 01/21/2019).

[180] International Atomic Energy Agency. *Cross Section Database for Medical Radioisotope Production: Production of Therapeutic Radionuclides*. URL: https://www-nds.iaea.org/radionuclides (visited on 01/21/2019).

[181] Martin, C.C., Christian, B.T., Satter, M.R., Nickerson, L.D.H., and Nickles, R.J. "Quantitative PET with Positron Emitters that Emit Prompt Gamma Rays". In: *IEEE Transactions on Medical Imaging* 14.4 (1995), p. 681.

[182] Pentlow, K.S., Finn, R.D., Larson, S.M., Erdi, Y.E., Beattie, B.J., and Humm, J.L. "Quantitative imaging of yttrium-86 with PET: the occurrence and correction of anomalous apparent activity in high density regions". In: *Clinical Positron Imaging* 3 (2000), p. 85.

[183] Herzog, H., Tellmann, L., Qaim, S.M., Spellerberg, S., Schmid, A., and Coenen, H.H. "PET quantitation and imaging of the non-pure positron-emitting iodine isotope ^{124}I". In: *Applied Radiation and Isotopes* 56 (2002), p. 673.

[184] Lubberink, M., Schneider, H., Bergstrom, M., and Lundqvist, H. "Quantitative imaging and correction for cascade gamma radiation of ^{76}Br with 2D and 3D PET". In: *Physics in Medicine and Biology* 47 (2002), p. 3519.

[185] Beattie, B.J., Finn, R.D., Rowland, D.J., and Pentlow, K.S. "Quantitative imaging of bromine-76 and yttrium-86 with PET: a method for the removal of spurious activity introduced by cascade gamma rays". In: *Medical Physics* 30 (2003), p. 2410.

[186] Buchholz, H.G., Herzog, H., Forster, G.J., Reber, H., Nickel, O., Rösch, F., and Bartenstein, P. "PET imaging with yttrium-86: comparison of phantom measurements acquired with different PET scanners before and after applying background subtraction". In: *European Journal of Nuclear Medicine and Molecular Imaging* 30 (2003), p. 716.

[187] Sandström, M., Tolmachev, V., Kairemo, K., Lundqvist, H., and Lubberink, M. "Performance of coincidence imaging with long-lived positron emitters as an alternative to dedicated PET and SPECT". In: *Physics in Medicine and Biology* 49 (2004), p. 5419.

[188] Duval, S., Breskin, A., Carduner, H., Cussonneau, J.-P., Lamblin, J., Le Ray, P., Morteau, E., Oger, T., Stutzmann, J.-S., and Thers, D. "MPGDs in Compton imaging with liquid-xenon". In: *Journal of Instrumentation* 4 (2009), P12008.

[189] Jacobstein, J.G. and Quinn, J.L. "Uptake of ^{206}Bi Citrate in Carcinoma of the Breast". In: *Radiology* 107.3 (1973), p. 677.

[190] Bigler, R.E., Russ G.A., and Laughlin, J.S. "Radiation dosimetry of ^{204}Bi- and ^{206}Bi-citrates". In: *The Journal of Nuclear Medicine* 17 (1976), p. 301.

[191] Lagunas-Solar, M.C., Carvacho, O.F., Nagahara, L., Mishra, A., and Parks, N.J. "Cyclotron production of no-carrier-added ^{206}Bi (6.24 d) and ^{205}Bi (15.31 d) as tracers for biological studies and for the development of alpha-emitting radiotherapeutic agents". In: *Applied Radiation and Isotopes* 38.2 (1987), p. 129.

[192] Kacperski, K., Spyrou, N.M., and Smith, F.A. "Three-gamma annihilation imaging in positron emission tomography". In: *IEEE Transactions on Medical Imaging* 23.4 (2004), p. 525.

[193] Kacperski, K. and Spyrou, N.M. "Performance of three-photon PET imaging: Monte Carlo simulations". In: *Physics in Medicine and Biology* 50 (2005), p. 5679.

[194] Abuelhia, E., Kacperski, K., and Spyrou, N.M. "Three-photon annihilation in PET: 2D imaging experiments". In: *Journal of Radioanalytical and Nuclear Chemistry* 271.2 (2007), p. 489.

[195] Gajos, A., Kamińska, D., Czerwiński, E., Alfs, D., Bednarski, T., Białas, P., Głowacz, B., Gorgol, M., Jasińska, B., Kapłon, Ł., Korcyl, G., Kowalski, P., Kozik, T., Krzemień, W., Kubicz, E., Mohammed, M., Niedźwiecki, Sz., Pałka, M., Pawlik-Niedźwiecka, M., Raczyński, L., Rudy, Z., Rundel, O., Sharma, N.G., Silarski, M., Słomski, A., Strzelecki, A., Wieczorek, A., Wiślicki, W., Zgardzińska, B., Zieliński, M., and Moskal, P. "Trilateration-based reconstruction of ortho-positronium decays into three photons with the J-PET detector". In: *Nuclear Instruments and Methods in Physics Research Section A: Accelerators, Spectrometers, Detectors and Associated Equipment* 819 (2016), p. 54.

[196] Kamińska, D., Gajos, A., Czerwiński, E., Alfs, D., Bednarski, T., Białas, P., Curceanu, C., Dulski, K., Głowacz, B., Gupta-Sharma, N., Gorgol, M., Hiesmayr, B.C., Jasińska, B., Korcyl, G., Kowalski, P., Krzemień, W., Krawczyk, N., Kubicz, E., Mohammed, M., Niedźwiecki, Sz., Pawlik-Niedźwiecka, M., Raczyński, L., Rudy, Z., Silarski, M., Wieczorek, A., Wiślicki, W., Zgardzińska, B., Zieliński, M., and Moskal, P. "A feasibility study of ortho-positronium decays measurement with the J-PET scanner based on plastic scintillators". In: *The European Physical Journal C* 76.8 (2016), p. 445. DOI: 10.1140/epjc/s10052-016-4294-3.

[197] Qaim, S.M. "Development of novel positron emitters for medical applications: nuclear and radiochemical aspects". In: *Radiochimica Acta* 99 (2011), p. 611.

[198] Usman, A.R., Khandaker, M.U., and Haba, H. "Cyclotron production of ^{48}V via ^{nat}Ti(d,x)^{48}V nuclear reaction; a promising radionuclide". In: *Journal of Physics: Conference Series* 860 (2017), p. 012029.

[199] Xuan Tham, L., Nagasawa, N., Matsuhashi, S., Ishioka, N.S., Ito, T., and Kume, T. "Effect of radiation-degraded chitosan on plants stressed with vanadium". In: *Radiation Physics and Chemistry* 61 (2001), p. 171.

[200] Rorat, E., Petelenz, B., Marczewska, B., and Ochab, E. "Thermoluminescence dosimetry of model line sources containing vanadium-48". In: *Radiation Measurements* 39 (2005), p. 495.

[201] Arbabi, A., Sadeghi, M., and Joharifard, M. "Irradiation and dosimetry of Nitinol stent for renal artery brachytherapy". In: *Applied Radiation and Isotopes* 67 (2009), p. 129.

[202] Michel, R., Brinkmann, G., and Stuck, R. "Integral Excitation Functions of α-Induced Reactions on Titanium, Iron and Nickel". In: *Radiochimica Acta* 32 (1983), p. 173.

[203] Hermanne, A., Sonck, M., Takács, S., Szelecsényi, F., and Tárkányi, F. "Excitation Functions of Nuclear Reactions Induced by Alpha Particles up to 42 MeV on ^{nat}Ti for Monitoring Purposes and TLA". In: *Nuclear Instruments and Methods in Physics Research Section B: Beam Interactions with Materials and Atoms* 152.2–3 (1999), p. 187.

[204] Uddin, M.S. and Scholten, B. "Excitation functions of alpha particle induced reactions on ^{nat}Ti up to 40 MeV". In: *Nuclear Instruments and Methods in Physics Research Section B: Beam Interactions with Materials and Atoms* 380 (2016), p. 15.

[205] Usman, A.R., Khandaker, M.U., Haba, H., Otuka, N., and Murakami, M. "Excitation functions of alpha particles induced nuclear reactions on natural titanium in the energy range of 10.4-50.2 MeV". In: *Nuclear Instruments and Methods in Physics Research Section B: Beam Interactions with Materials and Atoms* 399 (2017), p. 34.

[206] Chen, K.L. and Miller, J.M. "Comparison between reactions of alpha particles with Scandium-45 and deuterons with Titanium-47". In: *Physical Review* 134 (1964), B1269.

[207] Vlieks, A.E., Morgan, J.F., and Blatt, S.L. "Total Cross Sections for Some (α,n) and (α,p) Reactions in Medium-Weight Nuclei". In: *Nuclear Physics A* 224 (1974), p. 492.

[208] Hansper, V.Y., Tingwell, C.I.W., Tims, S.G., Scott, A.F., and Sargood, D.G. "The ^{45}Sc(α,p)^{48}Ti and ^{45}Sc(α,n)^{48}V Cross Sections". In: *Nuclear Physics A* 504 (1989), p. 605.

[209] Smith, S.V., Jones, M., and Holmes, V. "Production and Selection of Metal PET Radioisotopes for Molecular Imaging". In: *Radioisotopes*. Ed. by N. Singh. Rijeka: IntechOpen, 2011. Chap. 10. ISBN: 978-953-307-748-2. DOI: 10.5772/23947.

[210] Amjed, N., Hussain, M., Aslam, M.N., Tárkányi, F., and Qaim, S.M. "Evaluation of nuclear reaction cross sections for optimization of production of the emerging diagnostic radionuclide ^{55}Co". In: *Applied Radiation and Isotopes* 108 (2016), p. 38.

[211] Srivastava, S.C., Mausner, L.F., Kolsky, K.L., Mease, R.C., Joshi, V., Meinken, G.E., Pyatt, B., Wolf, A.P., Schlyer, D.J., Levy, A.V., and Fowler, J.S. "Production and use of cobalt-55 as an antibody label for PET imaging". In: *Journal of Labelled Compounds and Radiopharmaceuticals* 35 (1994), p. 389.

[212] Thisgaard, H., Olesen, M.L., and Dam, J.H. "Radiosynthesis of ^{55}Co- and ^{58m}Co-labelled DOTATOC for positron emission tomography imaging and targeted radionuclide therapy". In: *Journal of Labelled Compounds and Radiopharmaceuticals* 54 (2011), p. 758.

[213] Mastren, T., Marquez, B.V., Sultan, D.E., Bollinger, E., Eisenbeis, P., Voller, T., and Lapi, S.E. "Cyclotron Production of High-Specific Activity ^{55}Co and In Vivo Evaluation of the Stability of ^{55}Co Metal-Chelate-Peptide Complexes". In: *Molecular Imaging* 14 (2015), p. 526.

[214] Dam, J.H., Olsen, B.B., Baun, C., Hoilund-Carlsen, P.F., and Thisgaard, H. "In Vivo Evaluation of a bombesin analogue labeled with Ga-68 and Co-55/57". In: *Molecular Imaging and Biology* 18 (2016), p. 368.

[215] Garousi, J., Andersson, K.G., Dam, J.H., Olsen, B.B., Mitran, B., Orlova, A., Buijs, J., Ståhl, S., Löfblom, J., Thisgaard, H., and Tolmachev, V. "The use of radiocobalt as a label improves imaging of EGFR using DOTA- conjugated Affibody molecule". In: *Scientific Reports* 7.1 (2017), p. 5961.

[216] Nieweg, O.E., Beekhuis, H., Paans, A.M.J., Piers, D.A., Vaalburg, W., Welleweerd, J., Wiegman, T., and Woldring, M.G. "Detection of Lung Cancer with ^{55}Co-Bleomycin Using a Positron Camera. A Comparison with ^{57}Co-Bleomycin and ^{55}Co-Bleomycin Single Photon Scintigraphy". In: *Journal of Nuclear Medicine* 7 (1982), p. 104.

[217] Goethals, P., Volkaert, A., Vandewielle, C., Dierckx, R., and Lameire, N. "^{55}Co-EDTA for renal imaging using positron emission tomography (PET): A feasibility study". In: *Nuclear Medicine and Biology* 27.1 (2000), p. 77.

[218] Jansen, H.M.L., Pruim, J., v.d. Vliet, A.M., Paans, A.M.J., Hew, J.M., Franssen, E.J.F., de Jong, B.M., Kosterink, J.G.W., Haaxma, R., and Korf, J. "Visualization of damaged brain tissue after ischemic stroke with Cobalt-55 Positron Emission Tomography". In: *Journal of Nuclear Medicine* 35 (1994), p. 456.

[219] Jansen, H.M.L., Naalt, J., Zomeren, A.H., Paans, A.M.J., Minderhoud, M.J., and Korf, J. "Cobalt-55 positron emission tomography in traumatic brain injury, a pilot study". In: *Journal of Neurology, Neurosurgery, and Psychiatry* 60 (1996), p. 221.

[220] Jansen, H.M.L., Paans, A.M.J., v.d. Vliet, A.M., Duin, L.V.D., Bolwijn-Meijer, C.J.W., Pruim, J., Willemsen, A.T.M., Franssen, E.J., Minderhoud, J.M., and Korf, J. "Cobalt-55 positron emission tomography in ischemic stroke". In: *Clinical Neurology and Neurosurgery* 99 (1997), p. 6.

[221] Stevens, H., Jansen, H.M., Reuck, J.D., Lemmerling, M., Strijckmans, K., Goethals, P., Lemahieu, I., De Jong, B.M., Willemsen, A.T., and Korf, J. "^{55}Cobalt (Co) as a PET-tracer in stroke, compared with blood flow, oxygen metabolism, blood volume and gadolinium-MRI". In: *Journal of the Neurological Sciences* 171 (1999), p. 11.

[222] Reuck, J.D., Paemeleire, K., Santens, P., Strijckmans, K., and Lemahieu, I. "Cobalt-55 positron emission tomography in symptomatic atherosclerotic carotid artery disease: borderzone versus territorial infarcts". In: *Clinical Neurology and Neurosurgery* 106 (2004), p. 77.

[223] Jenkins, I.L. and Wain, A.G. "Excitation functions for the bombardment of ^{56}Fe with protons". In: *Journal of Inorganic and Nuclear Chemistry* 32 (1970), p. 1419.

[224] Lagunas-Solar, M.C. and Jungerman, J.A. "Cyclotron Production of Carrier-Free Cobalt-55, a New Positron-Emitting Label for Bleomycin". In: *Applied Radiation and Isotopes* 30 (1978), p. 25.

[225] Michel, R., Brinkmann, G., Weigel, H., and Herr, W. "Measurement and hybrid-model analysis of proton-induced reactions with V, Fe and Co". In: *Nuclear Physics A* 322 (1979), p. 40.

[226] Wenrong, Z., Hanlin, L., Weixiang, Y., and Jiantao, C. "Excitation functions for reactions induced by deuteron in iron". In: *Chinese Journal of Nuclear Physics* 17.2 (1995), p. 163.

[227] Al-Abyad, M., Comsan, M.N.H., and Qaim, S.M. "Excitation functions of proton-induced reactions on ^{nat}Fe and enriched ^{57}Fe with particular reference to the production of ^{57}Co". In: *Applied Radiation and Isotopes* 67 (2009), p. 122.

[228] Kim, K., Khandaker, M.U., Naik, H., and Kim, G. "Excitation functions of proton induced reactions on ^{nat}Fe in the energy region up to 45 MeV". In: *Nuclear Instruments and Methods in Physics Research Section B: Beam Interactions with Materials and Atoms* 322 (2014), p. 63.

[229] Tanaka, S., Furukawa, M., and Chiba, M. "Nuclear reactions of nickel with protons up to 56 MeV". In: *Journal of Inorganic and Nuclear Chemistry* 34 (1972), p. 2419.

[230] Michel, R., Bodemann, R., Busemann, H., Daunke, R., Gloris, M., Lange, H.-J., Klug, B., Krins, A., Leya, I., Lüpke, M., Neumann, S., Reinhardt, H., Schnatz-Büttgen, M., Herpers, U., Schiekel, Th., Sudbrock, F., Holmqvist, B., Condé, H., Malmborg, P., Suter, M., Dittrich-Hannen, B., Kubik, P.-W., Synal, H.-A., and Filges, D. "Cross sections for the production of residual nuclides by low- and medium-energy protons from the target elements C, N, O, Mg, Al, Si, Ca, Ti, V, Mn, Fe, Co, Ni, Cu, Sr, Y, Zr, Nb, Ba and Au". In: *Nuclear Instruments and Methods in Physics Research Section B: Beam Interactions with Materials and Atoms* 129 (1997), p. 153.

[231] Tárkányi, F., Szelecsényi, F., and Kopecky, P. "Excitation functions of proton induced nuclear reactions on natural nickel for monitoring beam energy and intensity". In: *Applied Radiation and Isotopes* 42 (1991), p. 513.

[232] Reimer, P. and Qaim, S.M. "Excitation function of proton induced reactions on highly enriched 58Ni with special relevance to the production of Co-55 and Co-57". In: *Radiochimica Acta* 80 (1998), p. 113.

[233] Al-Saleh, F.S., Al Mugren, K.S., and Azzam, A. "Excitation functions of (p,x) reactions on natural nickel between proton energies of 2.7 and 27.5 MeV". In: *Applied Radiation and Isotopes* 65 (2007), p. 104.

[234] Khandaker, M.U., Kim, K., Lee, M., Kim, K.S., and Kim, G. "Excitation functions of (p,x) reactions on natural nickel up to 40 MeV". In: *Nuclear Instruments and Methods in Physics Research Section B: Beam Interactions with Materials and Atoms* 269 (2011), p. 1140.

[235] Amjed, N., Tárkányi, F., Hermanne, A., Ditrói, F., Takács, S., and Hussain, M. "Activation cross-sections of proton induced reactions on natural Ni up to 65 MeV". In: *Applied Radiation and Isotopes* 92 (2014), p. 73.

[236] Valdovinos, H.F., Hernandez, R., Gravesa, S., Ellison, P.A., Barnhart, T.E., Theuer, C.P., Engle, J.W., Cai, W., and Nickles, R.J. "Cyclotron production and radiochemical separation of ^{55}Co and ^{58m}Co from ^{54}Fe, ^{58}Ni and ^{57}Fe targets". In: *Applied Radiation and Isotopes* 130 (2017), p. 90.

[237] Zaman, M.R. and Qaim, S.M. "Excitation functions of (d,n) and (d,α) reactions on highly enriched ^{54}Fe: Relevance to the production of high purity ^{55}Co at a small cyclotron". In: *Radiochimica Acta* 75 (1996), p. 59.

[238] Hermanne, A., Sonck, M., Takács, S., and Tárkányi, F. "Experimental study of excitation functions for some reactions induced by deuterons (10–50 MeV) on natural Fe and Ti". In: *Nuclear Instruments and Methods in Physics Research Section B: Beam Interactions with Materials and Atoms* 161–163 (2000), p. 178.

[239] Zaman, M.R., Spellerberg, S., and Qaim, S.M. "Production of ^{55}Co via the ^{54}Fe(d,n)- process and excitation functions of ^{54}Fe(d,t)^{53}Fe and ^{54}Fe(d,α)^{52m}Mn reactions from thresholds up to 13.8 MeV". In: *Radiochimica Acta* 91 (2003), p. 105.

[240] Nakao, M., Hori, J., Ochiai, K., Kubota, N., Sato, S., Yamauchi, M., Ishioka, N.S., and Nishitani, T. "Measurements of deuteron-induced activation cross-sections for IFMIF accelerator structural materials". In: *Nuclear Instruments and Methods in Physics Research Section A: Accelerators, Spectrometers, Detectors and Associated Equipment* 562 (2006), p. 785.

[241] Király, B., Takács, S., Ditrói, F., Tárkányi, F., and Hermanne, A. "Evaluated activation cross sections of longer-lived radionuclides produced by deuteron induced reactions on natural iron up to 10 MeV". In: *Nuclear Instruments and Methods in Physics Research Section B: Beam Interactions with Materials and Atoms* 267 (2009), p. 15.

[242] Závorka, L., Šimečková, E., Honusek, M., and Katovský, K. "The activation of Fe by deuterons at energies up to 20 MeV". In: *Journal of the Korean Physical Society* 59 (2011), p. 1961.

[243] Khandaker, M.U., Haba, H., Kanaya, J., and Otuka, N. "Activation cross-sections of deuteron-induced nuclear reactions on natural iron up to 24 MeV". In: *Nuclear Instruments and Methods in Physics Research Section B: Beam Interactions with Materials and Atoms* 316 (2013), p. 33.

[244] Avrigeanu, M., Avrigeanu, V., Bém, P., Fischer, U., Honusek, M., Katovský, K., Mănăilescu, C., Bojowald, J., Machner, H., Nann, H., Oelert, W., Rogge, M., and Turek, P. "Elastic deuteron scattering and optical model parameters at energies up to 100 MeV". In: *Physical Review C* 38 (2014), p. 1153.

[245] Blower, P.J., Lewis, J.S., and Zweit, J. "Copper radionuclides and radiopharmaceuticals in nuclear medicine". In: *Nuclear Medicine and Biology* 23 (1996), p. 957.

[246] McCarthy, D. W., Bass, L.A., Duffy Cutler, P., Shefer, R.E., Klinkowstein, R.E., Herrero, P., Lewis, J.E., Cutler, C.S., Anderson, C.J., and Welch, M.J. "High Purity Production and Potential Applications of Copper-60 and Copper-61". In: *Nuclear Medicine and Biology* 26 (1999), p. 351.

[247] Chao, K.S., Bosch, W.R., Mutic, S., Lewis, J.S., Dehdashti, F., Mintun, M.A., Dempsey, J.F., Perez, C.A., Purdy, J.A., and Welch, M.J. "A novel approach to overcome hypoxic tumor resistance: Cu-ATSM-guided intensity-modulated radiation therapy". In: *International Journal of Radiation Oncology, Biology, Physics* 49 (2001), p. 1171.

[248] Dehdashti, F., Mintun, M.A., Lewis, J.S., Bradley, J., Govindan, R., Laforest, R., Welch, M.J., and Siegel, B.A. "In vivo assessment of tumor hypoxia in lung cancer with ^{60}Cu-ATSM". In: *European Journal of Nuclear Medicine and Molecular Imaging* 30 (2003), p. 844.

[249] Dietz D.V., Dehdashti, F., Grigsby, P.W., Malyapa, R.S., Myerson, R.J., Picus, J., Ritter, J., Lewis, J.S., Welch, M.J., and Siegel, B.A. "Tumor hypoxia detected by positron emission tomography with ^{60}Cu-ATSM as a predictor of response and survival in patients undergoing neoadjuvant chemoradiotherapy for rectal carcinoma: a pilot study". In: *Diseases of the Colon & Rectum* 51 (2008), p. 1641.

[250] Lewis, J.S., Laforest, R., Dehdashti, F., Grigsby, P.W., Welch, M.J., and Siegel, B.A. "An Imaging Comparison of ^{64}Cu-ATSM and ^{60}Cu-ATSM in Cancer of the Uterine Cervix". In: *Journal of Nuclear Medicine* 49 (2008), p. 1177.

[251] Blosser, H.G. and Handley, T.H. "Survey of (p,n) Reactions at 12 MeV". In: *Physical Review* 100.5 (1955), p. 1340.

[252] Barrandon, J.N., Debrun, J.L., Kohn, A., and Spear, R.H. "Étude du dosage de Ti, V, Cr, Fe, Ni, Cu et Zn par activation avec des protons d'énergie limitée à 20 MeV". In: *Nuclear Instruments and Methods* 127 (1975), p. 269.

[253] Singh, B.P., Sharma, M.K., Musthafa, M.M., Bhardwaj, H.D., and Prasad, R. "A study of pre-equilibrium emission in some proton- and alpha-induced reactions". In: *Nuclear Instruments and Methods in Physics Research Section A: Accelerators, Spectrometers, Detectors and Associated Equipment* 562 (2006), p. 717.

[254] Uddin, M.S., Sudár, S., Spahn, I., Shariff, M.A., and Qaim, S.M. "Excitation function of the ^{60}Ni(p,γ)^{61}Cu reaction from threshold to 16 MeV". In: *Physical Review C* 93 (2016), p. 044606.

[255] Szelecsényi, F., Suzuki, K., Kovács, Z., Takei, M., and Okada, K. "Production possibility of $^{60;61;62}$Cu radioisotopes by alpha induced reactions on cobalt for PET studies". In: *Nuclear Instruments and Methods in Physics Research Section B: Beam Interactions with Materials and Atoms* 187 (2002), p. 153.

[256] Szelecsényi, F., Kovács, Z., Suzuki, K., Okada, K., Fukumura, T., and Mukai, K. "Formation of ^{60}Cu and ^{61}Cu via Co + ^{3}He reactions up to 70 MeV: production possibility of ^{60}Cu for PET studies". In: *Nuclear Instruments and Methods in Physics Research Section B: Beam Interactions with Materials and Atoms* 222 (2004), p. 364.

[257] Tanaka, S. "Reactions of Nickel with Alpha-Particles". In: *Journal of the Physical Society of Japan* 15 (1960), p. 2159.

[258] Yadav, A., Singh, P.P., Sharma, M.K., Singh, D.P., Unnati, Singh, B.P., Prasad, R., and Musthafa, M.M. "Large pre-equilibrium contribution in α + ^{nat}Ni interactions at $\approx$ 8–40 MeV". In: *Physical Review C* 78 (2008), p. 044606.

[259] Goethals, P., Coene, M., Slegers, G., Agon, P., Deman, J., and Schelstraete, K. "Cyclotron production of carrier-free ^{66}Ga as a positron emitting label of albumin colloids for clinical use". In: *European Journal of Nuclear Medicine and Molecular Imaging* 14 (1988), p. 152.

[260] Lewis, M.R., Reichert, D.E., Laforest, R., Margenau, W.H., Shefer, R.E., Klinkowstein, R.E., Hughey, B.J., and Welch, M.J. "Production and purification of gallium-66 for preparation of tumor-targeting radiopharmaceuticals". In: *Nuclear Medicine and Biology* 29 (2002), p. 701.

[261] Ellis, B.L. and Sharma, H.L. "Co, Fe and Ga chelates for cell labelling: a potential use in PET imaging". In: *Nuclear Medicine Communications* 20 (1999), p. 1017.

[262] Jalilian, A.R., Rowshanfarzad, P., Rahiminejad, A., Rajamand, A.A., Novinrooz, A.J., Bakhtiari, H., and Sarbadani, P. "[^{66}Ga]Oxine complex; preparation and stability as a possible PET radiopharmaceutical". In: *International Journal of Radiation Research* 1 (2003), p. 157.

[263] Ke, Ch., Mathias, C.J., and Green, M.A. "The folate receptor as a molecular target for tumor-selective radionuclide delivery". In: *Nuclear Medicine and Biology* 30 (2003), p. 811.

[264] Ke, Ch., Mathias, C.J., and Green, M.A. "Folate-receptor-targeted radionuclide imaging agents". In: *Advanced Drug Delivery Reviews* 56 (2004), p. 1143.

[265] Mathias, C.J., Lewis, M.R., Reichert, D.E., Laforest, R., Sharp, T.L., Lewis, J.S., Yang, Zh., Waters, D.J., Snyder, P.W., Low, Ph.S., Welch, M.J., and Green, M.A. "Preparation of ^{66}Ga- and ^{68}Ga-labeled Ga(III)-deferoxamine-folate as potential folate-receptor-targeted PET radiopharmaceuticals". In: *Nuclear Medicine and Biology* 30 (2003), p. 725.

[266] Ugur, O., Kothari, P.J., Finn, R.D., Zanzonico, P., Ruan, S., Guenther, I., Maecke, H.R., and Larson, S.M. "Ga-66 labeled somatostatin analogue DOTA-DPhe1-Tyr3-octreotide as a potential agent for positron emission tomography imaging and receptor mediated internal radiotherapy of somatostatin receptor positive tumors". In: *Nuclear Medicine and Biology* 29 (2002), p. 147.

[267] Hille, M., Hille, P., Uhl, M., and Weisz, W. "Excitation functions of (p,n) and (α,n) reactions on Ni, Cu and Zn". In: *Nuclear Physics A* 198 (1972), p. 625.

[268] Little, F.E. and Lagunas-Solar, M.C. "Cyclotron production of ^{67}Ga. Cross section and thick-target yields for the ^{67}Zn(p,n) and ^{68}Zn(p,2n) reactions". In: *Applied Radiation and Isotopes* 34 (1983), p. 631.

[269] Kopeckỳ, P. "Cross sections and production yields of ^{66}Ga and ^{67}Ga for proton reactions in natural zinc". In: *Applied Radiation and Isotopes* 41 (1990), p. 606.

[270] Tárkányi, F., Szelecsényi, F., and Kovács, Z. "Excitation Functions of Proton Induced Nuclear Reactions on Enriched ^{66}Zn, ^{67}Zn and ^{68}Zn. Production of ^{67}Ga and ^{66}Ga". In: *Radiochimica Acta* 50 (1990), p. 19.

[271] Hermanne, A., Walravens, N., and Cicchelli, O. "Optimization of isotope production by cross-section determination". In: *Nuclear Data for Science and Technology*. Ed. by S.M. Qaim. Springer Berlin Heidelberg, 1991, pp. 616–618. ISBN: 978-3-642-58113-7.

[272] Nortier, F.M., Mills, S.J., and Steyn, G.F. "Excitation function and yield of relevance to the production of ^{67}Ga by proton bombardment of ^{nat}Zn and ^{nat}Ga up to 100 MeV". In: *Applied Radiation and Isotopes* 42 (1991), p. 353.

[273] Szelecsényi, F., Boothe, T.E., Takács, S., Tárkányi, F., and Tavano, E. "Evaluated cross section and thick target yield data bases of Zn + p processes for practical applications". In: *Applied Radiation and Isotopes* 49.8 (1998), p. 1005.

[274] Szelecsényi, F., Steyn, G.F., Kovács, Z., van der Walt, T.N., Suzuki, K., Okada, K., and Mukai, K. "New cross-section data for the ^{66}Zn(p,n)^{66}Ga, ^{68}Zn(p,3n)^{66}Ga, ^{nat}Zn(p,x)^{66}Ga, ^{68}Zn(p,2n)^{67}Ga and ^{nat}Zn(p,x)^{67}Ga nuclear reactions up to 100 MeV". In: *Nuclear Instruments and Methods in Physics Research Section B: Beam Interactions with Materials and Atoms* 234.4 (2005), p. 375.

[275] Intrator, T.P., Peterson, R.J., Zaidins, C.S., and Roughton, N.A. "Determination of proton spectra by thick target radioactive yields". In: *Nuclear Instruments and Methods in Physics Research* 188 (1981), p. 347.

[276] Dmitriev, P.P. *Radionuclide Yield in Reactions with Protons, Deuterons, Alpha Particles and Helium-3: Handbook*. Vienna: International Atomic Energy Agency, 1986.

[277] Rowshanfarzad, P., Reza Jalilian, A., and Sabet, M., Akhlaghi, M. "Production and quality control of ^{66}Ga as a PET radioisotope". In: *International Journal of Radiation Research* 2.3 (2004), p. 149.

[278] Sadeghi, M., Enferadi, M., Aref, M., and Jafari, H. "Nuclear data for the cyclotron production of ^{66}Ga, ^{86}Y, ^{76}Br, ^{64}Cu and ^{43}Sc in PET imaging". In: *Nukleonika* 55.3 (2010), p. 293.

[279] Porges, K.G. "Alpha excitation functions of silver and copper". In: *Physical Review* 101.1 (1956), p. 225.

[280] Bryant, E.A., Cochran, D.R.F., and Knight, J.D. "Excitation functions of reactions of 7 to 24 MeV He^3 ions with Cu^{63} and Cu^{65}". In: *Physical Review* 130 (1963), p. 1512.

[281] Zhukova, O.A., Kanashevich, V.I., Laptev, S.V., and Chursin, G.P. "Excitation functions of reactions induced by alpha particles with maximum energy of 38 MeV on copper isotopes". In: *Izvestiya Natsional'noĭ Akademii Nauk Respubliki Kazakhstan. Seriya Fiziko-Matematicheskaya* 4 (1970), p. 1.

[282] Brinkman, G.A., Helmer, J., and Lindner, L. "Nickel and copper foils as monitors for cyclotron beam intensities". In: *Radiochemical and Radioanalytical Letters* 28 (1977), p. 9.

[283] Rizvi, I.A., Afzal Ansari, M., Gautam, R.P., Singh, R.K.Y., and Chaubey, A.K. "Excitation Function Studies of (α,xpyn) Reactions for ^{63,65}Cu and Pre-Equilibrium Effect". In: *Journal of the Physical Society of Japan* 56 (1987), p. 3135.

[284] Zweit, J., Sharma, H., and Downey, S. "Production of Gallium-66, a Short-Lived, Positron Emitting Radionuclide". In: *Applied Radiation and Isotopes* 38 (1987), p. 499.

[285] Bhardwaj, H.D., Gautam, A.K., and Prasad, R. "Measurement and analysis of excitation functions for alpha-induced reactions in copper". In: *Pramana* 31.2 (1988), p. 109.

[286] Mohan Rao, A.V., Mukherjee, S., and Rama Rao, J. "Alpha Particle Induced Reactions on Copper and Tantalum". In: *Pramana* 36 (1991), p. 115.

[287] Didik, V.A., Malkovich, R.Sh., Skoryatina, E.A., and Kozlovskii, V.V. "Experimental determination of the cross sections of nuclear reactions by the method of analysis of the concentration profiles of transmutation nuclides". In: *Atomic Energy* 77.1 (1994), p. 81.

[288] Singh, N.L., Patel, B.J., Somayajulu, D.R.S., and Chintalapudi, S.N. "Analysis of the Excitation Functions of (α,xnyp) Reactions on Natural Copper". In: *Pramana* 42.4 (1994), p. 349.

[289] Navin, A., Tripathi, V., Blumenfeld, Y., Nanal, V., Simenel, C., Casandjian, J.M., de France, G., Raabe, R., Bazin, D., Chatterjee, A., Dasgupta, M., Kailas, S., Lemmon, R.C., Mahata, K., Pillay, R.G., Pollacco, E.C., Ramachandran, K., Rejmund, M., Shrivastava, A., Sida, J.L., and Tryggestad, E. "Direct and compound reactions induced by unstable helium beams near the Coulomb barrier". In: *Physical Review C* 70 (2004), p. 044601.

[290] Rattan, S.S., Singh, R.J., Sahakundu, S.M., Prakash, S., and Ramaniah, M.V. "Alpha Particle Induced Reactions of ^{209}Bi and ^{63,65}Cu". In: *Radiochimica Acta* 39 (1986), p. 61.

[291] Sonck, M., Van Hoyweghen, J., and Hermanne, A. "Determination of the external beam energy of a variable energy Multiparticle cyclotron". In: *Applied Radiation and Isotopes* 47 (1996), p. 445.

[292] Tárkányi, F., Szelecsényi, F., Takács, S., Hermanne, A., Sonck, M., Thielemans, A., Mustafa, M.G., Shubin, Yu., and Zhuang, Y. "New Experimental Data, Compilation and Evaluation for the ^{nat}Cu(α,x)^{66}Ga, ^{nat}Cu(α,x)^{67}Ga and ^{nat}Cu(α,x)^{65}Zn Monitor Reactions". In: *Nuclear Instruments and Methods in Physics Research Section B: Beam Interactions with Materials and Atoms* 168 (2000), p. 144.

[293] Szelecsényi, F., Suzuki, K., Kovács, Z., Takei, M., and Okada, K. "Alpha Beam Monitoring via ^{nat}Cu + Alpha Processes in the Energy Range from 40 to 60 MeV". In: *Nuclear Instruments and Methods in Physics Research Section B: Beam Interactions with Materials and Atoms* 184.4 (2001), p. 589.

[294] Shahid, M., Kim, K., Kim, G., Zaman, M., and Nadeem, M. "Measurement of excitation functions in alpha induced reactions on ^{nat}Cu". In: *Nuclear Instruments and Methods in Physics Research Section B: Beam Interactions with Materials and Atoms* 358 (2015), p. 160.

[295] Usman, A.R., Khandaker, M.U., Haba, H., Otuka, N., Murakami, M., and Komori, Y. "Production cross-sections of radionuclides from α-induced reactions on natural copper up to 50 MeV". In: *Applied Radiation and Isotopes* 114 (2016), p. 104.

[296] Takács, S., Ditrói, F., Szucs, Z., Haba, H., Komori, Y., Aikawa, M., and Saito, M. "Crosschecking of alpha particle monitor reactions up to 50 MeV". In: *Nuclear Instruments and Methods in Physics Research Section B: Beam Interactions with Materials and Atoms* 397 (2017), p. 33.

[297] Lahiri, S., Banerjee, S., and Das, N.R. "Simultaneous Production of Carrier-free ^{65}Zn and ^{66,67,68}Ga in α-particle Activated Copper Target and their Separation with TOA". In: *Applied Radiation and Isotopes* 48.1 (1997), p. 15.

[298] Hosain, F., Emran, A., Spencer, R.P., and Clampitt, K.S. "Synthesis of radioarsenic labeled dimethylchloroarsine for derivation of a new group of radiopharmaceuticals". In: *Applied Radiation and Isotopes* 33.12 (1982), p. 1477.

[299] Emran, A., Hosain, F., Spencer, R.P., and Kolstad, K.S. "Synthesis and biodistribution of radioarsenic labeled dimethylarsinothiols: Derivatives of penicillamine and mercaptoethanol". In: *Nuclear Medicine and Biology* 11.3–4 (1984), p. 259.

[300] Ballard, B., Nortier, F.M., Birnbaum, E.R., John, K.D., Phillips, D.R., and Fassbender, M.E. "Radioarsenic from a portable ^{72}Se/^{72}As generator: a current perspective". In: *Current Radiopharmaceuticals* 5 (2012), p. 264.

[301] Ellison, P.A., Barnhart, T.E., Chen, F., Hong, H., Zhang, Y., Theuer, C.P., Cai, W., Nickles, R.J., and DeJesus, O.T. "High Yield Production and Radiochemical Isolation of Isotopically Pure Arsenic-72 and Novel Radioarsenic Labeling Strategies for the Development of Theranostic Radiopharmaceuticals". In: *Bioconjugate Chemistry* 27 (2016), p. 179.

[302] Nayak, T.K. and Brechbiel, M.W. "Radioimmunoimaging with Longer-Lived Positron-Emitting Radionuclides: Potentials and Challenges". In: *Bioconjugate Chemistry* 20 (2009), p. 825.

[303] Ravandi, F. "Arsenic trioxide: expanding roles for an ancient drug". In: *Leukemia* 18 (2004), p. 1457.

[304] Miller Jr., W.H., Schipper, H.M., Lee, J.S., Singer, J., and Waxman, S. "Mechanisms of action of arsenic trioxide". In: *Cancer Research* 62 (2002), p. 3893.

[305] Lu, J., Chew, E.-H., and Holmgren, A. "Targeting thioredoxin reductase is a basis for cancer therapy by arsenic trioxide". In: *Proceedings of the National Academy of Sciences of the United States of America* 104.30 (2007), p. 12288.

[306] Fuladvand, H., Bakhtiari, M., Sadeghi, M., and Amiri, M. "Pre-equilibrium effects on proton, deuteron, and alpha induced reactions for the production of ^{72}As as a PET imaging radioisotope". In: *Journal of Radioanalytical and Nuclear Chemistry* 298 (2013), p. 501.

[307] Basile, D., Birattari, C., Bonardi, M., Goetz, L., Sabbioni, E., and Salomone, A. "Excitation Functions and Production of Arsenic Radioisotopes for Environmental Toxicology and Biomedical Purposes". In: *Applied Radiation and Isotopes* 32 (1981), p. 403.

[308] Horiguchi, T., Kumahora, H., Inoue, H., and Yoshizawa, Y. "Excitation Functions of Ge(p,xnyp) Reactions and Production of ^{68}Ge." In: *Applied Radiation and Isotopes* 34.11 (1983), p. 1531.

[309] Spahn, I., Steyn, G.F., Nortier, F.M., Coenen, H.H., and Qaim, S.M. "Excitation functions of ^{nat}Ge(p,xn)^{71,72,73,74}As reactions up to 100 MeV with a focus on the production of ^{72}As for medical and ^{73}As for environmental studies". In: *Applied Radiation and Isotopes* 65 (2007), p. 1057.

[310] Enferadi, M., Sadeghi, M., and Nadi, H. "^{72}As, a Powerful Positron Emitter for Immunoimaging and Receptor Mapping: Study of the Cyclotron Production". In: *Radiochemistry* 53.4 (2011), p. 346.

[311] Al-Kourashi, S.H. and Boswell, G.G.J. "An isotope generator for ^{72}As". In: *Applied Radiation and Isotopes* 29 (1978), p. 607.

[312] Phillips, D.R., Hamilton, V.T., Nix, D.A., Taylor, W.A., Jamriska, D.J., Staroski, R.C., Lopez, R.A., and Emran, A.M. "Chemistry and Concept for an Automated ^{72}Se/^{72}As Generator". In: *New Trends in Radiopharmaceutical Synthesis, Quality Assurance, and Regulatory Control*. Ed. by A.M. Emran. Boston: Springer International Publishing, 1991, p. 173.

[313] Jennewein, M., Schmidt, A., Novgorodov, A. F., Qaim, S.M., and Rösch, F. "A no-carrier-added ^{72}Se/^{72}As radionuclide generator based on distillation". In: *Radiochimica Acta* 92 (2004), p. 245.

[314] Jennewein, M., Qaim, S.M., Kulkarni, P.V., Mason, R.P., Hermanne, A., and Rösch, F. "A no-carrier-added ^{72}Se/^{72}As radionuclide generator based on solid phase extraction". In: *Radiochimica Acta* 93 (2005), p. 579.

[315] Ballard, B., Wycoff, D., Birnbaum, E.R., John, K.D., Lenz, J.W., Jurisson, S.S., Cutler, C.S., Nortier, F.M., Taylor, W.A., and Fassbender, M.E. "Selenium-72 formation via ^{nat}Br(p,x) induced by 100 MeV protons: Steps towards a novel ^{72}Se/^{72}As generator system". In: *Applied Radiation and Isotopes* 70 (2012), p. 595.

[316] Chajduk, E., Doner, K., Polkowska-Motrenko, H., and Bilewicz, A. "Novel radiochemical separation of arsenic from selenium for ^{72}Se/^{72}As generator". In: *Applied Radiation and Isotopes* 70.5 (2012), p. 819.

[317] Wycoff, D.E., Gott, M.D., DeGraffenreid, A.J., Morrow, R.P., Sisay, N., Embree, M.F., Ballard, B., Fassbender, M.E., Cutler, C.S., Ketring, A.R., and Jurisson, S.S. "Chromatographic separation of selenium and arsenic: a potential ^{72}Se/^{72}As generator". In: *Journal of Chromatography A* 1340 (2014), p. 109.

[318] Feng, Y., Phipps, M.D., Phelps, T.E., Okoye, N.C., Baumeister, J.E., Wycoff, D.E., Dorman, E.F., Lake Wooten, A., Vlasenko, V., Berendzen, A.F., Wilbur, D.S., Hoffman, T.J., Cutler, C.S., Ketring, A.R., and Jurisson, S.S. "Evaluation of ^{72}Se/^{72}As generator and production of ^{72}Se for supplying ^{72}As as a potential PET imaging radionuclide". In: *Applied Radiation and Isotopes* 143 (2019), p. 113.

[319] Amiel, S. "Reactions of Alpha Particles with Germanium-70 and Zinc-70". In: *Physical Review* 116 (1959), p. 415.

[320] Calboreanu, A., Salagean, O., Pencea, C., Zimmer, K.W., and Ciocanel, A. "Formation and Decay of the Compound Nucleus in Alpha Induced Reaction on ^{70}Ge". In: *Revue Roumaine de Physique* 32 (1987), p. 725.

[321] Mushtaq, A. and Qaim, S.M. "Excitation Function of α- and ^{3}He-Particle Induced Nuclear Reactions on Natural Germanium: Evaluation of production routes for ^{73}Se". In: *Radiochimica Acta* 50 (1990), p. 27.

[322] Takács, S., Takács, M.P., Ditrói, F., Aikawa, M., Haba, H., and Komori, Y. "Activation cross sections of longer-lived radionuclides produced in germanium by alpha particle irradiation". In: *Nuclear Instruments and Methods in Physics Research Section B: Beam Interactions with Materials and Atoms* 383 (2016), p. 213.

[323] Mushtaq, A., Qaim, S.M., and Stöcklin, G. "Production of ^{73}Se via (p,3n) and (d,4n) Reactions on Arsenic". In: *Applied Radiation and Isotopes* 39.10 (1988), p. 1085.

[324] DeGraffenreid, A.J., Dedvedev, D.G., Phelps, T.E., Gott, M.D., Smith, S.V., Jurisson, S.S., and Cutler, C.S. "Cross-section measurements and production of ^{72}Se with medium to high energy protons using arsenic containing targets". In: *Radiochimica Acta* 107.4 (2019), p. 279. DOI: 10.1515/ract-2018-2931.

[325] Maziere, B. and Loc'h, C. "Radiopharmaceuticals labelled with bromine isotopes". In: *Applied Radiation and Isotopes* 37 (1985), p. 703.

[326] Martinot, J.L., Paillere-Martinot, M.L., Loc'h, C., Hardy, P., Poirier, M.F., Mazoyer, B., Beaufils, B., Maziere, B., Allilaire, J.F., and Syrota, A. "The estimated density of D2 striatal receptors in schizophrenia. A study with positron emission tomography and ^{76}Br-bromolisuride". In: *British Journal of Psychiatry* 158 (1991), p. 346.

[327] Martinot, J.L., Paillere-Martinot, M.L., Loc'h, C., Lecrubier, Y., Dao-Castellana, M.H., Aubin, F., Allilaire, J.F., Mazoyer, B., Maziere, B., and Syrota, A. "Central D2 receptors and negative symptoms of schizophrenia". In: *British Journal of Psychiatry* 164 (1994), p. 27.

[328] Hanaoka, H., Ohshima, Y., Suzuki, Y., Yamaguchi, A., Watanabe, S., Uehara, T., Nagamori, S., Kanai, Y., Ishioka, N.S., Tsushima, Y., Endo, K., and Arano, Y. "Development of a Widely Usable Amino Acid Tracer: ^{76}Br-α-Methyl-Phenylalanine for Tumor PET Imaging". In: *Journal of Nuclear Medicine* 56.5 (2015), p. 791.

[329] Jagoda, E.M., Lang, L., McCullough, K., Contoreggi, C., Moon Kim, B., Ma, Y., Rice, K.C., Szajek, L.P., Eckelman, W.C., and Kiesewetter, D.O. "[^{76}Br]BMK-152, a Nonpeptide Analogue, With High Affinity and Low Nonspecific Binding for the Corticotropin-Releasing Factor Type 1 Receptor". In: *Synapse* 65 (2011), p. 910.

[330] Loc'h, C., Mardon, K., Valette, H., Bruresco, C., Merlet, P., Syrota, A., and Maziere, B. "Preparation and pharmacological characterization of [^{76}Br]-metabrombenzylguanidine ([^{76}Br]mBBG)". In: *Nuclear Medicine and Biology* 21 (1994), p. 35.

[331] Scott-Robson, S., Capala, J., Carlsson, J., Malmborg, P., and Lundqvist, H. "Distribution and stability in the rat of a ^{76}Br/^{125}I-labelled polypeptide, epidermal growth factor". In: *Nuclear Medicine and Biology* 18 (1991), p. 241.

[332] Rossin, R., Berndorff, D., Friebe, M., Dinkelborg, L.M., and Welch, M.J. "Small-Animal PET of Tumor Angiogenesis Using a ^{76}Br-Labeled Human Recombinant Antibody Fragment to the ED-B Domain of Fibronectin". In: *Journal of Nuclear Medicine* 48.7 (2007), p. 1172.

[333] Gardelle, O., Roelcke, U., Vontobel, P., Crompton, N.E.A., Guenther, I., Bläuenstein, P., Schubiger, A.P., Blattmann, H., Ryser, J.E., Leenders, K.L., and Kaser-Hotz, B. "[^{76}Br]Bromodeoxyuridine PET in tumor-bearing animals". In: *Nuclear Medicine and Biology* 28 (2001), p. 51.

[334] Hassan, H.E., Qaim, S.M., Shubin, Yu., Azzam, A., Morsy, M., and Coenen, H.H. "Experimental studies and nuclear model calculations on proton-induced reactions on ^{nat}Se, ^{76}Se and ^{77}Se with particular reference to the production of the medically interesting radionuclides ^{76}Br and ^{77}Br". In: *Applied Radiation and Isotopes* 60 (2004), p. 899.

[335] Kovàcs, Z., Blessing, G., Qaim, S.M., and Stöcklin, G. "Production of ^{75}Br via ^{76}Se(p,2n)^{75}Br reaction at a compact cyclotron". In: *Applied Radiation and Isotopes* 36 (1985), p. 635.

[336] El-Azony, K.M., Suzuki, K., Fukumura, T., Szelecsényi, F., and Kovács, Z. "Excitation functions of proton induced reactions on natural selenium up to 62 MeV". In: *Radiochimica Acta* 97 (2009), p. 71.

[337] Janssen, A.G.M., Van Den Bosch, R.L.P., De Goeij, J.J.M., and Theelen, H.M.J. "The reactions ^{77}Se(p,n) and ^{78}Se(p,2n) as production routes for ^{77}Br". In: *Applied Radiation and Isotopes* 31.7 (1980), p. 405.

[338] Tolmachev, V., Lövqvist, A., Einarsson, L., Schultz, J., and Lundqvist, H. "Production of ^{76}Br by a low-energy cyclotron". In: *Applied Radiation and Isotopes* 49.12 (1998), p. 1537.

[339] Lundqvist, H., Malmborg, P., Långström, B., and Suparb Na Chiengmai. "Simple Production of ^{77}Br- and ^{123}I- and their Use in the Labelling of [^{77}Br]BrUdR and [^{123}I]IUdR". In: *Applied Radiation and Isotopes* 30 (1979), p. 39.

[340] De Jong, D., Kooiman, H., and Veenboer, J.Th. "^{76}Br and ^{77}Br from decay of cyclotron produced ^{76}Kr and ^{77}Kr". In: *Applied Radiation and Isotopes* 30 (1979), p. 786.

[341] Diksic, M., Galinier, J.-L., Marshall, H., and Yaffe, L. "^{79}Br and ^{81}Br(p,xn) and (p,pxn) Excitation Functions in the Energy Range 10–85 MeV". In: *Physical Review C* 19 (1979), p. 1753.

[342] Nozaki, T., Iwamoto, M., and Itoh, Y. "Production of ^{77}Br by Various Nuclear Reactions". In: *Applied Radiation and Isotopes* 30 (1979), p. 79.

[343] Sakamoto, K., Dohniwa, M., and Okada, K. "Excitation Function for (p,xn) and (p,pxn) Reactions on Natural $^{79+81}$Br, $^{85+87}$Rb, ^{127}I and ^{133}Cs up to E(p) = 52 MeV". In: *Applied Radiation and Isotopes* 36.6 (1985), p. 481.

[344] Deptula, C., Sen Han, K., Knotek, O., Mikołajewski, S., Popinenkova, L.M., Rurarz, E., and Zaitseva, N.G. "Excitation Function and Yields For Br-Nat(P,XN)Kr-76, Kr-77,Kr-79 Reactions at 100 MeV Bombarding Energy". In: *Nukleonika* 35 (1990), p. 79.

[345] Zaitseva, N.G., Deptula, C., Knotek, O., Kim, S.K., Mikolaevsky, S., Mikecz, P., Rurarz, E., Khalkin, V.A., Konov, V.A., and Popinenkova, L.M. "Cross Sections for the 100 MeV Proton-Induced Nuclear Reactions and Yields of Some Radionuclides Used in Nuclear Medicine". In: *Radiochimica Acta* 54 (1991), p. 57.

[346] de Villiers, D., Nortier, M., and Richter, W. "Experimental and theoretical excitation functions for ^{nat}Br(p,x) reactions". In: *Applied Radiation and Isotopes* 57 (2002), p. 907.

[347] Qaim, S.M. and Stöcklin, G. "Production of some medically important short-lived neutron-deficient radioisotopes of halogens". In: *Radiochimica Acta* 34 (1983), p. 25.

[348] Helus, F., Gasper, H., Rettig, W., and Maier-Borst, W. "Cyclotron production of ^{34m}Cl for biomedical use". In: *Journal of Radioanalytical and Nuclear Chemistry* 94 (1985), p. 149.

[349] DeJesus, O.T., Converse, A.K., and Nickles, R.J. "Development of ^{34m}Cl-labeled dopamine D1 agonists as PET imaging agents". In: *Journal of Labelled Compounds and Radiopharmaceuticals* 50 (2007), S339.

[350] Murali, D., Engle, J., Barnhart, T., Nickles, R., and DeJesus, O. "Synthesis of ^{34m}Cl labeled D1 agonists using electrophilic chlorination". In: *Journal of Nuclear Medicine* 52.S1 (2011), p. 1508.

[351] Lagunas-Solar, M.C., Carvacho, O.F., and Cima, R.R. "Cyclotron Production of PET Radionuclides: ^{34m}Cl (33.99 min; β^+ 53%; IT 47%) with Protons on Natural Isotopic Chlorine-containing Targets". In: *Applied Radiation and Isotopes* 43.11 (1992), p. 1375.

[352] Hintz, N.M. and Ramsey, N.E. "Excitation Functions to 100 MeV". In: *Physical Review* 88.1 (1952).

[353] Umbarger, C.J., Kemper, K.W., Nelson, J.W., and Plendl, H.S. "Excitation Functions for the Reactions ^{34}S(p,n)^{34}Cl and ^{31}P(α,n)^{34}Cl". In: *Physical Review C* 2.4 (1970), p. 1378.

[354] Zatolokin, B.V., Konstantinov, I.O., and Krasnov, N.N. "Thick Target Yields of ^{34m}Cl and ^{38}Cl Produced by Various Charged Particles On Phosphorus, Sulphur and Chlorine Targets". In: *Applied Radiation and Isotopes* 27 (1976), p. 159.

[355] Takei, M., Nagatsu, K., Fukumura, T., and Suzuki, K. "Remote control production of an aqueous solution of no-carrier-added ^{34m}Cl- via the ^{32}S(α,pn) nuclear reaction". In: *Applied Radiation and Isotopes* 65 (2007), p. 981.

[356] Abrams, D.N., Knaus, E.E., Wiebe, L.I., Helus, F., and Maier-Borst, W. "Production of ^{34m}Cl from a gaseous hydrogen sulfide target". In: *Applied Radiation and Isotopes* 35.11 (1984), p. 1045.

[357] Engle, J.W., Barnhart, T.E., DeJesus, O.T., and Nickles, R.J. "Production of ^{34m}Cl and ^{38}Cl via the (d,α) reaction on ^{36}Ar and ^{nat}Ar gas at 8.4 MeV". In: *Applied Radiation and Isotopes* 69.1 (2011), p. 75.

[358] Engle, J.W., Severin, G.W., Barnhart, T.E., Knutson, L.D., and Nickles, R.J. "Cross sections of the ^{36}Ar(d,α)^{34m}Cl, ^{40}Ar(d,α)^{38}Cl, and ^{40}Ar(d,p)^{41}Ar nuclear reactions below 8.4 MeV". In: *Applied Radiation and Isotopes* 70 (2012), p. 355.

[359] Lewis, C.M., Graves, S.A., Hernandez, R., Valdovinos, H.F., Barnhart, T.E., Cai, W., Meyerand, M.E., Nickles, R.J., and Suzuki, M. "^{52}Mn Production for PET/MRI Tracking Of Human Stem Cells Expressing Divalent Metal Transporter 1 (DMT1)". In: *Theranostics* 5.3 (2015), p. 227.

[360] Koretsky, A.P. and Silva, A.C. "Manganese-enhanced magnetic resonance imaging (MEMRI)". In: *NMR in Biomedicine* 17.8 (2004), p. 527.

[361] Silva, A.C., Hee Lee, J., Aoki, I., and Koretsky, A.P. "Manganese-enhanced magnetic resonance imaging (MEMRI): methodological and practical considerations". In: *NMR in Biomedicine* 17 (2004), p. 532.

[362] Wadghiri, Y.Z., Blind, J.A., Duan, X., Moreno, C., Yu, X., Joyner, A.L., and Turnbull, D.H. "Manganese-enhanced magnetic resonance imaging(MEMRI) of mouse brain development". In: *NMR in Biomedicine* 17.8 (2004), p. 613.

[363] Silva, A.C. and Bock, N.A. "Manganese-Enhanced MRI: An Exceptional Tool in Translational Neuroimaging". In: *Schizophrenia Bulletin* 34.4 (2008), p. 595.

[364] Massaad, C.A. and Pautler, R.G. "Manganese-Enhanced Magnetic Resonance Imaging (MEMRI)". In: *Methods in Molecular Biology* 711 (2011), p. 145.

[365] Cacace, A.T., Brozoski, T., Berkowitz, B., Bauer, C., Odintsov, B., Bergkvist, M., Castracane, J., Zhang, J., and Holt, A.G. "Manganese enhanced magnetic resonance imaging (MEMRI): a powerful new imaging method to study tinnitus". In: *Hearing Research* 311 (2014), p. 49.

[366] Crossgrove, J. and Zheng, W. "Manganese toxicity upon overexposure". In: *NMR in Biomedicine* 17.8 (2004), p. 544.

[367] Graves, S.A., Hernandez, R., Fonslet, J., England, C.G., Valdovinos, H.F., Ellison, P.A., Barnhart, T.E., Elema, D.R., Theuer, C.P., Cai, W., Nickles, R.J., and Severin, G.W. "Novel Preparation Methods of ^{52}Mn for ImmunoPET Imaging". In: *Bioconjugate Chemistry* 26.10 (2015), p. 2118.

[368] Kakavand, T., Mirzaii, M., Eslami, M., and Valizadeh, S. "Cyclotron production of ^{52}Mn and Monte Carlo benchmarking". In: *Journal of Radioanalytical and Nuclear Chemistry* 304 (2015), p. 669.

[369] A.A. Alharbi. "Experimental Results Evaluation and Theoretical Study for the Production of the Radio Isotope ^{52}Mn Using p, d and α- Projectiles on V and Cr Targets". In: *Arab Journal of Nuclear Sciences and Applications* 94.3 (2016), p. 216.

[370] Atcher, R. W., Friedman, A.M., and Huizenga, J.R. "Production of ^{52}Fe for Use in a Radionuclide Generator System". In: *International Journal of Nuclear Medicine and Biology* 7 (1980), p. 15.

[371] Steyn, G.F., Mills, S.J., Nortier, F.M., Simpson, B.R.S., and Meyer, B.R. "Production of ^{52}Fe via Proton-induced Reactions on Manganese and Nickel". In: *Applied Radiation and Isotopes* 41.30 (1990), p. 315.

[372] Titarenko, Yu.E., Batyaev, V.F., Titarenko, A.Yu., Butko, M.A., Pavlov, K.V., Florya, S.N., Tikhonov, R.S., Zhivun, V.M., Ignatyuk, A.V., Mashnik, S.G., Leray, S., Boudard, A., Cugnon, J., Mancusi, D., Yariv, Y., Nishihara, K., Matsuda, N., Kumawat, H., Mank, G., and Gudowski, W. "Measurement and simulation of the cross sections for nuclide production in Nb-93 and Ni-nat targets irradiated with 0.04- to 2.6-GeV protons". In: *Physics of Atomic Nuclei* 74 (2011), p. 537.

[373] Greene, M.W., Lebowitz, E., Richards, P., and Hillman, M. "Production of ^{52}Fe for Medical Use". In: *Applied Radiation and Isotopes* 21 (1970), p. 719.

[374] Akiha, F., Aburai, T., Nozaki, T., and Murakami, Y. "Yield of ^{52}Fe for the Reactions of ^{3}He and α on Chromium". In: *Radiochimica Acta* 18.2 (1972), p. 108.

[375] Mirzadeh, S. and Lambrecht, R.M. "Radiochemistry of germanium". In: *Journal of Radioanalytical and Nuclear Chemistry* 202 (1996), p. 7.

[376] Rösch, F. "Past, present and future of ^{68}Ge/^{68}Ga generators". In: *Applied Radiation and Isotopes* 76 (2013), p. 24.

[377] Velikyan, I. "^{68}Ga-Based Radiopharmaceuticals: Production and Application Relationship". In: *Molecules* 20 (2015), p. 12913.

[378] Chakravarty, R., Valdovinos, H.F., Chen, F., Lewis, C.M., Ellison, P.A., Luo, H., Meyerand, M.E., Nickles, R.J., and Cai, W. "Intrinsically Germanium-69 Labeled Iron Oxide Nanoparticle: Synthesis and In Vivo Dual-modality PET/MR Imaging". In: *Advanced Materials* 26.30 (2014), p. 5119.

[379] Porile, N.T., Tanaka, S., Amano, H., Furukawa, M., Iwata, S., and Yagi, M. "Nuclear reactions of Ga^{69} and Ga^{71} with 13-56 MeV protons". In: *Nuclear Physics* 43 (1963), p. 500.

[380] Johnson, C.H., Trail, C.C., and Galonsky, A. "Thresholds for (p,n) reactions on 26 intermediate-weight nuclei". In: *Physical Review* 136.6B (1964), B1719.

[381] Adam-Rebeles, R., Hermanne, A., Van Den Winkel, P., De Vis, L., Waegeneer, R., Tárkányi, F., Takács, S., and Takács, M.P. "^{68}Ge/^{68}Ga production revisited: excitation curves, target preparation and chemical separation – purification". In: *Radiochimica Acta* 101.8 (2013), p. 481.

[382] Hermanne, A., Adam-Rebeles, R., Tárkányi, F., Takács, S., and Ditrói, F. "Proton and deuteron induced reactions on ^{nat}Ga: Experimental and calculated excitation functions". In: *Nuclear Instruments and Methods in Physics Research Section B: Beam Interactions with Materials and Atoms* 359 (2015), p. 145.

[383] Stelson, P.H. and McGowan, F.K. "Cross Sections for (α,n) Reactions for Medium-Weight Nuclei". In: *Physical Review* 133.4B (1964), B911.

[384] Abu Issa, N.N., Antropov, A.E., Gusev, V.P., Zarubin P.P., Kolozhvari, A.A., and Smirnov, A.V. "The excitation function analysis of alpha-particles production on nuclei Zn-64,66,68 with energy 14.8–24.4 MeV". In: *39 Conf. Nucl. Spectrosc. Nucl. Struct., Tashkent, USSR* (1989), p. 350.

[385] Nagame, Y., Nakahara, H., and Furukawa, M. "Excitation Functions for α and ^{3}He Particles Induced Reactions on Zinc". In: *Radiochimica Acta* 46 (1989), p. 5.

[386] Aikawa, M., Saito, M., Ebata, S., Komori, Y., and Haba, H. "Activation cross sections of α-induced reactions on ^{nat}Zn for Ge and Ga production". In: *Nuclear Instruments and Methods in Physics Research Section B: Beam Interactions with Materials and Atoms* 427 (2018), p. 91.

[387] Rizvi, I.A., Bhardwaj, M.K., Afzal Ansari, M., and Chaubey, A.K. "Nonequilibrium Effects in alpha-particle-induced reactions on gallium isotopes". In: *Canadian Journal of Physics* 67 (1989), p. 870.

[388] Ismail, M. "Measurement and Analysis of the Excitation Function for Alpha-Induced Reactions on Ga and Sb Isotopes". In: *Physical Review C* 41.1 (1990), p. 87.

[389] Lambrecht, R.M., Gallagher, B.M., Wolf, A.P., and Bennett, G.W. "Cyclotron isotopes and radiopharmaceuticals–XXIX. ^{81,82m}Rb for positron emission tomography". In: *Applied Radiation and Isotopes* 31.6 (1980), p. 343.

[390] Rowshanfarzad, P., Reza Jalilian, A., Kiyomarsi, M., Sabet, M., Reza Karimian, A., Moradkhani, S., and Mirzaii, M. "Production, quality control and initial imaging studies of [^{82m}Rb]RbCl for PET studies". In: *Nukleonika* 51.4 (2006), p. 209.

[391] Yano, Y., Chu, P., Budinger, T.F., Grant, P.M., Ogard, A.E., Barnes, J.W., O'Brien, H.A.Jr., and Hoop, B.Jr. "Rubidium-82 Generators for Imaging Studies". In: *Journal of Nuclear Medicine* 18 (1977), p. 46.

[392] Kensett, M.J., Horlock, P.L., Waters, S.L., and Bateman, D.M. "Experience with a ^{82}Sr/^{82}Rb generator for clinical use". In: *Applied Radiation and Isotopes* 38.3 (1987), p. 227.

[393] Go, R.T., Marwick, T.H., Maclntyre, W.J., Saha, G.B., Neumann, D.R., Underwood, D.A., and Simpfendorfer, C.C. "A Prospective Comparison of Rubidium-82 PET and Thallium-201 SPECT Myocardial Perfusion Imaging Utilizing a Single Dipyridamole Stress in the Diagnosis of Coronary Artery Disease". In: *Journal of Nuclear Medicine* 31.12 (1990), p. 1899.

[394] Saha, G.B., Go, R.T., Macintyre, W.J., Marwick, T.H., Beachler, A., King, J.L., and Neumann, D.R. "Use of the ^{82}Sr/^{82}Rb Generator in Clinical PET Studie". In: *Nuclear Medicine and Biology* 17.8 (1990), p. 763.

[395] Di Carli, M.F., Dorbala, S., Meserve, J., El Fakhri, G., Sitek, A., and Moore, S.C. "Clinical Myocardial Perfusion PET/CT". In: *Journal of Nuclear Medicine* 48.5 (2007), p. 783.

[396] Klein, R., Adler, A., Beanlands, R.S., and deKemp, R.A. "Precision-controlled elution of a ^{82}Sr/^{82}Rb generator for cardiac perfusion imaging with positron emission tomography". In: *Physics in Medicine and Biology* 52 (2007), p. 659.

[397] Merhige, M.E., Breen, W.J., Shelton, V., Houston, T., D'Arcy, B.J., and Perna, A.F. "Impact of myocardial perfusion imaging with PET and ^{82}Rb on downstream invasive procedure utilization, costs, and outcomes in coronary disease management". In: *Journal of Nuclear Medicine* 48.7 (2007), p. 1069.

[398] Yoshinaga, K., Klein, R., and Tamaki, N. "Generator-produced rubidium-82 positron emission tomography myocardial perfusion imaging – From basic aspects to clinical applications". In: *Journal of Cardiology* 55 (2010), p. 163.

[399] Dhar, R. and Ananthasubramaniam, K. "Rubidium-82 Cardiac Positron Emission Tomography Imaging: An Overview for the General Cardiologist". In: *Cardiology in Review* 19.5 (2011), p. 255.

[400] Scholtens, A. and Barneveld, P.C. "Rubidium-82 myocardial perfusion PET/CT". In: *Tijdschrift voor Nucleaire Geneeskunde* 39 (2017), p. 1817.

[401] Grant, P.M., Erdal, B.R., and O'Brien, H.A.Jr. "A ^{82}Sr-^{82}Rb isotope generator for use in nuclear medicine". In: *Journal of Nuclear Medicine* 16.4 (1975), p. 300.

[402] Mausner, L.F., Prach, T., and Srivastava, S.C. "Production of ^{82}Sr by proton irradiation of RbCl". In: *Applied Radiation and Isotopes* 38 (1987), p. 181.

[403] Cackette, M.R., Ruth, T.J., and Vincent, J.S. "^{82}Sr Production from Metallic Rb Targets and Development of an ^{82}Rb Generator System". In: *Applied Radiation and Isotopes* 44.6 (1993), p. 917.

[404] Bilewicz, A., Barto, B., Misiak, R., and Petelenz, B. "Separation of ^{82}Sr from rubidium target for preparation of ^{82}Sr/^{82}Rb generator". In: *Journal of Radioanalytical and Nuclear Chemistry* 268.3 (2005), p. 485.

[405] Huszár, I., Youfeng, H., Jegge, J., and Weinreich, R. "Development of a production process for ^{82}Sr". In: *Journal of Labelled Compounds and Radiopharmaceuticals* 26 (1989), p. 168.

[406] Deptula, C., Khalkin, V.A., Sen Han, K., Knotek, O., Konov, V.A., Mikecz, P., Poponenkova, L.M., Rurarz, E., and Zaitseva, N.G. "Excitation functions and yields for medically generator Sr^{82}-Rb^{82}, Xe^{123}-I^{123} and Bi^{201}-Pb^{201}-Tl^{201} obtained with 100 MeV protons". In: *Nukleonika* 35 (1990), p. 3.

[407] Lagunas-Solar, M.C. "Radionuclide production with > 70-MeV proton accelerators: current and future prospects". In: *Nuclear Instruments and Methods in Physics Research Section B: Beam Interactions with Materials and Atoms* 69 (1992), p. 452.

[408] Gilabert, E., Lavielle, B., Neumann, S., Gloris, M., Michel, R., Schiekel, Th., Sudbrock, F., and Herpers, U. "Cross sections for the proton-induced production of krypton isotopes from Rb, Sr, Y, and Zr for energies up to 1600 MeV". In: *Nuclear Instruments and Methods in Physics Research Section B: Beam Interactions with Materials and Atoms* 145 (1998), p. 293.

[409] Ido, T., Hermanne, A., Ditrói, F., Szűcs, Z., Mahunka, I., and Tárkányi, F. "Excitation functions of proton induced nuclear reactions on ^{nat}Rb from 30 to 70 MeV. Implication for the production of ^{82}Sr and other medically important Rb and Sr radioisotopes". In: *Nuclear Instruments and Methods in Physics Research Section B: Beam Interactions with Materials and Atoms* 194 (2002), p. 369.

[410] Buthelezi, E.Z., Nortierb, F.M., and Schroeder, I.W. "Excitation functions for the production of ^{82}Sr by proton bombardment of ^{nat}Rb at energies up to 100 MeV". In: *Applied Radiation and Isotopes* 64 (2006), p. 915.

[411] Takács, S., Tárkányi, F., Hermanne, A., and Paviotti de Corcuera, R. "Validation and upgrading of the recommended cross section data of charged particle reactions used for production of PET radioisotopes". In: *Nuclear Instruments and Methods in Physics Research Section B: Beam Interactions with Materials and Atoms* 211 (2003), p. 169.

[412] Tárkányi, F., Qaim, S.M., and Stöcklin, G. "Excitation Functions of ^{3}He- and α-Particle Induced Nuclear Reactions on Natural Krypton: Production of ^{82}Sr at a Compact Cyclotron". In: *Applied Radiation and Isotopes* 39.2 (1988), p. 135.

[413] Tárkányi, F., Qaim, S.M., and Stöcklin, G. "Excitation Functions of High-Energy ^{3}He- and Alpha-Particle Induced Nuclear Reactions on Natural Krypton with Special Reference to the Production of ^{82}Sr". In: *Applied Radiation and Isotopes* 41.1 (1990), p. 91.

[414] Robertson, R., Graham, D., and Trevena, I.C. "Radioisotope production via 500 MeV proton-induced reactions". In: *Journal of Labelled Compounds and Radiopharmaceuticals* 19 (1982), p. 1368.

[415] Thomas, K.E. "Strontium-82 production at Los Alamos National Laboratory". In: *Applied Radiation and Isotopes* 38 (1987), p. 175.

[416] Kodina, G.E., Kurenkov, N.V., Kurchatova, L.N., Malinin, A.B., and Sheina, T.Yu. "Production of Strontium-82 and preparation of the rubidium-82 generator". In: *PSI Proceedings of the IVth International Workshop on Targetry and Target Chemistry*. 1992, p. 66.

[417] Lopci, E., Chiti, A., Castellani, M.R., Pepe, G., Antunovic, L., Fanti, S., and Bombardieri, E. "Matched pairs dosimetry: $^{124}I/^{131}I$ metaiodobenzylguanidine and $^{124}I/^{131}I$ and $^{86}Y/^{90}Y$ antibodies". In: *European Journal of Nuclear Medicine and Molecular Imaging* 38.S1 (2011), S28.

[418] Rösch, F., Herzog, H., and Qaim, S.M. "The Beginning and Development of the Theranostic Approach in Nuclear Medicine, as Exemplified by the Radionuclide Pair ^{86}Y and ^{90}Y". In: *Pharmaceuticals* 10 (2017), p. 56.

[419] Bandara, N., Stott Reynolds, T.J., Schehr, R., Bandari, R.P., Diebolder, P.J., Krieger, S., Xu, J., Miao, Y., Rogers, B.E., and Smith, C.J. "Matched-pair, $^{86}Y/^{90}Y$-labeled, bivalent RGD/bombesin antagonist, [RGD-Glu-[DO3A]-6-Ahx-RM2], as a potential theranostic agent for prostate cancer". In: *Nuclear Medicine and Biology* 62–63 (2018), p. 71.

[420] Goffredo, V., Paradiso, A., Ranieri, G., and Gadaleta, C.D. "Yttrium-90 (^{90}Y) in the principal radionuclide therapies: An efficacy correlation between peptide receptor radionuclide therapy, radioimmunotherapy and transarterial radioembolization therapy. Ten years of experience (1999–2009)". In: *Critical Reviews in Oncology/Hematology* 80 (2011), p. 393.

[421] Wright, C.L., Zhang, J., Tweedle, M.F., Knopp, M.V., and Hall, N.C. "Theranostic Imaging of Yttrium-90". In: *BioMed Research International* 2015 (2015), p. 481279.

[422] Nayak, T.K. and Brechbiel, M.W. "^{86}Y based PET radiopharmaceuticals: radiochemistry and biological applications". In: *Journal of Medicinal Chemistry* 7.5 (2011), p. 380.

[423] Schmitz, J. "The production of [^{124}I]iodine and [^{86}Y]yttrium". In: *European Journal of Nuclear Medicine and Molecular Imaging* 38.S1 (2011), S4.

[424] Rösch, F., Qaim, S.M., and Stöcklin, G. "Nuclear Data Relevant to the Production of the Positron Emitting Radioisotope ^{86}Y via the ^{86}Sr(p,n)- and $^{nat}Rb(^{3}He,xn)$-Processes." In: *Radiochimica Acta* 6 (1993), p. 1.

[425] Rösch, F., Qaim, S.M., and Stöcklin, G. "Production of the Positron Emitting Radioisotope ^{86}Y for Nuclear Medical Application". In: *Applied Radiation and Isotopes* 44.4 (1993), p. 677.

[426] Kettern, K., Linse, K.-H., Spellerberg, S., Coenen, H.H., and Qaim, S.M. "Radiochemical studies relevant to the production of ^{86}Y and ^{88}Y at a small-sized cyclotron". In: *Radiochimica Acta* 90 (2002), p. 845.

[427] Yoo, J., Tang, L., Perkins, T.A., Rowland, D.J., Laforest, R., Lewis, J.S., and Welch, M.J. "Preparation of high specific activity ^{86}Y using a small biomedical cyclotron". In: *Nuclear Medicine and Biology* 32 (2005), p. 891.

[428] Avila-Rodriguez, M.A., Nyeb, J.A., and Nickles, R.J. "Production and separation of non-carrier-added ^{86}Y from enriched ^{86}Sr targets". In: *Applied Radiation and Isotopes* 66 (2008), p. 9.

[429] Lukić, D., Tamburella, C., Buchegger, F., Beyer, G.-J., Čomor, J.J., and Seimbille, Y. "High efficiency production and purification of ^{86}Y based on electrochemical separation". In: *Applied Radiation and Isotopes* 67 (2009), p. 523.

[430] Elbinawi, A., Al-Abyad, M., Bashter, I., Seddik, U., and Ditrói, F. "Excitation function of proton induced nuclear reaction on strontium: Special relevance to the production of ^{88}Y". In: *Applied Radiation and Isotopes* 140 (2018), p. 272.

[431] Lövqvist, A., Humm, J.L., Sheikh, A., Finn, R.D., Koziorowski, J., Ruan, S., Pentlow, K.S., Jungbluth, A., Welt, S., Lee, F.T., Brechbiel, M.W., and Larson, S.M. "PET Imaging of ^{86}Y-Labeled Anti-Lewis Y Monoclonal Antibodies in a Nude Mouse Model: Comparison Between ^{86}Y and ^{111}In Radiolabels". In: *Journal of Nuclear Medicine* 42.8 (2001), p. 1281.

[432] McQuade, P., Miao, Y., Yoo, J., Quinn, T.P., Welch, M.J., and Lewis, J.S. "Imaging of Melanoma Using ^{64}Cu- and ^{86}Y-DOTA-ReCCMSH(Arg11), a Cyclized Peptide Analogue of α-MSH". In: *Journal of Medicinal Chemistry* 48 (2005), p. 2985.

[433] Baimukhanova, A., Radchenko, V., Kozempel, J., Marinova, A., Brown, V., Karandashev, V., Karaivanov, D., Schaffer, P., and Filosofov, D. "Utilization of (p,4n) reaction for ^{86}Zr production with medium energy protons and development of a ^{86}Zr→^{86}Y radionuclide generator". In: *Journal of Radioanalytical and Nuclear Chemistry* 316 (2018), p. 191.

[434] Sachdev, D.R., Porile, N.T., and Yaffe L. "Reactions of ^{88}Sr with protons of energies 7-85 MeV". In: *Canadian Journal of Chemistry* 45 (1967), p. 1149.

[435] Tárkányi, F., Hermanne, A., Ditrói, F., Takács, S., Szücs, Z., and Brezovcsik, K. "Investigation of activation cross sections for deuteron induced reactions on strontium up to 50 MeV". In: *Applied Radiation and Isotopes* 127 (2017), p. 16.

[436] S. Iwata. "Isomeric Cross Section Ratios in Alpha-Particle Reactions". In: *Journal of the Physical Society of Japan* 17 (1962), p. 1323.

[437] Demeyer, A., Chevarier, N., Chevarier A., and Tran Minh, D. "Reculs moyens, rapports isomériques et fonctions d'excitation pour les réactions induites par des particules alpha sur le rubidium". In: *Journal de Physique France* 32.8–9 (1971), p. 583.

[438] Guin, R., Das, S.K., and Saha, S.K. "Cross-sections and linear momentum transfer in α-induced reactions on ^{85}Rb". In: *Radiochimica Acta* 88 (2000), p. 435.

[439] Bigott, H.M., Mccarthy, D.W., Wüst, F.R., Dahlheimer, J.L., Piwnica-Worms, D.R., and Welch, M.J. "Production, processing and uses of ^{94m}Tc". In: *Journal of Labelled Compounds and Radiopharmaceuticals* 50 (2001), S119.

[440] Qaim, S.M. "The present and future of medical radionuclide production". In: *Radiochimica Acta* 100 (2012), p. 635.

[441] Nickles, R.J., Nunn, A.D., Stone, C.K., and Christian, B.T. "Technetium-94m-Teboroxime: Synthesis, Dosimetry and Initial PET Imaging Studies". In: *Journal of Nuclear Medicine* 34.7 (1993), p. 1058.

[442] Stone, C.K., Christian, B.T., Nickles, R.J., and Perlman, S.B. "Technetium 94m-labeled methoxyisobutyl isonitrile: Dosimetry and resting cardiac imaging with positron emission tomography". In: *Journal of Nuclear Cardiology* 1 (1994), p. 425.

[443] Luyt, L.G., Bigott, H.M., Welch, M.J., and Katzenellenbogen, J.A. "7α- and 17α-Substituted Estrogens Containing Tridentate Tricarbonyl Rhenium/Technetium Complexes: Synthesis of Estrogen Receptor Imaging Agents and Evaluation Using MicroPET with Technetium-94m". In: *Bioorganic & Medicinal Chemistry* 11 (2003), p. 4977.

[444] Rösch, F. and Qaim, S.M. "Nuclear Data Relevant to the Production of the Positron Emitting Technetium Isotope ^{94m}Tc via the ^{94}Mo(p,n)-reaction". In: *Radiochimica Acta* 62 (1993), p. 115.

[445] Rösch, F., Novgorodov, A.F., and Qaim, S.M. "Thermochromatographic Separation of ^{94m}Tc from Enriched Molybdenum Targets and its Large Scale Production for Nuclear Medical Application". In: *Radiochimica Acta* 64 (1994), p. 113.

[446] Bigott, H.M., Laforest, R., Liu, X., Ruangma, A., Wuest, F., and Welch, M.J. "Advances in the production, processing and microPET image quality of technetium-94m". In: *Nuclear Medicine and Biology* 33.7 (2006), p. 923.

[447] Uddin, M.S., Hagiwara, M., Tárkányi, F., Ditrói, F., and Baba, M. "Experimental studies on the proton-induced activation reactions of molybdenum in the energy range 22–67 MeV". In: *Applied Radiation and Isotopes* 60 (2004), p. 911.

[448] Kakavand, T., Aref, M., Rajabifar, S., and Razavi, R. "Cyclotron production of ^{94m}Tc via ^{94}Mo(p,n)^{94m}Tc reaction". In: *Indian Journal of Pure & Applied Physics* 51 (2013), p. 7.

[449] Hoehr, C., Morley, T., Buckley, K., Trinczek, M., Hanemaayer, V., Schaffer, P., Ruth, T., and Bénard, F. "Radiometals from liquid targets: ^{94m}Tc production using a standard water target on a 13 MeV cyclotron". In: *Applied Radiation and Isotopes* 70 (2012), p. 2308.

[450] Christian, B.T., Nickles, R.J., Stone, C.K., Mulnix, T.L., and Clark, J. "Improving the radionuclidic purity of ^{94m}Tc for PET imaging". In: *Applied Radiation and Isotopes* 46.2 (1995), p. 69.

[451] Denzler, F.-O., Rösch, F., and Qaim, S.M. "Excitation Functions of α-Particle Induced Nuclear Reactions on Highly Enriched ^{92}Mo: Comparative Evaluation of Production Routes for ^{94m}Tc". In: *Radiochimica Acta* 68 (1995), p. 13.

[452] Faßbender, M., Novgorodov, A.F., Rösch, F., and Qaim, S.M. "Excitation Functions of ^{93}Nb(^{3}He,xn)^{93m,g,94m,g,95m,g}Tc-Processes from Threshold up to 35 MeV: Possibility of Production of ^{94m}Tc in High Radiochemical Purity using a Thermochromatographic Separation Technique". In: *Radiochimica Acta* 65 (1994), p. 215.

[453] Branquinho, C.L., Hoffmann, S.M.A., Newton, G.W.A., Robinson, V.J., Wang, H.-Y., Grant, I.S., and Goodall, J.A.B. "Excitation Functions and Isomer Ratios in the Reactions ^{93}Nb(α,xn) (x = 1–4)". In: *Journal of Inorganic and Nuclear Chemistry* 41 (1979), p. 617.

[454] Agarwal, A., Rizvi, I.A., and Chaubey, A.K. "Excitation function studies of a induced reactions for niobium and preequilibrium effects". In: *Physical Review C* 65 (2002), p. 034605.

[455] Lubberink, M., Tolmachev, V., Widström, C., Bruskin, A., Lundqvist, H., and Westlin, J.-E. "^{110m}In-DTPA-D-Phe1-Octreotide for Imaging of Neuroendocrine Tumors with PET". In: *Journal of Nuclear Medicine* 43.10 (2002), p. 1391.

[456] Tolmachev, V., Bernhardt, P., Forssell-Aronsson, E., and Lundqvist, H. "^{114m}In, a candidate for radionuclide therapy: low-energy cyclotron production and labeling of DTPA-D-Phe-octreotide". In: *Nuclear Medicine and Biology* 27.2 (2000), p. 183.

[457] Tárkányi, F., Takács, S., Ditrói, F., Hermanne, A., Baba, M., Mohsena, B.M.A., and Ignatyuk, A.V. "New cross section data and review of production routes of medically used ^{110m}In". In: *Nuclear Instruments and Methods in Physics Research Section B: Beam Interactions with Materials and Atoms* 351 (2015), p. 6.

[458] Otozai, K., Kume, S., Mito, A., Okamura, H., Tsujino, R., Kanchiku, Y., Katoh, T., and Gotoh, H. "Excitation functions for the reactions induced by protons on Cd up to 37 MeV." In: *Nuclear Physics* 80 (1966), p. 335.

[459] Abramovich, S.N., Guzhovskij, B.Ja., Zvenigorodskij, A.G., and Trusillo, S.V. "Isobaric Analog Resonances Appearing during Elastic Scattering of Protons and in the (p,n) Reaction on ^{110,112,114,116}Cd". In: *Izvestiya Rossiiskoi Akademii Nauk USSR, Seriya Fizicheskaya* 39 (1975), p. 1688.

[460] Skakun, E.A., Klyucharev, A.P., Rakivnenko, Yu.N., and Romanii, I.A. "Excitation Functions of (p,n)- and (p,2n)-Reactions on Cadmium Isotopes". In: *Izvestiya Rossiiskoi Akademii Nauk USSR, Seriya Fizicheskaya* 39.1 (1975), p. 18.

[461] Kormali, S.M., Swindle, D.L., and Schweikert, E.A. "Charged particle activation of medium Z elements II. Proton excitation functions". In: *Journal of Radioanalytical and Nuclear Chemistry* 31 (1976), p. 437.

[462] Marten, M., Schtiring, A., Scobel, W., and Probst, H.J. "Preequilibrium Neutron Emission in ^{109}Ag(^{3}He,xn) and ^{111}Cd(p,xn) Reactions". In: *Zeitschrift für Physik A – Atoms and Nuclei* 322 (1985), p. 93.

[463] Nortier, F.M., Mills, S.J., and Steyn, G.F. "Excitation functions and production rates of relevance to the production of ^{111}In by proton bombardment of ^{nat}Cd and ^{nat}In up to 100 MeV". In: *Applied Radiation and Isotopes* 41 (1990), p. 1201.

[464] Tárkányi, F., Király, B., Ditrói, F., Takács, S., Csikai, J., Hermanne, A., Uddin, M.S., Hagiwara, M., Baba, M., Ido, T., Shubin, Yu.N., and Kovalev, S.F. "Activation cross-sections on cadmium: proton induced nuclear reactions up to 80 MeV". In: *Nuclear Instruments and Methods in Physics Research Section B: Beam Interactions with Materials and Atoms* 245 (2006), p. 379.

[465] Al-Saleh, F.S. "Cross sections of proton induced nuclear reactions on natural cadmium leading to the formation of radionuclides of indium". In: *Radiochimica Acta* 96 (2008), p. 461.

[466] Khandaker, M.U., Kim, K., Lee, M.W., Kim, K.S., Kim, G.N., Cho, Y.S., and Lee, Y.O. "Production cross-sections for the residual radionuclides from the ^{nat}Cd(p,x) nuclear processes". In: *Nuclear Instruments and Methods in Physics Research Section B: Beam Interactions with Materials and Atoms* 266 (2008), p. 4877.

[467] Büyükuslu, H., Kaplan, A., Yildirim, G., Aydin, A., Tel, E., and Bölükdemir, M.H. "Production cross sections of medical ^{110,111}In radionuclides". In: *Kerntechnik* 75.3 (2010), p. 103.

[468] Hermanne, A., Adam-Rebeles, R., Van den Winkel, P., Tárkányi, F., and Takács, S. "Activation of ^{112}Cd by deuteron induced reactions up to 50 MeV: An alternative for ^{111}In production?" In: *Nuclear Instruments and Methods in Physics Research Section B: Beam Interactions with Materials and Atoms* 339 (2014), p. 26.

[469] Hermanne, A., Daraban, L., Adam-Rebeles, R., Ignatyuk, A., Tárkányi, F., and Takács, S. "Alpha induced reactions on ^{nat}Cd up to 38.5 MeV: Experimental and theoretical studies of the excitation functions". In: *Nuclear Instruments and Methods in Physics Research Section B: Beam Interactions with Materials and Atoms* 268 (2010), p. 1376.

[470] Wasilevsky, C., De La Vega Vedoya, M., and Nassiff, S.J. "Excitation functions for (α,xn) reactions on ^{107}Ag and ^{109}Ag". In: *Journal of Radioanalytical and Nuclear Chemistry* 89.2 (1985), p. 531.

[471] Chaubey, A.K., Bhardwaj, M.K., Gautam, R.P., Singh, R.K.Y., Afzal Ansari, M., Rizvi, I.A., and Singh, H. "Pre-Equilibrium Decay Process in the Alpha Induced Reactions of Silver Isotopes". In: *Applied Radiation and Isotopes* 41 (1990), p. 401.

[472] Guin, R., Saha, S.K., Prakash, S., and Uhl, M. "Isomeric yield ratios and excitation functions in α-induced reactions on ^{107,109}Ag". In: *Physical Review C* 46.1 (1992), p. 250.

[473] Kakavand, T., Mirzaii, M., Eslami, M., and Karimi, A. "Nuclear model calculation and targetry recipe for production of ^{110m}In". In: *Applied Radiation and Isotopes* 104 (2015), p. 60.

[474] Mukhammedov, S., Vasidov, A., and Pardaev, É. "Application of proton and neutron activation method of analysis for the determination of elements with Z greater than 42". In: *Atomnaya Ehnergiya* 56.1 (1984), p. 50.

[475] Lundqvist, H., Scott-Robson, S., Einarsson, L., and Malmborg, P. "^{110}Sn/^{110}In – A New Generator System for Positron Emission Tomography". In: *Applied Radiation and Isotopes* 42.5 (1991), p. 447.

[476] de Klerk, J.M.H. "^{131}I Therapy: Inpatient or Outpatient?" In: *Journal of Nuclear Medicine* 41.11 (2000), p. 1876.

[477] Higashi, T., Kudo, T., and Kinuya, S. "Radioactive iodine (^{131}I) therapy for differentiated thyroid cancer in Japan: current issues with historical review and future perspective". In: *Annals of Nuclear Medicine* 26 (2012), p. 99.

[478] Blasberg, R.G., Roelcke, U., and Weinreich, R. "[^{124}I]-iododeoxyuridine imaging tumor proliferation". In: *Journal of Nuclear Medicine* 37 (May 1996).

[479] Blasberg, R.G., Roelcke, U., Weinreich, R., Beattie, B., von Ammon, K., Yonekawa, Y., Landolt, H., Guenther, I., Crompton, N.E.A., Vontobel, P., Missimer, J., Maguire, R.P., Koziorowski, J., Joachim Knust, E., Finn, R.D., and Leenders, K.L. "Imaging Brain Tumor Proliferative Activity with [^{124}I]Iododeoxyuridine". In: *Cancer Research* 60 (2000), p. 624.

[480] Roelcke, U., Hausmann, O., Merlo, A., Missimer, J., Maguire, R.P., Freitag, P., Radü, E.W., Weinreich, R., Gratzl, O., and Leenders, K.L. "PET Imaging Drug Distribution After Intratumoral Injection: The Case for ^{124}I-Iododeoxyuridine in Malignant Gliomas". In: *Journal of Nuclear Medicine* 43.11 (2002), p. 1444.

[481] Langen, K.J., Coenen, H.H., Roosen, N., Kling, P., Muzik, O., Herzog, H., Kuwert, T., Stöcklin, G., and Feinendegen, L.E. "SPECT studies of brain tumors with L-3-[^{123}I] iodo-alpha-methyl tyrosine: comparison with PET, ^{124}IMT and first clinical results". In: *Journal of Nuclear Medicine* 31 (1990), p. 281.

[482] Snook, D.E., Rowlinson-Busza, G., Sharma, H.L., and Epenetos, A.A. "Preparation and in vivo study of ^{124}I-labelled monoclonal antibody H17E2 in a human tumour xenograft model. A prelude to positron emission tomography (PET)". In: *British Journal of Cancer* 62.SX (1990), p. 89.

[483] Wilson, C.B., Snook, D.E., Dhokia, B., Taylor, C.V.J., Watson, I.A., Lammertsma, A.A., Lambrecht, R., Waxman, J., Jones, T., and Epenetos, A.A. "Quantitative measurement of monoclonal antibody distribution and blood flow using positron emission tomography and ^{124}iodine in patients with breast cancer". In: *International Journal of Cancer* 47 (1991), p. 344.

[484] Frey, P., Townsend, D., Flattet, A., De Gautard, R., Widgren, S., Jeavons, A., Christin, A., Smith, A., Long, A., and Donath, A. "Tomographic imaging of the human thyroid using ^{124}I". In: *Journal of Clinical Endocrinology and Metabolism* 63.4 (1986), p. 918.

[485] Phan, H.T.T., Jager, P.L., Paans, A.M.J., Plukker, J.T.M., Sturkenboom, M.G.G., Sluiter, W.J., Wolffenbuttel, B.H.R., Dierck, R.A.J.O., and Links, T.P. "The diagnostic value of ^{124}I-PET in patients with differentiated thyroid cancer". In: *European Journal of Nuclear Medicine and Molecular Imaging* 35.5 (2008), p. 958.

[486] Capoccetti, F., Criscuoli, B., Rossi, G., Ferretti, F., Manni, C., and Brianzoni, E. "The effectiveness of ^{124}I PET/CT in patients with differentiated thyroid cancer". In: *European Journal of Nuclear Medicine and Molecular Imaging* 53.5 (2009), p. 536.

[487] Kharazi, P., Atkins, F., Khorjekar, G., Chennupati, S., and Van Nostrand, D. "^{124}I in differentiated thyroid cancer: An educational exhibit". In: *Journal of Nuclear Medicine* 52.S1 (2011), p. 1069.

[488] Plyku, D., Hobbs, R.F., Huang, K., Atkins, F., Garcia, C., Sgouros, G., and Van Nostrand, D. "Recombinant Human Thyroid-Stimulating Hormone Versus Thyroid Hormone Withdrawal in ^{124}I PET/CT-Based Dosimetry for ^{131}I Therapy of Metastatic Differentiated Thyroid Cancer". In: *Journal of Nuclear Medicine* 58.7 (2017), p. 1146.

[489] Stepanek, J., Larsson, B., and Weinreich, R. "Auger-electron spectra of radionuclides for therapy and diagnostics". In: *Acta Oncologica* 35 (1996), p. 863.

[490] Azizakram, H., Sadeghi, M., Ashtari, P., and Zolfagharpour, F. "An overview of ^{124}I production at a medical cyclotron by ALICE/ASH, EMPIRE-3.2.2 and TALYS-1.6 codes". In: *Applied Radiation and Isotopes* 112 (2016), p. 147.

[491] Kondo, K., Lambrecht, R.M., Norton, E.F., and Wolf, A.P. "Cyclotron Isotopes and Radiopharmaceuticals-XXII, Improved Targetry and Radiochemistry for Production of ^{123}I and ^{124}I". In: *Applied Radiation and Isotopes* 28 (1977), p. 765.

[492] Scholten, B., Kovàcs, Z., Tárkányi, F., and Qaim, S.M. "Excitation Functions of ^{124}Te(p,xn)^{124,123}I Reactions from 6 to 31 MeV with Special Reference to the Production of ^{124}I at a Small Cyclotron". In: *Applied Radiation and Isotopes* 46.4 (1995), p. 255.

[493] Qaim, S.M., Hohn, A., Bastian, Th., El-Azoney, K.M., Blessing, G., Spellerberg, S., Scholten, B., and Coenen, H.H. "Some optimisation studies relevant to the production of high-purity ^{124}I and ^{120g}I at a small-sized cyclotron". In: *Applied Radiation and Isotopes* 58 (2003), p. 69.

[494] Sajjad, M., Bars, E., and Nabi, H.A. "Optimization of ^{124}I production via ^{124}Te(p,n)^{124}I reaction". In: *Applied Radiation and Isotopes* 64 (2006), p. 965.

[495] Nye, J.A., Avila-Rodriguez, M.A., and Nickles, R.J. "A new binary compound for the production of ^{124}I via the ^{124}Te(p,n)^{124}I reaction". In: *Applied Radiation and Isotopes* 65 (2007), p. 407.

[496] Aslam, M.N., Sudár, S., Hussain, M., Malik, A.A., Shah, H.A., and Qaim, S.M. "Evaluation of excitation functions of proton and deuteron induced reactions on enriched tellurium isotopes with special relevance to the production of iodine-124". In: *Applied Radiation and Isotopes* 68 (2010), p. 1760.

[497] Lambrecht, R.M., Sajjad, M., Qureshi, M.A., and Al-Yanbawi, S.J. "Production of iodine-124". In: *Journal of Radioanalytical and Nuclear Chemistry* 127 (1988), p. 143.

[498] Clem, R.G. and Lambrecht, R.M. "Enriched ^{124}Te targets for production of ^{123}I and ^{124}I". In: *Nuclear Instruments and Methods in Physics Research Section A: Accelerators, Spectrometers, Detectors and Associated Equipment* 303 (1991), p. 115.

[499] Weinreich, R. and Knust, E.J. "Quality assurance of iodine-124 produced via the nuclear reaction ^{124}Te(d,2n)^{124}I". In: *Journal of Radioanalytical and Nuclear Chemistry* 213.4 (1996), p. 253.

[500] Bastian, T., Coenen, H.H., and Qaim, S.M. "Excitation functions of ^{124}Te(d,xn)^{124,125}I reactions from threshold up to 14 MeV: comparative evaluation of nuclear routes for the production of ^{124}I". In: *Applied Radiation and Isotopes* 55 (2001), p. 303.

[501] Dmitriev, P.P. "Systematics of nuclear reaction yields for thick target at 22 MeV proton energy". In: *Vop. At. Nauki i Tekhn., Ser. Yadernye Konstanty* 2 (1983), p. 57.

[502] Kim, J.H., Lee, J.S., Lee, T.S., Park, H., and Chun, K.S. "Optimization studies on the production of high-purity ^{124}I using (p,2n) reaction". In: *Journal of Labelled Compounds and Radiopharmaceuticals* 50 (2007), p. 511.

[503] Akbari, R.B., Ott, R.J., Trott, N.G., Sharma, H.L., and Smith, A.G. "Radionuclide purity and radiation dosimetry of ^{124}I used in positron tomography of the thyroid". In: *Physics in Medicine and Biology* 31 (1986), p. 789.

[504] Hassan, K.F., Qaim, S.M., Saleh, Z.A., and Coenen, H.H. "Alpha-particle-induced reactions on ^{nat}Sb and ^{121}Sb with particular reference to the production of the medically interesting radionuclide ^{124}I". In: *Applied Radiation and Isotopes* 64 (2006), p. 101.

[505] Uddin, M.S., Hermanne, A., Sudar, S., Aslam, M.N., Scholten, B., Coenen, H.H., and Qaim, S.M. "Excitation functions of α-particle induced reactions on enriched ^{123}Sb and ^{nat}Sb for production of ^{124}I". In: *Applied Radiation and Isotopes* 69 (2011), p. 699.

[506] Litzenberg, D.W., Roberts, D.A., Lee, M.Y., Pham, K., Vander Molen, A.M., Ronningen, R., and Becchetti, F.D. "On-line monitoring of radiotherapy beams: Experimental results with proton beams". In: *Medical Physics* 26.6 (1999), p. 992.

[507] Enghardt, W., Crespo, P., Fiedler, F., Hinz, R., Parodi, K., Pawelke, J., and Ponisch, F. "Charged hadron tumour therapy monitoring by means of PET". In: *Nuclear Instruments and Methods in Physics Research Section A: Accelerators, Spectrometers, Detectors and Associated Equipment* 525 (2004), p. 284.

[508] Cambraia Lopes, P., Bauer, J., Salomon, A., Rinaldi, I., Tabacchini, V., Tessonnier, T., Crespo, P., Parodi, K., and Schaart, D.R. "First in situ TOF-PET study using digital photon counters for proton range verification". In: *Physics in Medicine and Biology* 61 (2016), p. 6203.

[509] D'Ascenzo, N., Gao, M., Antonecchia, E., Gnudi, P., Chen, H.-H., Chen, F.-H., Hong, J.-H., Hsiao, I.-T., Yen, T.-C., Wang, W., Xi, D., Zhang, B., and Xie, Q. "New Digital Plug and Imaging Sensor for a Proton Therapy Monitoring System Based on Positron Emission Tomography". In: *Sensors* 18 (2018), p. 3006.

[510] Oelfke, U., Lam, G.K.Y., and Atkins, M.S. "Proton dose monitoring with PET: quantitative studies in Lucite". In: *Physics in Medicine and Biology* 41 (1996), p. 177.

[511] Beebe-Wang, J., Vaska, P., Dilmanian, F.A., Peggs, S.G., and Schlyer, D.J. "Simulation of Proton Therapy Treatment Verification via PET Imaging of Induced Positron-Emitters". In: *2003 IEEE Nuclear Science Symposium. Conference Record (IEEE Cat. No.03CH37515)*. Vol. 4. 2003, pp. 2496–2500. DOI: 10.1109/NSSMIC.2003.1352399.

[512] Dauvergne, D., Freud, N., Krimmer, J., Létang, J. M., and Testa, E. "Prompt-Gamma Monitoring of Proton- and Carbon-Therapy. Combined Development of Time-of-Flight Collimated- and Compton-Cameras". In: *Acta Physica Polonica A* 127.5 (2015), p. 1445.

[513] Schueller, M.J., Nickles, R.J., Roberts, A.D., and Jensen, M. "Production and Extraction of [^{10}C]-CO_2 From Proton Bombardment of Molten $^{10}B_2O_3$". In: *AIP Conference Proceedings* 680 (2003), p. 1094.

[514] Amaudruz, P.-A., Batygov, M., Beltran, B., Bonatt, J., Boudjemline, K., Boulay, M.G., Broerman, B., Bueno, J.F., Butcher, A., Cai, B., Caldwell, T., Chen, M., Chouinard, R., Cleveland, B.T., Cranshaw, D., Dering, K., Duncan, F., Fatemighomi, N., Ford, R., Gagnon, R., Giampa, P., Giuliani, F., Gold, M., Golovko, V.V., Gorel, P., Grace, E., Graham, K., Grant, D.R., Hakobyan, R., Hallin, A.L., Hamstra, M., Harvey, P., Hearns, C., Hofgartner, J., Jillings, C.J., Kuźniak, M., Lawson, I., La Zia, F., Li, O., Lidgard, J.J., Liimatainen, P., Lippincott, W.H., Mathew, R., McDonald, A.B., McElroy, T., McFarlane, K., McKinsey, D.N., Mehdiyev, R., Monroe, J., Muir, A., Nantais, C., Nicolics, K., Nikkel, J., Noble, A.J., O'Dwyer, E., Olsen, K., Ouellet, C., Pasuthip, P., Peeters, S.J.M., Pollmann, T., Rau, W., Retière, F., Ronquest, M., Seeburn, N., Skensved, P., Smith, B., Sonley, T., Tang, J., Vázquez-Jáuregui, E., Veloce, L., Walding, J., and Ward, M. "Measurement of the scintillation time spectra and pulse-shape discrimination of low-energy β and nuclear recoils in liquid argon with DEAP-1". In: *Astroparticle Physics* 85 (2016), p. 1.

[515] Takács, S., Tárkányi, F., and Qaim, S.M. "Excitation function of ^{22}Ne(p,n)^{22}Na reaction: Possibility of production of ^{22}Na at a small cyclotron". In: *Applied Radiation and Isotopes* 47.3 (1996), p. 303.

[516] Mandal, B.Ch., Barua, L., Das, S.S., and Pal, G. "Development of a Ne gas target for ^{22}Na production by proton irradiation". In: *Review of Scientific Instruments* 87.3 (2016).

[517] Bodemann, R., Busemann, H., Gloris, M., Leya, I., Michel R., Schiekel, T., Herpers, U., Holmqvist, B., Condé, H., Malmborg, P., Dittrich-Hannen, B., and Suter, M. "New measurements of the monitor reactions ^{27}Al(p,x)^{7}Be, ^{27}Al(p,3p3n)^{22}Na, ^{27}Al(p,3pn)^{24}Na and ^{65}Cu(p,n)^{65}Zn". In: *Progress Report on Nuclear Data Research in the Federal Republic of Germany for the Period April I, 1994 to March 31, 1995*. Ed. by S.M. Qaim. 1995, p. 29.

[518] Ravn, H., Schulte, W.H., Rolfs, C., Waanders, F.B., and Kavanagh, R.W. "Production of ^{22}Na targets or positron sources by means of ion implantation". In: *Nuclear Instruments and Methods in Physics Research Section B: Beam Interactions with Materials and Atoms* 58.2 (1991), p. 174.